HIGH FIELD STARK EFFECTS IN DIATOMIC MOLECULES

BY

ETHAN ADAM SCARL

B.A., Reed College, 1961

M.S., Washington University, 1964

A THESIS SUBMITTED IN PARTIAL FULFILMENT OF

THE REQUIREMENTS FOR THE DEGREE OF

DOCTOR OF PHILOSOPHY

in the Department

of

PHYSICS

We accept this thesis as conforming to the required standard

THE UNIVERSITY OF BRITISH COLUMBIA

September, 1973

In presenting this thesis in partial fulfilment of the requirements for an advanced degree at the University of British Columbia, I agree that the Library shall make it freely available for reference and study. I further agree that permission for extensive copying of this thesis for scholarly purposes may be granted by the Head of my Department or by his representatives. It is understood that copying or publication of this thesis for financial gain shall not be allowed without my written permission.

Department of Physics

The University of British Columbia
Vancouver 8, Canada

Date October 6, 1973

ABSTRACT

A LoSurdo discharge was used to apply electric fields of more than 300 kV/cm to water vapor, a mixture of cyanogen and hydrogen, and ammonia, permitting the observation of Stark effects in the optical spectra of the OH, CH, and NH molecules, respectively. These experiments yielded the following values of the molecular electric dipole moment in the ground vibrational states:

$$\mu(OH,\ A\ ^2\Sigma^+) = 1.94_6 \pm 0.08_5\ D$$
$$\mu(OD,\ A\ ^2\Sigma^+) = 2.14_2 \pm 0.08_0\ D$$
$$\mu(CH,\ A\ ^2\Delta) = 0.88_7 \pm 0.04_5\ D$$
$$\mu(NH,\ X\ ^3\Sigma^-) = 1.38_9 \pm 0.04_3\ D\ .$$

The dipole moments of the $X\ ^2\Pi$ states in both OH and OD were also evaluated for v=0, 1, and 2, and were found to decrease as a function of v.

TABLE OF CONTENTS

LIST OF TABLES

LIST OF FIGURES

ACKNOWLEDGEMENTS

This is to express my gratitude to the two people whose patience and faith made this work possible: Professor F.W. Dalby, my research director, and Dona J. Scarl, my wife. I am in the debt of Professor Dalby for his many helpful discussions and his physical insight, and in the debt of Ms. Scarl for the effort and perseverance which were necessary to turn the work of physics into the physical work of this document.

This work was supported by the National Research Council of Canada.

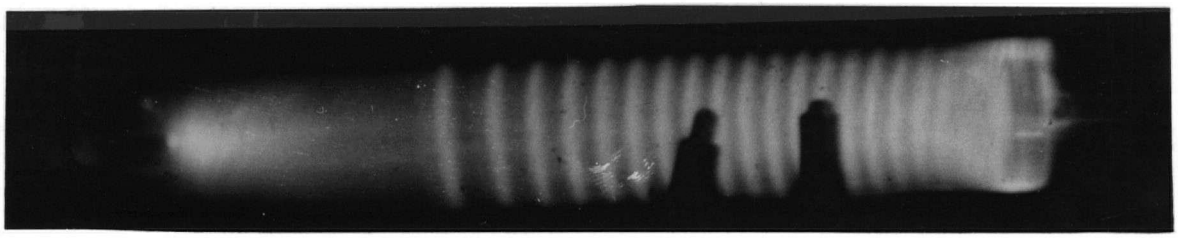

cathode (a) anode

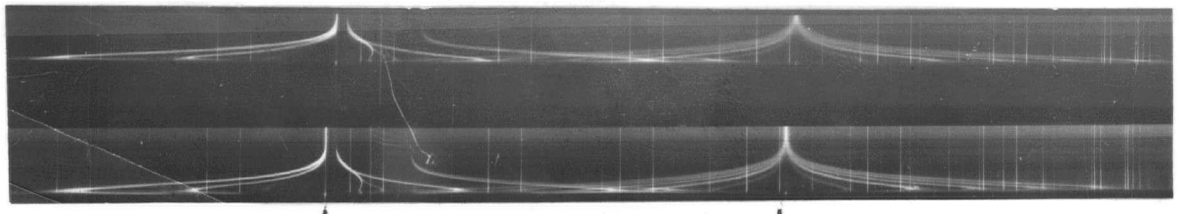

He 4922 Å (b) H_β 4861 Å

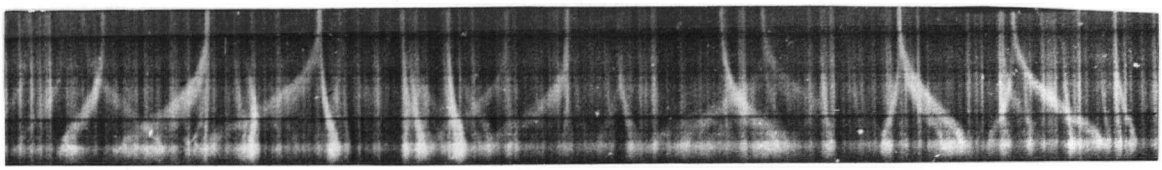

← λ (c)

Frontespiece

(a) The discharge tube, showing striations with dimethyl mercury over a 2 mm flush cathode. The picture is turned so that down is to the left.
(b) Stark effects in H_β (4861 Å) and He (4922 Å), photographed in second order. Other lines visible are from OH.
(c) Stark effects in molecular hydrogen (plate 257), photographed in first order, and showing approximately 5915 Å to 5985 Å. The plates were made with hydrogen and cyanogen at pressures totalling ~3.5 mm Hg, with about 11 kV applied voltage drawing 2 ma. The maximum field is about 165,000 kV/cm.

CHAPTER I

INTRODUCTION

Since the diatomic molecule represents the simplest possible chemical compound, it is important to be able to compare as wide a range of theoretical and experimental properties as possible. This will allow us to evaluate the accuracy of the particular calculational model used, and to have the fullest possible description of the molecules themselves. Conventional spectroscopy gives a great deal of information about the properties and structure of the molecular energy levels, and recent work with high-resolution resonance methods has yielded even more detailed information including details of the coupling of the various angular momenta with the magnetic moment of the nuclei. Much of this data, including the g-factors given Zeeman effect studies, can be accounted for in terms of the coupling schemes by which the different angular momenta interact (once the broad structure of the available electronic states has been determined), but the dependence upon the detailed structure of the molecular wavefunctions is not critical. Parameters which comprise relatively critical tests of the wavefunctions, and are readily calculated from them, are the molecular electric dipole and transition moments.

The simplest diatomic molecules for calculational purposes are the monohydrides. However, most of these are unstable, so that conventional methods (such as measurement

of dielectric constants) used to measure dipole moments of bulk or dissolved substances cannot be used. We have made use in this work of a method (the LoSurdo discharge) which allows the generation of high electric fields in the same general region of the discharge in which the molecules are formed.

Now, there are two distinct kinds of instability suffered by a diatomic molecule. It may be intrinsically unstable so that the isolated molecule spontaneously dissociates into separate atoms (i.e., the ground electronic state possesses no stable minimum of potential energy with respect to the distance between atoms), the most notable example being the He_2 molecule. However, in the overwhelming majority of known diatomic molecules, instability is not intrinsic, but rather due to very high chemical reactivity. These molecules will react not only with most other types of molecule, but with each other. Thus the molecules with which we are concerned have lifetimes which depend upon their concentrations and environment, and may be considered stable if kept sufficiently isolated. Such conditions of isolation cannot be easily realized in the laboratory, but may be found in the reaches of interstellar and intergalactic space. Since hydrogen is by far the most abundant material in these regions, it is clear that the hydrides of first-row elements must be important there. Indeed, CH was one of the first interstellar species discovered, and and the importance of OH in understanding interstellar conditions is now well known. Furthermore, all molecules

studied in this work have been detected in absorption in the spectra of the sun and other stars. Here again, a knowledge of the dipole moment is of particular interest since the absorption intensities of far infrared and microwave transitions (i.e., within the ground electronic and vibrational state) are proportional to its square.

The OH and OD molecules have been widely studied in their ground states, and we have used our high field plates together with a number of low field exposures to evaluate their dipole moments more accurately than had previously been done with this method, and to study variations with vibrational quantum number. By examining second order effects in Σ states where no first order effects are available, we have made the first reported determinations of the dipole moment in the ground state of NH, and in the first excited states of OH and OD. We were also able to substantially improve upon a previously reported value for the first excited state of CH.

Chapter II is intended to introduce the concept and role of "a dipole moment", and to detail assumptions later used in forming matrix elements. Chapters III through V provide the detailed quantum mechanical groundwork upon which our calculations are based. Chapter VI discusses the laboratory procedures and apparatus in detail, supplemented by the description of plate and field measurements in Chapter VII. The results for individual molecules are discussed in Chapters VIII - XI, and are summarized in Chapter XII along with those for the other first-row diatomic monohydride molecules.

The units which will normally be used throughout this work are described in Appendix A, while Appendix B provides a glossary of certain standard symbols which may be used without definition in the text. It is particularly important to note the unusual sign conventions for M, Λ, and Ω. Background introducing the reader to relevant aspects of the physics of glow discharges is given in Appendix C. A summary of some related theory and formulae are provided in Appendices D and E.

CHAPTER II

THE MOLECULAR DIPOLE MOMENT

1. Formulation of the Stark Perturbation for a Diatomic Molecule

The potential energy gained by a particle labeled i, of charge $+e_i$, while moving along an arc segment $d\vec{s}$ in an electric field $\vec{E}(x,y,z)$, is given by

$$dV_i = -e_i \vec{E} \cdot d\vec{s} \tag{1}$$

(the negative of the kinetic energy gained if the particle is free). If the field is uniform in both strength and direction and chosen to point in the positive z direction of the laboratory coordinates (x,y,z), then, integrating from the origin, the potential energy becomes

$$V_i = -e_i r_i E \cos\theta_i \tag{2}$$

with respect to its energy at the origin. Here r_i is the magnitude of the vector from the origin to the particle, and θ_i is the angle between $\vec{r}_i$ and the z axis. In applying this to a diatomic molecule with an axis of symmetry (internuclear axis) at angle θ from the z axis, and whose center of nuclear charge has been placed at the origin, we assign $\theta_i = \theta$ for all particles. While this is true

by definition in the case of the nuclei, for the electrons it represents the assumption of axial symmetry about the internuclear axis. In the absence of molecular rotation or external field, the time average of any θ_i must be θ. In other words, under the assumption that electronic motions are sufficiently faster than the rotation or vibration of the nuclei, the electrons can be considered to be located at their time-averaged positions on the internuclear axis, over the duration of a "snapshot" of the molecule with the nuclei fixed. The molecular potential energy can then be formed by summing Eq. (2) over all particles:

$$V = -\left(\sum_i e_i \zeta_i\right) E \cos\theta \qquad (3)$$

Here ζ is the coordinate along the internuclear axis in a cartesian coordinate system (ξ, η, ζ) fixed in the molecule (rotating coordinates), so that ζ_i is the ζ coordinate of particle i.

2. Classical Formulation

Eq. (3) can be used as a starting point for both classical and quantum mechanical consideration*. First, we note that the sum in Eq. (3) may be taken over the electrons only. (The origin has been taken to coincide with the center of nuclear charge, so that the nuclear contribution averages to zero.) This sum is therefore equal

*These arguments do not apply to charged molecules.

to the negative of the dipole moment $\vec{\mu}$, since it represents the net displacement of negative charge from the positive, while the dipole moment is defined as a vector from negative to positive charges (however, note that the e_i are all negative). Since θ is the angle between the z axis ($\vec{E}$) and the ζ axis ($\vec{\mu}$), Eq. (3) can be rewritten as

$$V = -\vec{\mu} \cdot \vec{E} \tag{4}$$

which is the usual classical expression.

If a molecule possesses a permanent dipole moment different from zero, which is a constant property of the molecule, then Eq. (4) says that the Stark effect will contribute an energy that is linear in the electric field. Whenever a Stark effect is found to be proportional to the square of the field, however, it is implied that the dipole moment is not constant, but is proportional to the field

$$\vec{\mu}_\alpha = \alpha\vec{E} , \tag{5}$$

and $\vec{\mu}_\alpha$ is interpreted as being an induced dipole moment, due to the distortion of molecular symmetry by the external field. The constant α is called the polarizability, and usually needs to be written as a tensor, since $\vec{\mu}_\alpha$ and $\vec{E}$ are not, in general, of the same direction.

3. Quantum Mechanical Formulation

In the notation of Landau and Lifshitz[1](p.294), $\hat{n}$ is the unit vector along the ζ axis, so that

$$n_z = \cos\theta$$

and

$$V = -(\sum_i e_i \zeta_i)\, n_z\, E \quad . \tag{6}$$

This is a form suitable for the separation of the coordinates of nuclear rotation from those of the nuclear vibration and electronic motions. n_z $(\cos\theta)$ is a function only of angular (rotational) variables, while the ζ_i do not contain these variables. If we assume that the matrix elements of Eq.(6) can be taken with respect to a separated wavefunction

$$\psi = \psi_r\, \psi_{ev} \quad , \tag{7}$$

then we may write

$$\langle \psi | V | \psi' \rangle = \langle \psi_{ev} | \sum_i e_i \zeta_i | \psi_{e'v'} \rangle \langle \psi_r | n_z | \psi_{r'} \rangle E \quad . \tag{8}$$

This is the quantum analogue of Eq. (4). The first bracket of Eq. (8) is taken to be the quantum mechanical expression for the dipole moment $\vec{\mu}$, and the second bracket describes the formation of the inner product in Eq. (4), which essentially

represents the transformation of $\vec{\mu}$ from molecule-fixed to space-fixed coordinates.

Some important properties of the dipole moment can be understood by examining its form in Eq. (8). If ψ_{ev} is the same as $\psi_{e'v'}$ (i.e., we consider the diagonal matrix element of V in the state ψ_{ev}), then it makes sense to regard $< \psi_{ev} |\sum_i e_i \zeta_i| \psi_{ev} >$ as the dipole moment of the molecule in the state ψ_{ev}:

$$\mu_{ev} \equiv < \psi_{ev}| \sum_i e_i \zeta_i |\psi_{ev} > \quad . \tag{9}$$

The value of μ_{ev} should be independent of rotational quantum numbers. The matrix elements of the Stark effect can thus be expressed in cm^{-1} as

$$F = \varepsilon < \psi_r | n_z | \psi_{r'} >$$

where (10)

$$\varepsilon \equiv \mu E/hc \quad .$$

If the molecule is homonuclear (i.e., both nuclei the same, as in H_2 or N_2^{14}) then it can be changed in no physical property (including μ) by an inversion of all coordinates through the origin, replacing the molecule-fixed coordinates (ξ_i, η_i, ζ_i) of the i^{th} particle by

$(-\xi_i, -\eta_i, -\zeta_i)$. This means that ψ_{ev} can be changed by at most a phase factor e^{iq} (with q real). The dipole moment is then given by*

$$\begin{aligned} \mu &= \langle \psi_{ev} | \sum e_i \zeta_i | \psi_{ev} \rangle \\ &= \langle \psi_{ev} e^{iq} | \sum e_i (-\zeta_i) | \psi_{ev} e^{iq} \rangle \\ &= \langle \psi_{ev} | \sum e_i (-\zeta_i) | \psi_{ev} e^{iq} e^{-iq} \rangle \\ &= \langle \psi_{ev} | \sum e_i (-\zeta_i) | \psi_{ev} \rangle \\ &= - \langle \psi_{ev} | \sum e_i \zeta_i | \psi_{ev} \rangle \\ &= -\mu \ , \end{aligned} \tag{11}$$

which can be satisfied only if $\mu=0$. When the molecule is not homonuclear, a coordinate inversion cannot be expected to leave the dipole moment unchanged (it will clearly change sign), and μ may in general be non-zero.

4. Parity and Inversion

The operation of inverting all electronic and nuclear coordinates through the origin will, if applied to the Stark potential, result in a selection rule which states that only states possessing opposite parity may interact. This is shown by Hougens[2] (p.23f) from a rigorous consideration of the properties of the associated symmetry operations, and by Landau and Lifshitz[1] (p.94f) by an algebraic argument. What follows is a more geometrical argument.

The Euler angle Θ in Eq. (8) ($n_z = \cos\Theta$) is defined as the angle from the positive z axis to the positive

*Eq. (11) contains three different meanings for the symbol "e",

ζ axis. Inversion does not change the direction of the space-fixed z axis, by our definition, but for each particle i it replaces z_i by $-z_i$. It is not obvious, however, whether or not the ζ axis changes direction. We shall see that it does not matter, as far as the effect upon Eq. (8) is concerned.

If the positive ζ axis changes direction under inversion, then the ζ coordinates of all particles are unchanged but θ becomes $\pi-\theta$. Since $n_z \rightarrow \cos(\eta-\theta) = -\cos\theta$ changes sign but the ζ_i are invariant, V changes sign as an operator.

If, on the other hand, the positive ζ-axis were to <u>not</u> change sign upon inversion (similar to the z axis), then θ remains invariant while all the ζ_i change their signs. Once again the sign of V changes, but this time from the $\sum_i e_i\zeta_i$ factor. The question of which factor changes sign is similar to the question pertaining to the inverse of a unit vector pointing north: Is it a vector of magnitude -1 pointing north, or a unit vector pointing south? However, there is a criterion for decision in the case of V, as will be seen below.

The geometric effect of an inversion of coordinates may be described equivalently as an operation in which particles are unaffected, but the senses of the space-fixed axes are reversed. The preceding arguments may be readily adapted to this convention.

Since the Stark perturbation V becomes $-V$ under <u>inversion, and $\psi \rightarrow \pm\psi$ (according to the parity of ψ), then</u>

which should not be confused: the electronic charge e_i, the exponential (2.718...) in e^{iq}, and the subscript denoting electronic wavefunction.

the matrix elements $\langle \psi | V | \psi' \rangle$ change sign unless ψ and ψ' are wave-functions of opposite parity. Since matrix elements are physically measurable quantities (Stark energies and interactions), they must be unaffected by inversion. Thus we have shown that when parity is a good quantum number (i.e., when the Hamiltonian is invariant under inversion) then the matrix elements of the Stark perturbation between unperturbed wavefunctions are zero except between wavefunctions of opposite parity.

The fact that the diagonal matrix elements of V are zero (for any wavefunction of definite parity) often leads to confusion by seeming to imply that the dipole moment of any pure rotational level (a Σ-state level or a Λ-doublet sublevel) is zero. To illuminate this problem, we may assume that the sign change in V under inversion is due to the second factor in Eq. (8) $\langle \psi_r | n_z | \psi_r \rangle$, rather than the first factor (dipole moment). By our previous discussion in this section, we are then forced to have the molecule-fixed (ζ) axis change sign, although the space-fixed (z) axis does not, under inversion.

That the sign change be associated with the Euler angles (rotational variables) is reasonable, since we can interpret our result as saying that the dipole moment, as a vector fixed in the molecule, has no component along any space-fixed axis as long as the wave functions possess inversion symmetry. Intuitively, this means that in any such state, the molecule spends as much time (or more precisely, has as much

probability of pointing) in any one direction as its opposite, thus leaving the time-averaged energies unchanged. It is not surprising, therefore, that to have a Stark effect in any single state, this inversion symmetry must be destroyed. This can only be done by mixing wavefunctions of opposite parity. The formula in Chapter IV for the first order correction to the wavefunction accomplishes exactly this.

From another point of view, it is readily seen that the Stark effect must destroy the parity of the wavefunctions. The unperturbed states have definite parity because the unperturbed Hamiltonian H_o is invariant under inversion (even though the molecule may not possess inversion symmetry, i.e., be homenuclear). This is due to the fact that space is isotropic, so that transforming all cartesian particle coordinates into their negatives affects no inter-particle separations, and thus no potential energies. Adding an electric field gives space a preferred direction: An inversion as described above does not change the direction of $\vec{E}$ (z axis) but does change the sign of V. Inversion thus transforms $H_o + V$ into $H_o - V$, and the parity operator no longer commutes with the full Hamiltonian.

5. The Transition Moment

The off-diagonal matrix elements of the dipole moment are often called transition moments and denoted by

$$(R_{e,e'})_\zeta = \langle \psi_{ev} | \sum_i e_i \zeta_i | \psi_{e'v'} \rangle . \qquad (12)$$

The electric dipole transition probability (intensity) of a transition occurring between the states described by ψ_{ev} and $\psi_{e'v'}$ is proportional to $|R_{e,e'}|^2$. (See Benedict and Plyler[4], p.61f, for a discussion of various modes of expressing transition probabilities.) $R_{e,e'}$ need not be zero for homonuclear molecules, unless ψ_e and $\psi_{e'}$ are of the same electronic inversion symmetry (g or u). Note that Eq. (12) gives only the ζ component of $R_{e,e'}$, but that ξ and η components are also present, in general.

A permanent dipole moment plays the role of transition moment for transitions from one level to another within a given electronic state, so that pure rotation bands are not found in homonuclear molecules. One might suppose from the foregoing that vibration-rotation bands may be found from a non-zero value of $R_{e,e}\zeta = \langle \psi_{ev} | \sum e_i \zeta_i | \psi_{ev'} \rangle$ (or the corresponding $R_{e,e}\xi$ or $R_{e,e}\eta$). The fact that such bands are not found (Herzberg[3], p.80) indicates that a vibrational wavefunction is separable from an electronic part: A coordinate inversion cannot affect the vibrational part (internuclear distances are unchanged), so by an argument similar to that surrounding Eq.(11), the transition moment is zero.

"Exceptions" to these rules (Herzberg[3], p.279) are found in a vibration-rotation band of H_2 which is attributed to electric quadrupole interactions, and some microwave lines

in O_2 and more recently in NO (see Brown, Cole, and Honey[4a] and references in Blum, Nill, and Strauss[4b]) attributed to a magnetic dipole mechanism. The quadrupole and magnetic mechanisms are much weaker than the electric dipole, when the latter is present. Moreover, vibration-rotation bands have been induced in hydrogen by strong electric fields (Crawford and Dagg[5]), by what Herzberg[3](p.280) calls "enforced dipole radiation". These are due to a field-induced dipole moment caused by the polarizability of the molecule, as defined in Eq. (5). Similar bands, probably due to the same mechanism, but induced through collisions rather than externally applied fields, have been seen in O_2 and N_2 (Crawford, Welsh, and Locke[6]).

A second order Stark effect is permitted in all diatomic molecules due to the transition moments to neighbouring electronic states $\psi_{e'v'}$ possessing the same values of S and Λ as ψ_{ev}. The ξ and η components of $R_{e,e'}$, permit transitions to states with Λ differing by one from ψ_{ev}, (Herzberg[3], p.241f). Now, for most molecules, such electronic states are too widely separated to produce much effect. In OH, for example, the closest such state to the $A\ ^2\Sigma^+$ is the $B\ ^2\Sigma^+$ state, which lies some 36,000 cm^{-1} higher. Assigning a rather high value of 1 debye to $R_{A,B}$ (the value is not known), a maximum value of $\frac{1}{3}$ to $\langle \psi_r | n_z | \psi_{r'} \rangle$, and an extremely high field of 1000 kV/cm to E, then the Stark effect (see Chapter IV) is given by the square of Eq. (8) divided by 36,000, or about $(\frac{1}{3} \times 1000/59.5)^2/36{,}000 \simeq 9 \times 10^{-4}$

cm^{-1}, which is about two orders of magnitude below our level of resolution. In a few molecules there exist closely spaced excited states among which sizable second order Stark effects are possible. The hydrogen molecule, in fact, shows the largest of all molecular Stark effects and these were observed (see references given by McDonald[7]) some 50 years before effects arising from permanent dipole moments (Phelps and Dalby[8]).

CHAPTER III

THE MATRIX ELEMENTS OF n_z

According to Eq.(10) of the preceding chapter, it is necessary to evaluate matrix elements of the form

$$< \psi_r | \; n_z \; | \psi_{r'} >$$

in order to calculate Stark effects due to a permanent dipole moment in a diatomic molecule. This matrix element can be factored into two or three segments, depending on the angular momenta present and on the coupling schemes which predominate. These factors are well known, and have here been taken from Landau and Lifshitz[1] (pp. 93, 104, and 295). The formulae and the details of their application are to be found in Appendix E. In this chapter, we shall briefly summarize the results in matrix form for reference purposes and as an aid to later chapters.

1. The $^1\Sigma$ State

The simple rotational structure of a $^1\Sigma^+$ state is shown to scale in Fig. 1. The rotational levels are labelled by J, and have energies given by $BJ(J+1)$ cm^{-1}. The parity signs shown must be reversed for a $^1\Sigma^-$ state.

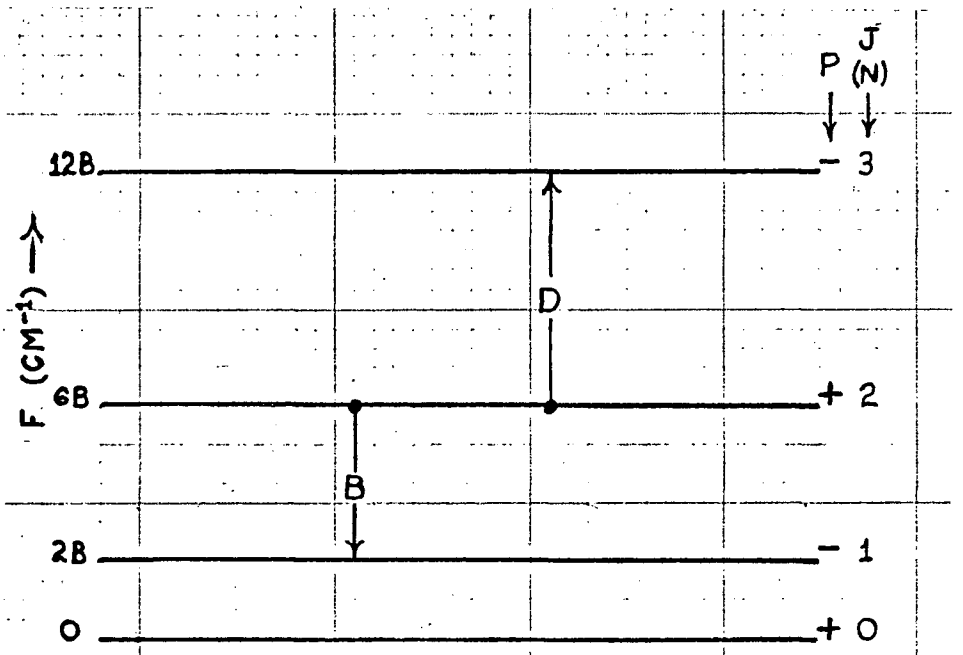

Fig. 1
Energy Levels of a $^1\Sigma^+$ State

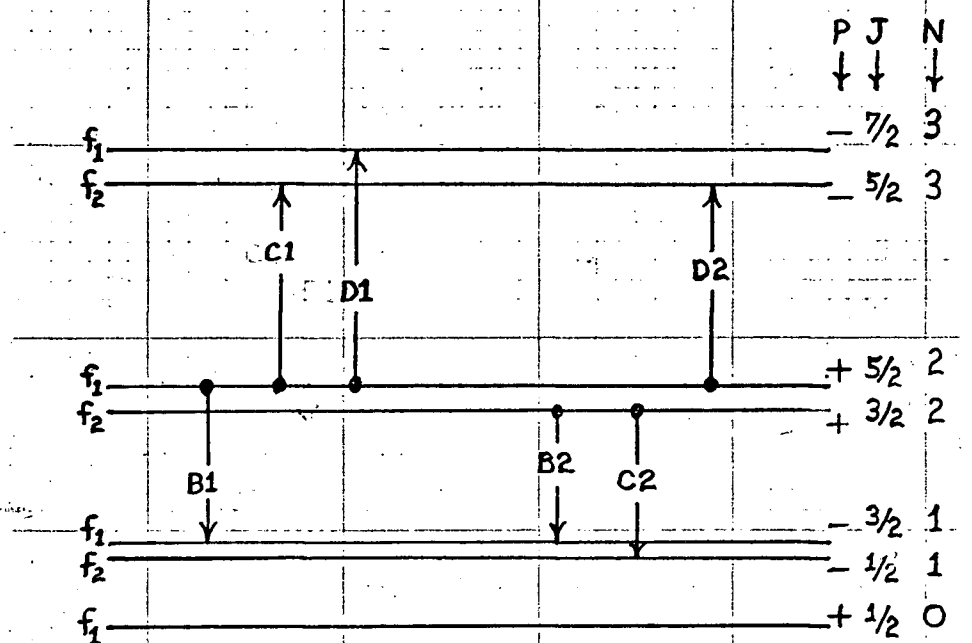

Fig. 2
Energy Levels of a $^2\Sigma^+$ State, with $\gamma = B/2$

It follows trivially from the discussion of $^1\Sigma$ states in Appendix E that the Stark effect displacements in a given energy level, due to the two interactions markeded B and D in Fig.1, are

$$F_B = -\varepsilon \sqrt{J^2 - M^2/(4J^2 - 1)} \tag{13}$$

and

$$F_D = -\varepsilon \sqrt{(J+1)^2 - M^2/(4(J+1)^2 - 1)} \quad , \tag{14}$$

where $\varepsilon = \mu E/hc$.

We show in Eq.(15) the squares of the matrix elements given in Eqs. (13) and (14), for the first few values of J in the $^1\Sigma$ state:

# →			1	2	3	4	5	6	7	8	9	10
↓	J →		0	1	1	2	2	2	3	3	3	3
	↓	M →	0	0	1	0	1	2	0	1	2	3
		↓										
1	0	0	0	$^1/_3$	0	0	0	0	0	0	0	0
2	1	0	$^1/_3$	0	0	$^4/_{15}$	0	0	0	0	0	0
3	1	1	0	0	0	0	$^1/_5$	0	0	0	0	0
4	2	0	0	$^4/_{15}$	0	0	0	0	$^9/_{35}$	0	0	0
5	2	1	0	0	$^1/_5$	0	0	0	0	$^8/_{35}$	0	0
6	2	2	0	0	0	0	0	0	0	0	$^1/_7$	0
7	3	0	0	0	0	$^9/_{35}$	0	0	0	0	0	0
8	3	1	0	0	0	0	$^8/_{35}$	0	0	0	0	0
9	3	2	0	0	0	0	0	$^1/_7$	0	0	0	0
10	3	3	0	0	0	0	0	0	0	0	0	0

(15)

2. The $^1\Pi$ State

From this point on, we shall do little more than summarize the formulae of Appendix E in matrix form. The squares of the matrix elements of n_z are given in Eq.(16).

# →			1	2	3	4	5	6	7	8	9
↓	J →		1	1	2	2	2	2	2	2	2
	↓	M →	0	1	0	1	2	0	1	2	3
		↓									
1	1	0	0	0	$^1/_4$	0	0	0	0	0	0
2	1	1	0	$^1/_4$	0	$^3/_{20}$	0	0	0	0	0
3	2	0	$^1/_4$	0	0	0	0	$^8/_{35}$	0	0	0
4	2	1	0	$^3/_{20}$	0	$^1/_{36}$	0	0	$^{64}/_{315}$	0	0
5	2	2	0	0	0	0	$^1/_9$	0	0	$^8/_{63}$	0
6	3	0	0	0	$^8/_{35}$	0	0	0	0	0	0
7	3	1	0	0	0	$^{64}/_{315}$	0	0	$^1/_{144}$	0	0
8	3	2	0	0	0	0	$^8/_{63}$	0	0	$^1/_{36}$	0
9	3	3	0	0	0	0	0	0	0	0	$^1/_{16}$

(16)

It is to be understood that each row and column is doubly degenerate with zero matrix elements between parities of like sign. By illustration, we reproduce the top corner of Eq.(16) in full detail (with p indicating parity) in Eq. (17). Hereafter, matrices will be given in the condensed form of Eq. (16) for all Λ-doubled electronic states. The order of the parity signs in Eq. (17) is not the same as they might appear, should degeneracy be removed by effects not considered.

J →			1	1	1	1	2	2	2	2	2	2
	M →		0	0	1	1	0	0	1	1	2	2
		p →	+	−	+	−	+	−	+	−	+	−
1	0	+	0	0	0	0	0	$^1/_4$	0	0	0	0
1	0	−	0	0	0	0	$^1/_4$	0	0	0	0	0
1	1	+	0	0	0	$^1/_4$	0	0	0	$^3/_{20}$	0	0
1	1	−	0	0	$^1/_4$	0	0	0	$^3/_{20}$	0	0	0

(17)

3. The $^2\Sigma$ State

The first several (squared) matrix elements of n_z are shown in Eq. (18):

# →				1	2	3	4	5	6	7	8	9
	N →			0	1	1	1	2	2	2	2	2
		J →		$\frac{1}{2}$	$\frac{1}{2}$	$\frac{3}{2}$	$\frac{3}{2}$	$\frac{3}{2}$	$\frac{3}{2}$	$\frac{5}{2}$	$\frac{5}{2}$	$\frac{5}{2}$
		M →		$\frac{1}{2}$	$\frac{1}{2}$	$\frac{1}{2}$	$\frac{3}{2}$	$\frac{1}{2}$	$\frac{3}{2}$	$\frac{1}{2}$	$\frac{3}{2}$	$\frac{5}{2}$
1	0	$\frac{1}{2}$	$\frac{1}{2}$	0	$\frac{1}{9}$	$\frac{2}{9}$	0	0	0	0	0	0
2	1	$\frac{1}{2}$	$\frac{1}{2}$	$\frac{1}{9}$	0	0	0	$\frac{2}{9}$	0	0	0	0
3	1	$\frac{3}{2}$	$\frac{1}{2}$	$\frac{2}{9}$	0	0	0	$\frac{1}{225}$	0	$\frac{6}{25}$	0	0
4	1	$\frac{3}{2}$	$\frac{3}{2}$	0	0	0	0	0	$\frac{1}{25}$	0	$\frac{4}{25}$	0
5	2	$\frac{3}{2}$	$\frac{1}{2}$	0	$\frac{2}{9}$	$\frac{1}{225}$	0	0	0	0	0	0
6	2	$\frac{3}{2}$	$\frac{3}{2}$	0	0	0	$\frac{1}{25}$	0	0	0	0	0
7	2	$\frac{5}{2}$	$\frac{1}{2}$	0	0	$\frac{6}{25}$	0	0	0	0	0	0
8	2	$\frac{5}{2}$	$\frac{3}{2}$	0	0	0	$\frac{4}{25}$	0	0	0	0	0
9	2	$\frac{5}{2}$	$\frac{5}{2}$	0	0	0	0	0	0	0	0	0

(18)

4. The $^2\Pi$ State

Eqs. (19) and (20) show the n_z^2 matrices of the $^2\Pi_{\frac{1}{2}}$ and the $^2\Pi_{\frac{3}{2}}$ states, respectively:

# →			1	2	3	4	5	6	7	8	9	10	11	12
↓	J →		$\frac{1}{2}$		$\frac{3}{2}$				$\frac{5}{2}$					
	↓ p→	M→ ↓	$-\frac{1}{2}$	$+\frac{1}{2}$	$-\frac{3}{2}$	$-\frac{1}{2}$	$+\frac{1}{2}$	$+\frac{3}{2}$	$-\frac{5}{2}$	$-\frac{3}{2}$	$-\frac{1}{2}$	$+\frac{1}{2}$	$+\frac{3}{2}$	$+\frac{5}{2}$
1	$\frac{1}{2}$	$-\frac{1}{2}$	0	$\frac{1}{9}$	0	0	$\frac{2}{9}$	0	0	0	0	0	0	0
2		$+\frac{1}{2}$	$\frac{1}{9}$	0	0	$\frac{2}{9}$	0	0	0	0	0	0	0	0
3		$-\frac{3}{2}$	0	0	0	0	0	$\frac{1}{25}$	0	0	0	0	$\frac{4}{25}$	0
4	$\frac{3}{2}$	$-\frac{1}{2}$	0	$\frac{2}{9}$	0	0	$\frac{1}{225}$	0	0	0	0	$\frac{6}{25}$	0	0
5		$+\frac{1}{2}$	$\frac{2}{9}$	0	0	$\frac{1}{225}$	0	0	0	0	$\frac{6}{25}$	0	0	0
6		$+\frac{3}{2}$	0	0	$\frac{1}{25}$	0	0	0	0	$\frac{4}{25}$	0	0	0	0
7		$-\frac{5}{2}$	0	0	0	0	0	0	0	0	0	0	0	$\frac{1}{49}$
8		$-\frac{3}{2}$	0	0	0	0	0	$\frac{4}{25}$	0	0	0	0	$\frac{9}{1225}$	0
9	$\frac{5}{2}$	$-\frac{1}{2}$	0	0	0	0	$\frac{6}{25}$	0	0	0	0	$\frac{1}{1225}$	0	0
10		$+\frac{1}{2}$	0	0	0	$\frac{6}{25}$	0	0	0	0	$\frac{1}{1225}$	0	0	0
11		$+\frac{3}{2}$	0	0	$\frac{4}{25}$	0	0	0	0	$\frac{9}{1225}$	0	0	0	0
12		$+\frac{5}{2}$	0	0	0	0	0	0	$\frac{1}{49}$	0	0	0	0	0

$^2\Pi_{\frac{1}{2}}$ (19)

# →			1	2	3	4	5	6	7	8	9	10
↓	J →		$\frac{3}{2}$				$\frac{5}{2}$					
	↓ p→	M→ ↓	$-\frac{3}{2}$	$-\frac{1}{2}$	$+\frac{1}{2}$	$+\frac{3}{2}$	$-\frac{5}{2}$	$-\frac{3}{2}$	$-\frac{1}{2}$	$+\frac{1}{2}$	$+\frac{3}{2}$	$+\frac{5}{2}$
1		$-\frac{3}{2}$	0	0	0	$\frac{9}{25}$	0	0	0	0	$\frac{8}{75}$	0
2	$\frac{3}{2}$	$-\frac{1}{2}$	0	0	$\frac{1}{25}$	0	0	0	0	$\frac{4}{25}$	0	0
3		$+\frac{1}{2}$	0	$\frac{1}{25}$	0	0	0	0	$\frac{4}{25}$	0	0	0
4		$+\frac{3}{2}$	$\frac{1}{25}$	0	0	0	0	$\frac{8}{75}$	0	0	0	0
5		$-\frac{5}{2}$	0	0	0	0	0	0	0	0	0	$\frac{9}{49}$
6		$-\frac{3}{2}$	0	0	0	$\frac{8}{75}$	0	0	0	0	$\frac{81}{1225}$	0
7	$\frac{5}{2}$	$-\frac{1}{2}$	0	0	$\frac{4}{25}$	0	0	0	0	$\frac{9}{1225}$	0	0
8		$+\frac{1}{2}$	0	$\frac{4}{25}$	0	0	0	0	$\frac{9}{1225}$	0	0	0
9		$+\frac{3}{2}$	$\frac{8}{75}$	0	0	0	0	$\frac{81}{1225}$	0	0	0	0
10		$+\frac{5}{2}$	0	0	0	0	$\frac{9}{49}$	0	0	0	0	0

$^2\Pi_{\frac{3}{2}}$ (20)

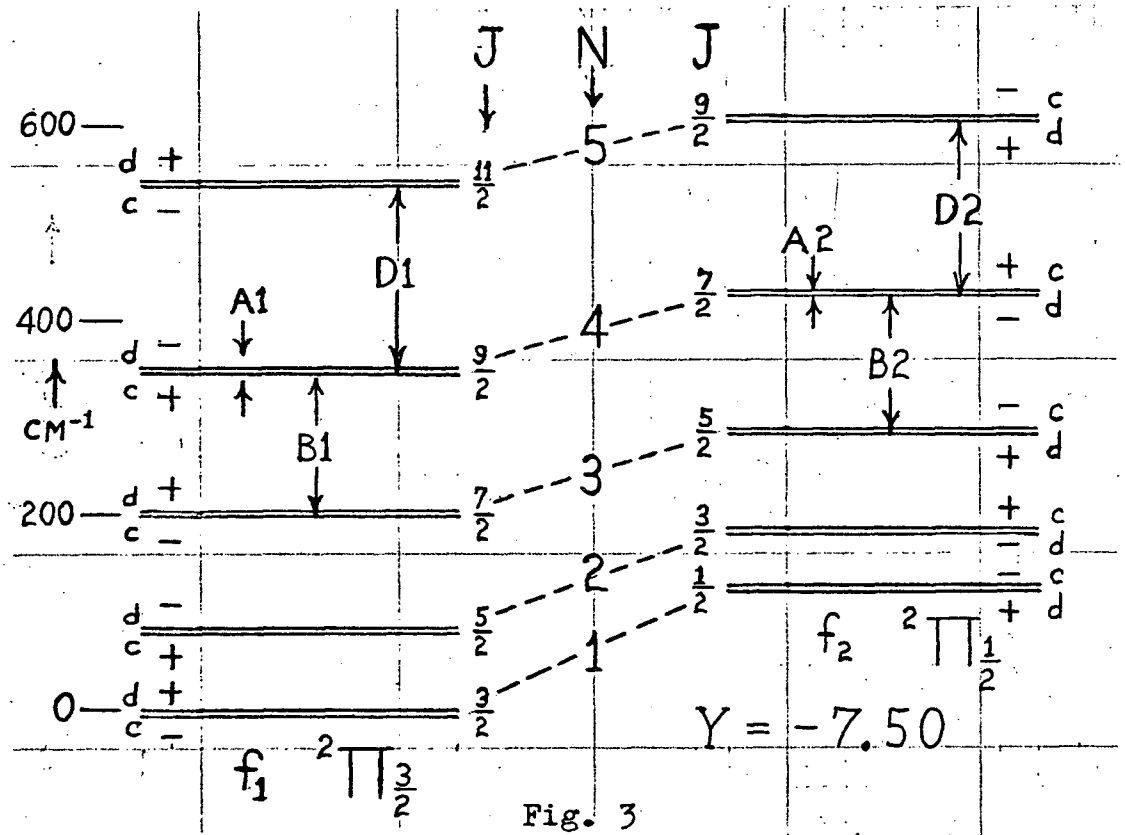

Fig. 3
Energy Levels of the $^2\Pi$ State of OH (v = 0), to Scale Except the Λ-doubling.

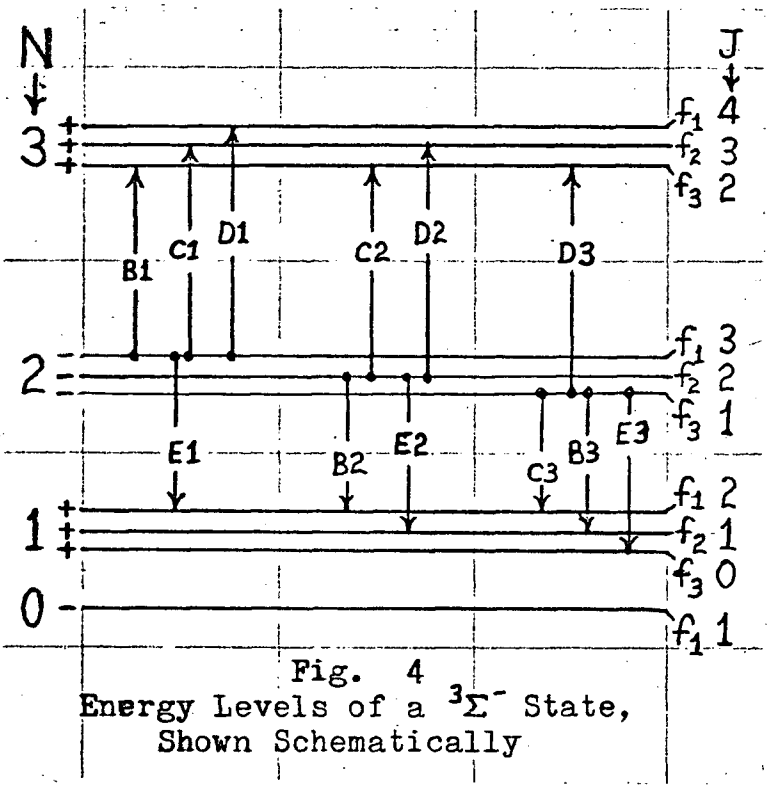

Fig. 4
Energy Levels of a $^3\Sigma^-$ State, Shown Schematically

5. The $^3\Sigma$ State

The squared matrix elements of n_z are shown in Eqs. (21a) and (21b):

N	J	M	0	1	1	1	1	1	1	2	2	2	2	2	2	2	2	2
			1	1	0	1	1	2	2	2	1	1	2	2	2	3	3	3	3
			0	1	0	0	1	0	1	2	0	1	0	1	2	0	1	2	3
0	1	0			$\frac{1}{9}$	0	0	$\frac{2}{9}$	0	0									
	1	1			0	0	$\frac{1}{6}$	0	$\frac{1}{6}$	0									
1	0	0	$\frac{1}{9}$	0							$\frac{2}{9}$	0	0	0	0	0	0	0	0
	1	0	0	0							0	0	$\frac{1}{5}$	0	0	0	0	0	0
	1	1	0	$\frac{1}{6}$							0	$\frac{1}{12}$	0	$\frac{3}{20}$	0	0	0	0	0
	2	0	$\frac{2}{9}$	0							$\frac{1}{225}$	0	0	0	0	$\frac{6}{25}$	0	0	0
	2	1	0	$\frac{1}{6}$							0	$\frac{1}{300}$	0	$\frac{1}{60}$	0	0	$\frac{16}{75}$	0	0
	2	2	0	0							0	0	0	0	$\frac{1}{15}$	0	0	$\frac{2}{15}$	0
2	1	0			$\frac{2}{9}$	0	0	$\frac{1}{225}$	0	0									
	1	1			0	0	$\frac{1}{12}$	0	$\frac{1}{300}$	0									
	2	0			0	$\frac{1}{5}$	0	0	0	0									
	2	1			0	0	$\frac{3}{20}$	0	$\frac{1}{60}$	0									
	2	2			0	0	0	0	0	$\frac{1}{15}$									
	3	0			0	0	0	$\frac{6}{25}$	0	0									
	3	1			0	0	0	0	$\frac{16}{75}$	0									
	3	2			0	0	0	0	0	$\frac{2}{15}$									
	3	3			0	0	0	0	0	0									

(21a)

($^3\Sigma$ state, continued)

N→		2	2	2	3	3	3	3	4	4	4	4	4
J→		0	1	2	0	1	2	3	0	1	2	3	4
↓	M→												
1	0	$\frac{6}{25}$	0	0	0	0	0	0	0	0	0	0	0
1	1	0	$\frac{9}{50}$	0	0	0	0	0	0	0	0	0	0
2	0	0	0	0	$\frac{8}{35}$	0	0	0	0	0	0	0	0
2	1	0	$\frac{1}{90}$	0	0	$\frac{64}{315}$	0	0	0	0	0	0	0
2	2	0	0	$\frac{2}{45}$	0	0	$\frac{8}{63}$	0	0	0	0	0	0
3	0	$\frac{1}{1225}$	0	0	0	0	0	0	$\frac{12}{49}$	0	0	0	0
3	1	0	$\frac{8}{11025}$	0	0	$\frac{1}{252}$	0	0	0	$\frac{45}{196}$	0	0	0
3	2	0	0	$\frac{1}{2205}$	0	0	$\frac{1}{63}$	0	0	0	$\frac{9}{49}$	0	0
3	3	0	0	0	0	0	0	$\frac{1}{28}$	0	0	0	$\frac{3}{28}$	0

(21b)

6. The $^3\Pi$ State

N→		1	2	2	3	3	3	4	4	4	4
J→		0	1	1	2	2	2	3	3	3	3
↓	M→										
1	0	0	$\frac{1}{3}$	0	0	0	0	0	0	0	0
2	1	$\frac{1}{3}$	0	0	$\frac{4}{15}$	0	0	0	0	0	0
2	1	0	0	0	0	$\frac{1}{5}$	0	0	0	0	0
3	2	0	$\frac{4}{15}$	0	0	0	0	$\frac{9}{35}$	0	0	0
3	2	1	0	$\frac{1}{5}$	0	0	0	0	$\frac{8}{35}$	0	0
3	2	2	0	0	0	0	0	0	0	$\frac{1}{7}$	0
4	3	0	0	0	$\frac{9}{35}$	0	0	0	0	0	0
4	3	1	0	0	0	$\frac{8}{35}$	0	0	0	0	0
4	3	2	0	0	0	0	$\frac{1}{7}$	0	0	0	0
4	3	3	0	0	0	0	0	0	0	0	0

$^3\Pi_0$ (22)

Eq. (22) shows the squared matrix elements of n_z in the $^3\Pi_0$ multiplet, while Eq. (23) shows the $^3\Pi_1$, and Eq. (24) the $^3\Pi_2$ multiplets. These are the pure case (a) matrix elements, and are shown in the condensed form where parity is suppressed (as in Eq.16). Note that in Eqs. (19) and (20) for the $^2\Pi$ state, parity is shown explicitly and must not be mistaken for the sign of M which has been suppressed as per Appendix B.

$^3\Pi_1$

N→	1	1	2	2	2	3	3	3	3	4	4	4	4	4
↓ J→	1	1	2	2	2	3	3	3	3	4	4	4	4	4
↓ M→	0	1	0	1	2	0	1	2	3	0	1	2	3	4
1 1 0	0	0	$\frac{1}{5}$	0	0	0	0	0	0	0	0	0	0	0
1 1 1	0	$\frac{1}{4}$	0	$\frac{3}{20}$	0	0	0	0	0	0	0	0	0	0
2 2 0	$\frac{1}{5}$	0	0	0	0	$\frac{8}{35}$	0	0	0	0	0	0	0	0
2 2 1	0	$\frac{3}{20}$	0	$\frac{1}{36}$	0	0	$\frac{64}{315}$	0	0	0	0	0	0	0
2 2 2	0	0	0	0	$\frac{1}{9}$	0	0	$\frac{8}{63}$	0	0	0	0	0	0
3 3 0	0	0	$\frac{8}{35}$	0	0	0	0	0	0	$\frac{5}{21}$	0	0	0	0
3 3 1	0	0	0	$\frac{64}{315}$	0	0	$\frac{1}{144}$	0	0	0	$\frac{25}{112}$	0	0	0
3 3 2	0	0	0	0	$\frac{8}{63}$	0	0	$\frac{1}{36}$	0	0	0	$\frac{15}{84}$	0	0
3 3 3	0	0	0	0	0	0	0	0	$\frac{1}{16}$	0	0	0	$\frac{5}{48}$	0
4 4 0	0	0	0	0	0	$\frac{5}{21}$	0	0	0	0	0	0	0	0
4 4 1	0	0	0	0	0	0	$\frac{25}{112}$	0	0	0	$\frac{1}{400}$	0	0	0
4 4 2	0	0	0	0	0	0	0	$\frac{15}{84}$	0	0	0	$\frac{1}{100}$	0	0
4 4 3	0	0	0	0	0	0	0	0	$\frac{5}{48}$	0	0	0	$\frac{9}{400}$	0
4 4 4	0	0	0	0	0	0	0	0	0	0	0	0	0	$\frac{1}{25}$

(23)

N →	1	1	1	2	2	2	2	3	3	3	3	3
↓ J →	2	2	2	3	3	3	3	4	4	4	4	4
↓ M →	0	1	2	0	1	2	3	0	1	2	3	4
1 2 0	0	0	0	$\frac{1}{7}$	0	0	0	0	0	0	0	0
1 2 1	0	$\frac{1}{9}$	0	0	$\frac{8}{63}$	0	0	0	0	0	0	0
1 2 2	0	0	$\frac{4}{9}$	0	0	$\frac{5}{63}$	0	0	0	0	0	0
2 3 0	$\frac{1}{7}$	0	0	0	0	0	0	$\frac{4}{21}$	0	0	0	0
2 3 1	0	$\frac{8}{63}$	0	0	$\frac{1}{36}$	0	0	0	$\frac{5}{28}$	0	0	0
2 3 2	0	0	$\frac{5}{63}$	0	0	$\frac{1}{9}$	0	0	0	$\frac{1}{7}$	0	0
2 3 3	0	0	0	0	0	0	$\frac{1}{4}$	0	0	0	$\frac{1}{12}$	0
3 4 0	0	0	0	$\frac{4}{21}$	0	0	0	0	0	0	0	0
3 4 1	0	0	0	0	$\frac{5}{28}$	0	0	0	$\frac{1}{100}$	0	0	0
3 4 2	0	0	0	0	0	$\frac{1}{7}$	0	0	0	$\frac{1}{25}$	0	0
3 4 3	0	0	0	0	0	0	$\frac{1}{12}$	0	0	0	$\frac{9}{100}$	0
3 4 4	0	0	0	0	0	0	0	0	0	0	0	$\frac{4}{25}$
4 5 0	0	0	0	0	0	0	0	$\frac{7}{33}$	0	0	0	0
4 5 1	0	0	0	0	0	0	0	0	$\frac{56}{275}$	0	0	0
4 5 2	0	0	0	0	0	0	0	0	0	$\frac{49}{275}$	0	0
4 5 3	0	0	0	0	0	0	0	0	0	0	$\frac{112}{825}$	0
4 5 4	0	0	0	0	0	0	0	0	0	0	0	$\frac{21}{275}$
4 5 5	0	0	0	0	0	0	0	0	0	0	0	0

$^3\Pi_2$

(24)

CHAPTER IV

PERTURBATION THEORY

1. Nondegenerate Perturbation Theory

The perturbation theory used in this work follows quite closely the time-independent theory formulated in Landau and Lifshitz[1] (pp.133-39). This method and the results for non-degenerate levels are summarized in this section. H_o is the unperturbed Hamiltonian, for which the eigenvalues W_n^0 and the corresponding wavefunctions ψ_n^0 are known:

$$H_o\psi_n^0 = W_n^0\psi_n^0 \quad . \tag{25}$$

The exact Hamiltonian is $H = H_o + V$, and has exact eigenvalues W_n and wavefunctions ψ_n. We then expand ψ_n in terms of the complete orthonormal set of wavefunctions ψ_n^0, with expansion coefficients c_{nm}:

$$\psi_n = \sum_m c_{nm}\psi_m^0 \quad . \tag{26}$$

The exact Schroedinger equation $H\psi_n = W_n\psi_n$ may be rewritten with Eqs.(25) and (26) to give

$$(W_n - W_k^0)c_{kn} = \sum_m V_{km}c_{nm} \quad , \tag{27}$$

where $V_{km} = \int \psi_k^{0*} V \psi_m \, dq$, with the integral being taken the full range of all coordinates q. Eq.(27) is used as the starting point in each order of approximation by substituting previously evaluated orders of approximation for W_n, c_{kn}, and c_{nm}. One first sets $k = n$ to find the next approximation in the energy, and then one stipulates that $k \neq n$ to find the next order of approximation to the c_{nk}'s. The value of c_{nn} is established by requiring that $\int \psi_n^* \psi_n dq = 1$ to the required degree of accuracy.

This procedure gives the familiar perturbation forms:

$$c_{nn}^0 = 1 \tag{28}$$
$$c_{nk}^0 = 0 \quad (k \neq n)$$

$$W_n^1 = V_{nn} \tag{29}$$

$$c_{nn}^1 = 0 \tag{30}$$
$$c_{nk}^1 = V_{nk}/U_k \quad (k \neq n)$$

$$W_n^{(2)} = \sum_m{}' \, |V_{nm}|^2/U_m, \tag{31}$$

where $U_i \equiv W_n^0 - W_i^0$, and the prime (') on the sum means that the term with $m=n$ is omitted. Extension of this procedure to third and fourth orders gives:

$$c_{nn}^{(2)} = -\tfrac{1}{2}\sum_m{}' |V_{mn}/U_m|^2$$

$$c_{nk}^{(2)} = \sum_m{}' \frac{V_{mn}V_{km}}{U_m U_k} - \frac{V_{nn}V_{nk}}{U_k^2} \tag{32}$$

$$W_n^{(3)} = \sum_m{}' \sum_j{}' \frac{V_{nm}V_{mj}V_{jn}}{U_j U_m} - \sum_m{}' \frac{V_{nn}|V_{nm}|^2}{U_m^2} \tag{33}$$

$$c_{nn}^{(3)} = \sum_m{}' \frac{V_{nn}V_{mn}^2}{U_m^3} - \sum_m{}' \sum_j{}' \frac{V_{mn}V_{jn}V_{mj}}{U_m^2 U_j} \tag{34}$$

$$c_{nk}^{(3)} = V_{nn}^2 V_{kn}/U_k^3 - \sum_m{}' \frac{V_{km}V_{mn}V_{nn} + \frac{1}{2}|V_{mn}|^2 V_{kn}}{U_m^2 U_k}$$

$$- \sum_m{}' \frac{V_{km}V_{mn}V_{nn} + V_{nm}^2 V_{kn}}{U_m U_k^2} + \sum_m{}' \sum_j{}' \frac{V_{km}V_{mj}V_{jn}}{U_j U_m U_k}$$

$$W_n^{(4)} = \sum_m{}' \frac{V_{nm}}{U_m} \sum_j{}' \frac{V_{nj}}{U_j} \sum_i{}' \frac{V_{im}V_{ij}}{U_i} - \sum_m{}' \frac{V_{mn}^2}{U_m^2} \sum_j{}' \frac{V_{jn}^2}{U_j} \tag{35}$$

$$+ V_{nn}^2 \sum_m{}' \frac{V_{mn}^2}{U_m^3} - 2\, V_{nn} \sum_m{}' \frac{V_{nm}}{U_m^2} \sum_j{}' \frac{V_{jn}V_{mj}}{U_j}$$

Morse and Feshbach[9] (p.1005) give a more elegant iterative formulation which, however, does not explicitly separate different orders of approximation.

We may think of a first order effect as being the direct effect of V on level n. A second order effect is

the effect of direct interactions with neighboring levels through V. Third order can then be interpreted as the effect on those levels which cause second order effects through the interactions of still other levels, and also from those changes in the first order effect caused by the first order corrections to the wavefunction. We shall see below, however, that degeneracy can raise the effective order of magnitude of an interaction.

We shall also make use of an expression containing terms to sixth order given by Kusch and Hughes[10] (p.139), which is evaluated explicitly for the N = 0 level of a rigid rotator (yielding nondegenerate energy levels suitable for the ground level of a Σ state):

$$W_n^\sigma \simeq \tfrac{1}{6}\frac{\varepsilon^2}{B} + \tfrac{11}{1080}\frac{\varepsilon^4}{B^3} - \tfrac{1}{725}\frac{\varepsilon^6}{B^5} \quad (cm^{-1}) \tag{36}$$

where $B = h/(8\pi^2 cI)$ is the rotational constant (I is the moment of inertia of the rotating molecule; ε, h, and c are as defined in App. A.).

2. Degenerate Levels

When energy levels are spaced sufficiently closely that V_{nm}/U_m is no longer small, then the results of the preceding section do not apply, and the matrix describing the interaction must be diagonalized directly. If n' and n" refer to different levels among the set of closely spaced levels which includes n, then the appropriate zero-

order wavefunction for the perturbation V is some linear combination

$$\psi^0_{n,corr} = c_{nn'}\,\psi^0_{n'} + c_{nn''}\,\psi^0_{n''} + \cdots \quad (37)$$

of whatever set of wavefunctions $\psi^0_{n'}$, $\psi^0_{n''}$ were chosen for the purpose of taking the matrix elements of V. If these energy levels were not perfectly degenerate to begin with, then the original wavefunctions $\psi^0_{n'}$, $\psi^0_{n''}$ will naturally be those of the unperturbed Hamiltonian (which includes whatever terms spoiled the degeneracy). In this case, the matrix of the unperturbed Hamiltonian is naturally diagonal and should be added to the matrix $V_{nn'}$ before diagonalization. This procedure will include the interaction of V with whatever parts of H_o were responsible for the unperturbed energy separations. Introduction of the perturbation will mix these original wavefunctions, as is described to first order by Eq. (30). Note that Eq. (30) is applicable as long as the perturbation is small compared to the (small) energy level separations. This procedure will now be applied to the two-fold "quasi-degeneracy" which occurs in the rotational levels of electronic states having $\Lambda > 0$ (Λ-doubling).

3. Λ-doublets

All diatomic molecules are symmetric with respect to any plane through the nuclei, in the time average over electronic motions. A reflection of the electronic coordinates in such a plane can therefore change the wavefunction by at most a phase factor (see Chap.II, Sec.3), which must be ± 1 (since two reflections are just an identity operator). For $\Lambda=0$ the energy levels are those of a rigid rotator and are not degenerate. A reflection will transform the electronic wavefunction ψ_e into $+\psi_e$ or $-\psi_e$, producing what is called a Σ^+ or a Σ^- state, respectively. If $\Lambda>0$, however, there is angular momentum along the internuclear axis, and the symmetric top model must be used. The symmetric top wavefunctions contain Λ and the azimuthal angle ϕ only through a phase factor $e^{\pm i\Lambda\phi}$ (Herzberg[3] p.118), the sign depending on the direction of Λ along the internuclear axis. Since a phase factor in the wavefunction cannot affect the energies, every such energy is doubly degenerate. This degeneracy is often partially removed by what can be viewed as a slight shift in the coupling of L (see, e.g., Hinkley, et al[11] or Veseth[12]) from the internuclear axis to that of nuclear rotation (transition from Hund's case (a) or (b) to case (d)). Alternatively, it may be viewed as due to an interaction with a nearby electronic state through the "Coriolis" terms ($J_+L_- + J_-L_+ + L_+S_- + L_-S_+$, see Chap.V) of the rotational Hamiltonian. In either case, the effect

is to slightly "spoil" Λ as a good quantum number. These effects are usually appreciable only for Π states perturbed by Σ states, and increase rapidly with rotation.

It is interesting to note that Λ-doubling does occur in $^3\Pi_0$ multiplets wherein $\Omega=0$, and may show sizable splittings even without rotation. Now the assumption that Λ, S, and Σ are good quantum numbers is based on small values of spin-orbit coupling. As the coupling increases, S begins to follow L itself rather than the time-averaged axial component of L, and Hund's case (c) is approached making multiplets hard to identify. As this happens, there is a gradual widening of the gap between the c and d Λ-doublet components of a $^3\Pi_0$ state; the $^3\Pi_{0_c}$ levels become a 0^+ case (c) state and the $^3\Pi_{0_d}$ levels become a 0^- state, having the properties of $^1\Sigma^+$ and $^1\Sigma^-$ rather than $^3\Pi$ states.

Each of the Λ-doublets has an additional $(2J+1)$-fold degeneracy, each of the sublevels having a different component M with respect to (say) the space-fixed z axis. This degeneracy is only removed by an external field and need not concern us here since the Stark perturbation V is diagonal in M.

When a wavefunction belongs to a degenerate eigenvalue, a coordinate reflection may do more than change a phase factor: It can transform the wavefunction into some other wavefunction in the space spanned by the set of wavefunctions of that eigenvalue (i.e., $\psi_{n'} \rightarrow \sum_n c_n \psi_n$). A reflec-

tion in a symmetry plane will change the sign of ϕ (Hougen[2], p.16) and thus change the form of $e^{+i\Lambda\phi}$ into $e^{-i\Lambda\phi}$ (and vice versa), but <u>not</u> into $\pm e^{i\Lambda\phi}$. When interactions removing degeneracy are included in H_o, however, each non-degenerate energy level must have definite parity so that the reflection changes ψ_e into $\pm\psi_e$. This means that the symmetric top wavefunctions $\psi_e = \chi\, e^{\pm i\Lambda\phi}$ (where χ does not contain Λ or ϕ) are not the correct zero-order wavefunctions for the interactions removing degeneracy. Rather, linear combinations must be used as per Eq.(37). In this case, it is easy to see that the simple linear combinations

$$\psi_e^+ = \chi(e^{i\Lambda\phi} + e^{-i\Lambda\phi})/\sqrt{2}$$
$$\psi_e^- = \chi(e^{i\Lambda\phi} + e^{-i\Lambda\phi})/\sqrt{2} \qquad (38)$$

are desired functions, since $\psi_e^{\pm} \rightarrow \pm\psi_e^{\pm}$. These then are the wavefunctions appropriate to Λ-doublets with no external fields. The sublevels described by ψ_e^+ are called "c" levels, and those described by ψ_e^- are called "d" levels. The parity of the sublevel is the product of the parity of ψ_e times that of the rotational wavefunction ψ_r (this latter is $(-1)^N$ for case (b) Σ states, and $(-1)^J$ for case (c) 0 states).

4. Stark Effects in a Λ-doublet

Wavefunctions ψ_e^+ and ψ_e^- (Eq.38) are not the zero-order functions appropriate to Λ-doublets in the presence of an electric field. These are found by diagonalizing the the perturbation V, given by Eq.(7). This is equivalent to solving

$$\sum_j (V_{nj} - W_n^1 \delta_{nj}) c_{nj}^0 = 0 , \qquad (39)$$

where j is summed over n', n",...,and δ_{nj} is one if n=j and zero if n≠j. Eq.(39) is derived (Landau and Lifshitz[1], p.137) from Eq.(27) using a first order approximation to the energy, and zero-order approximations to the wavefunction: $c_{nn} = c_{nn}^0$, $c_{nn'} = c_{nn'}^0$, ..., and $c_{nm} = 0$ ($m \neq n,n',n",...$). (We continue to use n for the quantum numbers of the level in which we are interested, to use n, n', n",... for levels degenerate with or close to n, and m for other levels which are sufficiently distant so that V_{nm}/U_m is small.) The system of linear equations in Eq.(39) has a solution for the c_{nj}^0 only if the matrix operator is singular and thus has a zero determinant:

$$|V_{nj} - W_n \delta_{nj}| = 0 \qquad (40)$$

The diagonal matrix elements V_{nn} are zero, but there are off-diagonal elements between the two Λ-doublet

levels of opposite parity. As noted in App. E, these matrix elements are diagonal in all quantum numbers except parity, and are given by

$$V_{nn'} = -\mu E \langle \psi_r^+ | n_z | \psi_r^- \rangle = -\frac{\mu E M \Omega}{J(J+1)} \tag{41}$$

where the superscripts on ψ indicate parity. Hund's case (a) coupling was assumed.

Ignoring other rotational levels, we have

$$V = \begin{array}{c} \\ H \\ L \end{array} \begin{array}{c} \begin{array}{cc} H & L \end{array} \\ \begin{pmatrix} 0 & V_{HL} \\ V_{HL} & 0 \end{pmatrix} \end{array} \tag{42}$$

where $V_{LH} = -\mu E M \Omega / J(J+1)$. The "H" and "L" indices indicate that these matrix elements were taken with respect to two wavefunctions arbitrarily (at present) labelled ψ_H and ψ_L, either one of which can be the sublevel of positive parity (and the other negative). Account must now be taken of imperfect degeneracy: There is another interaction in the field-free Hamiltonian which separates the sublevels by energies which may be comparable to V_{HL}. In principle, these terms causing Λ-doubling should be split off the unperturbed Hamiltonian and added to the Stark perturbation, and the matrix sum (taken with respect to the wavefunctions of perfectly degenerate energy levels) should be diagonal-

ized. In fact one does not need to evaluate the operators responsible for the splitting if one knows empirically their effect upon the energies. They have no off-diagonal matrix elements since the ψ^0 are their eigenfunctions (i.e., ψ_H and ψ_L). Taking zero energy to lie at the center of the unperturbed Λ-doublet whose splitting is 2δ ergs, we add the doublet energies to Eq.(42), and get

$$\begin{array}{c} \\ H \\ \\ L \end{array} \begin{array}{c} \begin{array}{cc} H & \quad L \end{array} \\ \begin{pmatrix} \delta & V_{HL} \\ \\ V_{HL} & -\delta \end{pmatrix} \end{array} , \tag{43}$$

before diagonalization. This means that ψ_H is the wavefunction of higher unperturbed energy, and ψ_L lower energy, regardless of parity. The perturbed energies W^1 are found by putting the matrix of Eq.(43) into Eq.(40):

$$\begin{vmatrix} \delta - W^1 & V_{HL} \\ V_{HL} & -\delta - W^1 \end{vmatrix} = 0 . \tag{44}$$

This equation has solutions for W^1:

$$\begin{aligned} W_A &= \sqrt{\delta^2 + V_{HL}^2} \\ W_S &= -\sqrt{\delta^2 + V_{HL}^2} \end{aligned} \tag{45}$$

where (again for the moment) "S" and "A" are arbitrary labels. Eq.(45) says that for small perturbations ($V_{HL} << \delta$),

the energies are $\pm\delta(1 + V_{HL}^2/\delta^2)^{\frac{1}{2}} \simeq \pm\delta(1 + V_{HL}^2/2\delta^2)$ which deviate quadratically in V_{HL} (and therefore E) from the unperturbed levels $\pm\delta$. For large perturbations ($V_{HL} >> \delta$) the energies are $\pm|V_{HL}|(1 + \delta^2/V_{HL}^2)^{\frac{1}{2}} \simeq \pm|V_{HL}|$ which are linear in V_{HL}. Thus Eq.(45) exhibits a transition from second to first order effects with increasing field strength as shown in Fig.5. A first order effect is not in contradiction with the conclusions reached in Chap.II, Sec.4, since the wavefunctions associated with W_A and W_S (see Eq.(49) below) are mixtures of wavefunctions of different parity (ψ_H and ψ_L): Parity is no longer a good quantum number, so the resulting wavefunctions no longer possess inversion symmetry and may indeed have diagonal matrix elements.

Two further points are important. Firstly, the higher and lower Λ-doublets move away from each other, always "repelling". Secondly, the Stark shift depends only on the absolute magnitude of V_{HL} so that the signs of μ, E, M, and Ω do not matter.

Eqs.(39) may now be solved for the c_{nj}^0 coefficients. In the case of W_S, we have

$$\begin{array}{c} \\ H \\ L \end{array} \begin{array}{c} \begin{array}{cc} H & \quad L \end{array} \\ \begin{pmatrix} \delta - W_S & V_{HL} \\ V_{HL} & -\delta - W_S \end{pmatrix} \end{array} \begin{pmatrix} c_{HS}^0 \\ c_{LS}^0 \end{pmatrix} = 0 , \qquad (46)$$

with a similar pair for W_A. This system is solved by

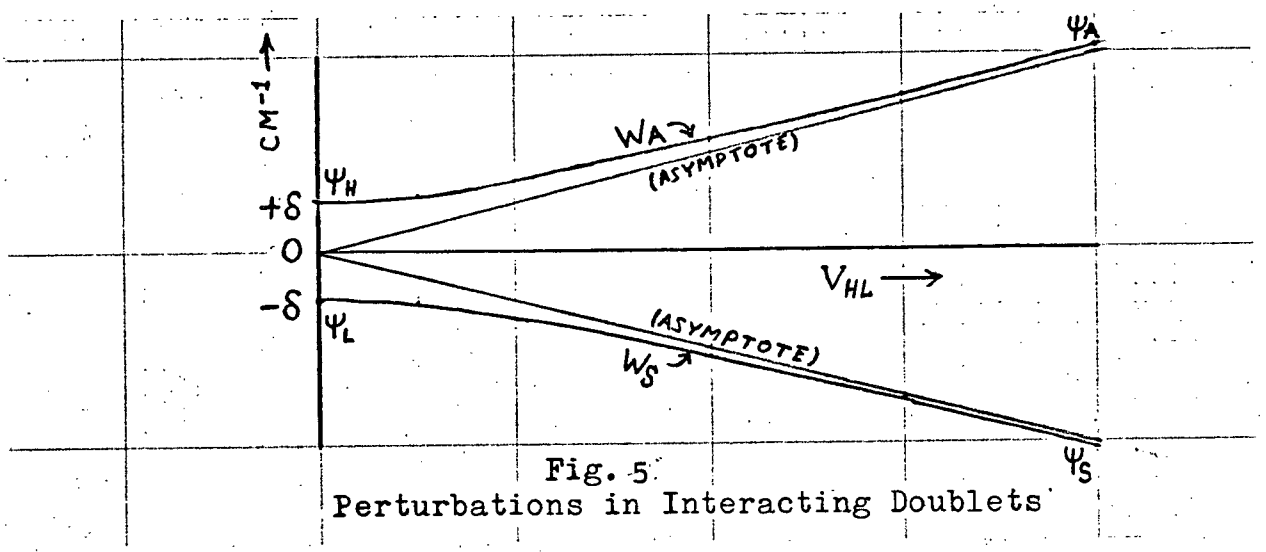

Fig. 5
Perturbations in Interacting Doublets

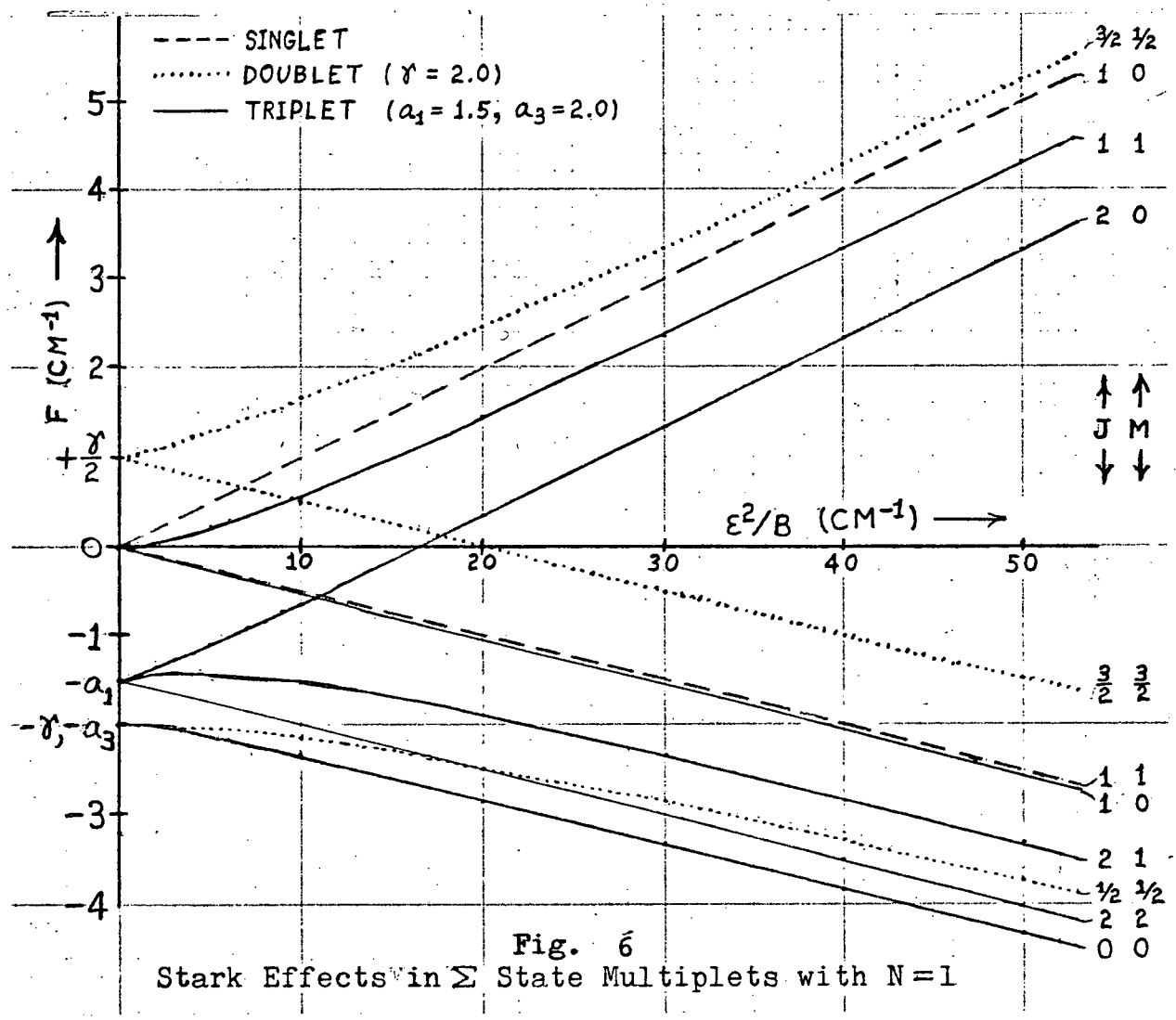

Fig. 6
Stark Effects in Σ State Multiplets with N=1

Herzberg[3] (p.282f.) in somewhat more general form, and the solutions can be written in matrix form as:

$$C \equiv \begin{matrix} \\ H \\ L \end{matrix} \begin{matrix} \begin{matrix} A & S \end{matrix} \\ \begin{pmatrix} c^0_{HA} & c^0_{HS} \\ c^0_{LA} & c^0_{LS} \end{pmatrix} \end{matrix} \equiv \begin{matrix} \begin{matrix} A & S \end{matrix} \\ \begin{pmatrix} c_1 & c_2 \\ -c_2 & c_1 \end{pmatrix} \end{matrix}, \tag{47}$$

where the two distinct matrix elements c_1 and c_2 are given by

$$\begin{aligned} c_1 &= +\{ \tfrac{1}{2} + \delta/2(\delta^2 + V^2_{HL})^{\frac{1}{2}} \}^{\frac{1}{2}} \\ c_2 &= +\{ \tfrac{1}{2} - \delta/2(\delta^2 + V^2_{HL})^{\frac{1}{2}} \}^{\frac{1}{2}} \quad . \end{aligned} \tag{48}$$

Eq.(47) says that the new zero-order wavefunctions appropriate to the Stark pertubation V_{HL} are of the form

$$\begin{aligned} \psi_A &= c_1\psi_H - c_2\psi_L \\ \psi_S &= c_2\psi_H + c_1\psi_L \ . \end{aligned} \tag{49}$$

In deriving c_1 and c_2 (Eq.48), the condition $c_1^2 + c_2^2 = 1$ was imposed, which ensures that $\int\psi^*_S\psi_S dq = \int\psi^*_A\psi_A dq = 1$, and that $\int\psi^*_S\psi_A dq = \int\psi^*_A\psi_S dq = 0$, so that ψ_S and ψ_A are orthonormal.

Examination of Eq.(48) shows that if $V_{HL} = 0$, then $c_1 = 1$ and $c_2 = 0$, so that

$$\begin{aligned} \psi_A &= \psi_H \\ &\qquad (V_{HL} \to 0), \\ \psi_S &= \psi_L \end{aligned} \tag{50}$$

whereas for extremely high fields, $c_1 = c_2 = 1/\sqrt{2}$, and

$$\begin{aligned} \psi_A &= (\psi_H - \psi_L)/\sqrt{2} \\ &\qquad (\delta \to 0), \\ \psi_S &= (\psi_H + \psi_L)/\sqrt{2} \end{aligned} \tag{51}$$

"justifying" the labels ψ_A and ψ_S, in this case, as antisymmetric and symmetric wavefunctions. Remembering that ψ_H and ψ_L correspond in some order to ψ_e^+ and ψ_e^- (Eq.38), we see that $\psi_A = \pm e^{-i\Lambda\phi}$ and $\psi_S = +e^{i\Lambda\phi}$ so that very high fields can be thought of as separating the molecular states into ones containing $+\Lambda$ and $-\Lambda$ as separately valid quantum numbers. This resembles a transition to Hund's case (d), although the analogy is very crude (e.g., removal of M-degeneracy).

It should be noted that C (Eq.47) is just the unitary matrix which must diagonalize Eq.(43):

$$C^{\sim}\begin{pmatrix} \delta & V_{HL} \\ V_{HL} & -\delta \end{pmatrix} C = \tag{52}$$

$$\begin{array}{c} \\ A \\ S \end{array} \begin{array}{c} \begin{array}{cc} \quad A & \qquad\qquad S \end{array} \\ \begin{pmatrix} (c_1^2 - c_2^2)\delta - 2c_1c_2V_{HL} & 2c_1c_2\delta + (c_1^2 - c_2^2)V_{HL} \\ 2c_1c_2\delta - (c_1^2 - c_2^2)V_{HL} & -(c_1^2 - c_2^2)\delta + 2c_1c_2V_{HL} \end{pmatrix} \end{array} .$$

Upon substitution of c_1 and c_2 from Eq.(48), the off-diagonal elements of Eq.(52) are found to be

$$\propto |V_{HL}| + V_{HL}$$

which is zero only if V_{HL} is negative. Eq.(52) then becomes

$$\begin{pmatrix} \sqrt{\delta^2 + V_{HL}^2} & 0 \\ 0 & -\sqrt{\delta^2 + V_{HL}^2} \end{pmatrix}, \tag{53}$$

in agreement with Eq.(35). However, the inequalities

$$V_{HL} < 0 < (c_1^2 - c_2^2)\delta < \delta < \sqrt{\delta^2 + V_{HL}^2}$$

imply that the signs shown in Eq.(53) can only result if $c_1 c_2 > 0$, ensuring that c_1 and c_2 are of like sign. Were $V_{HL} > 0$, however, it could be shown that $c_1 c_2 < 0$.

We have yet to deal with the off-diagonal matrix elements between states of different J. For this purpose we distinguish the transformations applying to the two interacting pairs of Λ-doublets by marking one of them with a "~", say the pair of higher energy. It is then convenient to define two coefficients b and d as follows:

$$\begin{aligned} b &= c_1 \tilde{c}_1 + c_2 \tilde{c}_2 \\ d &= c_1 \tilde{c}_2 - c_2 \tilde{c}_1 . \end{aligned} \tag{54}$$

It is readily shown that $b^2 + d^2 = 1$. We then obtain

$$V_{A\ddot{A}} = V_{S\ddot{S}} = bV_{H\ddot{H}}$$
$$V_{S\ddot{A}} = -V_{A\ddot{S}} = dV_{H\ddot{H}} \quad , \tag{55}$$

with the remaining elements following from matrix symmetry. We have used the fact that the order of parity in Λ-doublets usually alternates from one rotational level to the next (see Fig. 3) so that the wavefunctions ψ_L and ψ_H have the same parity (as do $\psi_{\ddot{L}}$ and $\psi_{\ddot{H}}$). Thus, we have $V_{H\ddot{H}} = V_{L\ddot{L}}$ and $V_{L\ddot{H}} = V_{\ddot{L}H} = 0$ for the old off-diagonal elements. As an example,

$$\begin{aligned} V_{S\ddot{A}} &= \langle c_2\psi_H + c_1\psi_L \,|V|\, \ddot{c}_1\psi_{\ddot{H}} - \ddot{c}_2\psi_{\ddot{L}} \rangle \\ &= c_2\ddot{c}_1V_{H\ddot{H}} - c_1\ddot{c}_2V_{L\ddot{L}} \\ &= d\,V_{H\ddot{H}} \quad . \end{aligned} \tag{56}$$

Using Eqs. (52) and (53) for the matrix elements of n_z, we apply these transformations to the $^2\Pi$ state matrix, which is shown in the first three rotational levels of the $^2\Pi_{\frac{1}{2}}$ state in Eq. (57) and the first two levels of the $^2\Pi_{\frac{3}{2}}$ state in Eq. (58). In these matrices, δ_i is the i^{th} Λ-doubling in that multiplet, and p is the sign of the parity. After applying the transformations of Eqs. (47)-(49), these matrices become those shown in Eqs. (59) and (60). In Eq. (59), $\Omega = \frac{1}{2}$, b_1 and d_1 are combinations of the c's pertaining to $J = \frac{1}{2}$ and $\frac{3}{2}$, while b_2 and d_2

$\Omega = \frac{1}{2}$

J,N →		$\frac{1}{2},1$		$\frac{3}{2},2$				$\frac{5}{2},3$					
	pM→	$-\frac{1}{2}$	$+\frac{1}{2}$	$-\frac{3}{2}$	$-\frac{1}{2}$	$+\frac{1}{2}$	$+\frac{3}{2}$	$-\frac{5}{2}$	$-\frac{3}{2}$	$-\frac{1}{2}$	$+\frac{1}{2}$	$+\frac{3}{2}$	$+\frac{5}{2}$
↓	↓												
$\frac{1}{2},1$	$-\frac{1}{2}$	δ_1	$-\frac{1}{3}\varepsilon$	0	0	$-\frac{\sqrt{2}}{3}\varepsilon$	0	0	0	0	0	0	0
	$+\frac{1}{2}$	$-\frac{1}{3}\varepsilon$	$-\delta_1$	0	$-\frac{\sqrt{2}}{3}\varepsilon$	0	0	0	0	0	0	0	0
$\frac{3}{2},2$	$-\frac{3}{2}$	0	0	$-\delta_2$	0	0	$-\frac{1}{5}\varepsilon$	0	0	0	0	$-\frac{2}{5}\varepsilon$	0
	$-\frac{1}{2}$	0	$-\frac{\sqrt{2}}{3}\varepsilon$	0	$-\delta_2$	$-\frac{1}{15}\varepsilon$	0	0	0	0	$-\frac{\sqrt{6}}{5}\varepsilon$	0	0
	$+\frac{1}{2}$	$-\frac{\sqrt{2}}{3}\varepsilon$	0	0	$-\frac{1}{15}\varepsilon$	δ_2	0	0	0	$-\frac{\sqrt{6}}{5}\varepsilon$	0	0	0
	$+\frac{3}{2}$	0	0	$-\frac{1}{5}\varepsilon$	0	0	δ_2	0	$-\frac{2}{5}\varepsilon$	0	0	0	0
$\frac{5}{2},3$	$-\frac{5}{2}$	0	0	0	0	0	0	δ_3	0	0	0	0	$-\frac{1}{7}\varepsilon$
	$-\frac{3}{2}$	0	0	0	0	0	$-\frac{2}{5}\varepsilon$	0	δ_3	0	0	$-\frac{3}{35}\varepsilon$	0
	$-\frac{1}{2}$	0	0	0	0	$-\frac{\sqrt{6}}{5}\varepsilon$	0	0	0	δ_3	$-\frac{1}{35}\varepsilon$	0	0
	$+\frac{1}{2}$	0	0	0	$-\frac{\sqrt{6}}{5}\varepsilon$	0	0	0	0	$-\frac{1}{35}\varepsilon$	$-\delta_3$	0	0
	$+\frac{3}{2}$	0	0	$-\frac{2}{5}\varepsilon$	0	0	0	0	$-\frac{3}{35}\varepsilon$	0	0	$-\delta_3$	0
	$+\frac{5}{2}$	0	0	0	0	0	0	$-\frac{1}{7}\varepsilon$	0	0	0	0	$-\delta_3$

(57)

$\Omega = \frac{3}{2}$

J,N →		$\frac{3}{2},1$				$\frac{5}{2},2$					
	pM→	$\frac{3}{2}$	$\frac{1}{2}$	$\frac{1}{2}$	$\frac{3}{2}$	$\frac{5}{2}$	$\frac{3}{2}$	$\frac{1}{2}$	$\frac{1}{2}$	$\frac{3}{2}$	$\frac{5}{2}$
↓	↓										
$\frac{3}{2},1$	$-\frac{3}{2}$	$-\delta_1$	0	0	$-\frac{3}{5}\varepsilon$	0	0	0	0	$-\sqrt{\frac{8}{75}}\varepsilon$	0
	$-\frac{1}{2}$	0	$-\delta_1$	$-\frac{1}{5}\varepsilon$	0	0	0	0	$-\frac{2}{5}\varepsilon$	0	0
	$+\frac{1}{2}$	0	$-\frac{1}{5}\varepsilon$	$+\delta_1$	0	0	0	$-\frac{2}{5}\varepsilon$	0	0	0
	$+\frac{3}{2}$	$-\frac{3}{5}\varepsilon$	0	0	$+\delta_1$	0	$-\sqrt{\frac{8}{75}}\varepsilon$	0	0	0	0
$\frac{5}{2},2$	$-\frac{5}{2}$	0	0	0	0	$+\delta_2$	0	0	0	0	$-\frac{3}{7}\varepsilon$
	$-\frac{3}{2}$	0	0	0	$-\sqrt{\frac{8}{75}}\varepsilon$	0	$+\delta_2$	0	0	$-\frac{9}{35}\varepsilon$	0
	$-\frac{1}{2}$	0	0	$-\frac{2}{5}\varepsilon$	0	0	0	$+\delta_2$	$-\frac{3}{35}\varepsilon$	0	0
	$+\frac{1}{2}$	0	$-\frac{2}{5}\varepsilon$	0	0	0	0	$-\frac{3}{35}\varepsilon$	$-\delta_2$	0	0
	$+\frac{3}{2}$	$\sqrt{\frac{8}{75}}\varepsilon$	0	0	0	0	$-\frac{9}{35}\varepsilon$	0	0	$-\delta_2$	0
	$+\frac{5}{2}$	0	0	0	0	$-\frac{3}{7}\varepsilon$	0	0	0	0	$-\delta_2$

(58)

$\Omega = \frac{1}{2}$

J,N →		$\frac{1}{2},1$		$\frac{3}{2},2$				$\frac{5}{2},3$					
↓	M→ ↓	A_2^1	S_2^1	A_2^3	A_2^1	S_2^1	S_2^3	A_2^5	A_2^3	A_2^1	S_2^1	S_2^3	S_2^5
$\frac{1}{2},1$	A_2^1	T_1	0	0	$-\frac{2}{3}b_1$	$-\frac{2}{3}d_1$	0	0	0	0	0	0	0
	S_2^1	0	$-T_1$	0	$+\frac{2}{3}d_1$	$-\frac{2}{3}b_1$	0	0	0	0	0	0	0
$\frac{3}{2},2$	A_2^3	0	0	T_2	0	0	0	0	$-\frac{2}{5}b_2$	0	0	$-\frac{2}{5}d_2$	0
	A_2^1	$-\frac{2}{3}b_1$	$+\frac{2}{3}d_1$	0	T_3	0	0	0	0	$-\frac{6}{5}b_2$	$-\frac{6}{5}d_2$	0	0
	S_2^1	$-\frac{2}{3}d_1$	$-\frac{2}{3}b_1$	0	0	$-T_3$	0	0	0	$+\frac{6}{5}d_2$	$-\frac{6}{5}b_2$	0	0
	S_2^3	0	0	0	0	0	$-T_2$	0	$+\frac{2}{5}d_2$	0	0	$-\frac{2}{5}b_2$	0
$\frac{5}{2},3$	A_2^5	0	0	0	0	0	0	T_4	0	0	0	0	0
	A_2^3	0	0	$-\frac{2}{5}b_2$	0	0	$+\frac{2}{5}d_2$	0	T_5	0	0	0	0
	A_2^1	0	0	0	$-\frac{6}{5}b_2$	$+\frac{6}{5}d_2$	0	0	0	T_6	0	0	0
	S_2^1	0	0	0	$-\frac{6}{5}d_2$	$-\frac{6}{5}b_2$	0	0	0	0	$-T_6$	0	0
	S_2^3	0	0	$-\frac{2}{5}d_2$	0	0	$-\frac{2}{5}b_2$	0	0	0	0	$-T_5$	0
	S_2^5	0	0	0	0	0	0	0	0	0	0	0	$-T_4$

(59) $\times \varepsilon$

$\Omega = \frac{3}{2}$

J,N →		$\frac{3}{2},1$				$\frac{5}{2},2$					
↓	M→ ↓	A_2^3	A_2^1	S_2^1	S_2^3	A_2^5	A_2^3	A_2^1	S_2^1	S_2^3	S_2^5
$\frac{3}{2},1$	A_2^3	T_1	0	0	0	0	$-\sqrt{\frac{8}{75}}b_1$	0	0	$-\sqrt{\frac{8}{75}}d_1$	0
	A_2^1	0	T_2	0	0	0	0	$-\frac{2}{5}b_1$	$-\frac{2}{5}d_1$	0	0
	S_2^1	0	0	$-T_2$	0	0	0	$+\frac{2}{5}d_1$	$\frac{2}{5}b_1$	0	0
	S_2^1	0	0	0	$-T_1$	0	$+\sqrt{\frac{8}{75}}d_1$	0	0	$-\sqrt{\frac{8}{75}}b_1$	0
$\frac{5}{2},2$	A_2^5	0	0	0	0	T_3	0	0	0	0	0
	A_2^3	$-\sqrt{\frac{8}{75}}b_1$	0	0	$-\sqrt{\frac{8}{75}}d_1$	0	T_4	0	0	0	0
	A_2^1	0	$-\frac{2}{5}b_1$	$-\frac{2}{5}d_1$	0	0	0	T_5	0	0	0
	S_2^1	0	$+\frac{2}{5}d_1$	$-\frac{2}{5}b_1$	0	0	0	0	$-T_5$	0	0
	S_2^3	$+\sqrt{\frac{8}{75}}d_1$	0	0	$-\sqrt{\frac{8}{75}}b_1$	0	0	0	0	$-T_4$	0
	S_2^5	0	0	0	0	0	0	0	0	0	$-T_3$

(60) $\times \varepsilon$

combine the $J = \frac{3}{2}$ and $J = \frac{5}{2}$ levels. The T's are defined as follows:

$$T_1 = (\tfrac{1}{9} + \delta_1^2/\varepsilon^2)^{\frac{1}{2}}$$
$$T_2 = (\tfrac{1}{25} + \delta_2^2/\varepsilon^2)^{\frac{1}{2}}$$
$$T_3 = (\tfrac{1}{225} + \delta_2^2/\varepsilon^2)^{\frac{1}{2}}$$
$$T_4 = (\tfrac{1}{49} + \delta_3^2/\varepsilon^2)^{\frac{1}{2}}$$
$$T_5 = (\tfrac{9}{1225} + \delta_3^2/\varepsilon^2)^{\frac{1}{2}}$$
$$T_6 = (\tfrac{1}{1225} + \delta_3^2/\varepsilon^2)^{\frac{1}{2}} .$$

In Eq.(60), $\Omega = \frac{3}{2}$, we have defined

$$T_1 = (\tfrac{9}{25} + \delta_1^2/\varepsilon^2)^{\frac{1}{2}}$$
$$T_2 = (\tfrac{1}{25} + \delta_1^2/\varepsilon^2)^{\frac{1}{2}}$$
$$T_3 = (\tfrac{9}{49} + \delta_2^2/\varepsilon^2)^{\frac{1}{2}}$$
$$T_4 = (\tfrac{81}{1225} + \delta_2^2/\varepsilon^2)^{\frac{1}{2}}$$
$$T_5 = (\tfrac{9}{1225} + \delta_2^2/\varepsilon^2)^{\frac{1}{2}} .$$

Note that a factor ε has been extracted from the transformed matrices. With the first order energies and zero order wavefunctions given by Eqs.(28) and (29), the second order energies can be shown (Landau and Lifshitz[1], p.139) to still be given by

$$W_n^{(2)} = \sum_m{}' \frac{V_{nm}^2}{U_m} , \tag{61}$$

but where the matrix elements are taken with respect to the proper zero order wavefunctions (Eq.49) so that the submatrices between nearly degenerate levels $V_{nn'}$ are diagonal and make no contribution (Eqs.59 and 60). Applying Eq.(61) to the transformed matrices (and remembering that

$b_i^2 + d_i^2 = 1$), we see that second order energies are identical to what we would have gotten by naively applying Eq.(31) to the unperturbed matrices of V (Eqs.57 and 58).

5. The Secular Equation for Σ State Multiplets

Hund's case (b) coupling describes most Σ states quite well, since the internuclear axis carries no component of orbital angular momentum to which the spin may be coupled. In "pure" case (b), the 2S+1 multiplets of energy levels with $N > 0$ are degenerate. This degeneracy is usually partly removed by spin-spin, spin-rotation, and spin-orbital coupling (Herzberg[3], p.223), but these sublevels remain close together compared to the rotational spacing, so that case (b) is still a fairly good description. Unlike the Λ-doublets treated above, the matrix elements between these nearby states are all zero, since all levels in these multiplets have the same parity. The matrix of Eq.(42) and its eigenvalues are all zero so that the correct choice of zero-order wavefunctions remains unspecified. Introducing the zero-field separation energies change nothing since these are already diagonal. (The matrices of Eq. (42) onwards are readily enlarged to $n \times n$, to describe the problem of Σ states of multiplicity n.) Nevertheless, if second order Stark effects become comparable to the spin splittings, then the interaction with whatever terms are causing the spin splittings must be included, and the resulting diagonalization must

determine the appropriate zero-order wavefunctions.

Landau and Lifshitz[1] (p.138) show, by the same methods outlined in Sec.1, that the appropriate equation is similar to Eq.(39):

$$\sum_j \left(X_{nj} - W_n^{(2)} \delta_{nj} \right) c_{nj} = 0 \quad , \tag{62}$$

but where

$$X_{nj} = \sum_m \frac{V_{nm} V_{mj}}{U_m} \tag{63}$$

replaces V_{nj}. The matrix X_{nj} has the standard second order terms along its diagonal, and its off-diagonal elements clearly connect the nearly degenerate but non-interacting levels n and j to each other through a third (and possibly distant) level m. This degree of indirectness is usually associated with third order effects. However, as with Λ-doubling, degeneracy has increased the effect by a full order of approximation. Here, an interaction with a relatively distant level has given the wavefunction a small component of opposite parity, and has weakened the rule preventing interactions between the spin multiplets. If these levels have only small components of opposite parity, they make up for it in proximity to one another, and may have second order effects considerably larger than $\sum V_{nm}^2/U_m$.

6. $^2\Sigma$ States, Interaction of Levels with N=1

The matrix elements of n_z in a $^2\Sigma$ state are the square roots of those in the matrix of Eq.(18), which defines the row and column numbers used in this section. Ignoring spin-splitting in the denominators of Eq.(63), the rotational levels are given by $BN(N+1)$ cm^{-1}. Only two values of U_m are needed: $U_{(N=0)} = 2B$, and $U_{(N=2)} = -4B$. We may now readily evaluate X_{nj}; for example,

$$\begin{aligned} X_{23} &= (-\mu E)^2 \frac{\sqrt{\frac{2}{9}}\sqrt{\frac{1}{9}}}{2Bhc} + (-\mu E)^2 \frac{\sqrt{\frac{1}{9}}\sqrt{\frac{1}{225}}}{(-4B)hc} \\ &= \frac{\sqrt{2}}{20} \frac{(\mu E)^2}{hcB} \quad \text{ergs}, \end{aligned} \tag{64}$$

or, converting to cm^{-1},

$$\begin{aligned} X^{\sigma}_{23} &\equiv X_{23}/hc \\ &= \left(\frac{\mu E}{hc}\right)^2 \frac{\sqrt{2}}{20B} \\ &= \frac{\sqrt{2}\varepsilon^2}{20B} \quad cm^{-1} \ . \end{aligned} \tag{65}$$

Similarly,

$$X^{\sigma}_{44} = \varepsilon^2 \frac{(\sqrt{1/25})^2}{-4B} + \varepsilon^2 \frac{(\sqrt{4/25})^2}{-4B} = -\frac{\varepsilon^2}{20B} \ . \tag{66}$$

Thus we obtain

$$X^{\sigma} = \frac{\varepsilon^2}{20B} \begin{array}{c} \begin{matrix} 2 & 3 & 4 \end{matrix} \\ \begin{pmatrix} 0 & \sqrt{2} & 0 \\ \sqrt{2} & 1 & 0 \\ 0 & 0 & -1 \end{pmatrix} \begin{matrix} 2 \\ 3 \\ 4 \end{matrix} \end{array} \tag{67}$$

If we include the spin splitting through a simple Hamiltonian of the form

$$H_r = hcB\vec{N}^2 + hc\gamma(\vec{N}\cdot\vec{S}) \ , \tag{68}$$

then it can be readily shown that f_2 levels are shifted by $-\frac{1}{2}\gamma(N+1)$, and f_1 levels by $+\frac{1}{2}\gamma N$. This gives the matrix

$$\begin{array}{c} \begin{matrix} 2 & 3 & 4 \end{matrix} \\ \begin{pmatrix} -\gamma & 0 & 0 \\ 0 & \frac{1}{2}\gamma & 0 \\ 0 & 0 & \frac{1}{2}\gamma \end{pmatrix} \begin{matrix} 2 \\ 3 \\ 4 \end{matrix} \end{array} \tag{69}$$

to be added to Eq.(67). To simplify notation, we define

$$\Gamma \equiv \frac{20B}{\varepsilon^2}\gamma \ . \tag{70}$$

The secular equation from Eq.(62) is now

$$\frac{\varepsilon^2}{20B} \times \begin{vmatrix} -\Gamma-F' & \sqrt{2} & 0 \\ \sqrt{2} & 1+\frac{1}{2}\Gamma-F' & 0 \\ 0 & 0 & -1+\frac{1}{2}\Gamma-F' \end{vmatrix} = 0 \tag{71}$$

where $F=\frac{\varepsilon^2}{20B}F'$ is the energy in cm^{-1}. The $J=M=\frac{3}{2}$ (X_{44}) corner is a 1×1 subdeterminant with immediate solution

$$F_4 = \frac{\varepsilon^2}{20B}(-1+\tfrac{1}{2}\Gamma) = -\frac{\varepsilon^2}{20B} + \tfrac{1}{2}\gamma \ , \quad (J=\tfrac{3}{2},\ M=\tfrac{3}{2}) \tag{72}$$

and the upper left 2×2 subdeterminant with $M=\frac{1}{2}$ gives

$$(F' + \Gamma)(F' - 1 - \tfrac{1}{2}\Gamma) - 2 = 0$$

or

$$F' + (\tfrac{1}{2}\Gamma - 1)F' - (2 + \tfrac{1}{2}\Gamma^2 + \Gamma) = 0, \tag{73}$$

where $F' = (20B/\varepsilon^2)F$. This equation has solutions

$$F' = \tfrac{1}{2}(1-\tfrac{1}{2}\Gamma) \pm (\tfrac{1}{4}(1-\tfrac{1}{2}\Gamma)^2 + 2 + \tfrac{1}{2}\Gamma^2 + \Gamma)^{\frac{1}{2}}, \tag{74}$$

which are written separately as

$$F_2 = \frac{\varepsilon^2}{40B} - \frac{\gamma}{4} - \tfrac{1}{2}\left(\left(\frac{3\varepsilon^2}{20B} + \frac{\gamma}{2}\right)^2 + 2\gamma^2\right)^{\frac{1}{2}}, \quad (J=M=\tfrac{1}{2})$$

$$F_3 = \frac{\varepsilon^2}{40B} - \frac{\gamma}{4} + \tfrac{1}{2}\left(\left(\frac{3\varepsilon^2}{20B} + \frac{\gamma}{2}\right)^2 + 2\gamma^2\right)^{\frac{1}{2}}, \quad (J=\tfrac{3}{2}, M=\tfrac{1}{2}). \tag{75}$$

Eqs. (72) and (75), which appear in a paper by Swartz and Trischka[13] (p.1089), are seen to yield the original spin splittings in the limit of $\varepsilon \to 0$. In the high field limit of $\gamma \to 0$, F_2 and F_4 approach $-\varepsilon^2/20B$, while F_3 approaches $+\varepsilon^2/10B$. These limits are just the Stark effects in the $M=1$ and $M=0$ sublevels, respectively, of the $J=N=1$ level of a $^1\Sigma$ state (as is readily calculated from Eqs. (15) and (31) above). We see that the degeneracy added by spin splitting does not alter the Stark effect in the limit of perfect degeneracy, unlike the directly interacting Λ-doublets. From this one would expect that the non-degenerate level $N=0$ should have a Stark effect which is independent of the multi-

plicity of the Σ state: This is readily verified by examination of the $^1\Sigma$, $^2\Sigma$, and $^3\Sigma$ matrices given in Chap.III where the sum over J' of the matrix elements squared is

$$\sum_{J'} \langle \psi_{0S} | n_z | \psi_{1J'} \rangle^2 = \tfrac{1}{3}$$

in each case (we use the notation ψ_{NJ}). Thus Eq.(36) may be applied to $^2\Sigma$ states even though it was derived for $^1\Sigma$.

7. $^3\Sigma$ States, Interaction of N=1 Levels

This calculation is very close to that of the last section. In a $^3\Sigma$ state three levels arise from N=1, with J= 0, 1, and 2. We use the empirical constants for the spin splitting: Using the f_2 (J=1) level, which has highest energy, as a reference, we take a_1 to be the energy difference (cm^{-1}) between the J=2 and J=1 levels, and a_3 to be the difference between J=0 and J=1. Evaluating X^σ of Eq.(63) we have for the secular equation:

J	M	# →	3	4	5	6	7	8
0	0	3	$-a_3'-F'$	0	0	$\sqrt{2}$	0	0
1	0	4	0	$-1-F'$	0	0	0	0
1	1	5	0	0	$\frac{1}{2}-F'$	0	$\frac{3}{2}$	0
2	0	6	$\sqrt{2}$	0	0	$1-a_1'-F'$	0	0
2	1	7	0	0	$\frac{3}{2}$	0	$\frac{1}{2}-a_1'-F'$	0
2	2	8	0	0	0	0	0	$-1-a_1'-F'$

$$\left| \quad \right| \frac{\varepsilon^2}{20B} = 0 \qquad (76)$$

where $a_1' = (20B/\varepsilon^2)a_1$, and $a_3' = (20B/\varepsilon^2)a_3$ (with F' as

in Eq.73). If we assume that $a_3 > a_1 > 0$, so that $F_{J=1} > F_{J=2} > F_{J=0}$ at zero field, then Eq.(76) gives the following results:

$$
\begin{aligned}
J=M=0: \qquad & F_3 = \tfrac{1}{2}\left(\frac{\varepsilon^2}{20B} - (a_1+a_3) - \left[(a_3-a_1+\frac{\varepsilon^2}{20B})^2 + 8(\frac{\varepsilon^2}{20B})^2\right]^{\frac{1}{2}}\right) \\
J=1,M=0: \qquad & F_4 = -\frac{\varepsilon^2}{20B} \\
J=M=1: \qquad & F_5 = \frac{\varepsilon^2}{40B} - \tfrac{1}{2}a_1 + \tfrac{1}{2}\left[a_1^2 + (\frac{3\varepsilon^2}{20B})^2\right]^{\frac{1}{2}} \\
J=2,M=0: \qquad & F_6 = \tfrac{1}{2}\left(\frac{\varepsilon^2}{20B} - (a_1+a_3) + \left[(a_3-a_1+\frac{\varepsilon^2}{20B})^2 + 8(\frac{\varepsilon^2}{20B})^2\right]^{\frac{1}{2}}\right) \\
J=2,M=1: \qquad & F_7 = \frac{\varepsilon^2}{40B} - \tfrac{1}{2}a_1 - \tfrac{1}{2}\left[a_1^2 + (\frac{3\varepsilon^2}{20B})^2\right]^{\frac{1}{2}} \\
J=M=2: \qquad & F_8 = -\frac{\varepsilon^2}{20B} - a_1
\end{aligned}
\tag{77}
$$

These solutions are illustrated along with those for the $^2\Sigma$ (Eqs.72 and 75) and $^1\Sigma$ cases, in Fig. 6.

CHAPTER V

INTERMEDIATE COUPLING

1. Introduction

In this chapter we will consider the modification of the wavefunctions and matrix elements of the Stark perturbation in multiplet Π and Δ states due to the fact that these states may not be properly described by Hund's case (a). The matrix elements of n_z for these states were derived for Chap. III using pure case (a) wavefunctions, or, more precisely, using the assumption that case (a) quantum numbers and their corresponding selection rules are valid). It is found that the energy levels of all states considered in this work can be described quite closely by considering them to lie along a continuum between pure case (a) and case (b) coupling, described by a single parameter Y. This parameter is a measure of the interaction energy between the electronic spin S and the axially averaged magnetic field from the orbital electronic angular momentum L. We may define Y to be the ratio of the coefficient of this coupling (A) to the rotational spacing constant (B).

Since case (a) wavefunctions form a complete set, the wavefunctions for case (b) or any intermediate coupling can be expressed as a linear combination of them. The problem of finding the appropriate linear combination is essentially the problem of diagonalizing the Hamiltonian.

2. The $^2\Pi$ State

2.1. Hamiltonian

The $^2\Pi$ state is treated in some detail by Hougen[2] (p.10ff). There are four possible case (a) wavefunctions, labeled as either $|\Omega>$ or $|\Omega J>$, and characterized by the following quantum numbers:

Wavefunction	Λ	S	Σ	Ω	J	M
$\left\|+\frac{3}{2}\right>$	+1	$\frac{1}{2}$	$+\frac{1}{2}$	$+\frac{3}{2}$	J	M
$\left\|+\frac{1}{2}\right>$	+1	$\frac{1}{2}$	$-\frac{1}{2}$	$+\frac{1}{2}$	J	M
$\left\|-\frac{3}{2}\right>$	-1	$\frac{1}{2}$	$-\frac{1}{2}$	$-\frac{3}{2}$	J	M
$\left\|-\frac{1}{2}\right>$	-1	$\frac{1}{2}$	$+\frac{1}{2}$	$-\frac{1}{2}$	J	M

When the 4×4 matrix of the Hamiltonian is evaluated with respect to these wavefunctions, in accordance with the discussion of Appendix D, it turns out that all matrix elements are zero between wavefunctions differing in the sign of Ω. The matrix is thus factored into a 2×2 block with positive Ω and another with negative Ω. Moreover the two sub-blocks are the same; for example $H_{11} = H_{33}$ and $H_{12} = H_{34}$. Thus the secular equation $|H - WI| = 0$ factors immediately into two identical quadratic equations in W. We interpret this to mean that each of the energy level solutions W is doubly degenerate, giving rise to the Λ doublets. When this happens, however, they are not separated into (for example) states with wavefunction $\left|\frac{3}{2}\right>$ and wavefunction $\left|-\frac{3}{2}\right>$, but rather into

symmetric and antisymmetric linear combinations of these which possess definite values of parity, as discussed in Chapter IV, Sec. 3. The sub-block of the wavefunctions $|\frac{3}{2}>$ and $|\frac{1}{2}>$ is

$$\begin{array}{c} \\ |\frac{3}{2}> \\ |\frac{1}{2}> \end{array} \begin{array}{c} \begin{array}{cc} |\frac{3}{2}> & |\frac{1}{2}> \end{array} \\ \begin{pmatrix} J(J+1) - \frac{7}{4} + Y/2 & -\sqrt{(J-\frac{1}{2})(J+\frac{3}{2})} \\ -\sqrt{(J-\frac{1}{2})(J+\frac{3}{2})} & J(J+1) + \frac{1}{4} - Y/2 \end{pmatrix} \end{array} \qquad (78)$$

where we have already dropped the terms $H_{ev} + B(L^2 - L_\zeta^2)$ from the diagonal and divided by hcB. We have defined $Y \equiv A/B$.

2.2. $J=\frac{1}{2}$

The energy level $J=\frac{1}{2}$ is a special case; since J cannot be less than $J_\zeta=\Omega$, the wavefunction $|\frac{3}{2}>$ does not exist. Eq. (78) is a 1×1 matrix yielding trivially the eigenvalue

$$F_{J=\frac{1}{2}} = B[\, J(J+1) + \tfrac{1}{4} - Y/2 \,] = B - A/2 \quad . \qquad (79)$$

Equally trivially, the wavefunction is simply $|\frac{1}{2}>$, or $|1\ \frac{1}{2}\ -\frac{1}{2};\ \frac{1}{2}\ J\ M>$ in the full $|\Lambda\ S\ \Sigma;\ \Omega\ J\ M>$ notation, and is pure case (a).

2.3. $J>\frac{1}{2}$

For all values of $J>\frac{1}{2}$, the full matrix of Eq. (78)

must be diagonalized. The secular equation yields the well known formulae of Hill and Van Vleck[18](p.261):

$$F_1 = B[\ (J+\tfrac{1}{2})^2 - 1 - \tfrac{1}{2}\sqrt{4(J+\tfrac{1}{2})^2 + Y(Y-4)}\ ]$$
$$F_2 = B[\ (J+\tfrac{1}{2})^2 - 1 + \tfrac{1}{2}\sqrt{4(J+\tfrac{1}{2})^2 + Y(Y-4)}\ ] \quad . \tag{80}$$

We shall not bother to add back the expectation value of $(H_{ev} + \tfrac{1}{2}(L^2 - L_\zeta^2))/hc$.

The matrix of Eq. (78) can be diagonalized more easily by first subtracting half the trace $((J - \tfrac{1}{2})(J + \tfrac{3}{2}))$ and noting the similarity to Eq. 43), using the solution of Eq. (45) plus $(J - \tfrac{1}{2})(J + \tfrac{3}{2})$.

The wavefunctions are obtained immediately from Eq. (49):

$$\psi_1 = c_1|\tfrac{1}{2}> + c_2|\tfrac{3}{2}>$$
$$\psi_2 = c_1|\tfrac{3}{2}> - c_2|\tfrac{1}{2}> \tag{81}$$

Eq. (48) reduces to

$$c_1 = \sqrt{(X + Y - 2)/2X}$$
$$c_2 = \sqrt{(X - Y + 2)/2X} \tag{82}$$

where $X \equiv \sqrt{4(J+\frac{1}{2})^2 + Y(Y-4)}$.

2.4. Hund's Cases as Limits

When $Y >> 2$ then

$$\bar{c}_1 \to 1, \quad \bar{c}_2 \to 0$$

so that

$$\begin{aligned} \Psi_1 &\to |\tfrac{1}{2}> \quad \leftrightarrow \quad {}^2\Pi_{\frac{1}{2}} \\ \Psi_2 &\to |\tfrac{3}{2}> \quad \leftrightarrow \quad {}^2\Pi_{\frac{3}{2}} \end{aligned} \tag{83}$$

which corresponds to a <u>regular</u> case (a). When $Y=2$ (as is the case for CH, to within experimental error) then

$$c_1 = c_2 = 1/\sqrt{2}$$

so that

$$\begin{aligned} \psi_1 &= (|\tfrac{1}{2}> + |\tfrac{3}{2}>)/\sqrt{2} \\ \psi_2 &= (|\tfrac{3}{2}> - |\tfrac{1}{2}>)/\sqrt{2} \end{aligned} \tag{84}$$

which corresponds to case (b). When $Y<2$, then $Y/2-1$ is negative, and $\bar{c}_2$ becomes larger than $\bar{c}_1$. For $Y<<2$ we have

$$c_1 \to 0, \quad c_2 \to 1 \ ,$$

so that

$$\begin{aligned} \psi_1 &\to |\tfrac{3}{2}> \quad \leftrightarrow \quad {}^2\Pi_{\frac{3}{2}} \\ \psi_2 &\to -|\tfrac{1}{2}> \quad \leftrightarrow \quad {}^2\Pi_{\frac{1}{2}} \end{aligned} \tag{85}$$

This corresponds to the inverted case (a), whose energy levels are illustrated in Fig. 3, Chap. V. The negative sign in Eq. (85) is the result of our choice of phases for the wavefunction, and causes no difficulties. Ψ_2 in all cases corresponds to the higher energy (F_2 in Eq. 80). Fig.7 illustrates the behavior of the energy levels of lowest J as a function of Y. It is seen that the $J=\frac{1}{2}$ level follows the $\Pi_{\frac{1}{2}}$ multiplet in both regular and inverted states, and that the pair of levels of same J shows a mutual repulsion which increases with $|Y|$.

Looking at the special case when Y=0 or 4, then from Eq. (80) we have

$$\begin{aligned} F_1 &= J^2 + 2J - \tfrac{1}{4} = (J + \tfrac{1}{2})((J + \tfrac{1}{2}) + 1) - 1 \\ F_2 &= J^2 - \tfrac{5}{4} \quad\quad = (J - \tfrac{1}{2})((J - \tfrac{1}{2}) + 1) - 1 \end{aligned} \tag{86}$$

which suggests that, if we define

$$\begin{aligned} N &\equiv J - \tfrac{1}{2} \quad (F_1 \text{ levels}) \\ \text{and} \qquad N &\equiv J + \tfrac{1}{2} \quad (F_2 \text{ levels}) \end{aligned} , \tag{87}$$

then we may write, for both multiplets:

$$F = N(N + 1) - 1 \tag{88}$$

This is the familiar N previously defined as the total angular momentum excluding spin. The eigenfunctions defined

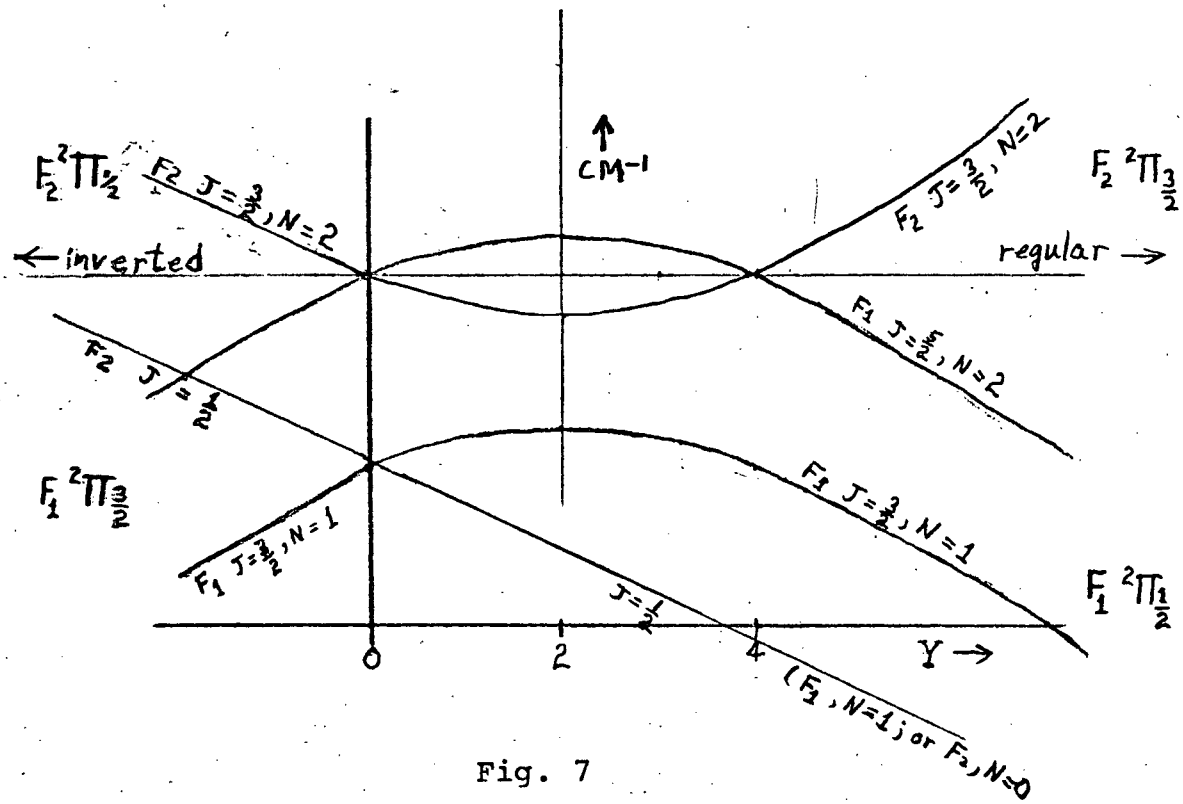

Fig. 7

$^2\Pi$ Energy Levels as a Function of Y

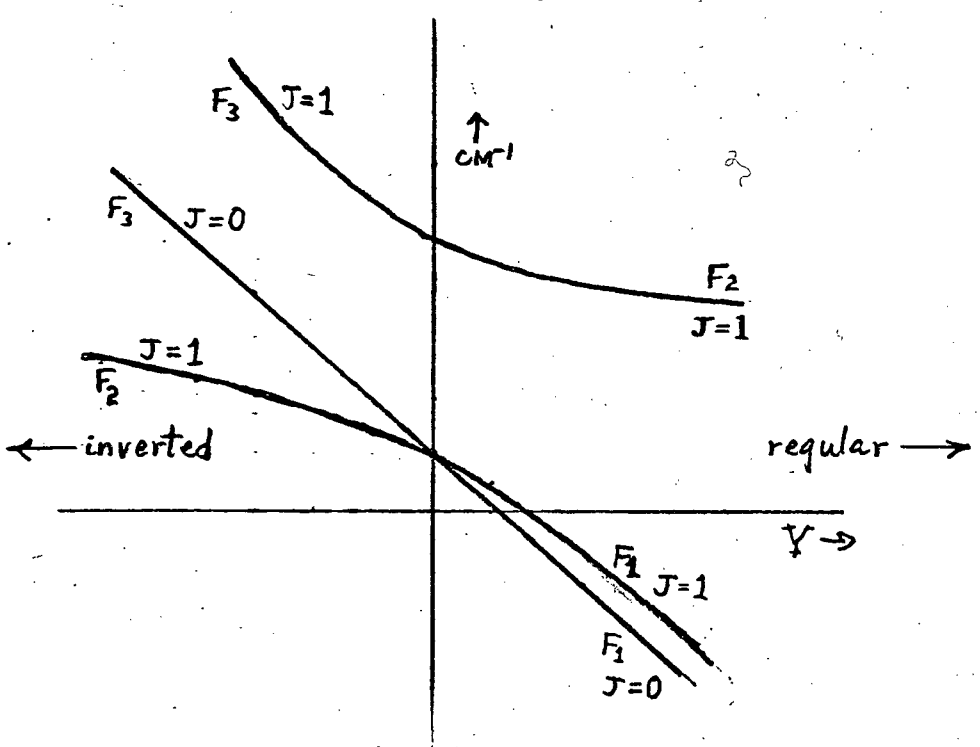

Fig. 8

$^3\Pi$ Energy Levels as a Function of Y

by Eq. (81) can be shown to be eigenfunctions of $(\vec{J}-\vec{S})^2$ when $Y=0$. Fig. 7 shows that levels of equal N do indeed lie close together in the case (b) region (small $|Y|$), and are indeed degenerate at $Y=0$ and 4. The exception is $J=\frac{1}{2}$ when $Y>4$, which follows the F_1 multiplet energy scheme but <u>not</u> the F_1 rule that $N=J-\frac{1}{2}$. It must be concluded that N is poorly defined in this level for all $Y>2$.

It should be noted that c_1 and c_2 are functions of J (Eq. 82), and that an increase in J (and therefore X) has the same effect on them as a decrease in Y. Thus case (b) is approached with increasing J in all cases, although this effect is more obvious when $|Y|$ is smaller.

2.5. Matrix Elements of n_z, Example

Eq. (81) is actually all we need to calculate the exact matrix elements of n_z from the pure case (a) forms given in Chap.III. The diagonal matrix element of the $J=\frac{3}{2}$, $M=\frac{3}{2}$, F_1 level, for example, is now

$$\begin{aligned} \langle \psi_1|n_z|\psi_1\rangle &= (c_1\langle \tfrac{1}{2}| + c_2\langle \tfrac{3}{2}|)n_z(c_1|\tfrac{1}{2}\rangle + c_2|\tfrac{3}{2}\rangle) \\ &= c_1^2\langle \tfrac{1}{2}|n_z|\tfrac{1}{2}\rangle + \langle \tfrac{3}{2}|n_z|\tfrac{3}{2}\rangle \\ &= \tfrac{1}{5}c_1^2 + \tfrac{3}{5}c_2^2 \end{aligned} \qquad (89)$$

using Eqs. (19) and (20). We depend here on the selection rule $\Delta\Sigma=0$, which implies $\Delta\Omega=0$ for electric dipole

transitions. This assures us, for example, that

$$< \tfrac{3}{2} \,|n_z|\, \tfrac{1}{2} > = 0 \ . \tag{90}$$

Similarly, the off-diagonal matrix element between this same level and the $J=\frac{3}{2}$, $M=\frac{3}{2}$, F_2 level (forbidden in pure case (a) is given by

$$< \psi_1 |n_z| \psi_2 > = (c_1 < \tfrac{1}{2}| + c_2 < \tfrac{3}{2}|) n_z (c_1 |\tfrac{3}{2} > - c_2 |\tfrac{1}{2} >) \tag{91}$$

$$= 2c_1 c_2 / 5 \ .$$

3. The $^3\Pi$ State

3.1. Hamiltonian

We take as a basis set the wavefunctions characterized as follows

Label	Λ	S	Σ	Ω	J	M
$\|2^+>$	+1	1	+1	+2	J	M
$\|1^+>$	+1	1	0	+1	J	M
$\|0^+>$	+1	1	-1	0	J	M
$\|0^->$	-1	1	+1	0	J	M
$\|1^->$	-1	1	0	-1	J	M
$\|2^->$	-1	1	-1	-2	J	M

Here $|0^+>$ is a pure case (a) wavefunction, which may be referred to as a $^3\Pi_{0+}$ state, etc. The 6×6 matrix of the Hamiltonian (Appendix D) taken with respect to these functions factors into two 3×3 blocks with zero matrix

elements between them. As in the $^2\Pi$ state, the two blocks are identical, producing Λ-doublets (pairs of levels of opposite parity which are degenerate to the approximation that we have used the correct Hamiltonian).

We shall consider only the 3×3 matrix corresponding to the states $|0^+J>$, $|1^+J>$, and $|2^+J>$ and will hereafter omit the superscript sign. The resulting matrix of H/hcB is given by

$$\begin{array}{c} \\ |0\ J> \\ |1\ J> \\ |2\ J> \end{array} \begin{array}{c} \begin{array}{ccc} |0\ J> & |1\ J> & |2\ J> \end{array} \\ \begin{pmatrix} -Y + x + 1 & -\sqrt{2x} & 0 \\ -\sqrt{2x} & x + 1 & -\sqrt{2x - 4} \\ 0 & -\sqrt{2x - 4} & Y + x - 3 \end{pmatrix} \end{array} \qquad (92)$$

where $x \equiv J(J+1)$ and terms in $H_{ev/hcB}$ and $L^2 - L_\zeta^2$ have been subtracted from the diagonal.

3.2. J=0

The $J=0$ energy level is a special case since the $|1>$ and $|2>$ states are not involved ($J \geq \Omega$). We therefore have

$$F_{\Omega J} \doteq F_{oo} = B[J(J+1) - Y + 1] = B(1 - Y), \qquad (93)$$

and a pure case (a) wavefunction

$$\psi_{oo} = |0\ 0> \ . \tag{94}$$

We maintain the notation $\psi_{\Omega J}$ for the "true" (intermediate case) wavefunctions, while continuing to use $|\Omega J>$ for the pure case (a) wavefunctions.

3.3. J=1

When J=1, we have $|0J>$ and $|1J>$, but still no $|2J>$ in our basis set. Our matrix to be diagonalized is now

$$\begin{array}{c} \\ |0\ 1> \\ |1\ 1> \end{array} \begin{array}{c} \begin{array}{cc} |0\ 1> & |1\ 1> \end{array} \\ \begin{pmatrix} -Y + x + 1 & -\sqrt{2x} \\ -\sqrt{2x} & x + 1 \end{pmatrix} \end{array} \tag{95}$$

which may be transformed to

$$\begin{array}{c} \\ |0\ 1> \\ |1\ 1> \end{array} \begin{array}{c} \begin{array}{cc} |0\ 1> & |1\ 1> \end{array} \\ \begin{pmatrix} -Y/2 & -2 \\ -2 & Y/2 \end{pmatrix} \end{array} \tag{96}$$

by substituting $x=2$ and subtracting $3 - Y/2$ from the diagonal. This is of the same form as Eq. (43) putting $\delta = -Y/2$ and $V_{HL} = -2$. Adding $(3 - Y/2)$ back to the

eigenvalues given by Eq. (45), we have

$$F_{01} = B(3 - Y/2 + \tfrac{1}{2}\sqrt{Y^2 + 16}) \tag{97}$$

$$F_{11} = B(3 - Y/2 - \tfrac{1}{2}\sqrt{Y^2 + 16}) \tag{98}$$

Here the higher eigenvalue has been assigned to the $|0\ 1>$ state, corresponding to an <u>inverted</u> $^3\Pi$ state ($Y<0$). For a regular state ($Y>0$), the signs before the radical must be reversed. The wavefunctions, from Eqs. (48) and (49), are

$$\begin{aligned} \psi_{01} &= c_1|0\ 1> - c_2|1\ 1> \\ \psi_{11} &= c_2|0\ 1> + c_1|1\ 1> \end{aligned}, \tag{99}$$

with

$$c_1 = \sqrt{(X - Y)/2X} \tag{100}$$

and

$$c_2 = \sqrt{(X + Y)/2X} \tag{101}$$

In NH, where $Y = 2.1344$ (Veseth[19], p.235f), we have

$$\begin{aligned} c_1 &= 0.857545 \\ c_2 &= 0.514410\ . \end{aligned} \tag{102}$$

These wavefunctions are for an inverted state, corresponding

to the eigenvalues of Eqs. (97) and (99), so that $c_1 > c_2$. For regular states, the "0" and "1" values of the "Ω" labels must be everywhere interchanged; equations (101) and (102) are unchanged except that $c_2 > c_1$. Matrix elements of n_z are calculated exactly as in the $^2\Pi$ case (Eqs. 89-91).

3.4. J=2

When J is larger than one, the full matrix of Eq. (97) must be used. In these cases, it was found convenient to calculate the eigenvectors and eigenvalues numerically, using a U.B.C. computer library program called DYSMAL. With a value of Y = -2.1344 appropriate to the NH molecule, the Hamiltonian matrix for J=2 (x=6) is

$$\begin{array}{c} \\ |0\ 2> \\ |1\ 2> \\ |2\ 2> \end{array} \begin{array}{c} \begin{array}{ccc} |0\ 2> & |1\ 2> & |2\ 2> \end{array} \\ \begin{pmatrix} 9.1344 & -3.46410 & 0 \\ -3.46410 & 7.00000 & -2.82843 \\ 0 & -2.82843 & 0.8656 \end{pmatrix} \end{array} \qquad (103)$$

This yields eigenvalues

$$\begin{aligned} F_{02}/B &= 11.96309 \\ F_{12}/B &= 5.46678 \\ F_{22}/B &= -0.42987\ , \end{aligned} \qquad (104)$$

the last of which is the ground level of the $^3\Pi$ state. The values of eigenvector components from the computer

printout are the coefficients in the expansion of the proper wavefunctions:

$$\begin{aligned}
\psi_{02} &= 0.7646921|0\ 2> - 0.6244334|1\ 2> + 0.1591504|2\ 2> \\
\psi_{12} &= 0.6268996|0\ 2> + 0.6637233|1\ 2> - 0.4080051|2\ 2> \\
\psi_{22} &= 0.1491402|0\ 2> + 0.4117697|1\ 2> + 0.8990011|2\ 2> .
\end{aligned} \tag{105}$$

3.5. Matrix Element of n_z, Example

As an example, we will evaluate the matrix element of n_z between the J=1 and J=2 levels of the $^3\Pi_1$ multiplet for M=0. Labeling the numerical coefficients in the expansion of ψ_{12} (above) as d_0, d_1, and d_2 for brevity, we have

$$\begin{aligned}
<\psi_{12}|n_z|\psi_{11}>_0 &= (d_0<0\ 2| + d_1<1\ 2| + d_2<2\ 2|)n_z \\
&\quad \times (c_2|0\ 1> + c_1|1\ 1>) \\
&= d_0c_2<0\ 2|n_z|0\ 1> + d_1c_1<1\ 2|n_z|1\ 1> \\
&= d_0c_2\sqrt{4/15} + d_1c_1\sqrt{1/5} \\
&\simeq 0.421 \qquad (M = 0)
\end{aligned} \tag{106}$$

where the c's come from Eqs. (100)-(102), and the pure case (a) matrix elements from Eqs. (22) and (23). Similarly, the matrix element for M = 1 between the same two levels is

$$\begin{aligned}
<\psi_{12}|n_z|\psi_{11}>_1 &= d_0c_2\sqrt{1/5} + d_1c_1\sqrt{3/20} \\
&\simeq 0.366 \qquad (M = 1) .
\end{aligned} \tag{107}$$

3.6. J=3

Finally, we will quote the results for NH in the case of J=3, for which the Hamiltonian matrix (Eq. 92) becomes

$$\begin{array}{c} \\ |0\ 3> \\ |1\ 3> \\ |2\ 3> \end{array} \begin{array}{c} \begin{array}{ccc} |0\ 3> & |1\ 3> & |2\ 3> \end{array} \\ \begin{pmatrix} 15.1344 & -4.8990 & 0 \\ -4.8990 & 13.0000 & -4.4721 \\ 0 & -4.4721 & 6.8656 \end{pmatrix} \end{array} \tag{108}$$

The eigenvalues are

$$\begin{aligned} F_{03}/B &= 19.75088 \\ F_{13}/B &= 11.26576 \\ F_{23}/B &= 3.96254\ , \end{aligned} \tag{109}$$

and the intermediate case wavefunctions:

$$\begin{aligned} \psi_{03} &= 0.7079958|0\ 3> - 0.6671749|1\ 3> + 0.2315591|2\ 3> \\ \psi_{13} &= 0.6669394|0\ 3> + 0.5238320|1\ 3> - 0.5298980|2\ 3> \\ \psi_{23} &= 0.2322366|0\ 3> + 0.5296014|1\ 3> + 0.8158361|2\ 3>\ . \end{aligned} \tag{110}$$

3.7. Hund's Case (b)

Although we will not demonstrate it algebraically, we can define a quantum number N for small values of |Y| such that levels of differing J but equal N lie close together. First we must form the standard classifications

of levels into F_1, F_2, and F_3 groups: When there are three levels of equal J (J>1) then the level of highest energy is called F_3, the lowest level called F_1, and the intermediate level F_2. Special definitions are needed when J<2. For regular (Y>0) states, the level with J=0 is called F_1 as is the lower of the two levels with J=1; The upper J=1 level is F_2. For inverted states (Y<0), the level with J=0 is called F_3 as is the J=1 level of higher energy; the J=1 level of lower energy is now called F_2. We are now able to define N by

$$N = J-1 \text{ for } F_1 \text{ levels}$$
$$N = J \text{ for } F_2 \text{ levels}$$
$$N = J+1 \text{ for } F_3 \text{ levels.}$$

Our previous discussions were based on the assumption of inverted levels (as exist in NH). Thus in Eqs (93), (97), (104) and (109), the levels with $\Omega=0$ (F_{00}, F_{01}, F_{02}, and F_{03}) are all F_3 levels (with N=1, 2, 3, and 4 respectively); the levels with $\Omega=1$ are F_2, and those with $\Omega=2$ are F_1. For the inverted $^3\Pi$ state:

$$F_1 \leftrightarrow {}^3\Pi_2$$
$$F_2 \leftrightarrow {}^3\Pi_1$$
$$F_3 \leftrightarrow {}^3\Pi_0 .$$

For a regular state, the correspondence becomes

$$F_1 \leftrightarrow {}^3\Pi_0$$
$$F_2 \leftrightarrow {}^3\Pi_1$$
$$F_3 \leftrightarrow {}^3\Pi_2 \ ,$$

and the eigenvalues must be redistributed among the available values of Ω in accordance with the above correspondence and the definitions of the preceding paragraph.

To clarify these relationships as much as possible, Fig. 8 illustrates the behavior of the lowest levels as a function of Y.

4. The $^2\Delta$ State

We shall encounter a $^2\Delta$ state in the CH molecule. It is to be treated in a way that is entirely analogous to the handling of $^2\Pi$ states. Our Hund's case (a) basis set is

Label	Λ	S	Σ	Ω	J	M
$\lvert+\frac{5}{2}>$	+2	$\frac{1}{2}$	$+\frac{1}{2}$	$+\frac{5}{2}$	J	M
$\lvert+\frac{3}{2}>$	+2	$\frac{1}{2}$	$-\frac{1}{2}$	$+\frac{3}{2}$	J	M
$\lvert-\frac{5}{2}>$	-2	$\frac{1}{2}$	$-\frac{1}{2}$	$-\frac{5}{2}$	J	M
$\lvert-\frac{3}{2}>$	-2	$\frac{1}{2}$	$+\frac{1}{2}$	$-\frac{3}{2}$	J	M

The Hamiltonian matrix taken with respect to these elements does again factor into two degenerate sets of levels (Λ-doublets) of opposite parity, and only the first pair of wavefunctions need be considered. With respect to these,

the matrix of the Hamiltonian is

$$\begin{array}{c} \\ |\tfrac{5}{2}\ J> \\ |\tfrac{3}{2}\ J> \end{array} \begin{array}{c} \begin{array}{cc} |\tfrac{5}{2}\ J> & \qquad |\tfrac{3}{2}\ J> \end{array} \\ \begin{pmatrix} Y + x - 23/4 & -\sqrt{x - 15/4} \\ -\sqrt{x - 15/4} & -Y + x - 7/4 \end{pmatrix} \end{array} \tag{111}$$

where $x = J(J+1)$. We may solve for the eigenvalues as before and assign them as

$$\begin{aligned} F_1/B &= (J+\tfrac{1}{2})^2 - 4 - \sqrt{(J+\tfrac{1}{2})^2 + Y(Y-4)} \\ F_2/B &= (J+\tfrac{1}{2})^2 - 4 - \sqrt{(J+\tfrac{1}{2})^2 + Y(Y-4)} \\ F_{J=\frac{1}{2}}/B &= 2 - Y \quad . \end{aligned} \tag{112}$$

Note the absence of a factor of $\frac{1}{2}$ in front of the radical, and of a 4 inside it as compared to Eq. (80) and in agreement with the formula of Hill and Van Vleck[18]. The wavefunctions are given by Eq. (81), replacing $|\frac{1}{2}>$ by $|\frac{3}{2}>$, and $|\frac{3}{2}>$ by $|\frac{5}{2}>$:

$$\begin{aligned} \psi_1 &= c_1|\tfrac{3}{2}> + c_2|\tfrac{5}{2}> \\ \psi_2 &= c_1|\tfrac{5}{2}> - c_2|\tfrac{3}{2}>, \end{aligned}$$

where c_1 and c_2 are still given by Eq. (82), interestingly enough, if X is now defined as

$$X = \sqrt{(J+\tfrac{1}{2})^2 + Y(Y-4)} \quad . \tag{113}$$

If $Y=0$ or 4, then it is again easily verified that Eq. (112) may be written in the form

$$\begin{aligned} F_1/B &= N(N+1) - 4 \quad , N \equiv J - \tfrac{1}{2} \\ F_2/B &= N(N+1) - 4 \quad , N \equiv J + \tfrac{1}{2} \quad , \end{aligned} \tag{114}$$

so that F_1 and F_2 levels of equal N are nearly degenerate when $|Y|$ is small, and we have Hund's case (b). The $J=\frac{3}{2}$ level changes from an F_1 level for $Y>2$ (regular state) to an F_2 level when $Y<2$ (inverted state) as did the $J=\frac{1}{2}$ level in the $^2\Pi$ case (Fig. 7). The F_1 levels form the $^2\Delta_{\frac{3}{2}}$ multiplet and F_2 the $^2\Delta_{\frac{5}{2}}$ multiplet in regular states, and vice versa in inverted states.

The calculation of matrix elements of n_z is entirely analogous to the case of the $^2\Pi$ state and will not be given here.

CHAPTER VI

APPARATUS

1. Early Work

LoSurdo[45] first used the cathode fall region of a glow discharge to generate Stark effects in atomic spectra. The physics of the glow discharge and related literature[21-44] are reviewed in App. C. It may seem a bit unfair, since the effects of electric fields upon the spectrum of hydrogen were discovered independently by LoSurdo[45] and Stark[46], that Stark was give the effect and LoSurdo the tube.

Extensive work has been done using this method of generating high fields[7,47-63] reporting fields as high as 1.2 MV/cm[47]. Most of this work has been on atomic spectra. Although a number of other elements have been studied[57-63], most attention has gone to atomic hydrogen and helium[7,47-55], for which theoretical treatments were available[50,64,65] Stark effects were also observed and partially analysed in molecular hydrogen[56,66-68], but in no other molecule until the work of Phelps and Dalby[8] in this laboratory. The largest body of published work is that of Ishida and co-workers[47-53,57-60,62] during the period 1928-1940. This group seemed able to more or less routinely produce fields in excess of 550 kV/cm. The

reasons why they have been able to achieve fields higher than those produced in this laboratory are not clear from examination of their published material. In different papers they attribute their success to such diverse factors as the use of beryllium[59] or tantalum[58] cathodes, a discharge vessel of large volume[47] a good fit between cathode wire and surrounding quartz[60] and the removal or adjustment of the "vanes" of their synchronous motor rectifier[47,48] and removal of the inductance[47] (apparently introducing strong ac components to the supply voltage). Scarcely any one of these factors has been mentioned more than once, however, making it seem unlikely that they were crucial. Illustrations[60,61] make it appear that the quartz enclosing the cathode wires was specially formed as part of a large segment of the discharge tube, a procedure which would have been most awkward in our experiments which used the order of 10^3 cathodes!

The other method used extensively to achieve fields of comparable strength is the "canal ray" approach. A canal ray discharge is an obstructed discharge (where the anode is moved inside the cathode dark space) with high voltage (30-60 kV) and low pressure (10^{-2} mm Hg). (See Francis[26], p.161f.) The particle beam can be extracted through an aperture in the cathode and passed between charged parallel plates to produce the field (see the illustration and references in Bethe and Salpeter[69], p.234).

2. Mechanism

The distinguishing feature of the LoSurdo discharge is a circular cathode area, usually the end of a wire whose sides are insulated by a quartz capillary tube, the small size of which serves to increase greatly the magnitude of the maximum electric field in the cathode fall. Variations are to be found in the literature to meet the requirements of special materials, such as Ishida and Fukishima's[62] canal ray to vaporise lithium, and Liden's[63] metal shield for use in sulfur hexaflouride. However, the persistent characteristic of LoSurdo discharge operation is that the smaller the cathode diameter, the larger is the electric field obtained for a given material, voltage, and pressure. The first result of reducing the cathode size must be to increase the current density. To be sure, it is observed in our work that smaller cathodes draw less current, but as a rough impression (for example), a two millimeter cathode draws about twice as much current as a one millimeter cathode. Since the area has changed fourfold, the current density is about twice as large in the one millimeter version. It should be noted that the size of the cathode does not enter directly into any of the calculations mentioned in section 1 (Ward[30], Warren[24], and Volkov[37]), but only through the relation between current and current density. All of these calculations, as well as Warren's[28] experimental results, confirm that the field is proportional to $J^{\frac{2}{3}}$

for most gases, although conditions in high voltage LoSurdo discharges are sufficiently different as to make comparison suspect. This conclusion can also be related to Eq. (C.9) or (C.11) or other early calculations (Cobine[22], pp. 223ff, Fig.8.8) similar to Warren's which show the length of the cathode fall to be a decreasing function of current density. Eq.(C.15) then shows (assuming a linear field) that the maximum field increases with J. On a more intuitive level, it can be argued that an increase in either factor of $J=\rho v$ must be connected with an increase in E (see Eqs.C.17 and C.18).

Since Kamke[42] found that the width at half current, on cathodes in abnormal glow discharges, was down around 1 mm at 20,000 volts, one might expect that increasing the cathode diameter past 2 mm should make less difference in the fields obtained at high voltages.

3. The Flush Cathode and Older Tube Design

The original form of the discharge vessel, as used by Phelps[14], Phelps and Dalby[8,70], Irwin[71], Irwin and Dalby[72], and Wong[73] is shown in Fig. 9a. The cathode was an aluminum wire polished flat and matched evenly with the ground end of the quartz tubing to which it is fitted. This design was used in certain portions of this work and will be referred to as the flush cathode. Wires of 0.5, 1.0, and 2.0 mm were used, corresponding to the bore sizes of quartz tubing which are readily available. The cathodes were

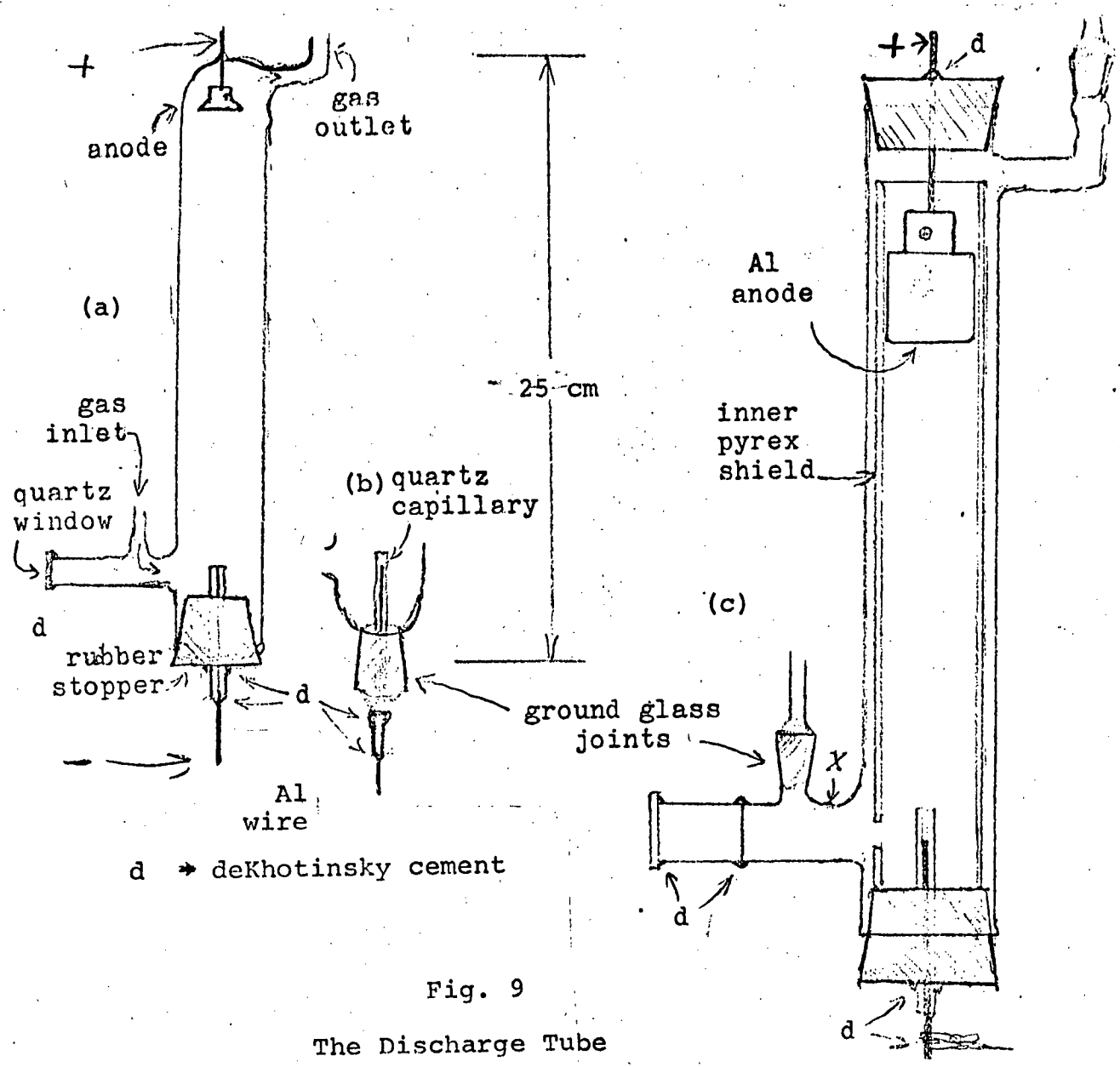

Fig. 9

The Discharge Tube

usually mounted in a hole through a rubber stopper (size $6\frac{1}{2}$). This was essentially the form of tube used for most of our early work with OH and OD. This tube was pyrex, about an inch in diameter and 10 inches long. The window was set on an extension of the tube to minimize sputtering or other contamination of the optical surface by the discharge. The anode was aluminum, about $\frac{3}{4}$ inch in its largest diameter, and clamped by a set screw to a tungsten wire sealed into the pyrex at the time of manufacture.

The gases or vapors were usually pumped in the indicated direction, attempting to minimize contamination. For a portion of the experiments with OH, the connecting glassware allowed this flow to be reversed. No effect of any kind was noted due to the flow direction, which is not surprising considering the small flow rates used in most experiments (1 to 50 cm^3/hr at standard temperature and pressure).

4. The Sunken Cathode

Fig. 9b shows the principal innovation in cathode design, due to F.W. Dalby, which differentiates the previously mentioned experiments from the later ones of Thomson and Dalby[74,75], Fisher[76], Scarl and Dalby[77], and this work. The quartz capillary tube is simply extended above the surface of the cathode, thus conforming more closely with the earlier Japanese designs[60,61]. This change allowed far higher voltages to be applied to the tube (over 20 kilovolts, as

opposed to around 7 kilovolts), as may be readily understood from the discussion of Appendix C, Sec. 8: The presence of constricting walls allow a far more effective focusing of ionic current, through positive charge accumulated on the walls over most of the cathode dark space. This not only results in a higher current density at cathode center and thus a higher electric field per applied volt, but keeps the discharge away from the cathode edges where arcing is far more probable. This type of cathode will be referred to as the sunken cathode. Its only clear disadvantage is loss of visibility due to sputtering, chemical accumulation, or other obscuration of the inner surface near the cathode. For many materials, these difficulties need not be serious, however.

The length of the capillary above the cathode surface did not appear to be very important in this work (perhaps excepting that with methanol), but its upper portions (positive column) would heat to an orange glow under conditions of high current if the capillary were sufficiently long. There was inconclusive evidence for better stability of a 1 mm cathode in cyanogen if the capillary was 2.2 to 2.8 mm above its surface. Fisher[76] found that the CO spectrum generated in CO_2 was brighter, the shorter the capillary extension. In general, the optimum distance above the cathode seems to be two or three millimeters, or roughly the length of the cathode dark space plus the negative glow and part of the Faraday dark space.

5. Details of Tube Assembly

5.1. Ground Glass vs. Rubber, and Other Failures

Also shown in Fig.9b is the ground glass joint and cathode holder introduced by R. Thomson to provide more consistent cathode positioning. The narrowness of the aperture, sensitivity of the joint lubricant to heat, and general inflexibility of this design led to its abandonment by the author in favor of a return to the rubber stopper. Crude as it may seem, the use of rubber stoppers gave quite dependable vacuums to the limit of our pumping range (3×10^{-2} mm Hg), with no need for the extra sealer mentioned by Phelps[14](p.36).

Prior to the development of the standardized polishing and running-in procedures described below (Secs. 7.2., 7.3.), a number of variations in cathode design were not considered successful, but are herewith described for completeness:

On the theory that cathode failure was caused by improper fit between the cathode and its enclosing capillary, a number of variations were tried which constricted the capillary at the level of the cathode surface, forming a barrier rim against which the cathode was tightly wedged. This made no particular improvement, and it is now believed that this fit is of small importance (contrary to the assertion of Ishida and Hiyama[60]).

On the theory that overheating was a cause of failure, some designs were tried which incorporated an ultra-long capillary extension above the cathode surface, with the vacuum seal being at the top instead of the bottom. With the essential part of the capillary hung in open air, air and water cooling were tried. The added cooling did not noticeably improve performance, and the long capillary seemed detrimental (Sec.4., above). When a water jacket was added, furthermore, the critical region could not be cleared of bubbles generated on the quartz.

Tin foil wrapped about the capillary, to reflect light leaving in other directions, seriously interfered with the discharge.

A hole drilled in the side of the capillary at cathode level (to prevent obscuration by sputtering and other deposits) interfered too much with the discharge symmetry, as compared with the much more distant shield used later (Sec. 5.4.). Interestingly, the top of the hole became white-hot at times, indicating electron rather than ion bombardment. Thinking that the presence of an alternate electrical path was responsible for the problem, the capillary top was bent outward and joined to a larger section which then enclosed the cathode region completely. This also failed to normalize the discharge. From what is written above about the role of the walls in focusing the discharge, this is not surprising.

5.2. The Cleanable Tube

The subsequent design is shown in Fig. 9c. All work here reported was done with this tube except that with OH and OD. It is of considerably larger volume than the older model, with a length of 13 inches and diameter of nearly two inches (45 mm I.D.). It was designed for ready cleaning, first and foremost: Both cathode and anode are readily withdrawn and replaced and the tube as a whole may be easily removed (ground glass joints) and disassembled (de Khotinsky cement) for cleaning.

5.3. The Window

The window was made larger to maintain the same solid angle of aperture as in the older version. It was mounted on an extension of ordinary tubing, which is cemented with deKhotinsky as shown. This was intended to allow flexibility in window placement and to allow the use of a window held with ceramic cement to withstand heating (intended for use in evaporating alkali metals from the window in an experiment which has not been performed). In practice, this arrangement makes it much easier to change windows without removing the whole tube, since they may be mounted on the extension while horizontal and then the assembly mounted with the cooled window as a handle. No trouble was encountered from melting of the deKhotinsky wax except when microwave excitation was applied in the region marked X in Fig. 9c (this was preventable by cooling with an air fan).

The windows were usually quartz 2.5 cm (O.D.) diameter and about 12.5 cm from the cathode.

5.4. The Shield

The straight cylindrical tube and rubber stopper allow the use of an inner glass shield, as shown, to minimize the frequency of cleaning the main tube. This shield simply sits on the rubber stopper, and is used routinely, even with sunken cathodes and clean-running materials, since its use offers no problem. The aperture in the shield, between cathode and window, was eventually reduced to about 5 mm wide by 11 mm high.

With cyanogen discharges, heavy orange and brown deposits were formed with each run. These seemed readily removable with a weak solution of HF, but a persistent discolouration was built up over many runs. The departmental glassblowers were able to remove this film with concentrated HF.

5.5. The Anode

The size and shape of the anode are usually considered to make very little difference to the discharge.[42] However, it has been found that using a large anode, which fits the inner pyrex shield quite closely, serves to confine positive column anode glow activity to within tube and prevent it from going up and past the sides of the anode. This is a distinct advantage in gases like cyanogen where bright areas

of the discharge cause a severe cleaning problem. The anode is cleaned as needed by either turning on a lathe or fine sanding, depending on the amount of the deposit. In dirty gases, the anode with its matched glass shield were usually changed along with the cathode after each run.

6. Details of Other Apparatus

Fig.10 gives a schematic diagram of the physical layout of the vacuum system. The vacuum, electrical, and optical systems are discussed in some detail in the subsections below. Some parts of these discussions will be of interest only to persons wishing to use the same apparatus themselves.

6.1. Sample Input Control

Adequate control of sample input flow was usually obtained with the Edward's High Vacuum, Ltd., type LB2B needle valves. This valve has a brass bellows activated by screw thread dial through a lever system with enough mechanical advantage to compensate for the rather wide included angle of the needle itself (around 25°). While the needle is stainless steel, the seat is brass and had some tendency to gall and seize shut if adjusted to close under the full pressure of its retention spring, providing at least one dangerous moment when used with silane. The valve should therefore be adjusted with hydrogen or helium (which have high flow rates) to just slightly past the point where no pressure can be detected in the system

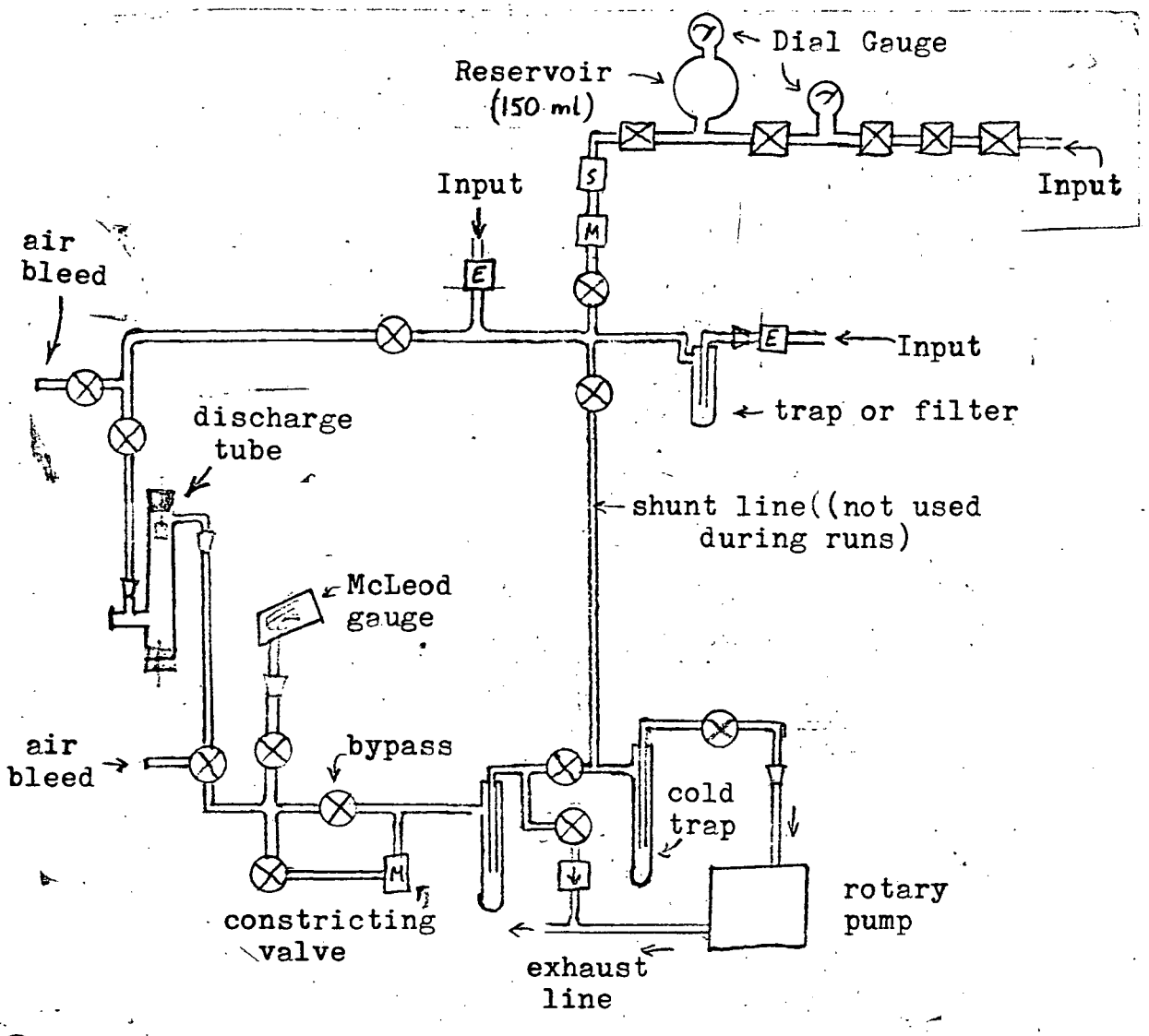

Fig. 10

Physical Schematic of Vacuum System

under full pumping.

The Edwards valves have been used satisfactorily with non-corrosive gases (He, H_2, N_2, Ar, O_2, CO_2) in cylinders with external pressure regulators. They are also used with non-corrosive liquids (H_2O, CH_3OH) with vapor pressures less than one atmosphere, in glass containers directly connected to a valve's "O"-ring entry port.

It was assumed that the melange of material in the Edward's valves was inappropriate to corrosive substances (NH_3, C_2N_2, BCl_3), so one input line has been fitted with valves from Nupro (Crawford Industries) which are made of either stainless steel or monel, with teflon or "Viton-A" gaskets and valve seats. In spite of a much smaller angle of inclusion (1° or 3°) of the needle, the direct connection of these valve needles to the outside dial meant that control was less satisfactory than with the Edwards valves. It must be added, however, that flow rates required of these corrosive substances were generally lower (1 cm^3 per hour at room temperature and roughly air pressure). Nevertheless it was found necessary to maintain a sizable reservoir of gas at less than atmospheric pressure, behind an "M" (metering valve, SS-4M) valve in series with an "S" (fine metering M-2SA) valve, to get usable control. A further disadvantage of these valves in that they cannot be used for off-on control (as can the Edward's valves), and need other valves in series with them for shutoff.

A sequence of volumes separated by shutoff valves

was used in place of a regulator for cyanogen. (Regulators were used with silane and ammonia.) Dial gauges capable of reading both pressure and vacuum were connected to the large volume preceding the needle valves, and the smaller volume preceding it. All components in this region were of stainless steel or monel, and connected with Swagelok (Crawford) or National Pipe Thread fittings. The shutoff valves were monel or stainless steel miniature forged body valves from Matheson; some difficulty was had with these valves with ammonia, apparently due to a hard polymer formed with a lubricant (most of these were usable again after thorough cleaning).

Further details are given below under the various chemical headings.

6.2. Pumping Rate Reduction and Pressure Measurement

A reduction in pumping flow rate was sometimes used to reduce consumption of the hazardous samples, or samples available in small amounts. At first the rubber hose to the vacuum pump was clamped off with a large "C" clamp and a wire inside (to prevent sealing shut). Later a needle valve (Nupro SS-4MA) was placed between the vacuum gauge and cold traps, with shutoff (series) and bypass (parallel) stopcocks. This valve could then be preset to a desired constriction, and then put in or out of the system with bypasses.

The liquid nitrogen trap is an effective pump for substances of higher boiling point than nitrogen (meaning

all gases used except hydrogen and helium). Thus having a constriction between the cold trap and vacuum pump was unsatisfactory, and it had to be placed upstream of the cold traps to be effective for all substances.

Pressure was measured with a McLeod mercury gauge which could be read to 0.01 mm Hg, and estimated to 0.002 mm Hg pressure. This is placed immediately downstream from the discharge tube and was moved to hang below the line to which it is attached so as to prevent contamination of the system from mercury spills. The McLeod gauge operates by compressing the gas, and thus gives inaccurately low readings for substances which as the vapors of liquids at room temperature (water, methanol, dimethyl mercury).

6.3. Cold Traps and Pump

A liquid nitrogen cold trap was often used to keep samples from fouling the vacuum pump oil or polluting the outside air. It was also used to keep mercury from the McLeod gauge out of the pump, but was expressly not used with silane to prevent dangerous accumulations of the substance in glassware. The trap was loaded with glass beads and NaOH pellets to chemically trap cyanogen.

The vacuum pump was a small Sargen-Welch rotary oil pump which was capable of evacuating the system to the limits of the McLeod gauge. The exhaust of the pump was led out of doors by some forty five feet of aluminum tubing and surgical rubber hose (except during the work with OH

and OD, where venting to room air was acceptable). When cyanogen was used, the pump exhaust was bubbled through a strong solution of NaOH and bleaching powder (also known as chlorinated lime or calcium chloride hypochlorite) before passing outdoors. When silane was used, the exhaust was bubbled through an outdoors water container to provide control of its spontaneous combustion.

Pressure within the system (greater than atmospheric) is potentially dangerous and could arise inadvertantly at unpredictable times from a needle valve left open, or from the melting of liquid oxygen or other gases caught in a sealed-off cold trap. To prevent this, a check valve was installed as shown in Fig. 10, upstream from the stopcocks which usually cut off pumping, and near the cold trap. It is made of monel and opens when the pressure in the system reaches $\frac{1}{3}$ lb/in^2 above atmospheric (pump exhaust) pressure. It forms an effective vacuum seal when closed, judging by McLeod gauge readings.

6.4. The Power Supply

The supply used almost exclusively was made up from what appeared to be heavy-duty war surplus components. For the convenience those who may need it or some similar design, it is described here briefly, and diagrammed schematically in Fig. 11.

This power supply is essentially a high voltage transformer controlled by a variac in its primary circuit, and

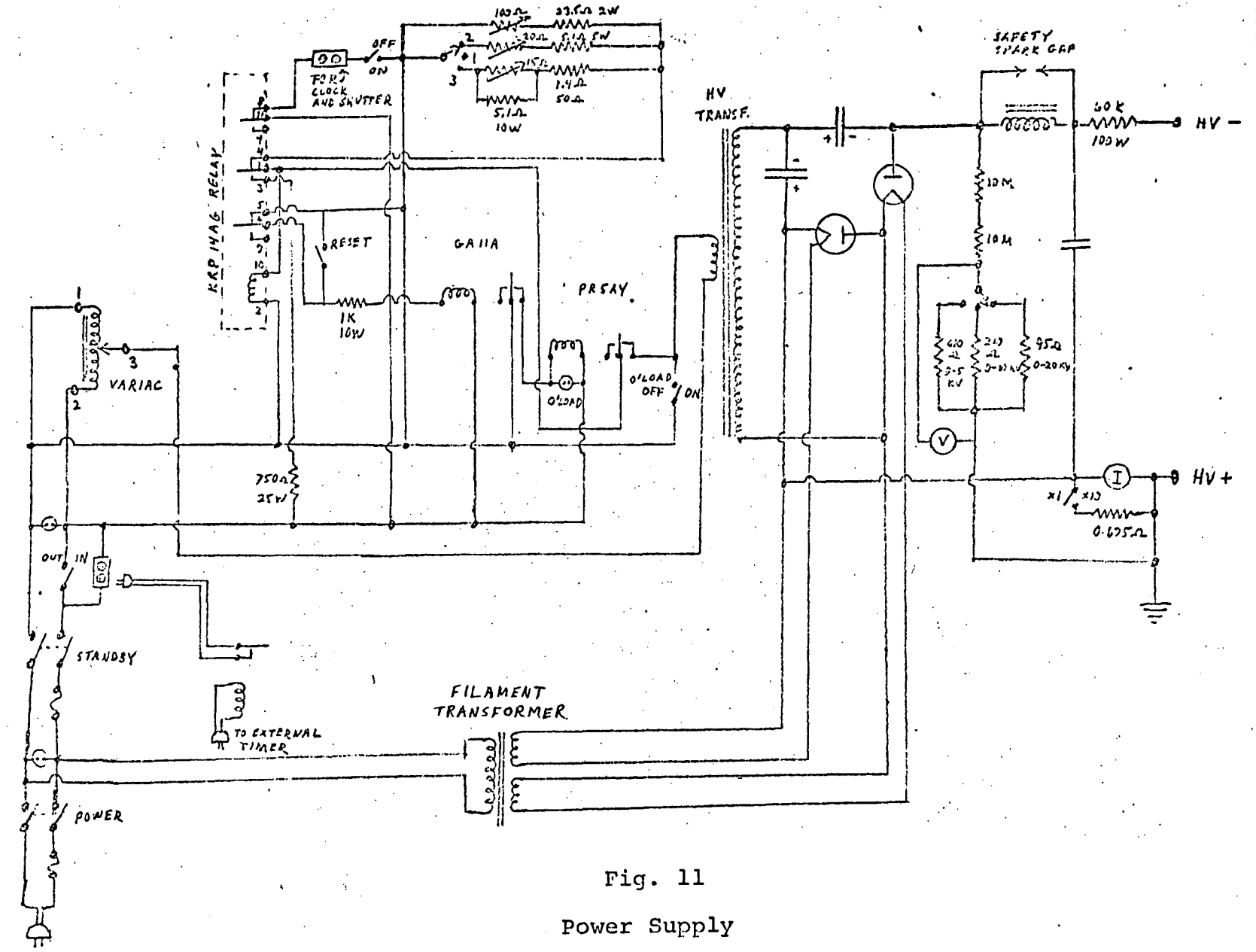

Fig. 11

Power Supply

rectified by a pair of diodes arranged with two large capacitors to form a voltage doubler: Alternate half-cycles of the AC input charge alternate capacitors, and the output voltage is taken across them as the sum.

Between the variac and high voltage transformer primary, an overload cutout circuit has been designed. The solenoid of the KRP 14AG relay is in series with the transformer primary, but this current is partially shunted past the relay by the resistor network (top center in Fig.11) which adjusts the tripping current from less than 1 mA to over 30 mA. When this relay is tripped by sufficient current in the primary circuit, it is held closed by the current flowing through the 750 ohm resistor. To give sufficient time delay for this resistor to establish a current path through its associated relay contacts, the primary circuit of the power supply is not interrupted by the KRP 14AG relay itself, but by another relay operated by a third relay which is operated by the KRP 14AG.

The 60 kΩ series resistor in the high voltage circuit is not critical in value, but must be present to limit current, or the cathode is likely to arc immediately.

The overload relay controls the power applied to a 110 VAC outlet on the side of the power supply, in to which the spectrograph shutter and a timing clock are usually plugged, so that the clock stops and shutter closes when overload conditions occur. Another outlet is in series with the primary circuit, serving as a point where an

external timer may break the circuit through a relay, as shown in Fig.11.

Another power supply was purchased (Peschel RPS 50-5R) with voltage regulation, 50 kV capacity, and overload trip, but was not often used due to problems in the regulation circuits and the relative inflexibility of its current overtrip.

Higher applied voltages were sometimes obtained by elevating the anode potential with a second power supply. Voltages in excess of 5 or 6 kV are dangerous since the plasma could conduct the voltage to all parts of the system, including table and pump. (Negative voltages applied to the cathode can not do this since they are confined to the cathode region. Most of the plasma is nearly at anode potential.)

6.5. The Spectrograph

The useful portion of this work was done entirely with a 3.4 meter Ebert spectrograph (Jarrel-Ash 70-000) using a grating ruled with 30,000 lines per inch and blazed at an angle corresponding to 10,000 Å. This type of spectrograph has a single mirror (masked into two segments) at one end, inclined at a slight angle. At the other end, corresponding to the focal length of the mirror, is set the entrance slit and photographic plates. The grating is mounted near the center, and rotated to set the spectral range observed. Thus, light from the slit is

collimated and reflected toward the grating; the desired segment of the spectrum (dispersed) is reflected back to the mirror which focuses it upon the plates.

6.6. Plate Handling in the Spectrograph

The plates contain a range of about 1000 Å in first order (500 Å in second order, etc.) over both plates (50 cm), decreasing slightly at the longer wavelength settings. Thus we get dispersions of roughly 2 Å/mm in first order, 1 Å/mm in second order, etc. The center of this range can be set from 6000 Å to 14 000 Å by rotating the grating, but there are significant intensity losses when set far from 10 000 Å.

As the plates sit in the holder, high frequencies tend toward the holder handle, and the image is inverted. Most plates numbered 150 or greater are coded by a scratch in the corner of the emulsion at the low wavelength (high frequency) end and the upper edge (as mounted, thus towards the bottom of the discharge). These scratches are made with a pen-knife at the time of placement in the plate holder.

Plates are numbered individually, although used in pairs. Thus, plates 47 and 48 were exposed simultaneously, and the odd numbered plate (47) is the low wavelength member of the pair.

The plate holder may be moved vertically to give more than one exposure per plate. For example, if the slit

mask is set to reveal a slit 10 mm high, and the plate holder is moved 12 mm between exposures, then the exposed regions will be separated by 2 mm. Since the LoSurdo discharge leaves the plate virtually unexposed below (the image of) the top of the cathode, exposures may be set more closely together, depending on the positioning of the cathode image on the slit. Only the central 40 mm of the plates' 50 mm height is dependably usable.

Different exposures on multiply exposed plates are referred to by lower case Greek letters in chronological order of exposure.

The best plates for long exposures are Kodak type Ia-O, or Ia-E in the yellow and red. When a little more intensity is available, IIa (-O, -D, or -F) plates offer finer grain and lower background fog at relatively small cost in sensitivity. 103a-0 plates are comparable in speed, but their advantage over IIa-0 is questionable.

6.7. Lens

An achromatic lens composed of two quartz lenses (plano-convex with curved sides inwards) with distilled water between was used to focus the image of the discharge onto the slit. This lens with about $1\frac{5}{8}$" diameter, and 5" focal length transmits light down to around 2200 Å satisfactorily. A lens of $2\frac{1}{2}$" diameter (5" F.L.) made of Suprasil I (Amersil, Inc.) is also available, and is alleged to transmit satisfactorily to below 1800 Å. It

is not achromatic, however, and must be focused through calculations based on available refractive index data.

6.8. Alignment

The equipment is readily aligned optically by the use of a double-ended laser. Set on two lab jacks within the barrel of the spectrograph, one end is aimed at the grating center as determined by a mask supplied with the spectrograph. The other end retraces the optical axis to the mirror and out through the slit (set wide). First the apparatus table height is set so that the laser beam hits the window at mid height (lens removed), with the table leveled by bubble level. Then a stopper with a carefully centered cathode, wire, or wooden rod is placed in the discharge tube, and the table moved sideways till the beam is centered upon it. Finally, the clamp holding the discharge tube in place is loosened and retightened with the tube turned so that the beam hits the window at centre.

At runtime (see Subsec. 7.3. below), the lens is focused upon a piece of white cardboard slipped into the slit mask's slot, after brightening the discharge with helium. Although the lens was adjusted horizontally to hit the slit, in most of this work, by aiming at a thin inkline drawn previously on the cardboard, a recent innovation allows this crucial adjustment to be made more directly: A heavy duty speedometer cable has been fitted with prongs to fit holes in the horizontal positioning knob of the lens.

This may be pulled free of that knob, as well as turned, from the other end. By this means the lens may be horizontally positioned to give the most light through the slit, by looking directly over the grating and out the slit with one's head within the barrel of the spectrograph.

7. Cathode Manufacture

It is felt that a significant benefit from this research has been the development of a method for making and running-in sunken cathodes which gives at least 80% success in bringing cathodes to 20 000 applied volts with satisfactorily constant operation.

7.1. Materials

Most cathodes used in this work have been sunken aluminum cathodes of one millimeter diameter. However, carbon cathodes of one and two millimeter diameters were used extensively during the low voltage work on OH and OD.

Beryllium was also used occasionally; no particular improvement was noted, although operation was satisfactory. The difficulty of machining beryllium safely (its dust is highly toxic) discouraged us from turning it down to a proper fit with available quartz capillary tubing. Attempts at diameter reduction by heated drawing through a drawplate were unsuccessful. Since the available wires (0.050" and 0.100" diameters) would have to be turned down by only

about 20% (to 0.038" and 0.078", respectively), however, this remains a possibility for future experimentation.

Iron, copper, and molybdenum were also tried and found unsatisfactory due to heavy sputtering or chemical deposit, although Wong[73] has used molybdenum with HCl.

Carbon used for cathode manufacture was made from spectroscopically pure carbon or graphite rod (National Carbon) which is available in an especially dense form. These rods were usually turned down from $\frac{1}{4}$" stock by mounting in a drill press and sanding with hand-held emery paper (220 grit). 2 mm cathodes could be made easily by this method, but 1 mm lengths were very difficult to make this way due to their extreme fragility. It was discovered that 1 mm carbon or graphite rods can be cut from heavier stock on a lathe, if the cut is from the end in one pass. Nevertheless, these fragile rods broke so easily that a system was devised wherein a short length of rod was wedged against the quartz with a piece of thin wire from below. The advantages of carbon, even for low voltage work, seem doubtful in retrospect. Much of the inspiration for working with carbon came from one particular cathode (2mm, plates 67/68) which ran at over 10 kV for a total of more than 15 hours (a record for any cathode), but neither voltage or durability were duplicated in later efforts.

The aluminum wire used in most experiments came from a lot of $\frac{1}{8}$" wire from Wilkinson Co. Ltd., and was drawn down to a variety of sizes to fit 0.5, 1, and 2 mm

I.D. tubing. The wire usually used for 1 mm cathodes was actually 0.033" in diameter. This wire was not sold as quality material, and its exact composition is not known, but it is called 99% pure with iron and copper likely the dominant impurities. A far purer aluminum wire was obtained from Electronic Space Products Inc. (Los Angeles), rated 99.999% pure, but results with it were generally poor. Very pure aluminum is soft and much harder to work by normal methods, but even after wire had been obtained to fit available quartz, no cathodes made therefrom ever achieved high voltages. This work was done before the polishing and running-in procedures (described below) were developed, so the rejection of pure materials may not be justified.

Quartz was General Electric type 204 clear fused quartz capillary tubing. Its dimensions are not dependable from sample to sample; 10% variations were observed, although manufacturer's tolerance is some 23%! Since attempts at re-using quartz lengths (by cleaning or moving the wire) were never successful, and the quartz is relatively inexpensive (ten or fifteen cents per cathode), our usual policy was to fit cathode wires to the quartz rather than attempting to draw the quartz.

Rubber stoppers and deKhotinsky cement are the standard types available from Central Scientific Co. The latter has been recently improved and called Sealstix cement; its resistance to polymerization upon reheating

gives a decisive advantage over previously available products.

7.2. Polishing

Although this work can claim authority only in polishing the 1 mm aluminum sunken cathodes which comprised the bulk of our experiments, the polishing methods used with other types of cathode shall be described briefly. The procedure described for the standard aluminum 1 mm cathode is sufficient to produce dependable results; since the entire process can be carried out in about 15 minutes, no attempt was made to determine whether or not all steps described are actually necessary.

To grind an aluminum cathode from a previously used wire, about $\frac{1}{16}$" should be removed each time to ensure the center hole from the last run (see Subsec. 7.3.) has been eliminated. The wire is placed in a piece of quartz tubing similar to (but shorter than) the tubing in which it is to be used, and held in place by a spot of deKhotinsky cement with the wire end to be removed projecting from a flat end. It is convenient to keep using the same piece of quartz for this purpose, since the end will have been polished flat by its first use. The bulk of the aluminum stub is removed with a fairly coarse grade of emery paper (220 grit or "fine" grade). An intermediate paper (320 grit) may be used to bring the aluminum nearly down to the quartz end. From this point 600 grit paper (i.e., coated with particles which have been filtered through a mesh of

600 wires/inch) is used: The wire in holder is held vertically by hand and ground with first moderate (hand-weight) pressure, then more lightly in a circular or "figure 8" motion. A drop or two of water is placed on the emery paper and the process continued wet for another minute with soft backing beneath (e.g., paper towels). Wiping the end clean with tissue, it is then inspected with a magnifying lens. There will always be residual defects visible, but the object is to keep them small and of uniform texture.

When the surface is satisfactory, the wire is removed from its holder and cleaned of the deKhotinsky. DeKhotinsky is best removed by scraping with fingernails, after a slight heating to soften its grip. The wire is then mounted in a drill press chuck where it may be turned at slow or medium speed. Here the corners are rounded with 600 grit emery, bracing the turning wire lightly with the fingers and always moving the grit away from the polished face to avoid building up ridges of soft metal. The rounded portion of the wire end should be some 10% to 15% of its diameter, as determined by examination under lens, after cleaning with tissue.

A piece of quartz is cut to length; if this is to be a flush cathode, one end should be polished flat with 600 grit paper. The length should be just long enough to extend the desired distance above the cathode (usually two or three mm in a sunken cathode) and only a few mm below the stopper so as to leave maximum air cooling for

the wire. Both wire and capillary are now washed: first under a forced stream of toluene from a wash bottle, next ethanol to remove the toluene, then a hard jet of tap water followed by a distilled water rinse. A final rinse with ethanol and a directed airstream from a fan will speed drying, although there appears to be no harm in letting the cathode dry under vacuum if a cold trap is present.

The wire is inserted flat end (top) into the quartz, then set (bottom first) into a rubber stopper which has been wiped down with toluene. DeKhotinsky is dripped and then melted onto the bottom quartz-rubber join and then the quartz-metal join.

The assembled cathode is installed into the discharge tube a little at a time with assistance from the vacuum, checking constantly the vertical positioning. A very slight amount of vacuum grease (just enough to produce a faint gloss over the contact area) on the rubber stopper is found to improve reproducibility of position.

It is probably unwise to expose a finished cathode to air for more than a day or so prior to running-in. It seems likely that the presence of aluminum oxide may cause a "spray" discharge (Druyveseyn and Penning[27],p.139f) in which positive ions are trapped on a thin insulating layer, yielding high enough fields to cause field emission capable of damaging the cathode surface. Such processes taking place inside an already-formed hole would be unlikely to disturb the discharge, however, and may prolong cathode

life by reducing sputtering (see Sec. 7.4., below). Thus it may be predicted that oxidizing gases (O_2, CO_2, CO, H_2O) would be poor choices for initiating a cathode, but harmless after running in.

Among a number of apparently unsuccessful polishing techniques tried were: the use of hydrofluoric acid or chromic-sulfuric cleaning solution on the aluminum, the use of Brasso, polishing paper, crocus cloths, and grindstones, the achievement of a mirror-like polished surface with a commercial polishing table, and the use of a highly purified aluminum cathode material.

Carbon cathodes can be polished to a shiny finish merely by the application of 600 grit emery. Since carbon is porous, it cannot be put in contact with outside air; usually a fine wire is wrapped about the end of the rod and all exposed carbon covered with deKhotinsky. (Needless to say, carbon rods are not washed).

Beryllium rods were polished merely by holding with gloved hand and rubbing on emery cloth under flowing water. As further protection against toxic dust, a recommended inhalator was worn.

7.3. Running-In

The following method for breaking in sunken 1 mm cathodes has proven satisfactory. After "washing" the system once or twice with enough hydrogen to give clearly audible pumping noise, the system is evacuated to

what should be markedly less than 10 microns (0.010 mm Hg) pressure. After warmup, the power supply is set to 3 kV. Hydrogen pressure is gradually increased until the discharge becomes visible through blue fluorescence in the quartz above sunken cathodes, or a glow becomes visible in the cathode center. This must be done somewhat cautiously because of the negative resistance region (see App.C) which can lead one to draw excessively heavy initial current. About 0.3 mA is proper at this point, corresponding to 1.6 mm Hg pressure of hydrogen. As a guess, all currents should be doubled for 2 mm and halved for 0.5 mm cathodes.

After leaving the cathode running in this condition for about five minutes to initiate the process of forming the central hole, the voltage is increased.

The physics of running in a cathode surface is probably much as suggested by Loeb[23](p.472) for the case of a wire length (as opposed to end): As the field is increased at the surface, at some point will be an upward projecting irregularity of sharper curvature than elsewhere. Here the field will be highest, and eventually field emission (Appendix C,Sec.7) will become significant. Further field increase will create such high current density that the metal will vaporise and a sparking process take place which is likely to destroy the irregularity which gave rise to it. Actually the spark may create points of even higher curvature which should cause a sequence of sparks (Fig.12a and 12b) before the irregularity is effectively removed. Points of

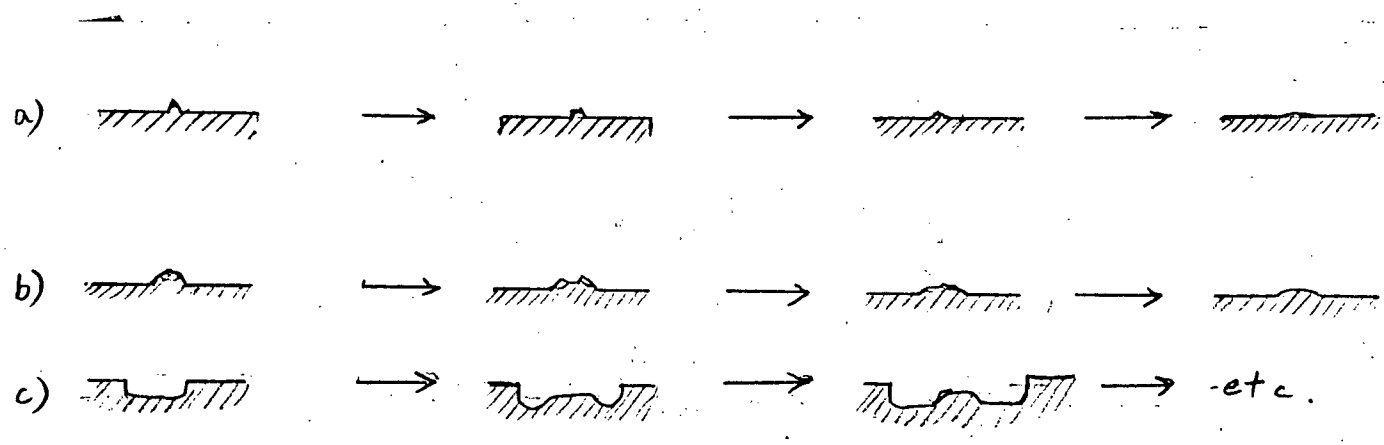

Fig. 12

Elimination of Cathodic Irregularities of Positive Curvature.

sharp negative curvature (pits) would not be affected. However, it is possible to visualize a number of geometries which, given sufficiently destructive sparks, could lead to the propagation or exacerbation of surface defects and the destruction of the cathode by continuous sparking. One such possibility is shown in Fig.12c. To best help a cathode to achieve a given voltage, then,one should raise the voltage relatively slowly, or in small jumps, so that the energy per spark is minimized.

In practice, it is found that a good rate of voltage increase is about 0.4 kV/minute. This allows the voltage to reach 20 kV in less than 45 minutes. Shorter running-in times are desirable simply on the grounds that they use less of the total cathode lifetime. If flashing (sparking at the cathode) persists more than a few flashes at any point, one or two minutes spent at that voltage may stabilize it. If longer times seem necessary, or flashing persists at each adjustment, going to higher voltage is probably useless.

Hydrogen is found to be an excellent gas for running-in. It tends to stabilize defects which would become worse if the medium were helium, for example. The best current for 1 mm cathodes is 1.2 to 1.4 mA, although 0.6 to 1.0 mA may be used below 10 kV. The lower currents are desirable simply on the grounds that they cause less sputtering. The currents described usually correspond to pressures of about 2.0 mm Hg of hydrogen at

low voltages and 1.0 mm Hg at high voltages. It may be suggested that the stabilizing effects of hydrogen at pressures greater than 1 mm Hg may be related to the observation of Davis and Vanderslice[36](p.226) that this is where H^+ and H_3^+ ions begin to predominate over H_2^+ ions.

When the cathode reaches 10 kV, enough helium is introduced to bring up the current to 1.8 or 2.0 mA, for just long enough to allow the brightened discharge image to be focused upon white cardboard placed in front of the spectrograph slit (Sec. 6.8.). The helium is shut off before aligning the image horizontally onto the slit.

Running-in by placing a high voltage across the electrodes with no gas sample was unsuccessful; since a high field gradient cannot be formed without the assistance of space-charge, it is unsurprising that this made little difference.

Once the desired running voltage has been reached the problem remains of introducing the materials under investigation. It seems that this in general is a unique problem for each material and must be resolved by trial and error.

7.4. Cathode Failure and Sputtering

It is presumed that the useful life of an operating cathode is determined by one more of the following limitations:

(1) Material originating from the cathode deposited on the internal walls of a sunken cathode capillary causes

the light from the discharge to be absorbed or scattered.

(2) Products of chemical reactions in the gas (possibly involving material from the cathode) obscure the discharge as in (1).

(3) Products of chemical reactions, as in (2), deposit on the cathode so as to destroy the cathode fall region and/or radial focusing mechanism (e.g., creating "spray" discharge; see Sec. 7.2. above).

(4) Material leaving the cathode destroys the field-handling capability established during running-in, by creating surface defects which are not capable of self-repair (Sec. 7.3. above).

(5) Reaction products or cathode materials are deposited on the internal wall of a sunken cathode, or the quartz end of a flush cathode, so as to form a conducting surface which increases the effective cathode area and current beyond allowable limits.

Undoubtedly, (4) was the cause of the vast majority of operation failures encountered in this work (with H_2O, D_2O, NH_3, and others). Evidence for this comes from the fact that cathodes rarely break down all at once after flawless operation; usually an isolated flash or a sequence of flashing activity (seen by magnifier to be sparking at the cathode) will occur during a run, followed by a return to quiet, thus indicating that self-reparable flaws have been created.

Runs are rarely terminated due to reason (1)

(sputtering obscuration). After having stopped for other reasons, however, impaired visibility (and even damage to the quartz) is often noted.

Chemical obscuration (2) often terminated runs made with silane or cyanogen. The latter left deposits appearing to be carbon; silane deposits are of unknown composition. Failure due to chemical deposit on the cathode surface (3) was also usually confined to these materials. It seems to be typical of such substances that their introduction into the discharge caused a <u>decrease</u> in current. This last effect was often used to judge concentration.

Failure due to conductive deposits near the cathode (5) were rare in these experiments, although some such spectacular failures did occur if a large excess of trimethylaluminum, silane or cyanogen was inadvertantly admitted. If these deposits were not too heavy, they could sometimes be burned away in purer hydrogen. Phelps[14](p.42) noted failures from this cause with volatile hydrocarbons.

Both Phelps[14](p.39) and Wong[73](p. 12f) describe an actual lowering of the cathode surface by "burning away" as a cause of termination, but this was not found in experiments reported here, excepting certain carbon cathodes in which the central hole became so enlarged that only a thin shell remained which was difficult to distinguish from a wall deposit.

The removal of material from the cathode, described in (1) and (4) above, is referred to as <u>sputtering</u>. It is

believed to be due to the impact of positive ions knocking neutral atoms (or even negative ions) from the cathode. This is a complex phenomenon dependent upon the nature of the gas and cathode, diffusion (pressure) of atoms in the gas, and the ionic energy and density, and has sizable literature of its own (see Francis[26],p. 154ff, for example). Early work found that the rate of mass loss by sputtering was proportional to the cathode fall voltage, with or without an additive (negative) constant. More recent work emphasizes a power dependence upon the current. At very low pressures (long free path), sputtering is independent of pressure. At the pressures encountered in our experiments, however, the sputtering rate decreases with increasing pressure, supposedly due to diffusion of sputtered particles back to the cathode, or perhaps through an ionization process. Takatsu and Toda[78], for example, have attempted to evaluate the sputtering as being proportional to I^a/p^b where a and b are positive constants.

Sputtering seems to increase with ion mass; it has been found that aluminum sputters much more heavily under argon than hydrogen or helium, but mercury compounds did not sputter badly.

Loeb[23](p.601) gives a list of sputtering rates for a number of metals under hydrogen, which Plesse[79] has noted corresponds fairly well to their heats of sublimation. This list shows aluminum as having one of the lowest sputtering rates, with only magnesium and tantalum substantially lower

(beryllium is not included). According to Kueck and Brewer[80], however, this is due to the presence of a stable layer of oxide. According to this presumption, a cathode should be run-in after polishing (as has already been noted) before exposure to air so that the central pit may be sputtered out easily, and then allowed to oxidize before actual use (running in air, perhaps). Within the pit, a sputtered oxide might likely re-attach itself and not be lost. Deliberate oxidation has not been tried, although it seems that accidental oxidation after run-in has not been deleterious.

8. Experiments

In Table I (and the notes thereafter) is presented a list of experimental conditions pertaining to those photographs which contributed to the results of this work. A general description now follows of various substances run, and the results or lack thereof.

8.1. Hydrogen

Hydrogen has been discussed in detail in Sec. 7.3. above. It runs very well and is noticeably stabilizing at higher pressures (over 1.0 mm Hg). H_α is very bright, and the short exposures needed to photograph it in either first (3 - 7 min) order or second order (8 - 15 min) make it plausible to photograph H_α before and after an exposure in regions where a hydrogen line is not readily

TABLE I

Experimental Conditions (see notes at end)

Photo	V kV.	I ma.	p mm.Hg	t hr.	Grating	Gases, Vapors	Use	Spect. Order	Field Max,	Source
1/2	12.0	2.6	1.5	2.5	96500	H_2O,He	OH	3	95.1	Hβ
13/14	16.0	1.0	1.4	0.5	"	" ,"	cal.He	2	122.4	"
35/36	15.1	0.7	1.5	3.0	"	D_2O,"	OD	3	179.8	Dβ
39/40	19.5	?	1.6	3.0	"	" ,"	OD	3	243.0	"
45/46	19.0	1.7	1.8	1.7	"	H_2O,"	OH	3	276.7	Hβ
53/54β	12.0	1.4	1.5	6.0	96500	H_2O,He	OH	3	176.7	Hβ
55/56	21.6	2.2	1.3	?	"	" ,"	OH	3	226.9	"
59/60α	18.4	1.3	1.5	1.7	"	" ,"	OH	3	319.3	"
59/60β	18.4	1.3	1.3	4.7	"	" ,"	OH	3	285.1	"
125/26α	6.2	0.8	1.3	1.6	"	D_2O,"	OD	3	118.9	Dβ
125/26β	8.1	0.6	0.8	4.3	96500	D_2O,He	OD	3	68.4	Dβ
127/28α	6.8	0.7	0.6	1.9	"	" ,"	OD	3	54.5	"
127/28β	4.0	1.6	0.5	4.6	"	D_2O	OD	3	25.4	"
127/28γ	6.8	0.7	1.2	0.6	"	" ,He	OD	3	87.0	"
131/32α	5.0	0.6	0.3	2.2	96710	D_2O	OD	3	39.3	Dγ
133/34β	7.6	0.7	1.8	0.8	96710	D_2O,He	OD	3	96.0	Dγ
133/34γ	5.3	0.7	1.8	0.8	"	" ,"	OD	3	62.8	"
135/36γ	7.1	2.0	?	0.4	96596	D_2O	OD	3	77.4	Dβ
137/38α	6.5	2.1	0.7	1.5	96600	H_2O	OH	3	45.4	Hβ
137/38β	6.0	0.6	?	1.3	"	"	OH	3	69.2	Hβ
137/38γ	5.3	0.7	0.7	3.2	96600	H_2O	OH	3	54.9	Hβ
139/40α	8.5	1.0	0.4	0.9	"	"	OH	3	69.1	Hβ
139/40γ	7.4	0.7	?	1.8	"	" ,He	OH	3	59.1	Hβ
139/40δ	6.0	1.0	?	0.2	"	" ,"	OH	3	46.2	Hβ
141/42α	7.3	0.6	0.7	2.8	"	" ,"	OH	3	56.9	Hβ
141/42β	6.6	1.9	?	0.6	96600	H_2O,He	OH	3	47.2	Hβ
141/42γ	5.3	1.0	0.7	1.7	"	" ,"	OH	3	37.4	Hβ
143/44α	8.2	1.1	0.8	1.0	"	" ,"	OH	3	64.4	Hβ
145/46β	6.1	1.6	0.5	?	96490	" ,"	OH	3	50.1	Hβ
263/64γ	14.4	2.0	2.6	0.1	94990	H_2,C_2N_2, He	Hα	2	230.3	Hα
263/64δ	"	"	"	3.1	96825	" " "	CH,CN	2	"	264γ
263/64ε	12.9	2.0	2.5?	0.1	94990	" " "	Hα	2	208.3	Hα
263/64ζ	"	"	"	5.5	96825	" " "	CH,CN	2	"	264ε
269/70β	11.6	2.4	1.5	2.4	96325	NH_3	NH	3	197.9	Hβ
271/72α	14.9	1.5	2.2	0.2	97575	H_2,C_2N_2	Hα	1	247.3	Hα
271/72β	"	"	"	3.7	96825	" "	CH,CN	2	"	271α
273/74α	11.8	1.9	2.0	0.5	96325	NH_3,He	NH	3	213.2	He
273/74β	13.3	1.6	2.1	3.7	96340	" ,"	NH	3	216.7	Hβ
275/76α	14.3	2.3	2.6	2.8	"	" ,"	NH	3	230.9	He
275/76γ	17.5	1.9	1.6	1.3	"	" ,"	NH	3	287.8	He
283/84β	13.2	3.6	3.5	3.4	97575	NH_3,He	Hα,cal.(using NH			
289/90β	21.8	1.7	?	0.6	"	H_2,He	Hα	1	372.0	Hα

TABLE I (con't)

Notes to Table I

Photo: Plate and photograph designations are explained in Sec. 6.6, above.

V: This is the applied voltage in kV, as read from the power supply meter. The breakdown of a functional relationship between V and the resulting electric fields, clearly evident in the table, is partly due to variation in current or cathode size, and partly due (in runs numbered less than 100) to recalibration of the voltmeter, but is nevertheless often unexplained.

I: This is the total tube current, read at the power supply.

p: The pressure is read on the McLeod gauge downstream from the discharge tube.

t: This is the total exposure time in hours.

Grating: This setting determines the spectral ranges to reach the plate.

Use: This is the use to which the photograph has been put in this work, not necessarily the use originally intended.

Field: This gives the maximum measured field in kV/cm, and an indication of the source of this measurement.

Slit: The spectrograph slit is usually set to 40μ or 45μ width, and occasionally 50μ. The slit was normally masked to a height of more than 7 mm and less than 12 mm, but a portion of this image was below the cathode surface so that the apparent height was smaller.

Plate type: Kodak type Ia-O, 2" x 10" unbacked spectroscopic plates were used except that plates 1/2 and 13/14 were on 103a-O plates, and plate 36, plates 263 through 272, and plates 283 through 290 used type Ia-E.

Cathode: Cathodes were aluminum of diameter 1 mm excepting as follows: Runs 1/2 and 13/14 used 2 mm aluminum; runs 125/26$_\beta$, 127/28$_\alpha$, 127/28$_\beta$, 131/32$_\alpha$, 137/38$_\alpha$, and all of plates 139 through 146 used 2 mm carbon cathodes; finally runs 127/28$_\gamma$, 133/34$_\alpha$, 133/34$_\gamma$, 135/36$_\gamma$, 137/38$_\beta$, and 137/38$_\gamma$ used 1 mm carbon.

Further details: More detailed description is contained in a series of six laboratory notebooks; a plate index of all plates made is to be found at the back of Book IV.

available for field calibration (Thomson and Dalby[75]). H_β and H_γ are considerably weaker and may require hours of exposure. The secondary (molecular) spectrum is easily obtained with large Stark effects, and can be a nuisance above 5000 Å. Standard purity H_2 gas was satisfactory. An in-line (7μ) filter was used in later work, but is thought to have been unnecessary.

8.2. Helium

Helium runs fairly well and very cleanly (low sputtering), but is rather unstable at higher voltages when used alone. Helium was used for running-in all of the cathodes used with H_2O and D_2O (below), but generally needed those substances for stability above 10 kV. Alone, at some given voltage, helium might require two or three times as much pressure as hydrogen to draw the same current. The neutral helium lines can be photographed easily, and plates have been obtained showing high dispersion Stark effects on all identifiable (and some forbidden) lines in regions covered. The 5015 Å and 4922 Å lines have been used for field calibration with NH. Ishida and Hiyama[50] remark that helium brightens the atomic spectrum of hydrogen, at the expense of the molecular. This effect was not noted here. The hydrogenic lines of helium II have been observed (see, e.g., 4685 Å on plates 53/54), but much more weakly. Standard purity gas from Canadian Liquid Air, Ltd. was satisfactory.

8.3. Argon

Argon was found to cause heavy sputtering with aluminum. A carbon cathode lasted a bit longer, and was also tried by Fisher[76](p.38), but argon seems unsatisfactory as a "carrier" gas.

8.4. Nitrogen, Oxygen, Air, Nitric Oxide

All of these gases operate without difficulty at moderate voltages. Oxygen shows atomic lines in the visible, and ionized oxygen lines have been observed with considerable Stark broadening. The other listed gases give the first and second positive bands of N_2 and the first negative bands of N_2^+ very strongly, along with various atomic lines. The spectrum of NO was not observed with these gases in any combination. Other oxides of nitrogen (N_2O, N_2O_3, NO_2) are available but have not been tried as of this writing. The mentioned bands of N_2 and N_2^+ are common impurity spectra. The (1,0) and (0,0) bands of the N_2 second positive system have shown weak Stark effects on selected lines. The yellow-green color of "active nitrogen" has been observed at the tube edges, but not in the discharge itself.

8.5. Aluminum, Trimethylaluminum

Aluminum atomic lines appear readily with cathodes made of the metal, showing Stark broadening and shifts. Attempts to observe the well-known $^1\Pi - {}^1\Sigma^+$ band of

AlH at 4241 Å, by running aluminum cathodes under H_2 or H_2 and $Al(CH_3)_3$, were unsuccessful. The CH band at 4314 was weakly observed with the latter combination. $Al(CH_3)_3$ (obtained from Alfa Inorganics, Inc.) was not tried extensively since it is spontaneously flammable in air. It was handled much as was silane, except that no regulator was used (due to its low vapor pressure) and the material was trapped in a cold trap containing NaOH. (After removal, the trap was simply allowed to thaw in privacy). $Al(CH_3)_3$ was a noticeable current suppressor, occasionally left a metallic deposit, and was quite destructive of cathodes.

8.6. Water and Heavy Water

These substances had been found to operate well by Phelps and Dalby[8]. They were run with helium in this work, principally because the advantages of hydrogen had not then been recognized. (Phelps[14], p.41, rejected hydrogen, apparently because of the complication of the molecular spectrum.) Sample was usually introduced into the discharge after having been brought up to several kV with helium and signs of instability appeared. The (0,0) band of the $A^2\Sigma^+ - X^2\Pi$ system, at 3064 Å, is very strong, and appears commonly as an impurity. Other vibrational bands weaken rapidly with increasing v', v", or Δv, and transitions from higher electronic states have not been observed in a LoSurdo discharge. The sample was held in a vessel directly

attached to a needle valve input, and was caught in a liquid nitrogen trap. The water's needle valve setting was not very critical, sometimes being run wide open. The H_2O was distilled tap water, while the D_2O was obtained from Merck, Sharp, and Dohme.

8.7. Methanol

CH_3OH was used to generate the 4314 Å band of CH, following the method of Phelps[14](p.41) and Phelps and Dalby[70]. Oddly, while the substance seemed to operate quite well, and left no discernable chemical deposits, the spectra obtained in this way were exceedingly weak. Phelps had no difficulty obtaining ample intensity. This may be due to the use of the sunken cathode, since no flush cathodes were tried with this material. (See also Sec. 8.14., below.) The handling of methanol is similar to that of water.

8.8. Dimethyl Mercury

Here we attempted, and failed, to obtain the 4017 Å band of the $A^2\Pi_{\frac{1}{2}} - X^2\Sigma$ system of HgH. Sufficient $Hg(CH_3)_2$ was run in the discharge (with hydrogen) so that mercury droplets coated the shield wall of the discharge tube, but the desired spectrum did not appear. It has been noted by McCurdy[81] and Compton, Turner, and McCurdy[82] that HgH can be seen in the positive columns of glow discharges. We cannot verify this, but only note that the spectrum does

not appear in our cathode glow. Larger concentrations of $Hg(CH_3)_2$ were effective in producing bright striations in the upper tube.

Our sample was obtained from Alfa Inorganics, and was handled much like water, but its disposition was treated with care because of its well-known toxicity in water. A bulb with a built-in shutoff stopcock had to be abandoned when the sample proved too readily soluble in the stopcock grease.

8.9. Diethyl Zinc

This was run with hydrogen in search of the 4300 Å band of ZnH, analogous to HgH, but with no better luck. Diethyl zinc is a spontaneously combustible substance in air, and left a white powder (undoubtedly ZnO) in the system when mixed thinly with air. Due to the failure of this substance, along with methylated mercury and aluminum, to produce the spectrum of the associated hydride, experiments of this type were curtailed even though methylated (or ethylated) forms of tin, lead, cadmium, and germanium were available.

8.10. Phosphorous Oxychloride

This substance, also known as phosphoryl chloride ($POCl_3$), was used to look for the brighter bands of the $B^2\Sigma^+ - X^2\Pi$ (β-band) system of PO. The failure of this search was likely due to the fact that this substance

destroyed the discharge. The cathode glow was soon replaced by a curiously stable system of turquoise sparks, which were photographed but did not yield reproducible band spectra in the region of observation. Due to its highly corrosive nature, the $POCl_3$ was fed through the monel and stainless steel input system from a stainless steel sample cylinder; otherwise it was handled as water.

8.11. Silane

SiH_4 was capable of running fairly well over flush cathodes, but would too quickly obscure inner quartz walls to be used with a sunken cathode. The 4142 Å band of the $A^2\Delta \rightarrow X^2\Pi$ transition (analogous to the similar system of CH) has been photographed, but the fields available with the flush cathode appeared to be too low to give splittings (confirming theoretical calculations which indicate a relatively low dipole moment). SiH_4 is current-depressing, indicating that a chemical layer may be deposited quickly over the cathode surface and burn in equilibrium for continued operation. Another peculiarity noted was that electric fields exceeding some 60 000 V/cm could not be obtained, even though the applied voltage might range from 5.5 to over 9 kV. The sample, obtained from Matheson, Inc., was fed to the system through copper tubing and a (brass) helium regulator. In spite of Matheson's recommendation to use only corrosion-resistant materials, no difficulty was encountered. No cold trap was used, to avoid

accumulations of the substance in glassware, but the pump exhaust was fed out of doors and bubbled through a water trap to prevent backup. No problems were encountered, although the exploding bubbles of silane and hydrogen could be surprisingly powerful. In later work during a cold spell, the pumping efficiency was adversely affected when the outside water froze.

8.12. Beryllium with Hydrogen, Oxygen, or Water

It was hoped that either the 4988 Å band of the $A^2\Pi \rightarrow X^2\Sigma^+$ transition of BeH, or the brighter bands (e.g., 4708 Å) of the $C^1\Sigma^+ \rightarrow X^1\Sigma^+$ transition of BeO might be seen while running hydrogen or oxygen, respectively, over a beryllium cathode. Although the BeO band is between two Σ states, second order Stark effects should be large since a large dipole moment is expected (Yoshimine[83]).

Hydrogen over beryllium definitely failed to give BeH, and oxygen failed to give the BeO spectrum. A peculiar and very fuzzy spectrum did appear under oxygen, however, just where the BeH bands were expected! The broadness of the lines makes identification very difficult, but the formation seems to be roughly justifiable in terms of BeH, which has a very confused spectrum with all $\Delta v=0$ bands superimposed. BeH is expected to have quite a small dipole moment (around 0.25 debye as compared to about 7.54 D for BeO; see Cade and Huo[84], and Bender and Davidson[85]), making it seem unlikely that the fuzziness should

be due to Stark effects. This spectrum was also seen when run under helium and water, but no more strongly than under oxygen. The short distance above the cathode wherein this spectrum is visible gives evidence that beryllium is a constituent. This spectrum is quite weak in all cases, requiring several hours exposure.

8.13. Boron Trichloride

This is a volatile corrosive liquid which was handled much the same as $POCl_3$. It seems to be destructive of cathodes, and, in the very brief series of trials here reported, no long exposures were obtained. The $A^1\Pi \rightarrow X^1\Sigma$ system of BCl ((0,0) band at 2720 Å) was not seen, although it had been observed by F.W. Dalby and S.Y. Wong (unpublished) some time earlier with a much faster spectrograph. This failure is further explained by our having attempted to see the bands in fifth order.

8.14. Cyanogen

Thomson and Dalby[74] had earlier found that the violet bands of CN ($B^2\Sigma^+ \rightarrow X^2\Sigma^+$, (0,0) band at 3883 Å) could be excited in a discharge containing cyanogen (C_2N_2). The main effort here was directed towards observing the red bands ($A^2\Pi \rightarrow X^2\Sigma^+$, (0,0) band at 11 000 Å, but with bands reported down into the blue). Cyanogen is a dirty material to run, as well as being highly toxic, and would spoil sunken cathodes readily by obscuring the quartz above

the cathode (particularly at the negative glow). Certain of the red bands were observed, although the better exposures were taken with flush cathodes. This was accomplished with the aid of Ia-E spectroscopic plates; beyond the range of these plates (over 6600 Å, say), the hope of recording red band spectra is small. It has been found that the violet bands are far easier to obtain, and a number of new Stark phenomena have been observed therein. It was found, moreover, that the 4314 Å band of CH (Sec. 8.7., above) was observable with more intensity under a mixture of cyanogen and hydrogen than with methanol, and it is from the work with cyanogen that our information concerning CH was obtained. This is the only example known to this author wherein elements introduced without a pre-existing bond were chemically joined by this discharge.

Cyanogen was fed into the system through the sequence of monel or stainless steel pipes and valves indicated in Fig.10. This method was made all the more feasible by the fact that cyanogen in the cylinder is a liquid with vapor pressure of 60 pounds at room temperature. It was caught before the pump by a cold trap loaded with NaOH pellets and glass beads, and, as a final precaution, the pump exhaust was bubbled through a mixture of NaOH and calcium chloride hypochlorite before going out the window.

At one point, serious trouble occured when sunken cathodes were observed to blacken above the cathode during running-in with hydrogen. This deposit could sometimes be

burnt off at higher voltage (12 kV or higher) but more often caused flare phenomena leading to cathode destruction. At this point an in-line filter of 7 micron pore size was placed in-line at the hydrogen input, but to no avail. It was finally decided that cyanogen absorbed by the system's vacuum grease was the culprit (even though CN spectra were never observed visually during run-in), and the problem was solved by careful cleaning and performing the running-in sequence at full pumping rate. The constricting valve (see Fig.10) was placed in line (to reduce sample consumption) only after running-in and before introducing cyanogen.

Beautiful striations in the anode region could be obtained at high concentrations of C_2N_2, particularly with flush cathodes. The number of striations is useful as an indication of C_2N_2 pressure. For a sunken cathode, for example, an appropriate concentration is found to occur when the first striation just appears as a velvety glow on the anode surface.

8.15. Ammonia

It had been found by Irwin[71] and Irwin and Dalby[72] that ammonia would yield the 3359 Å $A^3\Pi \rightarrow X^3\Sigma^-$ (0,0) band and 3240 Å band ($c^1\Pi \rightarrow a^1\Delta$, (0,0)) of the NH molecule.

Ammonia had been found to behave quite nicely in the discharge at the lower voltages used by the previous workers. At higher potentials, however, very cursory work

indicated that failure was more likely when running-in a cathode with ammonia alone. It thus seemed desirable to run-in our cathodes by the well-established method using hydrogen (Sec. 7.3.). After a number of experiments had been tried, however, it was found that when ammonia was introduced into the discharge at high voltage, heavy sparking invariably ensued which destroyed the cathode and even shattered the quartz. Upon even more persistant effort, the same thing happened while running-in hydrogen. The rather unlikely conclusion was reached that a small amount of ammonia contaminating a hydrogen discharge was highly destructive, even though higher ammonia concentrations might not be. At fault was a leaky shut-off valve in the ammonia input line, and general absorption by the vacuum greases. The cure involved placing a stopcock on the input line, cleaning out old grease, and abondoning all pumping constrictions. After running-in the hydrogen, the system was "washed" with helium before introducing the ammonia.

In contrast to Irwin's work, these experiments showed a persistent impurity spectrum consisting of the strong (0,0) band of the nitrogen second positive system, which happens to directly overlap the $A \rightarrow X$ (1,1) and part of the (0,0) bands. Once recognized, however, these nitrogen lines proved to be valuable as reference lines. Examination of the nearby (1,0) second positive band led to the discovery of Stark effects in nitrogen.

9. Other Means of Excitation

A strong source of excitation, albeit without electric fields, is often useful.

One such is a microwave generator. A standard diathermy unit ("Radarmed", Deutsche Elektronik GMBH) was used which could deliver the order of 100 mW of power at 2425 MHz. It was capacitively coupled by simply placing short leads across the neck of the discharge tube at the point marked "X" in Fig. 9c.

Another method is to merely reverse the electrodes with an old sunken cathode. This produces an intense positive column within the capillary over (what is now) the anode. This method is of brightness comparable to the microwave excitation; it does not require refocusing of the lens, but should probably not be used with a cathode which is still expected to perform at high fields.

Either method can produce strong reference exposures, for all spectra which are normally observable in the cathode glow region (and many which are not) in a matter of minutes.

CHAPTER VII

THE MEASUREMENT OF THE PLATES AND THE CALIBRATION OF ELECTRIC FIELDS

1. Plate Measurement

All measurements were made on a microdensitometer/comparator kindly made available to us by Dr. A. M. Crooker. This instrument has vertical and horizontal positioning controls calibrated to one micron accuracy, a "zoom" lens providing variable magnification, and a visual projection as well as photoelectric sweep of the central portion of the field, with digital readout. Without removing one's gaze from the field of vision, one may cause to be punched on an IBM 026 keypunch a sequence of data including the horizontal setting in microns, an intensity reading at field center, and a choice of a single identification character. These data cards were punched in a format which allowed the inclusion of wavelength (or cm^{-1}) and line identification data, to be read directly by a computer program. This program (called WNINT) picks out lines with supplied wavelengths (or wavenumbers) to be standards, and interpolates the remaining horizontal measurements with a fourth order polynomial function. Interpolated wavelengths and/or wavenumbers are printed out in a choice of orders, as are dispersions formed from the derivative of the polynomial.

The program also sums over (at most two) intermixed sequences of component measurements, printing out separate averages with standard deviations, and can punch these on cards for processing by other programs.

Most of the automatic features of the comparator could not be used because of the peculiar problems associated with measuring (often very weak) Stark shifted components. All such measurements were done by eye using the projected image, although wavelength standards (e.g., OH lines of high angular momentum J) were often measured using the oscilloscope display of the photoscan feature which greatly facilitated the measurement of such "ordinary" lines.

Each measurement was repeated from four to sixteen times (averaging about seven), depending on the point's apparent reproduceability. The measurements of molecular Stark effects and wavelength standards were made at nearly maximum magnification (about fifty). The much broader and more curved helium and Balmer hydrogen lines were measured at considerably lower magnification without loss of accuracy.

The plates were aligned vertically rather than horizontally on the comparator platform: They were rotated until vertical comparator motion produced minimum variation in the position of (high J) lines showing no Stark effects, as judged by the oscilloscope photoscan. The vertical position of maximum field would vary across the plate, in general, due to imperfect perpendicularity of the spectrum.

2. Calibration of Electric Fields

Electric fields were measured by essentially the same method used by previous workers in this laboratory: calibration by means of the Balmer lines of hydrogen. Expressions for the Stark effect through third order in these lines have been assembled by Ishida and Hiyama[50], reprinted by Condon and Shortley[64](p.398ff), and found to agree reasonably well with experiment (see same references). Condon and Shortley express the displacements D' of a given component as

$$D'_{\pm} = \pm aE - bE^2 \pm cE^3 , \qquad (115)$$

where the upper signs give the displacement of the component to higher energy, and the lower signs give its displacement to lower energy. The coefficients a, b, and c are given for the different components of H_α, H_β, and H_γ by both Ishida and Hiyama[50] and Condon and Shortley[64](p.403), relating D' in cm^{-1} to E in MV/cm.

Unfortunately, these coefficients were calculated by Ishida and Hiyama using rather crude values for Planck's constant, the speed of light, and the electronic mass and charge as were then available. Using the recent values for these constants[86]:

$$h = 6.626196 \times 10^{-27} \text{ erg-sec}$$

$$c = 2.997925 \times 10^{10} \text{ cm/sec}$$

$e = 4.803250 \times 10^{-10}$ esu

$m = 9.104599 \times 10^{-28}$ gm (reduced mass of H)

the older values of a are found to be high by about 0.67%, while b and c were high by about 2% and 3% respectively. Tables II and III give improved values of these constants for OH and OD, respectively. This and all previous work done in this laboratory used the old constants[8,14,70-77]. All fields reported in these researches must be increased, and dipole moments decreased, by 0.67%. Dipole moments will simply be corrected by the 0.67% factor in this work, rather than recalculating fields and replotting the graphs. To facilitate comparison with the graphs and original calculations, the uncorrected fields are listed in the tabulations. Corrected versions of previous results from this laboratory have been included in Chap. XII for reference purposes. The change in field produced by these corrections in higher orders than first may be generally ignored. The least deviated components (e.g., the 2σ component of H_β) show far and away the highest second and third order effects; even in this worst case at a highest field of 320 kV/cm, however, the second order term is 8.3% of the total so that a 2% correction will change the total by less than 0.2%; other components give much less effect.

The dipole moment ratios as reported in Scarl and Dalby[77](p.2831) are not affected by this correction (see

TABLE II

Stark Effect Coefficients for the First Three Balmer Lines of Atomic Hydrogen, Derived from Improved Constants

Line	Label	a	b	c
H_α	4π	255.85	6.185	0.159
	3π	191.89	6.085	0.085
	2π	127.92	6.584	0.003
	1σ	63.96	6.035	0.082
	$0\sigma 1$	0.00	5.076	0.000
	$0\sigma 2$	0.00	6.574	0.000
H_β	10π	639.62	34.41	2.966
	8π	511.70	35.27	2.056
	6π	383.77	37.61	1.011
	6σ	383.77	35.22	2.056
	$4\sigma 1$	255.85	32.87	1.118
	$4\sigma 2$	255.85	37.66	1.008
	2σ	127.92	36.80	0.003
H_γ	18π	1151.32	127.9	28.35
	15π	959.44	131.6	21.91
	13σ	831.51	131.7	21.91
	12π	767.55	139.7	14.44
	$10\sigma 1$	639.62	127.9	15.48
	$10\sigma 2$	639.62	139.7	14.45
	5π	319.81	139.4	7.40
	3σ	191.89	139.4	7.40
	2π	127.92	143.4	0.003
	$0\sigma 1$	0.00	131.5	0.00
	$0\sigma 2$	0.00	143.4	0.00

TABLE III

Stark Effect Coefficients for Deuterium, from Improved Coefficients

Line	Label	a	b	c
D_α	4π	255.78	6.181	0.159
	3π	191.84	6.081	0.085
	2π	127.88	6.579	0.003
	1σ	63.94	6.031	0.082
	$0\sigma 1$	0.00	5.072	0.000
	$0\sigma 2$	0.00	6.569	0.000
D_β	10π	639.44	34.38	2.962
	8π	511.56	35.24	2.053
	6π	383.66	37.58	1.010
	6σ	383.66	35.19	2.053
	$4\sigma 1$	255.78	32.84	1.116
	$4\sigma 2$	255.78	37.63	1.007
	2σ	127.88	36.78	0.003
D_γ	18π	1151.00	127.8	28.31
	15π	959.18	131.4	21.88
	13σ	831.28	131.6	21.88
	12π	767.34	139.6	14.42
	$10\sigma 1$	639.44	127.8	15.46
	$10\sigma 2$	639.44	139.6	14.43
	5π	319.72	139.3	7.39
	3σ	191.84	139.3	7.39
	2π	127.88	143.3	0.003
	$0\sigma 1$	0.00	131.4	0.00
	$0\sigma 2$	0.00	143.3	0.00

Chapter IX), although μ_Σ and μ_Π both are.

In computing fields from observed Balmer displacements, it is often convenient to treat the absolute value of Eq.(115):

$$D_\pm \equiv | D'_\pm | = aE \pm bE^2 + cE^3 , \tag{116}$$

where the upper and lower signs retain their meaning as in Eq.(115). The formulae for the reversion of series give, from Eq.(116):

$$E_\pm = D_\pm/a \pm bD_\pm^2/a^2 + (2b^2/a - c)D_\pm^3/a^4 , \tag{117}$$

where E_+ and E_- are, in principle, the same.

An alternative formulation employs the splitting S, defined as the difference between the two displacements of Eq.(115), or the sum of those in Eq.(116):

$$S = 2aE + 2cE^3. \tag{118}$$

The reversion of this form gives

$$E = S/2a - cS^3/8a^4 , \tag{119}$$

which is different from the average of E_+ and E_- in Eq.(117). Clearly, Eqs.(116) and(117) are to be used when one side of a component is unavailable, while Eqs.(118) and

(119) are used when the undeviated position is at all uncertain. When full information is available, the two methods add redundancy to the field measurement, as do the several Balmer components. When only a linear approximation is to be used, however, the last method (S/2a) is accurate to second order but the other is not.

A computer program (FIELD) has been used throughout this work which calculates all possible combinations of available components and presents them as two averages, corresponding to $D_{\pm}$ and S. A best value is chosen, possibly after the elimination of uncertain components, which is usually the one with lowest mean deviation.

The coefficients of components differing only in second (or higher) order terms are averaged together, since such components are never resolved.

In work with OD, the corresponding Balmer lines of deuterium are used. According to formulae in Ishida and Hiyama for a, b, and c, the coefficient a is proportional to $1/m$, b to $1/m^3$, and c to $1/m^5$, where m is the reduced mass of the two particle system. Since the reduced mass of hydrogen is smaller than that of deuterium by a factor of about 0.99973, the coefficients for deuterium are smaller than for hydrogen by the corresponding powers of this factor. The resulting coefficients are listed in Table III.

In some of the plates taken with ammonia (NH), the Balmer line (H_{β}) intended to be used in field determin-

ation was too weak to be useful, but helium lines were clearly visible. To use the helium lines for the determination of field strengths (see Chap. VI, Table I), it was decided not to use the calculations of Foster[65] on the Stark effect in helium, but to use instead an assortment of plates (taken during previous work with OH) showing the helium lines (4922 Å and 5015 Å) with good H_β lines. The fields were interpolated using the WNINT program (see Sec.1, above) with helium displacements in cm^{-1} used in place of plate measurements and electric fields (times ten) in place of wavelengths (the program had already been used to determine the wavenumbers of the helium lines with respect to OH or NH standards in the ordinary way). Fields thus found were averaged over the four helium components used (two each from 4922 Å and 5015 Å). Deviations quoted were obtained from this average. Data used in calibrating the helium lines is listed in Table IV.

The only other variation from the use of Balmer lines in field calibration was in the determination of the ratio μ_Σ/μ_Π in OH and OD. In these experiments, the fields at each vertical level were obtained from the splitting of the $P_{12}(1)$ line at that level, as described in Chap. IX, below.

TABLE IV

Helium Calibration Data

Shown are the measured deflections in cm^{-1} of the two low-frequency allowed components (labeled 4 and 6) of the 4922 A line, and the high-frequency components (labeled 1 and 2) of the 5015 A line.

OH Run number	Field kV/cm	Helium Component Deflection 1	2	4	6
13/14	122.3	7.49	4.85	-29.2	-52.1
$53/54_{\beta}$	176.7	15.5	10.15	-42.9	-83.8
55/56	226.9	23.1	15.5	-56.1	-108.8
45/46	276.7	32.0	21.8	-70.5	-131.3
$59/60_{\beta}$	285.1	32.8	22.0	-72.5	-136.8
$59/60_{\alpha}$	319.3	38.1	27.0	-78.9	-148.5
1/2	95.1	n.a.	n.a.	-22.0	-40.6

CHAPTER VIII

THE $^2\Pi$ STATES OF OH AND OD

1. The Lines

This work has extended the results of Phelps[14] and Phelps and Dalby[8] by obtaining more data, some at higher fields, for the (0,0) and (1,1) bands of OH. A number of the low-field plates were sufficiently exposed to show discernable components of the appropriate lines in the (2,2) band, in spite of the low vibrational temperature of this discharge. Furthermore, analogous results were obtained for the same bands in OD. See Chap. VI, (particularly Sec. 8.6.) above for a description of the methods of generating these spectra.

There are four lines, designated $P_{12}(1)$, $Q_2(1)$, $Q_{12}(1)$, and $R_2(1)$, which correspond to $A\,^2\Sigma^+ \rightarrow X^2\Pi$ transitions ending at the $J=\frac{1}{2}$ $(N=1)$ level of the $^2\Pi_{\frac{1}{2}}$ state. According to the theory in Chap. IV above, these lines will be split by the first order Stark effect into only two components. In this notation, (see Fig. 13) the letters O, P, Q, R, and S signify that the quantum number N changes by 2, 1, 0, -1, and -2, respectively, during the emission process. $P_{12}(1)$, for example, indicates a transition in which N increases by one in going from an f_1 to an f_2 level, and

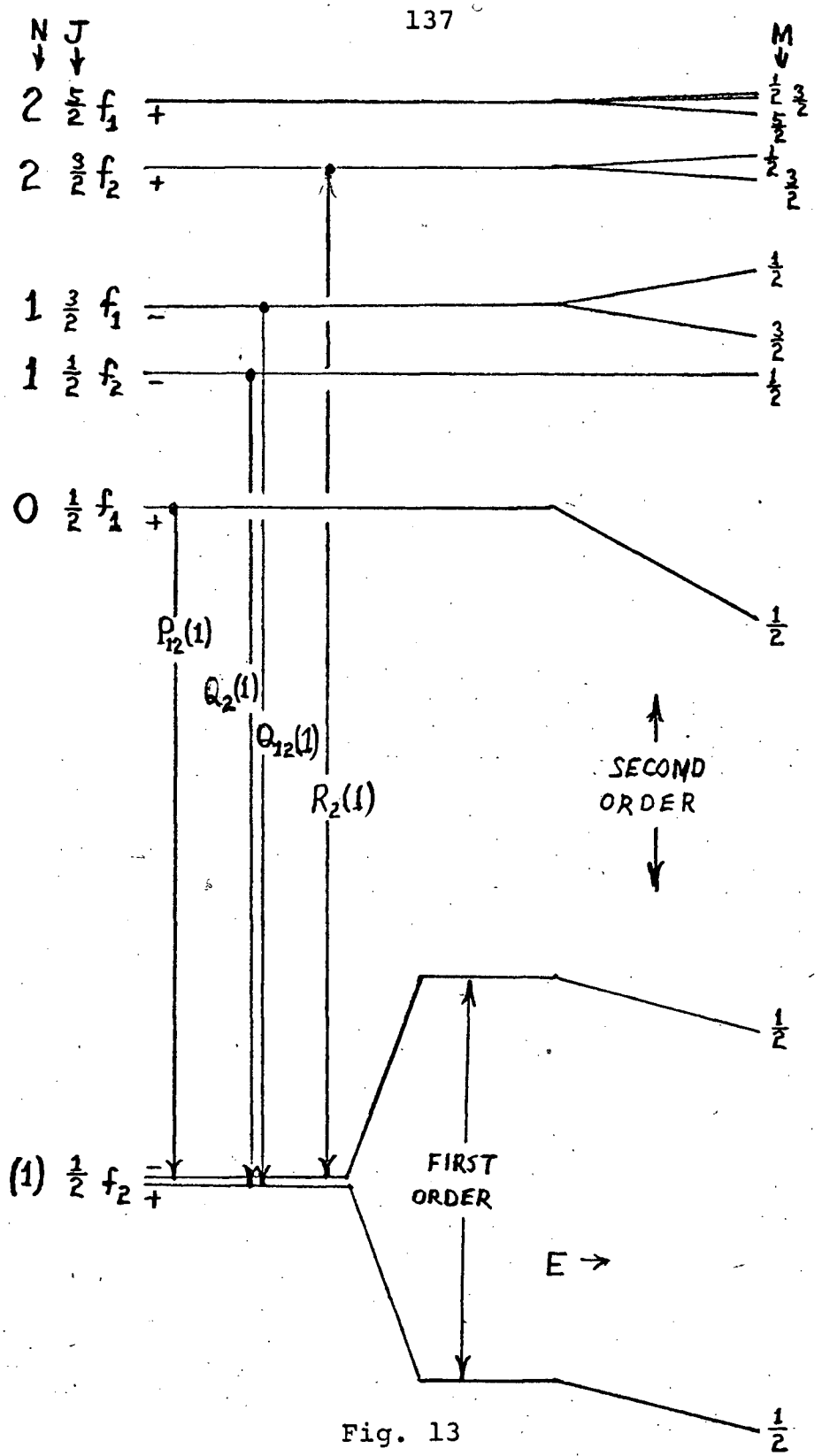

Fig. 13

Allowed transitions and Stark Effects Involving the $^2\Pi_{\frac{1}{2}}$, $J=\frac{1}{2}$ Energy Level of OH. Only second order effects are to scale. The second order effects shown do not include the interaction with spin-splitting.

in which the value of N in the lower state is one. Only the $P_{12}(1)$ line is "clean", as we shall see, in the sense that the upper state also has $J=\frac{1}{2}$ which (being non-degenerate with respect to different M) shifts in second order (Fig. 13) but does not split in any order and so cannot affect the observed splitting.

The $R_2(1)$ line has an upper state with N=2, $J=\frac{3}{2}$, and is split in second order into $M=\frac{1}{2}$ and $\frac{3}{2}$ components. Ignoring any interactions with spin splitting, the Σ state Stark effects for these levels are given by $\varepsilon^2/60B$ $(M=\frac{1}{2})$ and $-\varepsilon^2/60B$ $(M=\frac{3}{2})$ (using Eq. (31) and Eq. (18)), where $\varepsilon=\mu E/hc$. The upper state thus splits by $\varepsilon^2/30B$. Setting $\varepsilon=10$, corresponding to $\mu=2$ D and E = 300 kV/cm (see App. A), and putting $B = 17\ cm^{-1}$, we get a splitting of about $0.20\ cm^{-1}$ which is about 0.028 mm on our plates (at $7\ cm^{-1}/mm$ in third order), or less than a linewidth. The spin splitting in the $A\ ^2\Sigma^+$ state of OH ($5\gamma/2 = 0.56\ cm^{-1}$) is sufficiently larger than the Stark splitting that the interaction with spin (Chap. IV, Sec. 6) may be neglected. (In OD, the Stark effects are larger and spin splitting smaller, but we do not use the $R_2(1)$ line at field larger than 70 kV/cm, so that this approximation still holds.) In any event, both components of the first order splitting in the $^2\Pi$ state are equally affected, so that any skewness in the lineshape due to upper state effects should not affect the first-order splitting. In fact, the results from $R_2(1)$

and $P_{12}(1)$ transitions are consistent even at highest fields.

The $Q_2(1)$ line is complicated by the presence of its satellite, the $Q_{12}(1)$ line. While the $Q_2(1)$ is only shifted by second order effects in its upper state (and then only through interaction with the spin splitting), the $Q_{12}(1)$ upper state exhibits splitting in second order (Fig.13). However, the $Q_{12}(1)$ has but half the intensity of the $Q_2(1)$, according to the formulae of Earls[87], and the $Q_{12}(1)$ is further weakened by the splitting in the upper state. In OH the two lines can often be resolved, while in OD (at our resolution) the $Q_{12}(1)$ can only skew the line profile of the $Q_2(1)$. It is felt that these effects can be taken into account visually during measurement. This line has given results consistent with other lines in OH with v=2, and in OD with v=0 and 2.

Fig. 2 illustrates the expected appearance of these lines in high fields, while Figs. 3 and 4 show sample photographs of each band.

2. The Methods

The measurements were converted into wavenumbers using the interpolation program WNINT as described in Chap.VII. Wavelength standards were obtained by measuring a number of the high J lines of OH and OD with negligible Stark effect. The wavelengths/wavenumbers of the OH lines were taken from Dieke and Crosswhite[88] for all bands.

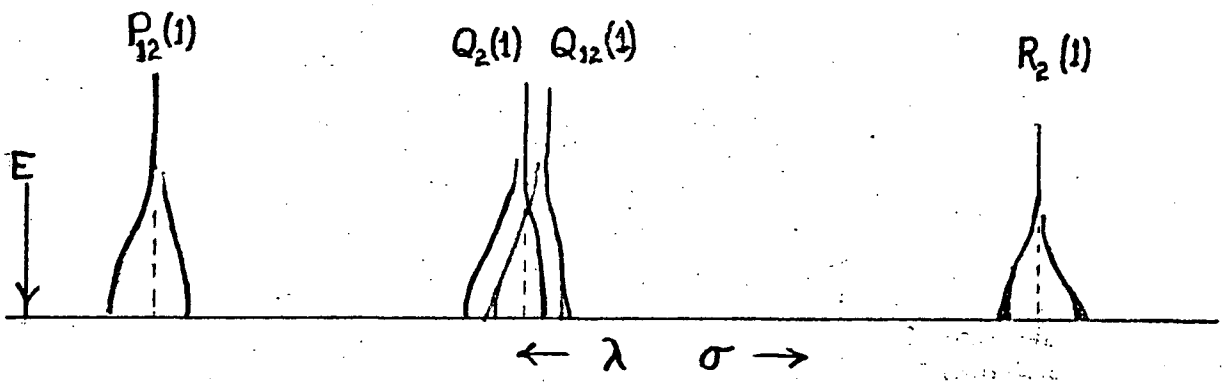

Fig. 14

Schematic Detail of the Transitions of Fig. 13 in a field of varying intensity. This is drawn as it would appear on a high field plate, with the cathode surface indicated by the horizontal line.

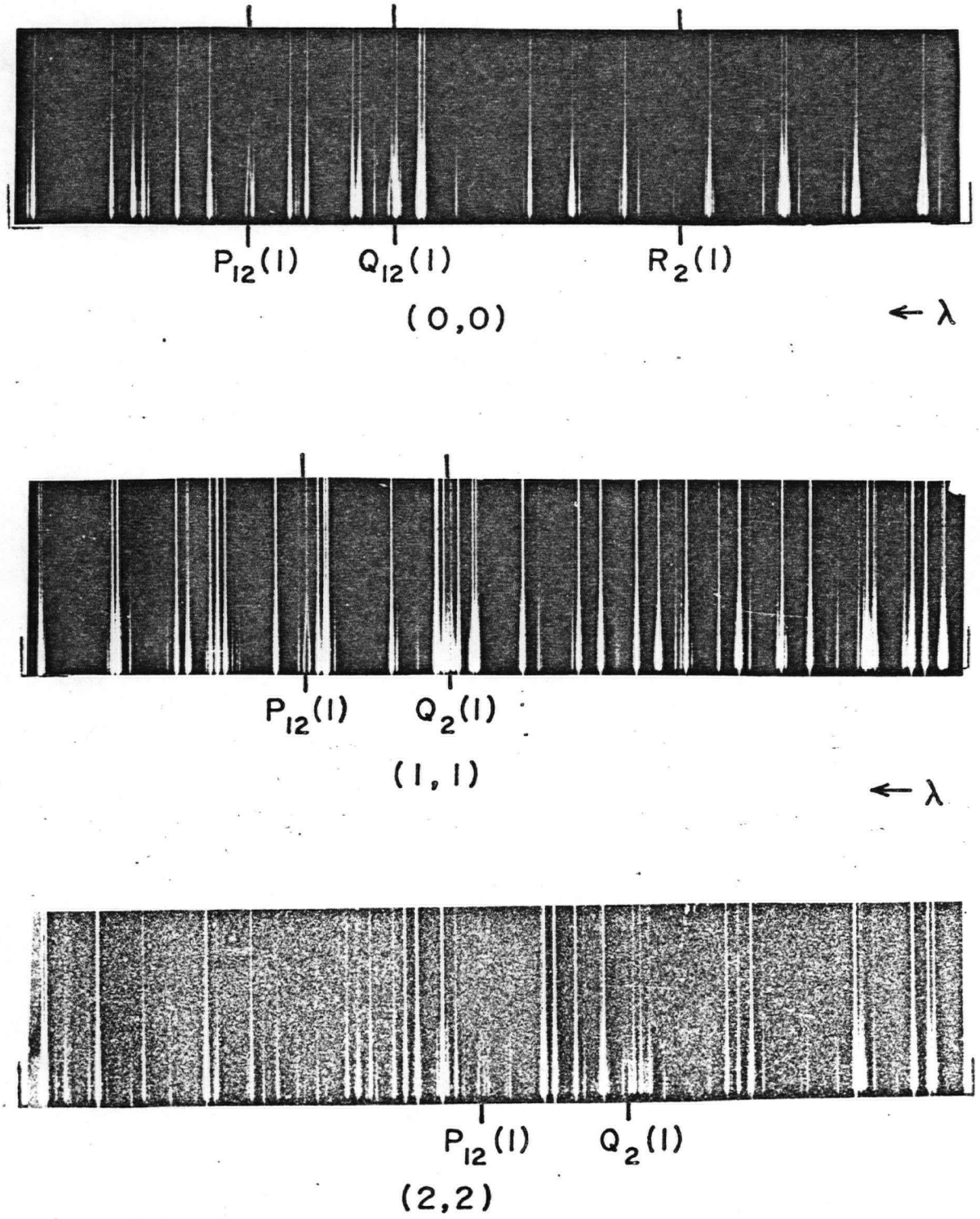

Fig. 15

The A → X Bands of OH at low field.

Plate 140α. The electric field is 69.1 kV/cm.

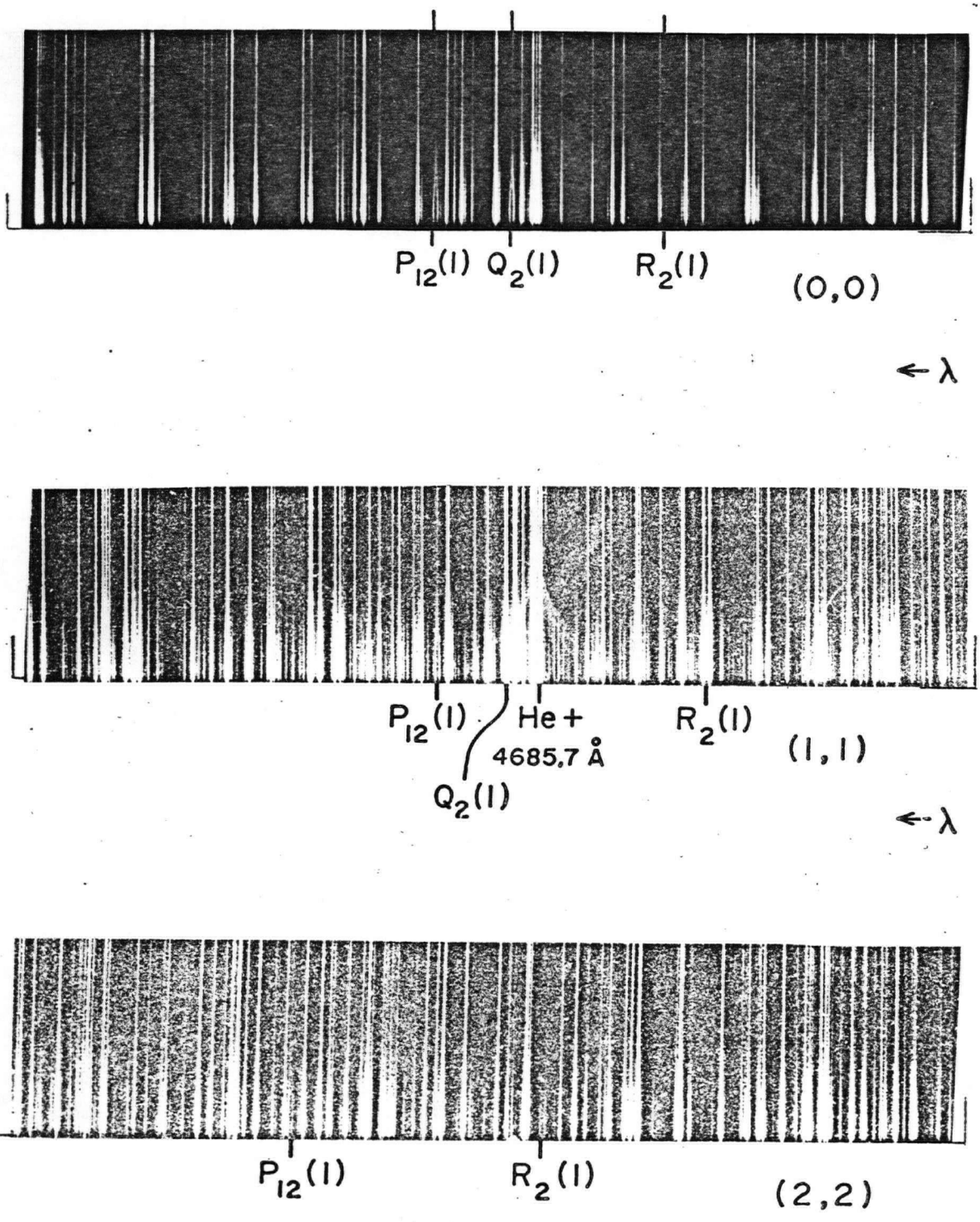

Fig. 16

The A → X Bands of OD at Low Field. Plate 127α

The electric field is 54.5 KV/cm.

For OD, in the (0,0) band standards were taken from (usually) Oura and Ninomiya[89] and from Ishaq[90]. For the higher vibrational bands of OD, wavelengths are available from Ishaq[91] and Sastry[92]. However, lines of the overlapping (0,0) were generally used as wavelength standards.

Dipole moments were determined by setting

$$\frac{S}{2} = \left[\left(\frac{\varepsilon M\Omega}{J(J+1)}\right)^2 + \delta^2\right]^{\frac{1}{2}} = \sqrt{\varepsilon^2/9 + \delta^2} \qquad (120)$$

where S is the observed splitting (upper minus lower component) in cm^{-1}, and δ is half the Λ-doubling. This formula is derived from Eqs. (9), (45), and (E.19, App.E). The second line is only true for $J = M = \Omega = \frac{1}{2}$. Eq. (120) may be rewritten

$$E = \frac{89.322}{\mu}\sqrt{S^2 - (2\delta)^2}\ , \qquad (121)$$

so that the electric field (kV/cm) is in direct proportion to the square root quantity, the latter being referred to as the corrected splitting (Phelps[14,8]) and denoted by S', with a constant of proportionality which determines μ directly. This constant is obtained from the slope of a plot showing the corrected splitting as a function of field. A computer program making use of a least squares routine (LQF) was used to fit a straight line through the

data.

The Λ-doubling, 2δ, has been calculated for $J=\frac{1}{2}$, v=0 (in both OH and OD) using the formulae of Dousmanis, Sanders, and Townes[93] (their Eqs. 21-23). Using their experimentally determined constants α_p, β_p, and λ (which we call Y), we obtain 0.158 cm^{-1} for OH and 0.104 cm^{-1} for OD in this level. It should be pointed out that the value of Y (their λ) obtained by Dousmanis, Sanders, and Townes (7.444 for OH, v=0) is now thought to be in error (Clough, Curran, and Thrush[94]; Lee, Tam, Larouche, and Woonton[95]; Radford[96]; Poynter and Beaudet[97]), with the greatest claim for accuracy being made by Poynter and Beaudet (Y = 7.5009±0.0001).

For the excited vibrational states, we assumed in Scarl and Dalby[77] that the Λ-doublings were the same as for v=0. We made an estimate based on the "pure precession hypothesis" which assumes that the $^2\Sigma$ and $^2\Pi$ states arise from the same electron having L=1 (but different $M_L=\Lambda$) and allows the Dousmanis, Sanders, and Townes' matrix elements α_p and β_p to be evaluated simply in terms of B_v and Y_v (Scarl and Dalby[77], p. 2827). This estimate indicated that the Λ-doubling decreases by some 2% per unit v, which affects the corrected splittings by 0.1% or less. Another estimate, based on some rough values for α_p and β_p in OH recently published in Lee, Tam, Larouche, and Woonton[95], give Λ-doublings of 0.151 cm^{-1} and 0.143 cm^{-1} for, respectively, the v=1 and 2 levels

with $J=\frac{1}{2}$ in OH. This is more like a decrease of 5% per unit v, but will still be expected to make little difference. This may be verified by examination of the graphs of v=1 and 2 in Figs. 18 and 19. Since points at lower fields do not deviate consistently below the line through the origin (conversely, the higher field points do not deviate above the line), we may conclude that the use of Λ-doublings which are undoubtedly on the high side has little effect.

Information can be obtained also from the four-fold splittings due to the $J=\frac{3}{2}$ level of the $^2\Pi_{\frac{3}{2}}$ state (i.e., the $P_1(1)$, $Q_1(1)$, $R_1(1)$, and $S_{21}(1)$ lines and associated satellites) on a number of plates. For example, data from the $M_\Pi=\frac{3}{2}$ components of the $Q_1(1)$ line has been included in the data for OH, v=2. For the purposes of the plotting and slope-fitting program, the observed splittings were converted to the "effective" splitting of the equivalent $J=\frac{1}{2}$ level, in order to compensate for differences in the matrix elements and Λ-doublings. I.e., in terms of previous notation, we solve for an effective half-splitting S_{eff} in terms of the observed splitting S by setting

$$\begin{aligned} \varepsilon &= \tfrac{5}{3}k[(S/2)^2 - \delta^2_{J=\frac{3}{2}}]^{\frac{1}{2}} \\ &= \tfrac{1}{3}[(S_{eff}/2)^2 - \delta^2_{J=\frac{1}{2}}]^{\frac{1}{2}} , \end{aligned} \tag{122}$$

where $\delta_{J=\frac{1}{2}} = 0.158\ cm^{-1}$ and $\delta_{J=\frac{3}{2}} = 0.0556\ cm^{-1}$. The

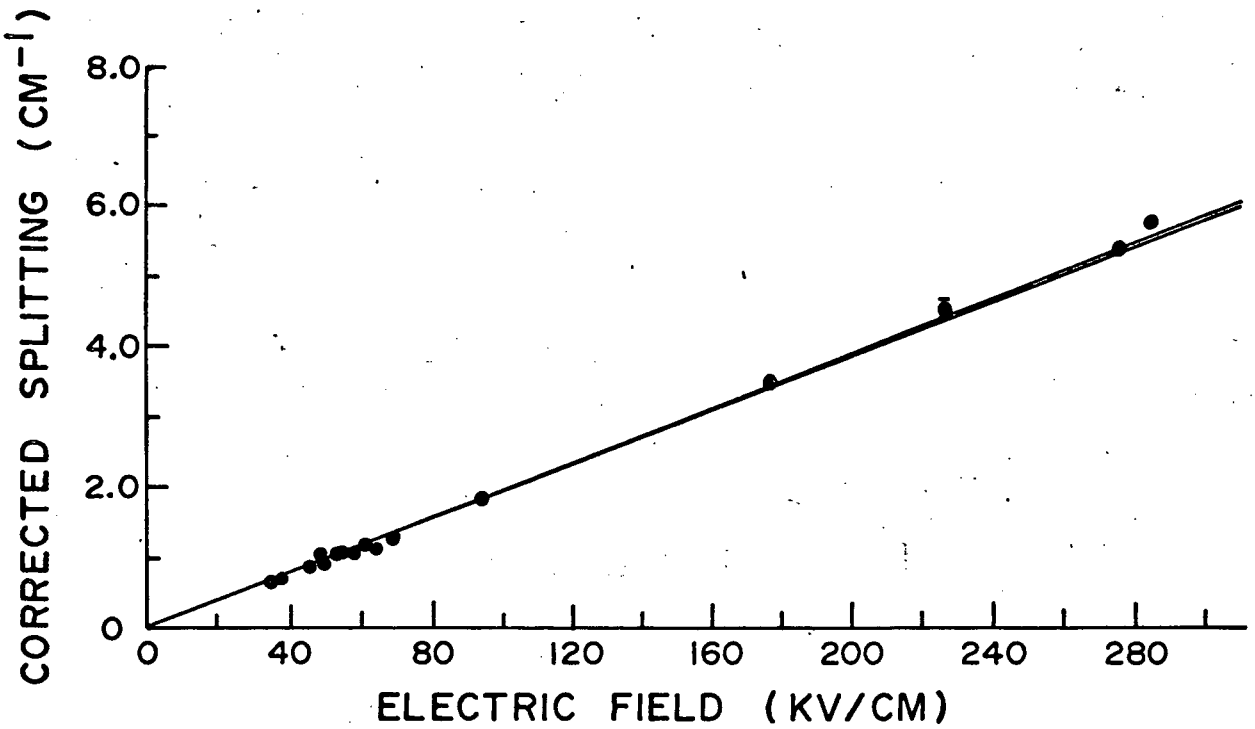

FIG. 17, S' vs. E for OH, v = 0.

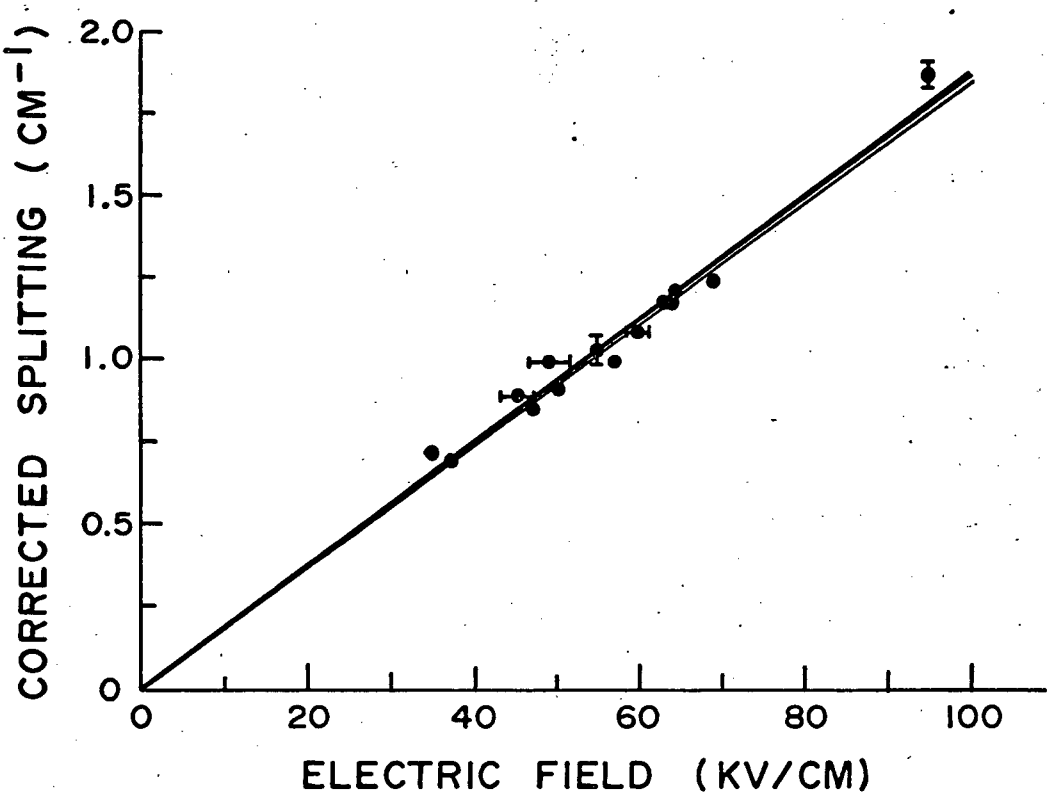

FIG. 18, S' vs. E for OH, v = 1

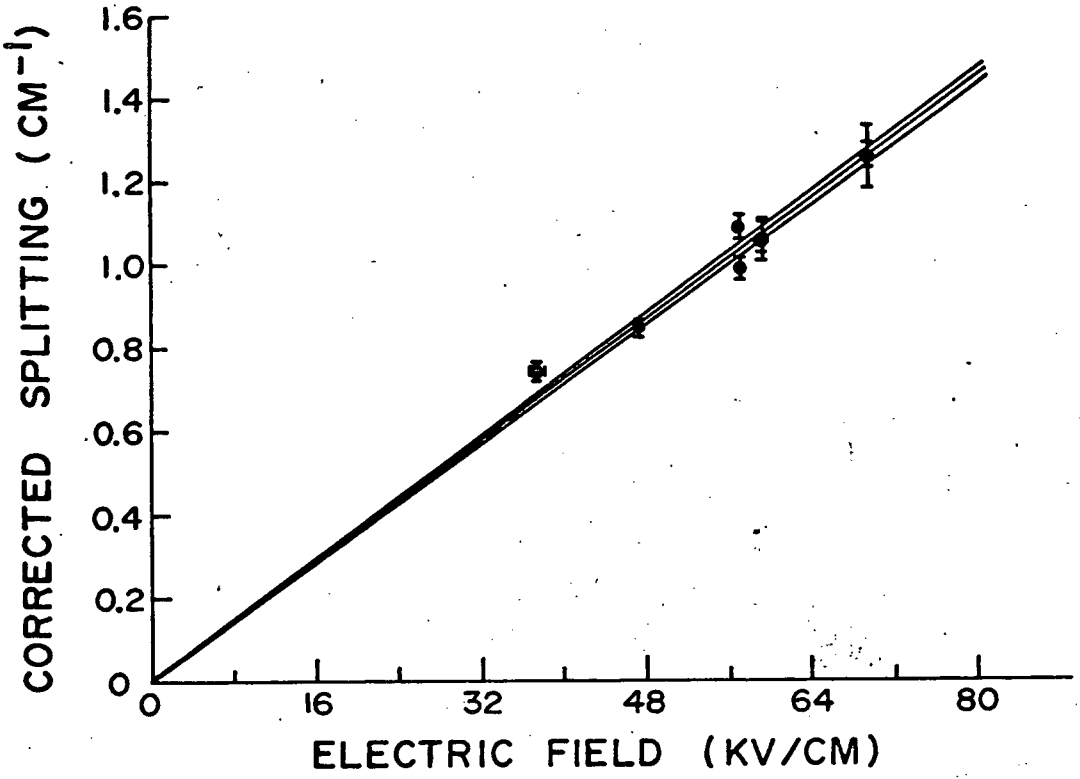

FIG. 19, S' vs. E for OH, v = 2

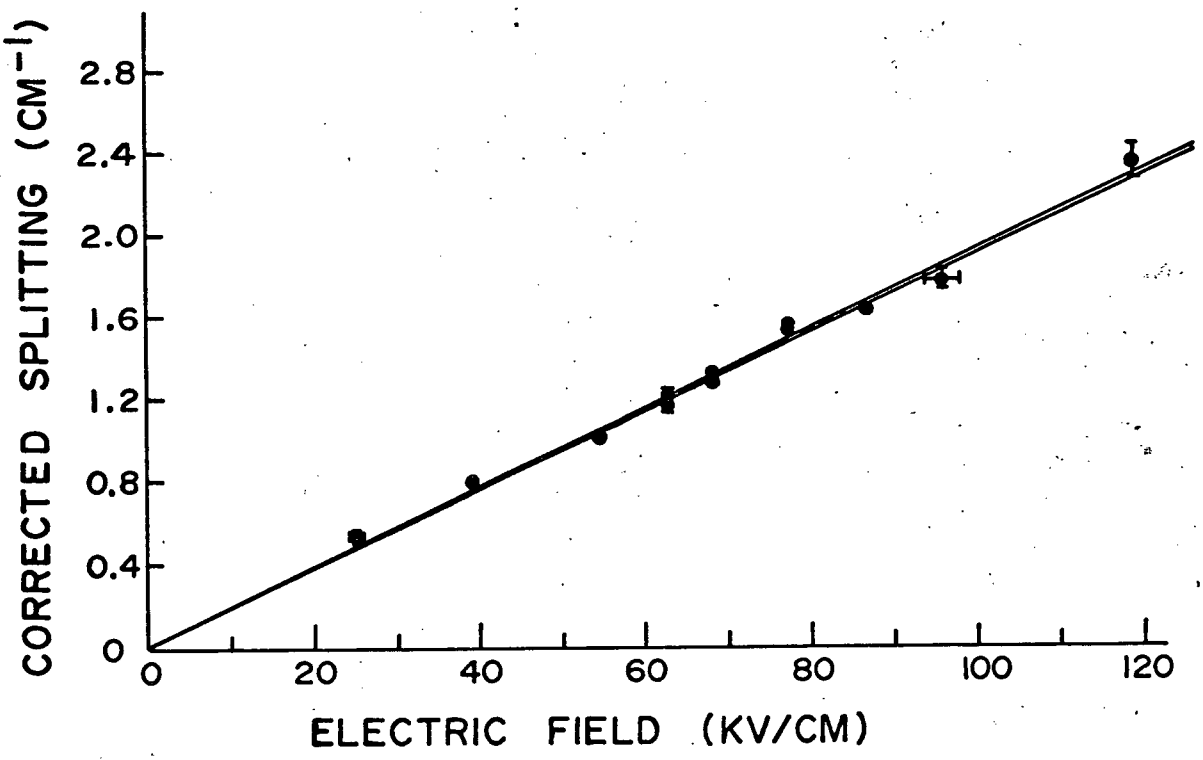

FIG. 20, S' vs. E for OD, v = 0.

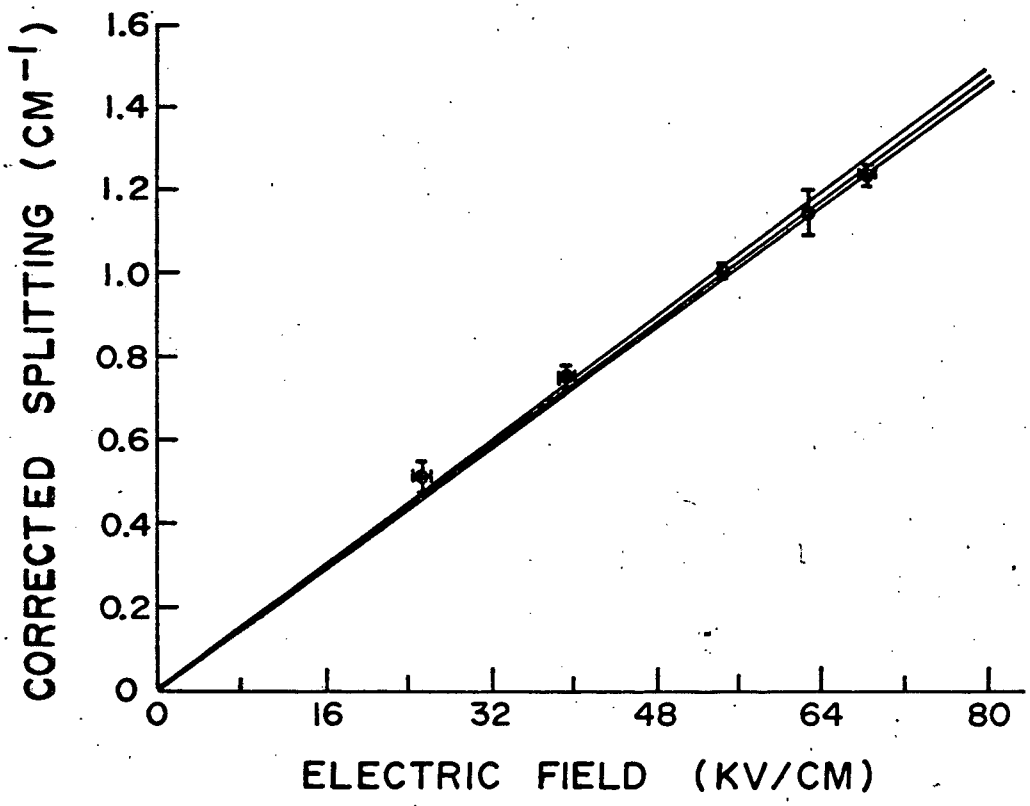

FIG. 21, S' vs E for OD, v = 1.

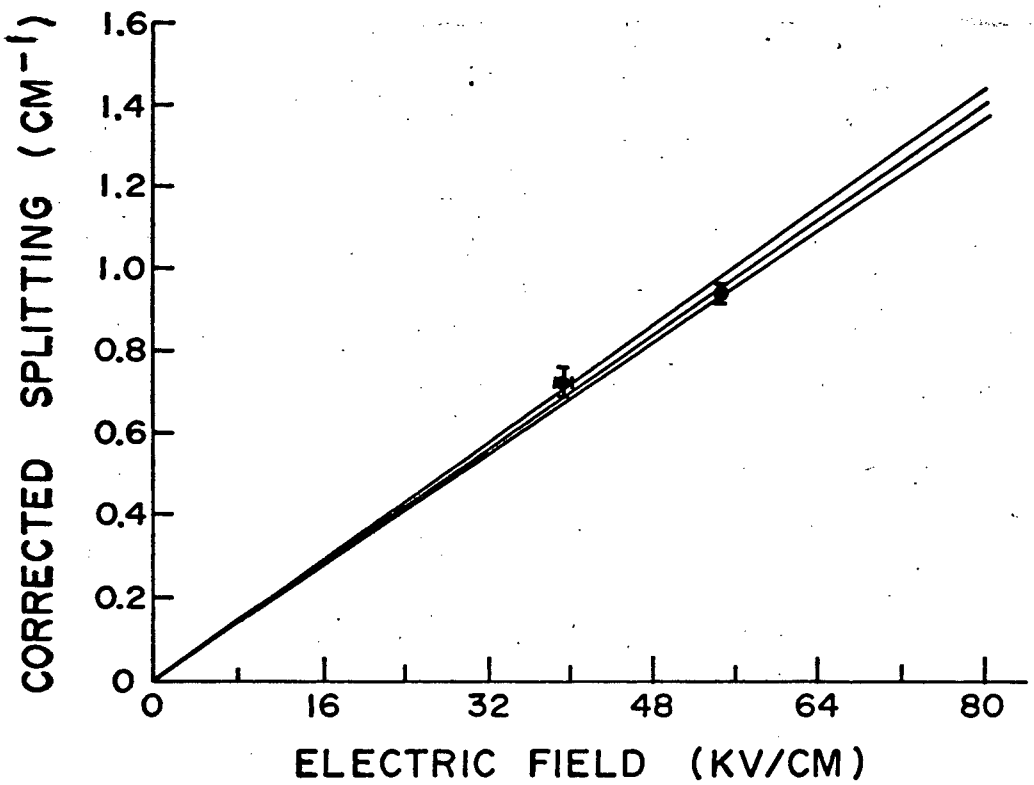

FIG. 22, S' vs. E for OD, v = 2.

quantity k here represents a correction to the matrix element $\frac{5}{3}$ due to the deviation of the coupling scheme from pure case (a). This effect was not considered (k=1) in the results presented below. Since the data from the $Q_1(1)$, v=2, fell right inbetween the data from the $P_{12}(1)$ and $Q_2(1)$ lines, the inclusion of these points from plates 140α and 140γ had the effect of more heavily weighting the two highest field points in the slope-fitting (Fig.19). Taking $Y = -8.15$ (Lee, Tam, Larouche, and Woonton[95]) for v=2, and using Eqs. (82) and (89), we get $k = 0.98$, which is essentially the same as the value of Phelps and Dalby[8] (v=0). Thus it is clear that the dipole moment derived from the $Q_1(1)$ line is about two percent lower than $J=\frac{1}{2}$ results. Since this is the same order of magnitude as the assigned tolerances, it is doubtful that this represents a significant difference.

3. The Results

Tables I through VI give the data used in obtaining the resulting dipole moments. In the first column, "R2" means the $R_2(1)$ line, etc. Those lines marked with an asterisk (*) for v=0 and 1 of OH were taken from the data of Phelps[14] (p.80, also Phelps and Dalby[8]), and the associated plate designations are also his. S is the splitting of the line in cm^{-1}, and S' is the "corrected splitting" (the square root in Eq. (121)) in cm^{-1}. E is the electric field in kV/cm. ΔS' and ΔE are the

TABLE V

Splittings and Fields Used for Calculating the Dipole Moment of the $^2\Pi$ State in OH for v= 0

Line	Plate	S	S'	ΔS'	E	ΔE
R2*	E-27L*	0.675	0.656	0.020	34.90	0.80
P12	141γ	0.725	0.708	0.017	37.36	0.75
R2	141γ	0.698	0.680	0.017	37.36	0.75
P12	137α	0.893	0.879	0.020	45.35	2.00
R2	137α	0.885	0.871	0.043	45.35	2.00
P12	139δ	0.860	0.845	0.020	46.18	0.20
R2	139δ	0.869	0.855	0.042	46.18	0.20
Q2	139δ	0.870	0.856	0.020	46.18	0.20
P12	141β	0.923	0.909	0.031	47.23	0.30
R2	141β	0.878	0.864	0.016	47.23	0.30
R2*	E-22*	1.043	1.031	0.010	49.20	2.40
P12	145β	0.961	0.948	0.008	50.14	0.50
R2	145β	0.954	0.941	0.022	50.14	0.50
R2*	6/23/63*	1.052	1.040	0.020	52.90	0.50
R2*	E-27U*	1.093	1.082	0.010	54.80	0.50
P12	137γ	1.071	1.059	0.026	54.87	0.50
R2	137γ	1.041	1.029	0.016	54.87	0.50
P12	141α	1.067	1.055	0.030	56.87	0.50
R2	141α	1.066	1.054	0.018	56.87	0.50
P12	139γ	1.125	1.114	0.013	59.06	0.60
R2	139γ	1.111	1.100	0.013	59.06	0.60
R2*	6/25/63*	1.156	1.145	0.010	59.90	1.30
R2*	F-10*	1.202	1.192	0.010	63.10	1.00
P12	143α	1.179	1.168	0.034	64.45	0.40
R2	143α	1.158	1.147	0.026	64.45	0.40
P12	139α	1.285	1.275	0.021	69.11	0.80
R2	139α	1.283	1.273	0.021	69.11	0.80
P12	137β	1.284	1.274	0.019	69.25	0.50
R2	137β	1.302	1.292	0.024	69.25	0.50
R2	1	1.861	1.854	0.022	95.10	0.40
R2	53β	3.500	3.496	0.066	176.70	0.70
P12	55	4.494	4.491	0.095	226.90	0.50
R2	55	4.514	4.511	0.125	226.90	0.50
P12	45	5.407	5.405	0.066	276.70	2.80
R2	59β	5.750	5.748	0.081	285.10	1.80

*Data from Phelps (see text).

TABLE VI

Data for Calculating the $^2\Pi$ Dipole Moment in OH
v = 1

Line	Plate	S	S'	ΔS'	E	ΔE
P12*	E-27L*	0.729	0.712	0.020	34.90	0.80
P12	142γ'	0.705	0.687	0.019	37.36	0.70
P12	138α	0.901	0.888	0.021	45.35	2.00
P12	142β	0.870	0.856	0.023	47.23	0.30
P12*	E-22*	1.003	0.990	0.010	49.20	2.40
P12	145β	0.928	0.914	0.019	50.14	0.50
P12*	E-27U*	1.040	1.028	0.010	54.80	0.50
P12	138γ'	1.039	1.027	0.045	54.87	0.50
P12	142α	1.003	0.990	0.012	56.87	0.50
P12	140γ'	1.103	1.092	0.020	59.06	0.60
P12*	6/25/63*	1.094	1.083	0.010	59.90	1.30
P12*	F-10*	1.181	1.170	0.010	63.10	1.00
P12	143α	1.210	1.200	0.030	64.45	0.40
P12	140α	1.250	1.240	0.011	69.11	0.80
P12	1	1.870	1.863	0.040	95.10	0.40

*Data from Phelps (see text).

TABLE VII

Data for Calculating the $^2\Pi$ Dipole Moment in OH
v = 2

Line	Plate	S	S'	ΔS'	E	ΔE
P12	142γ'	0.764	0.747	0.023	37.36	0.75
P12	142β	0.868	0.854	0.021	47.23	0.30
P12	142α	1.010	0.998	0.027	56.87	0.50
Q2	142α	1.111	1.100	0.031	56.87	0.50
P12	140γ'	1.071	1.061	0.019	59.06	0.60
Q2	140γ'	1.088	1.079	0.041	59.06	0.60
Q1	140γ'	1.912*	1.062	0.048	59.06	0.60
P12	140α	1.282	1.272	0.029	69.11	0.80
Q2	140α	1.276	1.266	0.076	69.11	0.80
Q1	140α	2.288*	1.271	0.030	69.11	0.80

*See text with regard to the $Q_1(1)$ line.

TABLE VIII

Data for Calculating the $^2\Pi$ Dipole Moment in OD
v = 0

Line	Plate	S	S'	S'	E	E
R2	127β	0.537	0.527	0.034	25.35	0.90
P12	132α	0.790	0.783	0.025	39.34	0.80
P12	127α	1.002	0.997	0.014	54.49	0.50
Q2	127α	1.021	1.016	0.017	54.49	0.50
R2	127α	1.023	1.018	0.022	54.49	0.50
P12	134γ	1.216	1.212	0.013	62.84	0.50
Q2	134γ	1.159	1.154	0.033	62.84	0.50
R2	134γ	1.218	1.214	0.028	62.84	0.50
P12	125β	1.317	1.313	0.012	68.39	0.70
Q2	125β	1.277	1.273	0.018	68.39	0.70
R2	125β	1.295	1.291	0.043	68.39	0.70
P12	135γ	1.543	1.540	0.038	77.40	0.50
Q2	135γ	1.518	1.514	0.042	77.40	0.50
P12	127γ	1.629	1.626	0.020	86.95	0.40
Q2	127γ	1.631	1.628	0.034	86.95	0.40
Q2	134β	1.770	1.767	0.050	96.00	2.30
Q2	125α	2.341	2.339	0.081	118.95	0.80

TABLE IX

Data for Calculating the $^2\Pi$ Dipole Moment of OD
v = 1

Line	Plate	S	S'	ΔS'	E	ΔE
P12	127β	0.522	0.512	0.037	25.35	0.90
P12	132α	0.758	0.751	0.026	39.34	0.80
P12	127α	1.013	1.008	0.019	54.49	0.50
P12	134γ	1.152	1.147	0.052	62.84	0.50
P12	125β	1.234	1.236	0.026	68.39	0.70

L

TABLE X

Data for Calculating the $^2\Pi$ State Dipole Moment in OD, v = 2

Line	Plate	S	S'	ΔS'	E	ΔE
P12	132∝	0.729	0.722	0.036	39.34	0.80
P12	127∝	0.947	0.941	0.023	54.49	0.50

TABLE XI

Experimental Values of the Dipole Moment in the $^2\Pi$ State

Molecule	v	μ(D)	Δμ(D)	Source
OH	0	1.70_9	0.02_9	This work
	0	1.72^9	0.02^9	Phelps and Dalby[8]
	0	1.66^0	0.01^0	Powell and Lide[98] ($J=\frac{?}{2}, \Omega=\frac{3}{2}$)
	1	1.64_6	0.05_1	This work
	1	1.65^6	0.04^1	Phelps and Dalby[8]
	2	1.62^6	0.04_5	This work
OD	0	1.68_4	0.03_2	This work
	1	1.63^5	0.02^3	This work
	2	1.55_1	0.06^3_1	This work

errors associated with S' and E. We derived $\Delta S'$ from a standard deviation over several (usually about six) different measurements of the same two components, while the ΔE comes from the standard deviation over the different components of the Balmer line which were averaged to obtain E. In the v=1 bands of both OH and OD, overlapping of the $R_2(1)$ and $Q_2(1)$ lines impaired their usefulness. In OD with v=2, it was thought best to eliminate a number of doubtful measurements (these lines were usually just barely visible), even though this reduced the usable data to two points. The listed values of E have not been corrected in accordance with the tables given in Chap.VII. However, the resulting values of μ given in Table XI (including those from Phelps and Dalby) have been reduced by the prescribed 0.67% (after the calculation by the least squares fit). The results given in Table XI are illustrated in Fig.23. It may be noted that the self-consistent field (SCF) calculations of Cade and Huo[84] give a value of 1.78 D, which is about as far above our result for OH (v=0) as the measurements of Powell and Lide[98] (on the $^2\Pi_{\frac{3}{2}}$, $J=\frac{7}{2}$ level) and the configuration interaction (CI) calculations of Bender and Davidson[85] lie below.

Cade[99] gives a graph (his Fig. 7a) showing calculated dependence of the dipole moment upon the internuclear distance. Measurements from this graph give the dependence as

155

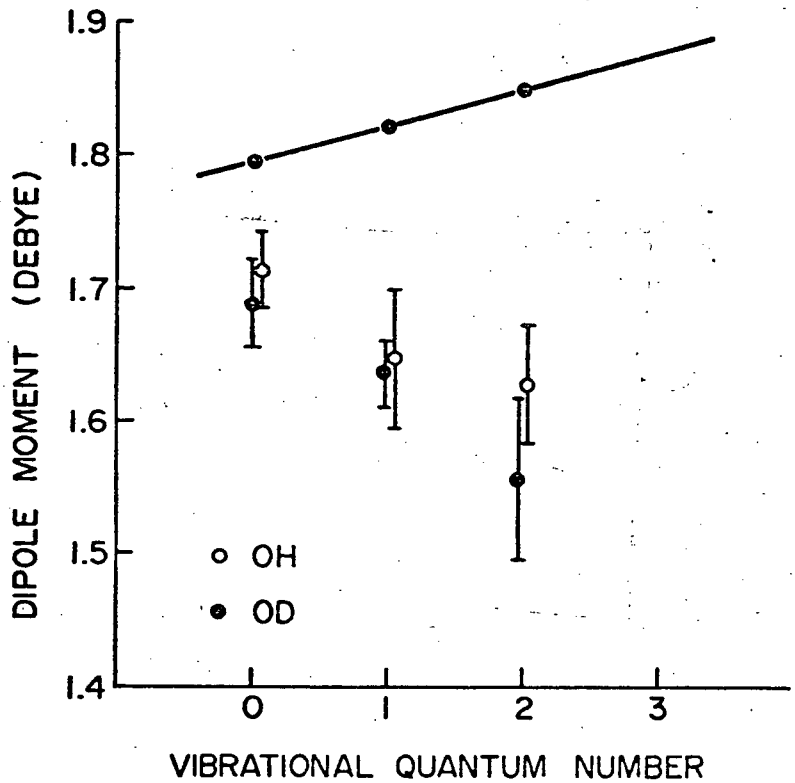

FIG. 23 Dipole moments of OH and OD as a function of v. The points joined by the solid curve are based on the calculations of Cade (1967).

$$\mu = 1.7803 + 0.8940(r - r_e) - 0.22137(r - r_e)^2 \qquad (123)$$

where μ is in debyes and the internuclear distance r (and its equilibrium value r_e) are in Angstroms. Taking the matrix elements of Eq. (123) (see Phelps and Dalby[8], Scarl and Dalby[77]) for the desired values of v, we obtain the corresponding curve for μ as a function of v, shown as the smooth curve in Fig. 23. It is noted that this function appears to be in decided disagreement with our results, both in magnitude and slope. Cade[100] has commented that this disagreement is "not surprising", in view of certain difficulties encountered in his calculations.

The implications of our measured values of $\partial\mu/\partial v$ upon the vibrational transition probability in the $^2\Pi$ state are discussed in Scarl and Dalby[77].

CHAPTER IX

THE A $^2\Sigma^+$ STATES OF OH AND OD

1. Introduction

The ability to photograph spectra of OH and OD at high dispersion in fields in excess of 200,000 V/cm has enabled us to measure second order Stark effects. A part of the second order effect is due to the $^2\Sigma^+$ upper state of the 3064 Å bands, and evaluating this contribution will allow us to calculate the dipole moment of this state.

In discussing the method by which this is done, the following nomenclature is adopted:

C = the undeviated (zero-field) line position (in cm^{-1}).

U = the position of the higher frequency component.

L = the position of the lower frequency component.

x = U + L - 2C, called the asymmetry (note that this is $|U - C| - |L - C|$).

y = $(U - L)^2$, in cm^{-2}, called the splitting squared.

The $P_{12}(1)$ line has distinct advantages over any other, in that the upper state has a large second order shift without splitting and is uncomplicated by spin interactions. The only other lines coming from this upper state are the $O_{12}(1)$ and $P_1(1)$, both of which have lower states split into four (rather than just two) components. Moreover the O_{12} branch is quite weak and the $P_1(1)$ suffers from

overlap, so the $P_{12}(1)$ has been used exclusively for this study.

For this line, according to Eq. (45), the first order effect in the Λ-doublets of the $^2\Pi$ state is given by

$$W_{\Pi}^{(1)} = \pm(V^2 + \delta^2)^{\frac{1}{2}} = \pm(\varepsilon_{\Pi}^2/9 + \delta^2)^{\frac{1}{2}} \quad . \tag{124}$$

Since second order terms do not affect the splitting (see Fig. 24), we may also write

$$|W_{\Pi}^{(1)}| = (U - L)/2 = y^{\frac{1}{2}}/2 \quad . \tag{125}$$

For the $P_{12}(1)$ line, the second order effects are given by

$$W_{\Pi} = - \frac{2\varepsilon^2}{27B_{\Pi}} \tag{126}$$

and

$$W_{\Sigma} = - \frac{\varepsilon^2}{6B_{\Sigma}} \tag{127}$$

where the energy levels have been assumed to be given by $B_{\Pi}\ J(J+1)$ and $B_{\Sigma}\ N(N+1)$ respectively. Corrections to Eq. (126) due to intermediate coupling are considered in Sec. 5.

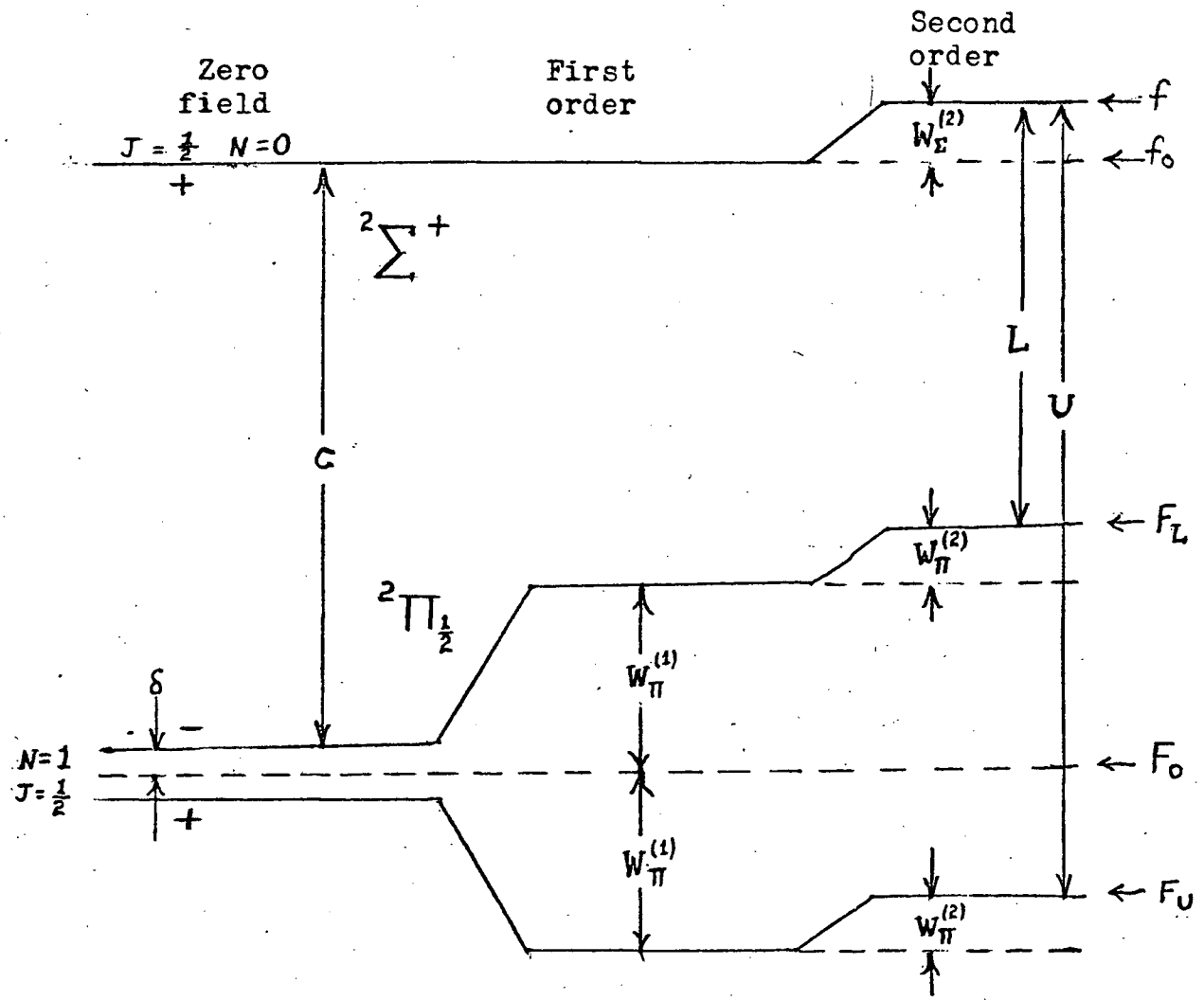

Fig. 24

Schematic diagram of Stark effects in a transition between sublevels of a $^2\Sigma^+ \rightarrow {}^2\Pi$ band. First and second order effects are shown separately for clarity. The parities are shown as they exist in the Π state of OH. The signs of the second order terms are defined positive as shown.

Allowing for the fact that Eq. (124) defines the zero of energy to lie midway between the Λ-doublets in the $J_\Pi = \frac{1}{2}$ level, we can express $W_\Sigma^{(2)}$ in terms of the component positions by

$$\begin{aligned} W_\Sigma^{(2)} &= \tfrac{1}{2}(U + L - 2C - 2p\delta + 2\, W_\Pi^{(2)}) \\ &= x/2 - p\delta + W_\Pi^{(2)} \ . \end{aligned} \tag{128}$$

The preceding equations lead to a "linear" relationship between the splitting squared and the asymmetry:

$$y = kx - 2k\delta + 4\delta^2 \ , \tag{129}$$

where

$$k = \tfrac{4}{9}[(\mu_\Sigma/\mu_\Pi)^2/3B_\Sigma - 4/(27B_\Pi)]^{-1} \tag{130}$$

In Eqs. (129) and (130) we have a linear equation which may be fitted to measured data to yield (the absolute value of) the ratio μ_Σ/μ_Π, independently of any external measurement of electric fields.

2. Measurement of the Line and Slope Fitting

The measurements were done in the manner described in Chap. VII, with the plate aligned so that spectral lines not shifted by the field (e.g., high-J lines) remained centered in the cross-hairs while the plate was moved vertically. Then, starting in a region of fairly low field (at a vertical position where the two Stark components

of the $P_{12}(1)$ line were just resolvable), the position of the upper and lower components (U and L) were measured alternately several times (usually four times each, but in some cases many more). The plate was then moved vertically to a higher field region by 0.2 mm, and this process repeated into the region of maximum field.

The position of the line at zero field (C) was measured directly at the line top, and the dispersion of the spectrum was calibrated by the measurement of several high-J lines at both zero-field and maximum field.

These measurements were averaged for each component and level by the WNINT computer program (see Chap VII) which punched out cards bearing the averages and their standard deviations. These were then processed (see also Sec. 4 below) by a rather complex program called QUAFF which formed the variables x and y from the data (see Sec. 3) and fitted them with a straight line by a least-squares computer library routine (LQF). This program assigned weights to the points, defined inversely proportional to the standard errors in x and/or y, but limiting a single weight to be no larger than the mean weight than (arbitrarily) $\frac{3}{2}$ of the standard deviation taken over all weights. A subroutine of QUAFF (called PLT) was capable of graphing the data and fitted lines in a variety of ways, drawing the graphs of Figs.28 -30. (A modification of QUAFF was used to fit and graph the data of Chap.VIII for the $^2\Pi$ states of OH and OD.)

A system of weighting more heavily points in the higher field region according to some power of y was tried, but rejected. A number of points were rejected intuitively in the low field region (where the asymmetry is intrinsically inaccurate). Points were omitted which seemed to have undue influence on the slope, while at higher fields they were eliminated where there existed reason to believe them in error based on the appearance of the line at that level.

Figs. 25 through 27 show all photographs used in this study except two of those from the (1,1) band of OH. While it may be seen that overlapping is a problem at some level of almost every picture, it is an advantage of this method that such points may be dropped readily from the calculation.

3. The Zero-Field Position

There are a number of different ways of obtaining the position (C) of the undeviated line. The measured line top may be referenced to the standard lines as measured at either the top or bottom of the spectrum. Alternatively, one may use the value given in the same source literature as the wavelength standards. All such different values are in agreement to within $0.13\ cm^{-1}$, but even so the choice will affect the results. Since x is a linear function of C, and y does not depend upon C at all, a wrong choice of C will not affect the slope of the fitted line (and thus the derived μ_Σ/μ_Π), but will merely shift all points horizontally together.

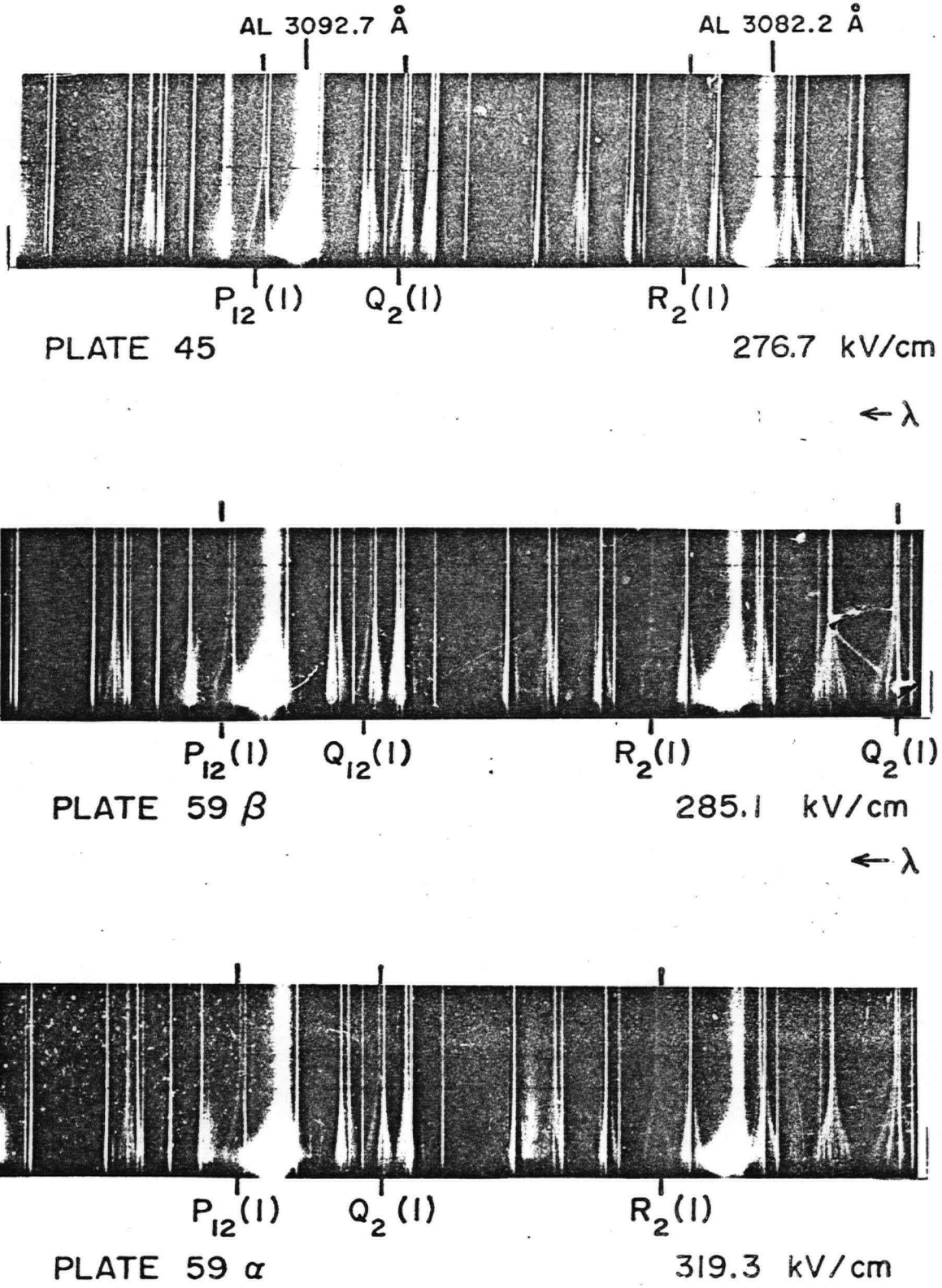

Fig. 25

The (0,0) A → X band of OH at high field.

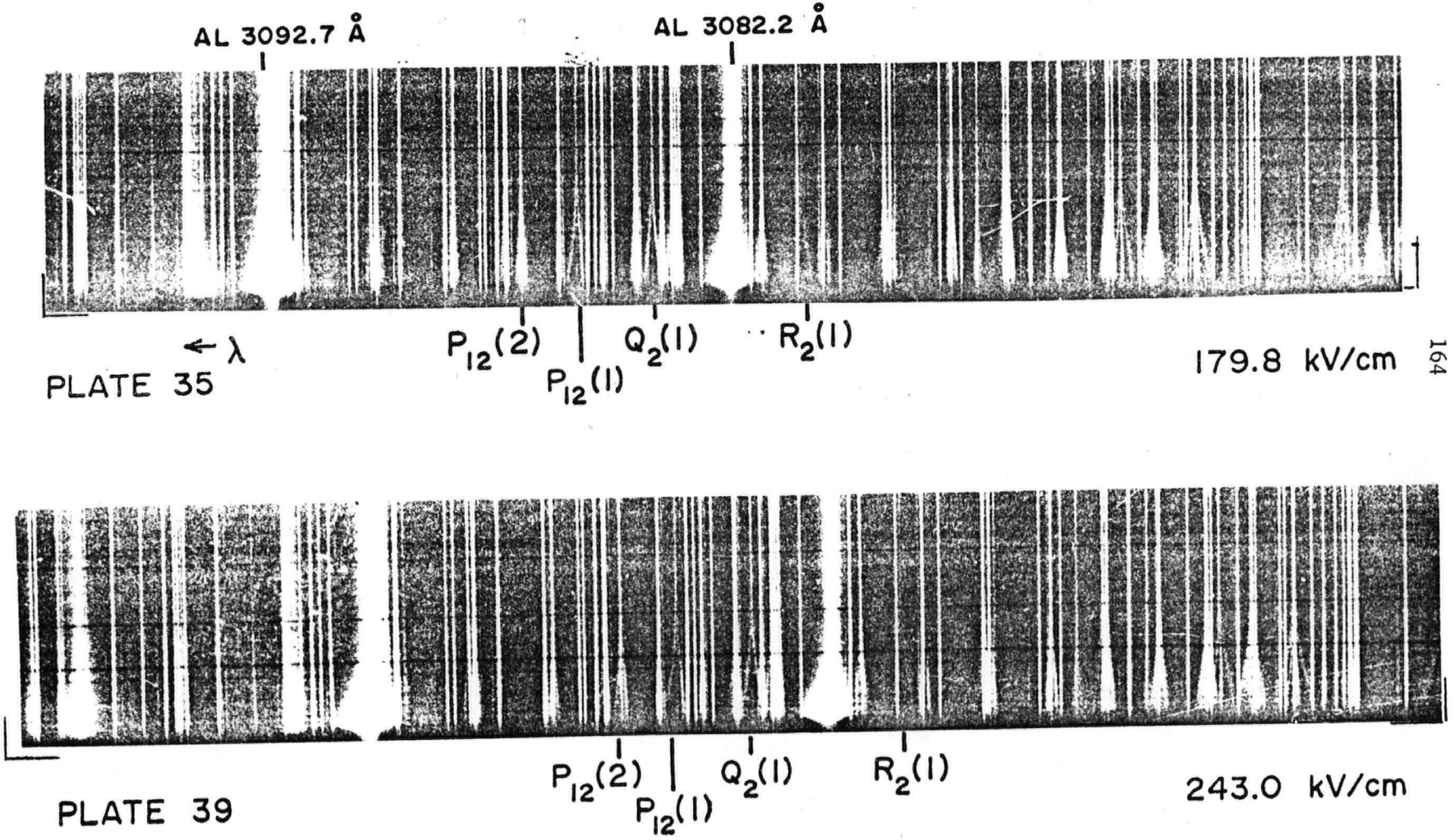

Fig. 26

The (0,0) A → X band of OD at high field

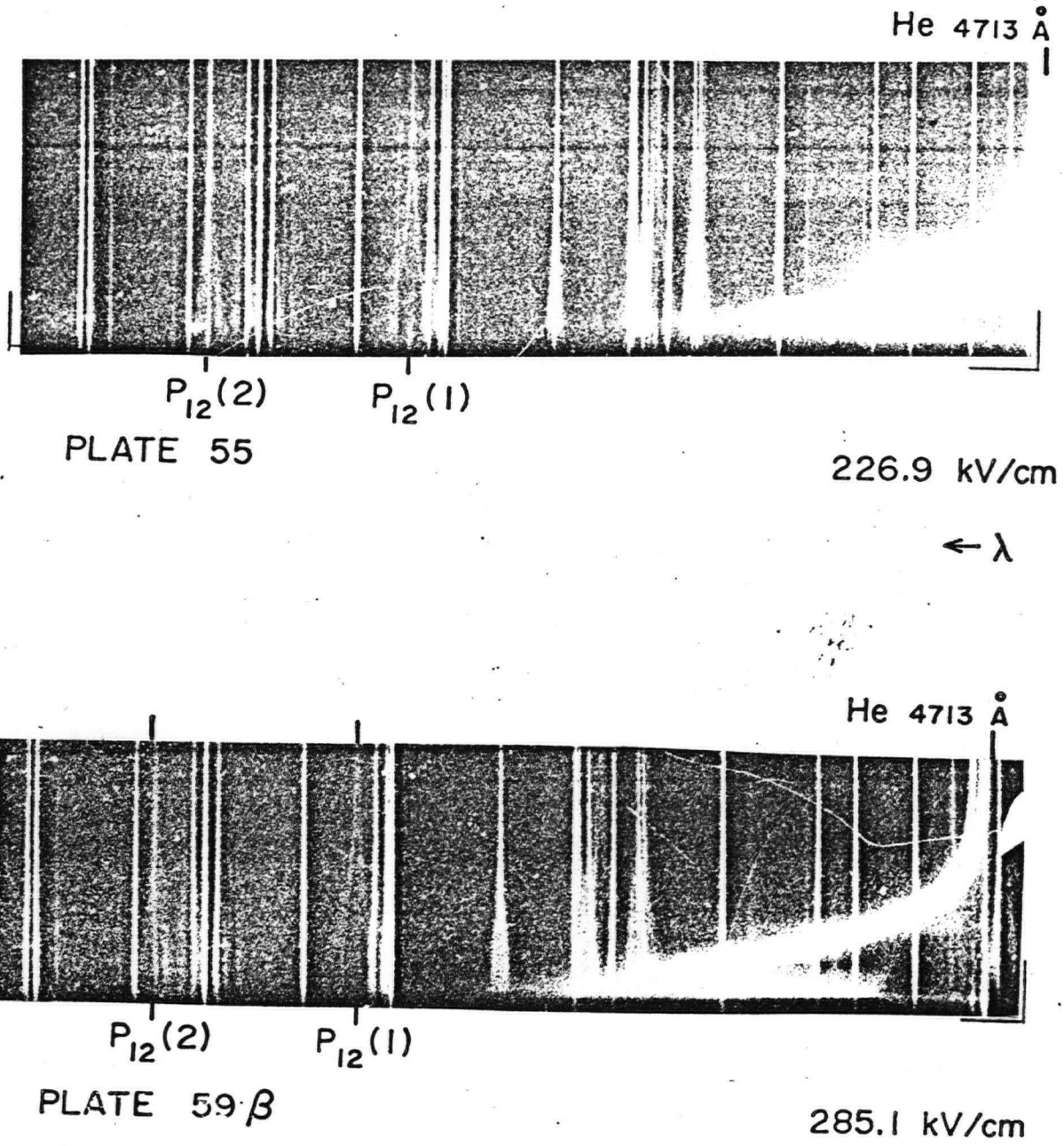

Fig. 27

The (1,1) A → X band of OH at high field.

Thus, for any single line, μ_Σ/μ_Π can be obtained independently of C as well as E. If measurements from more than one photograph are to be superimposed on the same graph, however, an inconsistency in the measurement of C from one plate to another can affect the resultant best fit slope.

We have chosen to treat C as a free parameter (for each photograph) which may be adjusted to bring the points from different photographs together. These adjustments are listed in Table XII by the heading "Relative Adjustment in C". They are all less than $0.15\ cm^{-1}$, corresponding to about 20 microns on the plate (less than half a linewidth), but may affect results by as much as 2 percent. Now, since the slope k is of the order of $-10\ cm^{-1}$ in OD, and the order of $-24\ cm^{-1}$ in OH, and δ is of the order of $0.06\ cm^{-1}$, the term $4\delta^2$ in Eq. (129) is negligible compared to the $2k\delta$ term. Thus the graph of Eq. (129) should cross the x axis near $x=2\delta$. The change in C required to ensure that this actually happens is given in Table XII under the heading "Absolute Adjustment to C". The actual values of C thus obtained are listed in the first data column of Table XIII. The fact that these values are all positive (while still less than a linewidth) indicates that there may be a small systematic error in the vertical alignment process. It may also be noted that adding these increments to C tended to cause the asymmetries associated with a number of the low field points to become negative, where they had previously been positive (by our definitions,

TABLE XII

Corrections to the Zero-Field Positions

of the $P_{12}(1)$

Band	Position from the Literature (cm^{-1})	Run	Relative Adjustment in C (cm^{-1})	Absolute Adjustment in C (cm^{-1})
OH (0,0)	32314.19 (Dieke and Crosswhite[88])	59β	0.000	0.080
		45	-0.014	0.066
		59α	0.130	0.210
OD (0,0)	32397.83 (Ishaq[90])	39	0.000	0.127
		35	0.045	0.172
OH (1,1)	31733.71 (Dieke and Crosswhite[88])	59β	0.000	0.021
		53β	0.145	0.166
		59α	0.133	0.154
		55	0.050	0.071

TABLE XIII

Data for μ_Σ/μ_Π: Adjusted Absolute C and Mean Measured Values of U and L, with Errors.

Band	Run	Level Label	Components in cm^{-1} C	ΔC	U	ΔU	L	ΔL
OH (0,0)	59β	3	32314.132	.025	32314.895	.058	32313.456	.011
		4			14.974	.015	13.308	.061
		5			15.206	.024	13.128	.009
		6			15.276	.006	13.011	.023
		7			15.344	.021	12.805	.039
		8			15.441	.060	12.455	.038
		9			15.741	.035	12.115	.096
		0			15.997	.094	11.700	.063
		B			16.352	.048	10.850	.092
		C			16.419	.038	10.647	.126
		D			16.518	.020	10.552	.080
	45	5	32314.118	.030	32315.202	.003	32313.316	.053
		6			15.277	.006	13.197	.039
		7			15.315	.006	13.009	.032
		8			15.438	.008	12.657	.015
		9			15.707	.039	12.299	.022
		0			15.939	.050	11.979	.039
		A			16.162	.033	11.651	.005
		B			16.219	.022	11.390	.030
		C			16.334	.027	11.108	.046
		D			16.433	.016	10.876	.026
	59α	3	32314.262	.027	32315.148	.040	32313.411	.037
		4			15.209	.073	13.172	.009
		5			15.343	.018	12.984	.054
		6			15.397	.046	12.836	.054
		7			15.662	.079	12.377	.035
		8			15.955	.003	12.111	.021
		9			16.380	.017	11.575	.089
		0			16.487	.029	11.170	.140
		A			16.666	.028	10.641	.075
		D			16.626	.054	10.529	.054

TABLE XIII (cont'd)

Band	Run	Level Label	Components in cm^{-1} C	ΔC	U	ΔU	L	ΔL
OD (0,0)	39	3	32397.914	.031	32398.657	.040	32397.033	.033
		4			98.730	.056	96.893	.048
		5			98.870	.042	96.513	.071
		6			98.926	.067	96.357	.110
		7			98.994	.027	96.026	.062
		8			99.042	.036	95.736	.049
		9			99.152	.055	95.466	.087
		0			99.180	.070	94.958	.090
		D			99.305	.078	94.700	.046
	35	5	32397.956	.023	32398.680	.024	32396.750	.062
		6			98.794	.014	96.667	.022
		7			98.930	.037	96.453	.016
		8			98.969	.006	96.225	.021
		9			99.009	.010	95.916	.023
		0			99.039	.013	95.748	.020
		A			99.114	.024	95.608	.035
		D			99.208	.029	95.553	.109
OH (1,1)	53β	1	31733.765	.043	31734.235	.040	31733.380	.016
		2			34.310	.040	33.340	.023
		3			34.404	.040	33.140	.028
		4			34.407	.028	32.915	.017
		5			34.536	.045	32.856	.008
		6			34.775	.039	32.703	.027
		7			34.942	.017	32.465	.044
		8			35.004	.023	32.187	.031
		9			35.044	.010	31.995	.009
		0			35.043	.046	31.884	.027
		D			35.162	.037	31.769	.036
	55	2	31733.813	.058	31734.399	.022	31733.327	.045
		3			34.484	.048	33.218	.029
		4			34.455	.036	33.126	.019
		5			34.648	.061	33.020	.038
		6			34.877	.025	32.619	.049
		7			34.932	.012	32.300	.075
		8			35.140	.048	32.086	.047
	59α	5	31733.742	.034	31734.859	.017	31732.377	.003
		6			35.029	.007	32.123	.066
		7			35.084	.028	31.853	.010
		8			35.345	.059	31.558	.097
		9			35.466	.243	30.916	.045

TABLE XIII(cont'd)

Band	Run	Level Label	Components in cm^{-1} C	ΔC	U	L
OH	598*	1	31733.766	.045	31734.184	31733.253
(1,1)		2			34.427	33.163
cont'd		3			34.552	33.073
		4			34.635	32.976.
		5			34.816	32.754
		6			35.017	32.386
		7			35.031	32.066
		8			35.385	31.802
		9			35.732	31.421

*see footnote, Table XIV

the asymmetry of the $P_{12}(1)$ line should always be negative).

This adjustment of C may be viewed as a "smoothing" of error in the single measurement of C, much as the slope-fitting process is a smoothing of errors in the multiply-measured U and L.

4. Higher Order Corrections

The effects of higher order terms were included. Expressions (33) and (35) were evaluated using the matrices of Eq. (18) and Eq. (59). The results for the $^2\Sigma$ state were in agreement with Eq. (36).

For the $^2\Pi$ state, in the approximation that (in the notation of Chap. IV) $b^2 \simeq 1$, $d^2 \simeq 0$, and $(\varepsilon \langle \psi_r | n_z | \psi_r \rangle / \delta)^2$ is large, the resulting expressions simplify to

$$W_\Pi \simeq \pm\tfrac{1}{3}\varepsilon_\Pi - \tfrac{2}{27}\frac{\varepsilon_\Pi^2}{B_\Pi} \mp \tfrac{8}{1215}(\varepsilon_\Pi^3/B_\Pi^2) + \tfrac{11}{21870}(\varepsilon_\Pi^4/B_\Pi^3). \quad (131)$$

No allowance for intermediate coupling has been made in the preceding formula (despite the erroneous use of "B_{eff}" in the denominators of these expressions in Scarl and Dalby[77]).

The dipole moment ratio μ_Σ/μ_Π was first calculated without any higher order corrections, as described in Sec. 2 above. The resulting value of μ_Σ was used in Eq. (36) and the terms of higher than second order were calculated and subtracted from the observed positions of U and L. This

was in practice done by a small computer program called HIGH ORDERS which accepted the cards for input to QUAFF and repunched them with corrected U and L values. The corrected values were re-run by QUAFF. When the new value of μ_Σ was introduced into HIGH ORDERS, and the original wavenumbers reprocessed, no significant differences were found from the previous run, and so this data was not rerun through QUAFF. The accuracy of the data for OH, v=1, did not appear to justify such fine corrections, and none were made in this case.

5. Corrections for Intermediate Coupling

The value of W_Π should be corrected from its case (a) value of $2/27B_\Pi$ (Eq. 126) to account for the fact that coupling in the $^2\Pi$ state of OH and OD is intemediate between Hund's cases (a) and (b). While the $J=\frac{1}{2}$ level is pure case (a) and needs no correction in first order, the second order term requires correction in two ways: (1) the energy levels are no longer given by $BJ(J+1)$ so that the energy denominator ($3B_\Pi$) needs correction, and (2) since the two energy levels with $J=\frac{3}{2}$ have some mutual mixing in their wavefunctions, the matrix elements appearing in Eq. (59) require correction.

According to Eq. (81), in an inverted state the wavefunctions $\psi_{\Omega J}$ are given by

$$\psi_{\frac{3}{2}\frac{3}{2}} = c_1|\tfrac{1}{2}> + c_2|\tfrac{3}{2}>$$
$$\psi_{\frac{1}{2}\frac{3}{2}} = c_1|\tfrac{3}{2}> - c_2|\tfrac{1}{2}> \quad , \tag{132}$$

where the fractions refer to Ω, the kets indicate case (a), $J=\frac{3}{2}$ wavefunctions, and c_1 and c_2 are given by Eq. (82). By the methods illustrated in Chap. V, it readily follows that

$$< \psi_{\frac{1}{2}\frac{1}{2}}|n_z|\psi_{\frac{3}{2}\frac{3}{2}} > = c_1 < \tfrac{1}{2}\tfrac{1}{2}|n_z|\tfrac{1}{2}\tfrac{3}{2} > = \sqrt{2}c_1/3 \quad ,$$

and (133)

$$< \psi_{\frac{1}{2}\frac{1}{2}}|n_z|\psi_{\frac{1}{2}\frac{3}{2}} > = -c_2 < \tfrac{1}{2}\tfrac{1}{2}|n_z|\tfrac{1}{2}\tfrac{3}{2} > = -\sqrt{2}c_2/3 \quad .$$

We therefore have

$$W_{\Pi} = \left[\frac{\frac{2}{9}c_2^2}{F_{\frac{1}{2}\frac{1}{2}} - F_{\frac{1}{2}\frac{3}{2}}} + \frac{\frac{2}{9}c_1^2}{F_{\frac{1}{2}\frac{1}{2}} - F_{\frac{3}{2}\frac{3}{2}}} \right] \epsilon_{\Pi}^2 \quad . \tag{134}$$

The value of Y was taken to be -7.501 in OH (v=0), -7.800 in OH (v=1) (from Lee, Tam, Larouche, and Woonton[95]), and -13.954 in OD (Dousmanis, Sanders, and Townes[93]). From these one obtains c_1 and c_2 as follows:

	OH (0,0)	OD (0,0)	OH (1,1)
c_1^2 =	0.03025	0.01138	0.02858

(135a)

	OH (0,0)	OD (0,0)	OH (1,1)	
c_2^2 =	0.96975	0.98862	0.97142	. (135b)

The energy denominators in Eq. (134) were obtained directly for both OH cases by averaging (over the spin splitting and Λ-doublings) the differences between term values given by Dieke and Crosswhite[88](p.49f), giving

	v = 0	v = 1	
$F_{11}^{22} - F_{13}^{22}$ =	-61.31 cm^{-1}	-58.86 cm^{-1}	
$F_{11}^{22} - F_{33}^{22}$ =	126.26 cm^{-1}	126.785 cm^{-1}.	(136)

For OD, term values are not directly available, and the energy differences were found from the line identifications of Oura and Ninomiya[89] and Ishaq[90]. For the first difference In Eq. (136), $Q_2(2) - R_2(1) = -31.16$, $O_{12}(2) - P_{12}(1) = -30.81$, and $P_2(2) - Q_2(1) = -31.48$, from Oura and Ninomiya, giving an average of -31.15 cm^{-1}. Ishaq's data was judged less consistent here. The second difference in Eq. (136) was calculated from $P_1(1) - P_{12}(1)$, yielding an average of 130.70 cm^{-1} from the two sources.

In calculating for OH the $^2\Sigma$ state term differences were taken from Dieke and Crosswhite[88](p.47) (although negligible error results from the use of $2B_\Sigma$), giving -33.83 cm^{-1} for v=0, and -32.18 cm^{-1} for v=1. In OD, $2B_\Sigma$ was used with B_Σ = 9.037 cm^{-1} (Carlone and Dalby[101], p.1955). Spin splitting does not affect the N_Σ=0 level, since it is small compared to $2B_\Sigma$.

6. Results

Our experimental data has been summarized in Tables XIII and XIV. Solving Eq. (130) for μ_Σ/μ_Π:

$$\mu_\Sigma/\mu_\Pi = \sqrt{\tfrac{4}{3}B_\Sigma(1/k + 1/3B_\Pi)} \qquad (137)$$

This relation, operating on the slopes (k) in Table XV, does yield the results listed in that table as "μ_Σ/μ_Π, corrected". These results differ from those of Scarl and Dalby[77] because, in that paper, the matrix elements were not corrected for intermediate coupling. Those values listed as "μ_Σ/μ_Π, from QUAFF" include no correction for coupling, so that $U_\Pi = -2/27B_\Pi$, and $U_\Sigma = -1/6B_\Sigma$. The errors labeled "Statistical" come from the output of the least squares fit routine, while those labeled "Assigned" were obtained by inspection of the range of slope fit consistent with the graphs of Figs. 28 - 30. This data may be compared with the microwave measurement by Weinstock and Zare[102], using Stark effect level crossings, which yielded a considerably lower value (1.72±0.10 D) for the dipole moment of OD for v=0. SCF orbital calculations by Cade[100] give 2.04 D in OH (v=0). Weinstock and Zare[102] refer (their refs. nos. 17 and 25) to calculations by S. Green giving 1.96 D, and some other unpublished configuration interaction calculations by Mulder and Lester yielding 1.9 D, although the isotopes and vibrational states were not specified. While these calculations are in good agreement with results for OH

TABLE XIV

Data for μ_Σ/μ_Π: U and L as Corrected for High Order Terms, x and y as Used by QUAFF.

Band	Run	Level Label	U	L	x	Δx	y	Δy
OH	59β	3	32314.895	32313.456	0.247	.077	2.071	.170
(0,0)		4	14.974	13.308	0.180	.080	2.776	.209
		5	15.205	13.128	.231	.056	4.314	.106
		6	15.275	13.011	.184	.055	5.126	.108
		7	15.342	12.805	.045	.067	6.436	.225
		8	15.437	12.455	-.210	.087	8.892	.424
		9	15.734	12.114	-.254	.114	13.104	.740
		0	15.985	11.698	-.419	.124	18.378	.970
		B	16.327	10.843	-.932	.115	30.074	1.138
		C	16.386	10.638	-1.078	.141	33.039	1.513
		D	16.481	10.541	-1.080	.096	35.284	.980
	45	5	32315.201	32313.316	.309	.080	3.553	.200
		6	15.276	13.197	.270	.072	4.322	.164
		7	15.313	13.009	.119	.068	5.308	.150
		8	15.435	12.657	-.111	.062	7.717	.094
		9	15.702	12.299	-.202	.075	11.580	.305
		0	15.931	11.978	-.294	.080	15.626	.501
		A	16.150	11.649	-.404	.069	20.259	.300
		B	16.202	11.386	-.615	.071	23.194	.358
		C	16.212	11.102	-.789	.080	27.144	.556
		D	16.405	10.868	-.930	.067	30.658	.338
	59α	3	32315.148	32313.411	.162	.077	3.014	.189
		4	15.208	13.172	-.011	.091	4.145	.300
		5	15.342	12.984	-.065	.078	5.560	.268
		6	15.395	12.836	-.160	.089	6.548	.363
		7	15.658	12.377	-.356	.102	10.765	.567
		8	15.948	12.110	-.333	.058	14.730	.163
		9	16.364	11.572	-.455	.105	22.963	.868
		0	16.460	11.163	-.768	.153	28.058	1.515
		A	16.570	10.630	-1.191	.097	35.284	.951
		D	16.585	10.596	-1.290	.094	36.833	.927

TABLE XIV (cont'd)

Band	Run	Level Label	U	L	x	Δx	y	Δy
OD (0,0)	39	3	32398.655	32397.033	.120	.081	2.631	.168
		4	98.726	96.892	.056	.096	3.364	.271
		5	98.863	96.511	-.189	.103	5.532	.388
		6	98.915	96.354	-.294	.143	6.559	.660
		7	98.976	96.019	-.567	.092	8.744	.400
		8	99.014	95.725	-.824	.087	10.818	.400
		9	99.110	95.447	-1.006	.120	13.418	.754
		0	99.119	94.929	-1.515	.130	17,556	.955
		D	99.218	94.656	-1.688	.110	20.812	.826
	35	5	32398.676	32396.749	-.151	.081	3.713	.256
		6	98.788	96.666	-.116	.053	4.503	.111
		7	98.920	96.450	-.200	.061	6.101	.199
		8	98.955	96.220	-.395	.051	7.480	.119
		9	98.990	95.909	-.671	.052	9.493	.155
		0	99.013	95.738	-.819	.052	10.753	.156
		A	99.079	95.593	-.898	.063	12.152	.296
		D	99.169	95.536	-.865	.122	13.199	.820

TABLE XIV (cont'd)

Band	Run	Label Level	U	L	x	Δx	y	Δy
OH (1,1)	53β	1	(Same as Table II, no high order corrections applied)		.085	.096	.731	.074
		2			.111	.098	.924	.089
		3			.014	.099	1.598	.123
		4			-.208	.092	2.226	.098
		5			-.138	.097	2.822	.154
		6			-.052	.098	4.285	.196
		7			-.123	.098	6.126	.233
		8			-.339	.094	7.924	.217
		9			-.513	.087	9.030	.081
		0			-.602	.101	9.948	.336
		D			-.599	.100	11.472	.350
	55	2			.100	.126	1.149	.107
		3			.076	.129	1.603	.142
		4			-.045	.123	1.766	.108
		5			.042	.136	2.650	.234
		6			-.130	.128	5.090	.248
		7			-.394	.139	6.917	.400
		8			-.400	.134	9.303	.410
	59α	5			-.328	.070	6.150	.084
		6			-.412	.095	8.433	.385
		7			-.627	.074	10.414	.192
		8			-.660	.132	14.288	.858
		9			-1.181	.256	20.566	2.241
	59β*	1			-.181	.090	.867	.090
		2			-.028	.090	1.598	.090
		3			.007	.090	2.187	.090
		4			-.077	.090	2.752	.090
		5			-.048	.090	4.244	.090
		6			-.215	.090	6.912	.090
		7			-.520	.090	8.773	.090
		8			-.430	.090	12.802	.090
		9			-.465	.090	18.516	.090

*Due to the low quality of the photograph, only one reading per level was taken in Run 59_{β} (1,1), so that statistical errors are meaningless.

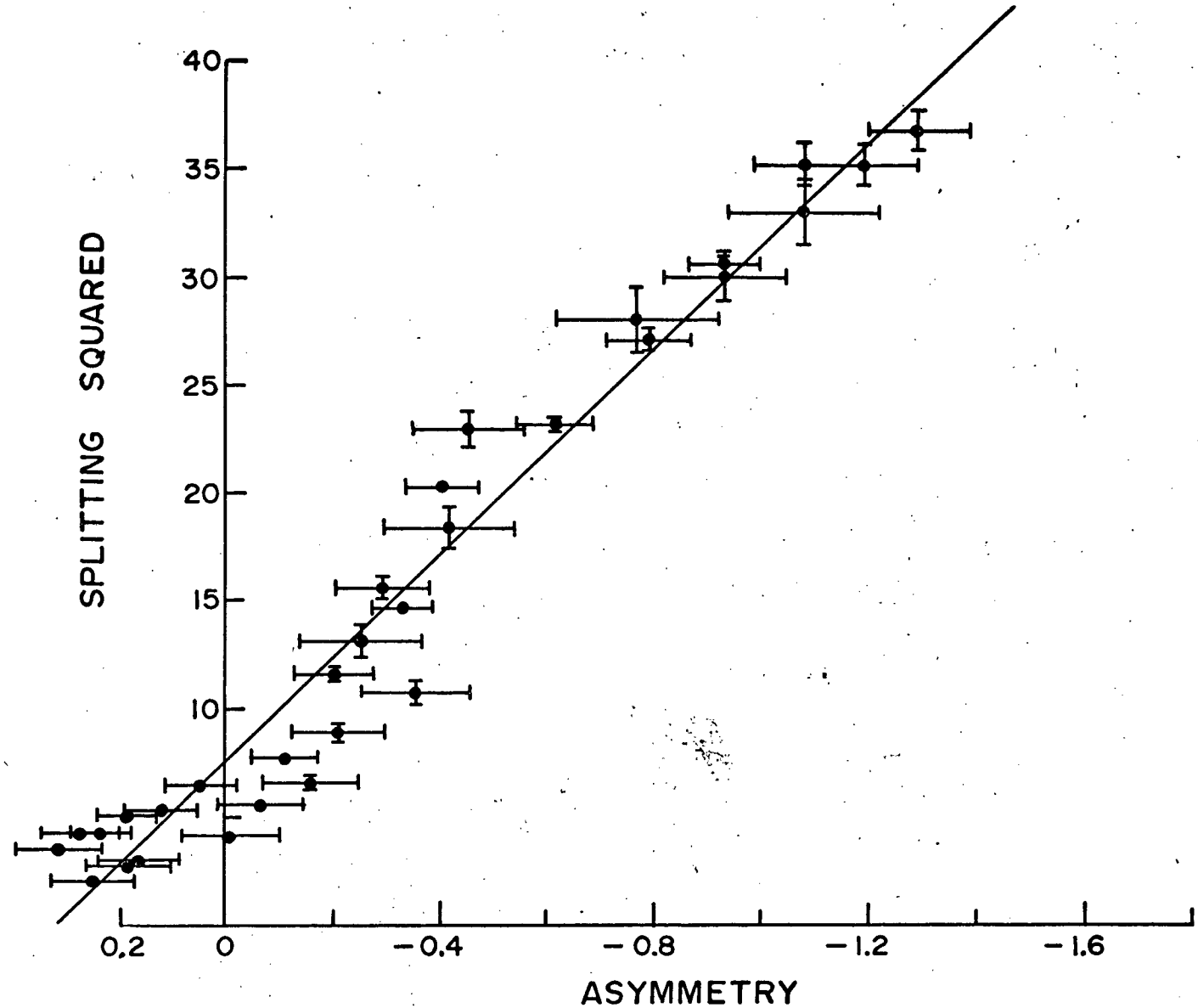

FIG. 28, Determination of μ_Σ / μ_Π for OH, v=0.

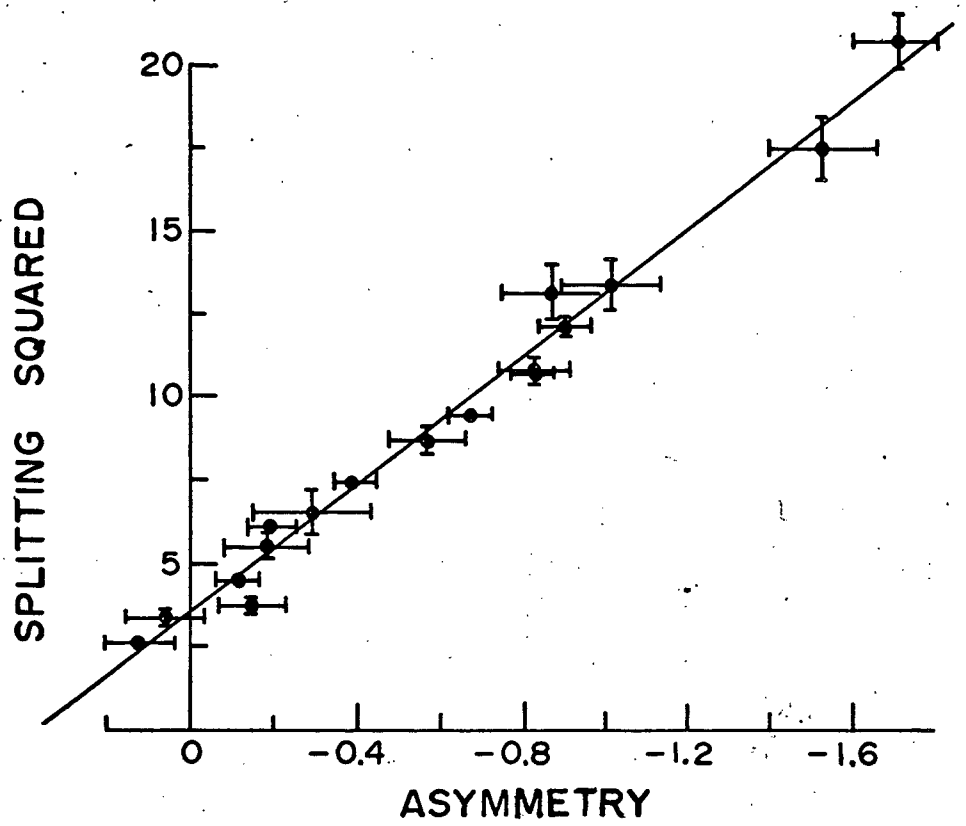

FIG. 29, Determination of μ_Σ/μ_Π for OD, v = 0.

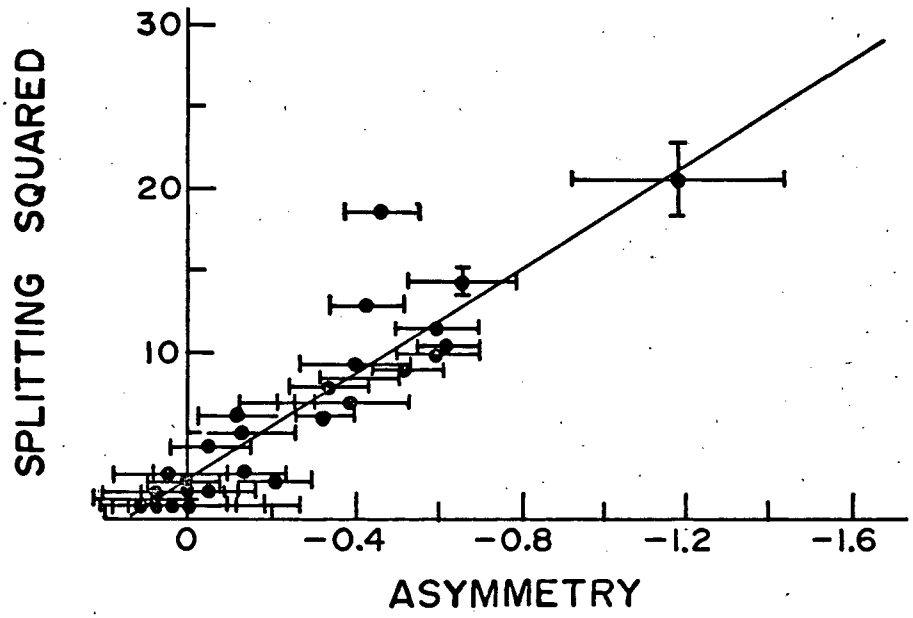

FIG. 30, Determination of μ_Σ/μ_Π for OH, v = 1.

TABLE XV

Dipole Moments in the $^2\Sigma$ State

Band	OH (0,0)	OD (0,0)	OH (1,1)
Slope	-23.868	-9.7465	-15.872
μ_Σ/μ_Π, from QUAFF	1.16_4	1.28_1	1.3_3
Error from Slope-Fit	0.01_6	0.01_6	0.05
μ_Σ/μ_Π, Corrected	1.13_9	1.27_2	1.3_0
Assigned Error	0.04_5	0.04_0	0.2_5
μ_Σ (taking μ_Π from Table XI)	1.94_6	2.14_2	2.1_4
Error in μ_Σ	0.08_5	0.08_0	0.4_1

obtained here, the source of the disagreement with the measurements Weinstock and Zare remains unclear. Neither is it clear that the larger value of μ_A obtained for OD (as compared to OH) is significant.

7. The $P_{12}(2)$ Line in OD

As noted in Scarl and Dalby[77], the $P_{12}(2)$ line in OD appears rather surprisingly like a triplet in high fields. This may be seen in the (0,0) band in Fig. 26, and in the (1,1) band in Fig. 31. This line is actually a composite of twelve components from both the $P_2(2)$ and $P_{12}(2)$. The Stark effect in the upper state is comparable to, and interacts strongly with, the spin splitting. The resulting Stark effects are given by Eqs. (72) and (75).

Due to the inaccuracy of the older analyses of the OD spectrum, it was felt advisable to remeasure the splitting constant γ from our plates. Averaging the splitting between main and satellite lines divided by $(N+\frac{1}{2})$, we get

$$\gamma(\text{OD, } v=0) = 0.121 \pm 0.005 \text{ cm}^{-1} \quad . \tag{138}$$

This is in agreement with a value of 0.125 cm^{-1} calculated from the formula and data of Dousmanis, Sanders, and Townes[93] (p.1743) under the assumption that the matrix elements of L_y are the same in upper and lower states.

Using the spin-splitting given by Eq. (133) and a Λ-doubling in the $^2\Pi_{\frac{1}{2}}$, $J=\frac{3}{2}$ level of 0.197 cm^{-1}

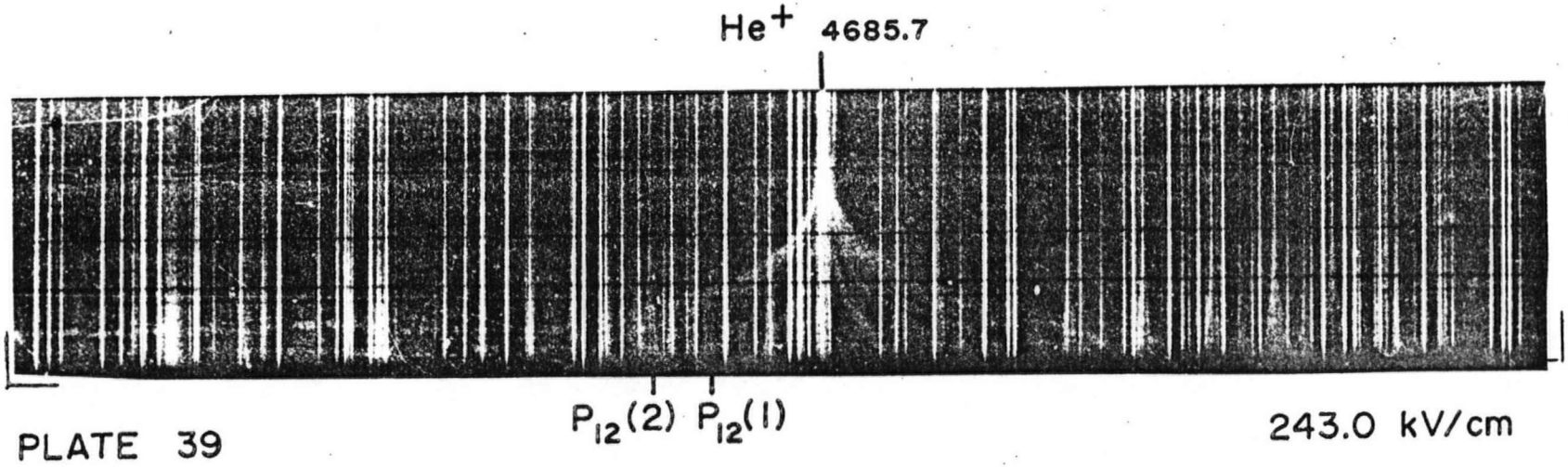

Fig. 31

The (1,1) A → X band of OD at high field.

(calculated from the formulae and data of Dousmanis, Sanders, and Townes[93]), we obtain the net Stark effects shown in Fig. 32. In this figure, all Stark effects are to scale with respect to the Λ-doubling and spin splitting. The components arising from these levels are shown in Fig. 33 separated into π and σ components ($\Delta M=0$ or ± 1, respectively). The positions of the observed components (plate 39) are indicated by the large circles (information on their polarization is not available). The bar lengths in Fig. 33 are proportional to the component intensities, which were calculated from wavefunctions corrected to first order in the Stark effect, and using the formulae of Earls[87] for unperturbed intensities. In principal, a precise determination of the relative intensities among the Stark components should yield information about the signs of the dipole moments (see, for example, Thomson and Dalby[74]). Such an evaluation of intensities is not possible, however, considering the poorness of fit between observed and calculated components in Fig. 33. A comparison between the relatively bright leftmost component (-1.5 cm^{-1}) and the barely visible component (?) near -0.7 cm^{-1} (interpreting observed intensities as the sum of nearby components) shows that the leftmost one is strongest and the next one weakest when the dipole moments in the upper and lower states are oppositely oriented, but the predicted intensity of the leftmost component is always less than the other (contrary to observation), so such interpretation is in serious doubt. Note also the absence of

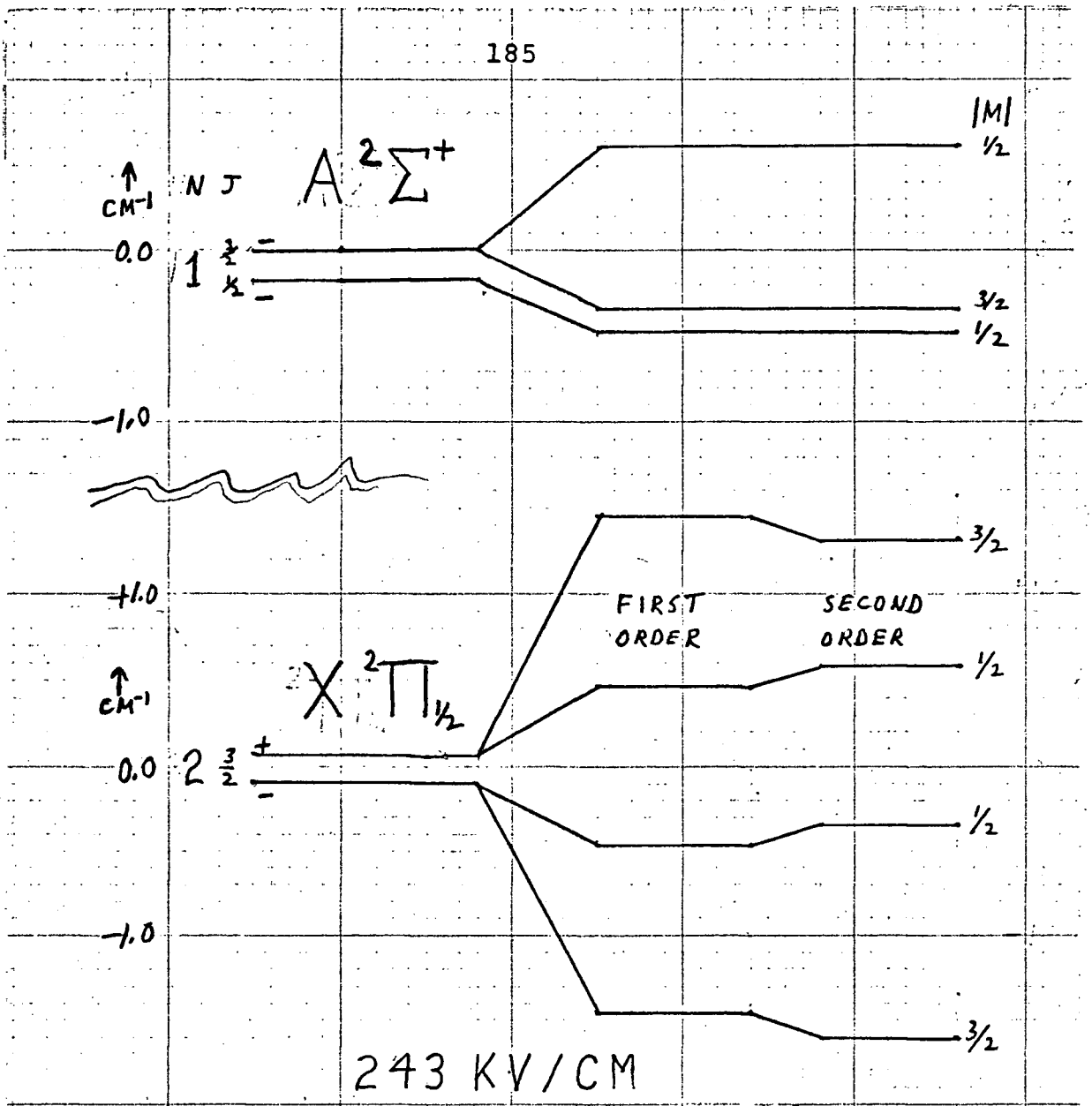

Fig. 32
Stark Effects in the $P_{12}(2)$ Line of OD

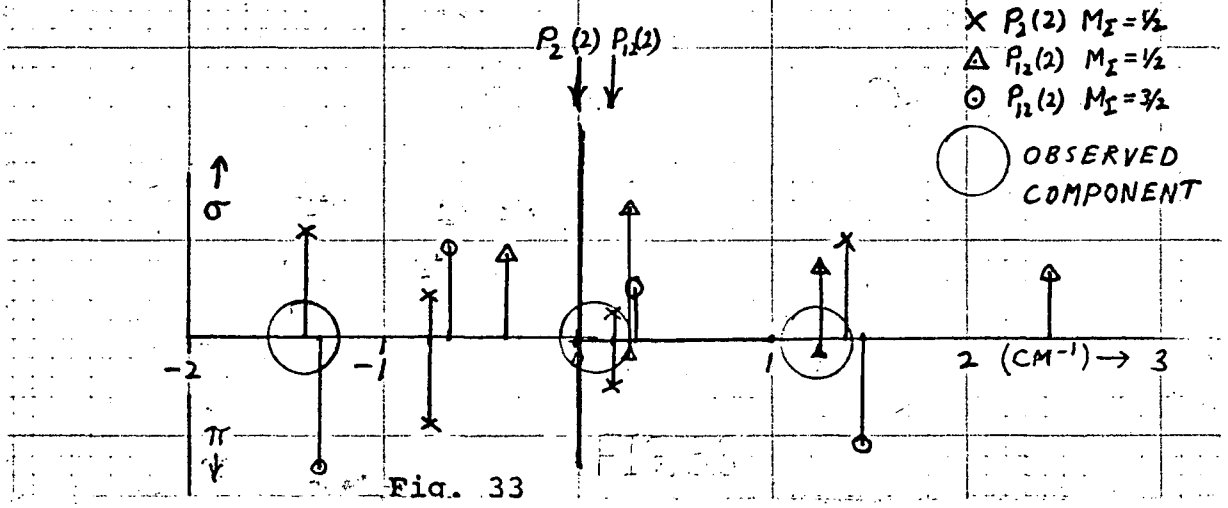

Fig. 33
Intensities in the $P_{12}(2)$ Line of OD

the component predicted to lie near 2.5 cm^{-1}. No simple assumption about observed polarizations makes the explanation much clearer, but the analysis does seem to throw some light on the peculiar overall appearance of the line.

CHAPTER X

THE $A\,^2\Delta$ STATE OF CH

1. The Production of the Spectrum

The $A\,^2\Delta \rightarrow X^2\Pi$ (0,0) band of CH at 4314 Å has been observed in second order during runs in which the discharge vessel contained cyanogen (C_2N_2) and hydrogen. (Unusably weak images of the band had also been obtained while running dimethyl mercury, diethyl zinc, and methanol. See Chap. VI, Sec. 8.)

Since no Balmer lines appear in this region of the spectrum, preliminary exposures (5 - 10 min.) of H_α were taken immediately preceding each photograph. At the start of the main exposure, no operating parameters other than grating angle and plate position were changed. H_α was exposed in first order for run 271_β, and in second order for runs 264_δ and 263_ζ.

The 4314 Å band is characterized by large and ubiquitous Stark effects due to the first order Stark effects in the ground state and still larger ones in the $^2\Delta$ state. However, even the simplest line ($J = \frac{3}{2}$ $J = \frac{1}{2}$) has eight principal components and moreover, is overlapped in our plates by components of neighbouring lines. The most isolated lines of low J are the $Q_1(2)$ and $Q_1(3)$, the latter of which was also used in the earlier work of Phelps[14] and

Phelps and Dalby[70]. Although these lines are composed of fourteen and twenty principal components, respectively, they exhibit clearly visible envelopes which have the appearance of doublets. Although (being in second order) we have lost the resolution which allowed Phelps to make his measurement, we nonetheless have high enough fields to render the envelopes readily measurable. In addition we have eliminated calculational shortcomings in Phelps' treatment.

The three spectra used in calculating the dipole moment of the $^2\Delta$ state are reproduced in Fig. 34. These plates were calibrated using frequencies given by Douglas and Routly[103](p.308) for the 4216 Å (0,1) band of CH, as well as the 4347.5 Å and 4358.35 Å lines of mercury which appear on the same plates.

2. Energy Level Structure

The spectra of the $^2\Delta \rightarrow {}^2\Pi$ transition have been analyzed by Gero[104] and vibrationally extended by Kiess and Broida[105] who give improved spectroscopic constants. From Kiess and Broida we take for the coupling constants: $Y = -0.0659$ in the $^2\Delta$ state and $Y = 2.00$ in the $^2\Pi$ state. (Keiss and Broida actually give $Y(Y - 4) = -4.02 \pm 0.05$ for $v=0$ in the $^2\Pi$ state, but it must be noted that values of $Y(Y - 4)$ less than -4 result in complex solutions for Y. Keiss and Broida also give empirical formulae for the $^2\Pi$ state Λ-doubling, but we will prefer the values of Douglas and Elliott[106]. The $^2\Delta$ state may be taken to

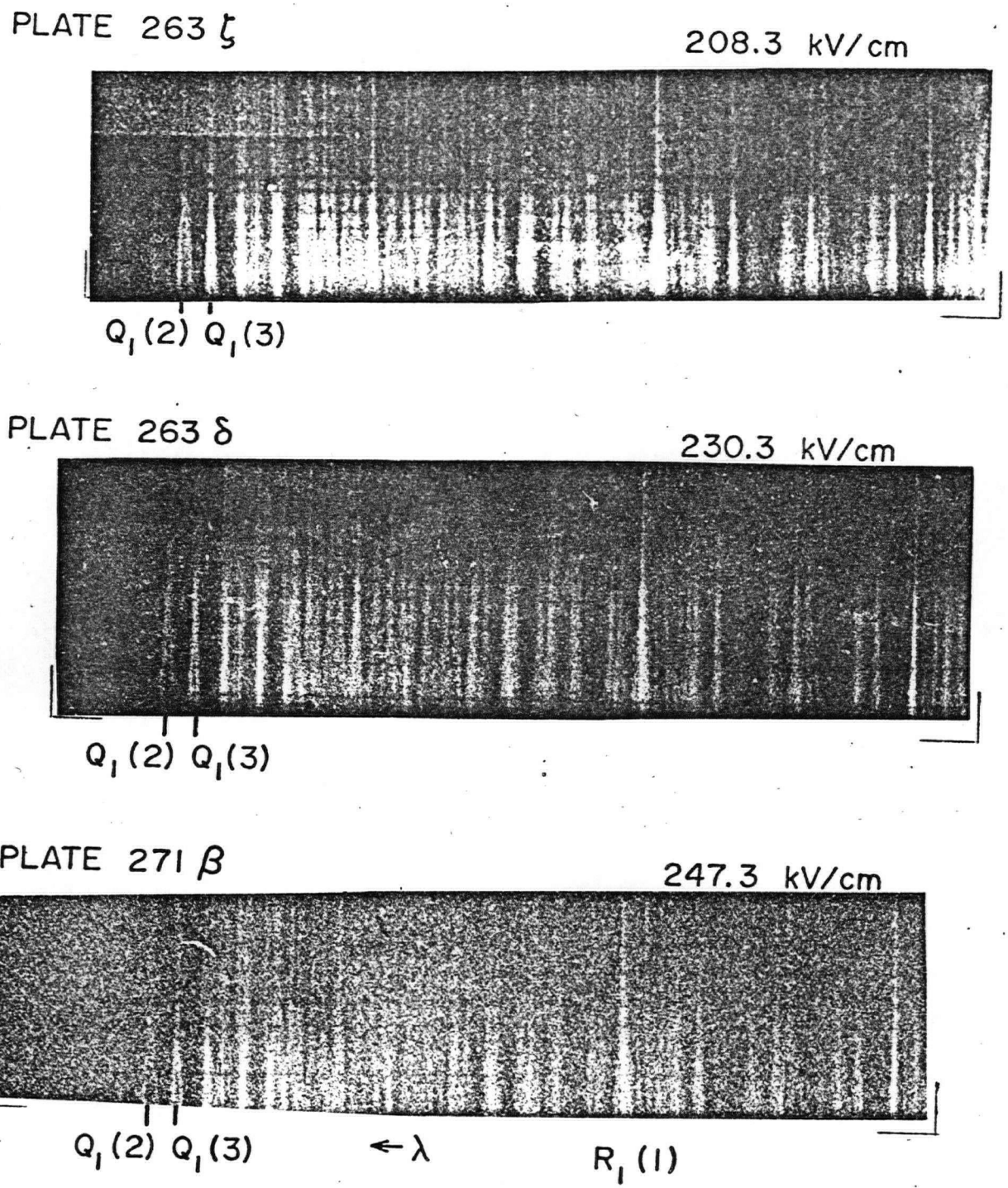

Fig. 34

The (0,0) A → X band of CH

have negligibly small Λ-doubling (Douglas and Elliott[106]).

Using the above values of Y, the energy levels of the two states may be found from Eqs. (80) and (112). These are shown in Fig. 35, in which the levels are drawn to scale within each electronic state. In the upper state, the F_1 levels have dropped slightly below the F_2 levels of same N due to the small negative magnitude of Y. In the ground state, however, the positive Y is consistent with $\Pi_{\frac{1}{2}}$ levels lying lower than $\Pi_{\frac{3}{2}}$ levels of the same N, but the $\Pi_{\frac{1}{2}}$ multiplet is rather curiously considered F_2. The fact that the F_1 levels lie higher than F_2 is typical of case (b) coupling.

3. The Assignment of M

In evaluating dipole moments from the $Q_1(2)$ and $Q_1(3)$ lines, we are faced with the problem of deciding which components form the brightest parts of the envelope. The relative intensities of the different components are proportional to the squares of the transition moments between the two states (see Chap. II). Although the transition moment is not easily evaluated, its dependence on M is readily established.

Light which is polarized parallel to the electric field has intensity proportional to the square of the matrix element of n_z (where $\vec{\mu} = |\mu|\hat{n}$) which is diagonal in M (and also in J, since we are dealing with the Q-branch). Thus, for parallel polarized light, the intensities are

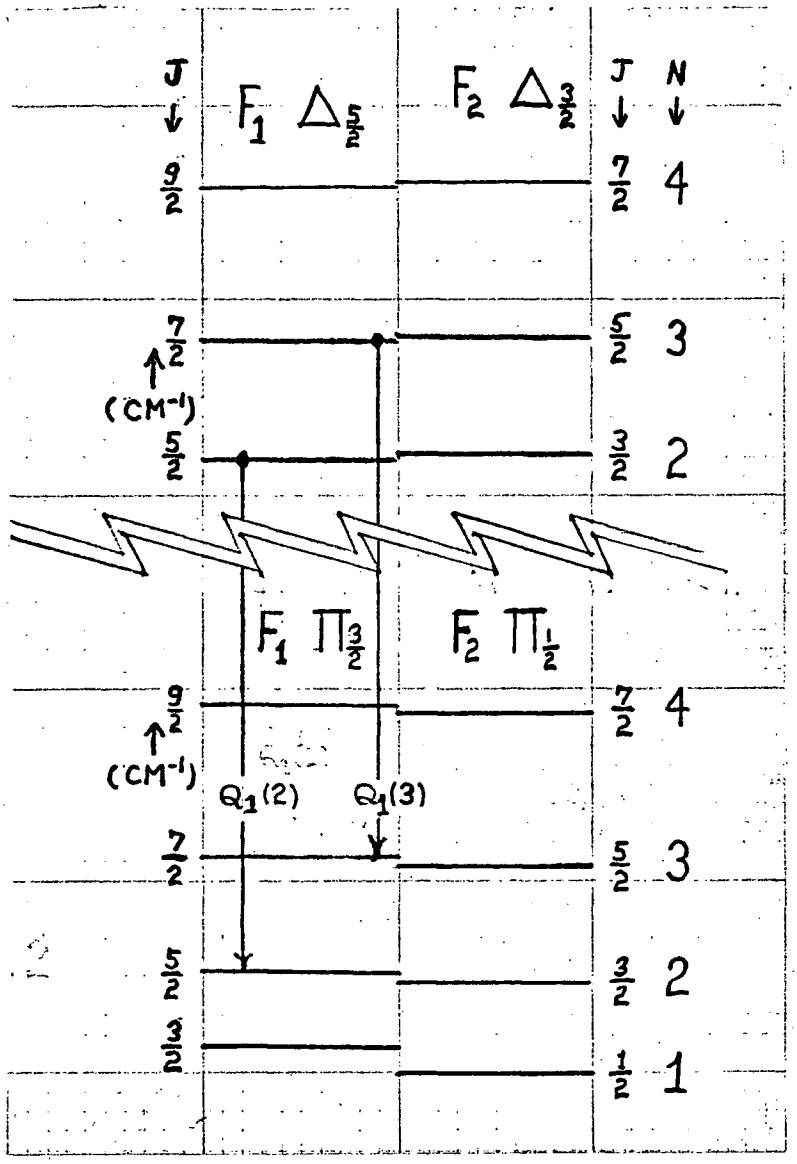

Fig. 35

A $^2\Delta \rightarrow X\ ^2\Pi$ Transitions in CH

proportional to M^2 (see Landau and Lifshitz[1], p. 93). For light polarized perpendicularly to the electric field, the intensity is proportional to $< J\ M|n_x + in_y|J\ M - 1 >^2$, the M-dependence of which is given by $\frac{1}{4}(J - M + 1)(J + M)$ (see Condon and Shortley[64], p. 63)*. Under assumptions which will be detailed in Sec. 6 below, the positions of the various components may be calculated to lie as shown in Fig. 36. This figure shows the expected components of the $Q_1(2)$ and $Q_1(3)$ lines in a field of 208 kV/cm (plate 264ζ) with length representing intensity, horizontal position representing displacement in cm^{-1} from the line center (the average of the c and d components), and the component being shown above or below the horizontal axis according as its polarization is parallel or perpendicular. We see that the averages of the components on each side of center fall in roughly the same position for both parallel and perpendicular components, but that the parallel polarized components have the sharper peak (particularly on the outer side). Since our plates are of long exposures at low light intensities, we may expect the emulsion's reciprocity failure to further emphasize strong components at the expense of weaker ones. Examining the spectra in Fig. 34, we observe a sharp doublet appearance in both lines, and particularly in the better resolved $Q_1(2)$. This appearance is very difficult to explain unless the perpendicular components are excluded. We shall therefore assume that we are principally

*Note that the factor of $\frac{1}{4}$ is missing from the expressions given by Landau and Lifschitz[1](p.93).

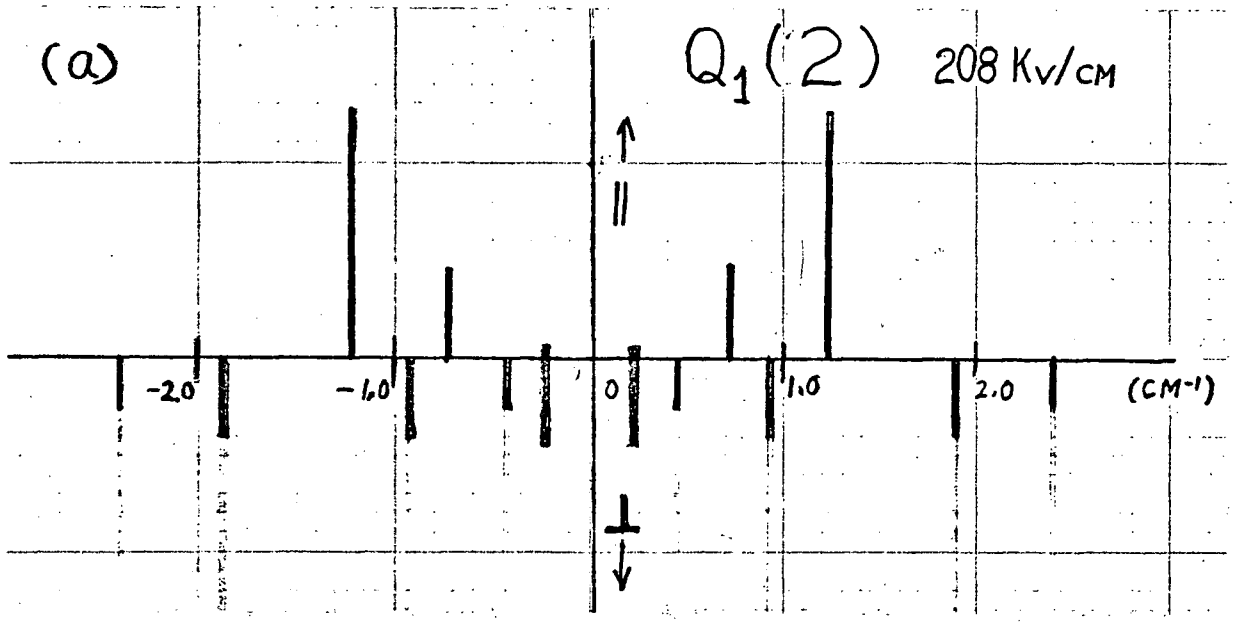

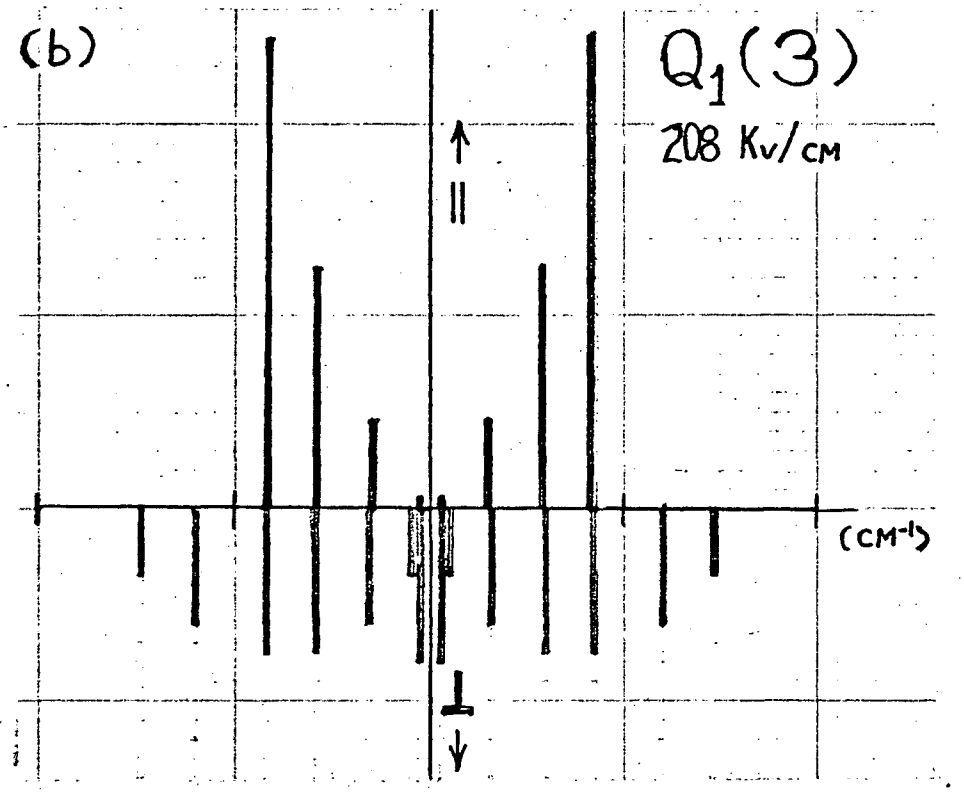

Fig. 36
Predicted Components of the $Q_1(2)$ and $Q_1(3)$ Lines

seeing parallel polarization for instrumental reasons. It is clear from Figs. 34 and 36 that the assumption of Phelps[14](p.87), that the envelope corresponds to the outermost perpendicular component ($M=J \rightarrow M=J-1$), is not warranted here. We instead interpret the envelope as representing the transition $M=J \rightarrow M=J$.

4. The Diagonal Matrix Elements of n_z

Since both the $^2\Pi$ and $^2\Delta$ states are nearly case (b), we must evaluate the effect of intermediate coupling upon the diagonal case (a) matrix elements of n_z, given by $M\Omega/J(J+1)$. We use the notation of Chap. V wherein $|\psi_{\Omega J}>$ represents the actual (intermediate case) wavefunctions and $|\Omega J>$ is the pure case (a) wavefunction, but we should be unusually careful since the Ω in $|\psi_{\Omega J}>$ is a very bad quantum number whose assignment depends on correspondences such as Eqs. (83) and (85).

In the case of the $^2\Pi$ state, $Y = 2.00$ which is the special case of pure case (b). Here the wavefunctions $|\psi_{\frac{3}{2}J}>$ and $|\psi_{\frac{1}{2}J}>$ are exactly given by Eq. (84) so that $c_1 = c_2 = 1/\sqrt{2}$. We can scarcely decide which of ψ_1 and ψ_2 in that equation should be called $|\psi_{\frac{3}{2}J}>$, but it does not matter since the diagonal matrix elements are

$$\begin{aligned} <\psi_{\Omega J}|n_z|\psi_{\Omega J}> &= \frac{\sqrt{2}}{2}\{<\tfrac{1}{2}\,J| \pm <\tfrac{3}{2}\,J|\} \\ &\quad \times \frac{\sqrt{2}}{2}\{|\tfrac{1}{2}\,J> \pm |\tfrac{3}{2}\,J>\} \\ &= \tfrac{1}{2}\{<\tfrac{1}{2}\,J|n_z|\tfrac{1}{2}\,J> + <\tfrac{3}{2}\,J|n_z|\tfrac{3}{2}\,J> \end{aligned} \tag{139}$$

$$\langle \psi_{\Omega J}|n_z|\psi_{\Omega J}\rangle = \tfrac{1}{2}\{\tfrac{1}{2}M/J(J+1) + \tfrac{3}{2}M/J(J+1)\}$$

$$= M/J(J+1) \quad , \qquad (139)\ \text{(Cont'd)}$$

which are independent of the choice of wavefunctions in the first line.

In the case of the $^2\Delta$ state, we make the association appropriate to inverted states (analogous to Eq. 83) and write

$$\psi_1 = |\psi_{\frac{5}{2}J}\rangle = c_1|\tfrac{3}{2}\rangle + c_2|\tfrac{5}{2}\rangle$$
$$\psi_2 = |\psi_{\frac{3}{2}J}\rangle = c_1|\tfrac{5}{2}\rangle - c_2|\tfrac{3}{2}\rangle \quad , \qquad (140)$$

where c_1 and c_2 are given by Eq. (82), with $Y = -0.0659$, as

$$c_1 = 0.40087$$
$$c_2 = 0.91613 \qquad (J = \tfrac{5}{2}) \qquad (141)$$

and

$$c_1 = 0.49386$$
$$c_2 = 0.86954 \qquad (J = \tfrac{7}{2}) \quad . \qquad (142)$$

With these constants, the diagonal matrix elements are readily evaluated as

$$\langle \psi_1|n_z|\psi_1\rangle = (0.26735)M \qquad (J = \tfrac{5}{2})$$
$$\langle \psi_2|n_z|\psi_2\rangle = (0.14324)M \quad . \qquad (J = \tfrac{7}{2}) \qquad (143)$$

5. The Splitting Formulae

When a pair of Λ-doublets becomes substantially mixed by the Stark interaction, they are described by the wavefunctions ψ_A and ψ_S of Eq. (51) and it is easily shown that when transitions occur between two states (each of which contains such Λ-doublets), then transitions from (for example) the ψ_A of one state will go to either the ψ_S or the ψ_A of the other state (but not both), and the choice will depend on the relative signs of the dipole moments in the two states and not on their initial parities. When the dipole moments have the same signs, then we have $\psi_S \leftrightarrow \psi_S$ and $\psi_A \leftrightarrow \psi_A$ (see, for example, the simplified discussion in Phelps[14], p.28ff*). By observing that this was the case for the $^2\Delta \rightarrow {}^2\Pi$ bands of CH, Phelps[14] (p.76f) showed that the two dipole moments here have like signs. Fig. 37 shows the allowed transitions at zero and high fields, and the resulting appearance of the line. Thus the net splitting of line is just twice the difference between the Stark shifts of the two components.

Denoting the splitting in the $Q_1(2)$ line by S_1, that of the $Q_1(3)$ line by S_2, and using the matrix elements of Eqs. (139) and (143) with M=J, we have

---

*Note however the error at the bottom of p.30 in Phelps : The last complete sentence on that page should read: "This (changing the relative sign of the dipole moments) is equivalent to reversing the sign of the coefficient...(c_2) in the description of one of the states and..." (changing the relative sign of the dipole moments).

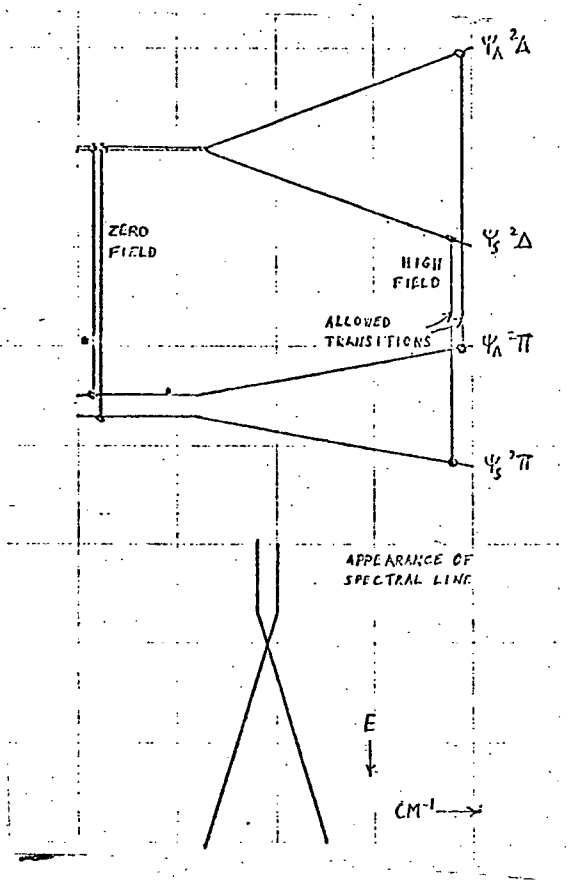

Fig. 37

Appearance of the Stark Effect in a $\Delta \rightarrow \Pi$ Line

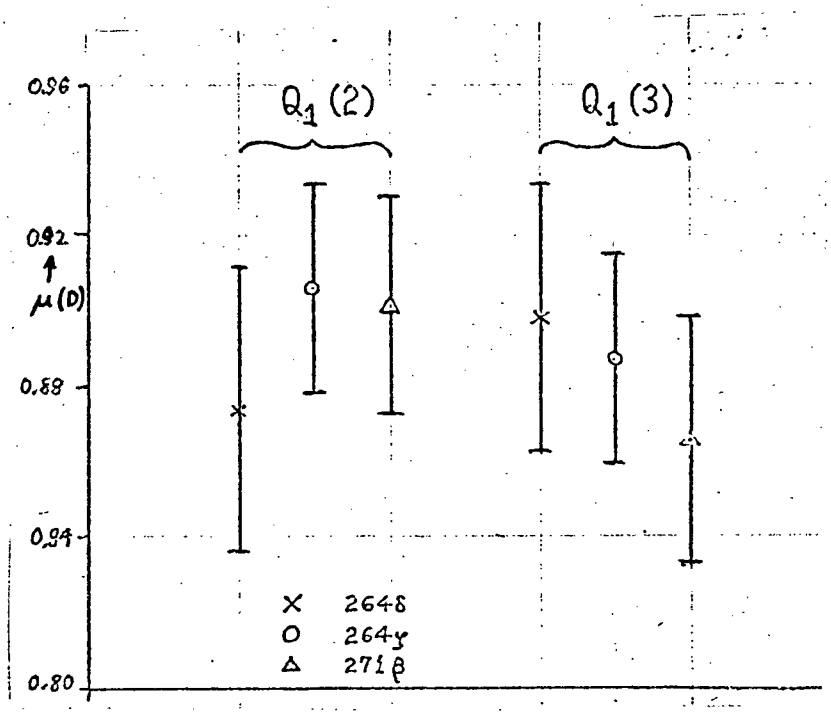

Fig. 38

Dipole Moment of the $A\ ^2\Delta$ State

$$S_1 = 1.337\varepsilon_\Delta - \sqrt{(2\delta_1)^2 + (4\varepsilon_\Pi/7)^2}$$

$$S_2 = 1.003\varepsilon_\Delta - \sqrt{(2\delta_2)^2 + (4\varepsilon_\Pi/9)^2} \qquad (144)$$

where $2\delta_1$ is the Λ-doubling of the $^2\Pi$, $J=\frac{5}{2}$ level, and $2\delta_2$ is the Λ-doubling of the $^2\Pi$, $J=\frac{7}{2}$ level. (We have treated the Λ-doubling in the $^2\Delta$ state as negligibly small.) These equations may be separately solved for $\varepsilon_\Delta = \mu_\Delta E/hc$, and thus for μ_Δ.

6. Results

The $Q_1(2)$ and $Q_1(3)$ lines shown in Fig. 34 were measured on the comparator and treated as simple doublets. The measured values of S_1 and S_2, as well as the parameters E and $\varepsilon_\Pi = \mu_\Pi E/hc$, are shown in Table XVI along with the calculated values of μ_Δ. We have taken $\mu_\Pi = 1.46 \pm 0.06$ from the work of Phelps and Dalby[70], and Λ-doublings $2\delta_1 = 0.159\ cm^{-1}$, $2\delta_2 = 0.373\ cm^{-1}$ from Douglas and Elliott[106]. The observed values of μ_Δ are illustrated in Fig. 38. We have adopted $0.89_3 \pm 0.04_5$ D as a best value of μ_Δ. Reducing this by 0.67 % gives our result:

$$\mu_\Delta = 0.88_7 \pm 0.04_5 \ . \qquad (145)$$

Some additional tolerance has been included as an allowance for such systematic errors as may arise from measuring the electric field in non-simultaneous exposures of H_α (the

Plate	264δ	264φ	271β	Phelps
S_1 (cm^{-1})	1.289 ± .091	1.316 ± .056	1.531 ± .078	--
S_2 (cm^{-1})	0.945 ± .025	0.811 ± .030	0.881 ± .075	0.373
E (kv/cm)	230.3 ± 5.0	208.3 ± 0.8	247.3 ± 1.1	66.
ε_π	5.65 ± .26	5.11 ± .21	6.06 ± .25	1.62
μ_Δ (J = 5/2)	0.874 ± .038	0.906 ± .028	0.901 ± .029	--
μ_Δ (J = 7/2)	0.898 ± .036	0.887 ± .028	0.865 ± .033	1.06

TABLE XVI

Measurements and Results for the $^2\Delta$ State of CH

dispersion of which was calculated from still other plates made at the same grating angle). That such errors are reasonably small, and that our assumption is appropriate concerning the interpretation of the apparent doublet splittings (Sec. 3) are attested to by the overall consistency of the data and, in particular, by the agreement between results from the $Q_1(2)$ and $Q_1(3)$ lines. It should be pointed out that the value of Eq. (145), along with the other data referred to in this section, was used in calculating the splittings of Fig. 37.

The last column in Table XVI lists the data used by Phelps[14](p.87) in his calculation. Phelps arrived at a value of $1.13 \pm .17$ for μ_Δ, but, when carried through the calculation with corrections for intermediate coupling, this data gives $\mu_\Delta = 1.06 \pm .15$ (maintaining Phelps' error at 15%). This is within tolerance of our result.

CHAPTER XI

THE X $^3\Sigma^-$ STATE OF NH

1. Observed Spectra

The NH (imidogen) molecule has a principle resonance band at 3360 Å which was first analyzed in detail by Funke[107], and is known to be the (0,0) band of an A $^3\Pi_i \rightarrow$ X $^3\Sigma^-$ transition. This band was reanalyzed by Dixon[108] who obtained it in absorption and thereby identified most of the 27 possible branches. The nearby (1,1) band has been reanalyzed by Murai and Shimauchi[109], who also extended the identifications of satellites in the (0,0) band. The (1,1) band is also visible on our plates, but its dense central region is overlapped by the head of the intense (0,0) band (at 3371 Å) of the second positive group of N_2, which always appeared as an impurity. Another band that is normally obtained at the same time is the 3240 Å band due to a c $^1\Pi \rightarrow$ a $^1\Delta$, (0,0) transition which has been analyzed by several authors (Pearse[110], Dieke and Blue[111], Nakamura and Shidei[112], and Shimauchi[113]).

The A $^3\Pi \rightarrow$ X $^3\Sigma^-$ and c $^1\Pi \rightarrow$ a $^1\Delta$ bands have been previously observed in this laboratory by Irwin[71] and Irwin and Dalby[72] who were able to determine the dipole moments of three of these four states. Since the fields available to Irwin and Dalby did not exceed 100 kV/cm, the

second order effects due to the $X\ ^3\Sigma^+$ state were too small to permit the dipole moment in the ground state to be evaluated. In the experiments reported here, the 3360 Å band has been observed with fields as high as 287 kV/cm, which is sufficient to allow this dipole moment to be measured with an error from internal consistency of about 3%.

The four bands referred to above are visible in each exposure often with H_β and He lines in second order

An attempt was also made to photograph the $c\ ^1\Pi \rightarrow b\ ^1\Sigma^+$ band at 4502 Å. While it is believed that lines of this spectrum have been observed, they were much too weak to allow second order effects in the $b\ ^1\Sigma^+$ state to be observed.

Our high-wavelength (even-numbered) plates contain the low-J lines of the $A\ ^3\Pi_i \rightarrow X\ ^3\Sigma^-$, (0,0) band, and these have been calibrated using high-J lines from that same band (wavenumbers from Dixon[108]), as well as lines from the (1,1) band (using the data of Murai and Shimauchi[109]) and from the $C\ ^3\Pi_u \rightarrow B\ ^3\Pi_g$, 2nd positive (0,0) band of N_2 (using the identifications of Coster, Brons, and van der Ziel[114]). The low wavelength (odd-numbered) plates usually contain H_β as well as the 4922 Å and 5015 Å helium lines. These were calibrated using the identifications of Pearse[110] for the 3240 Å band, and high-J lines of the triplet R-branch from Dixon[108].

2. Energy Level Structure and Constants

The $A\ ^3\Pi_i \rightarrow X\ ^3\Sigma^-$ bands of NH have been successively analyzed, with the extraction of revised constants, by Funke[107], Dixon[108], Murai and Shimauchi[109], Horani, Rostas and Lefebvre-Brion[115], and Veseth[19]. However, we only require that the energy differences between neighboring levels be known in order to evaluate second order effects, and a value for the spin-coupling parameter Y. We shall use Veseth's[19] constants: For the $^3\Pi_i$ state (v=0) he gives $B_\Pi = 16.3018_3$, and $A = -34.79_4$; for the $^3\Sigma^+$ state, $B_\Sigma = 16.3748_2$. Thus we use

$$Y = A/B_\Pi = -2.134_4 \quad . \tag{146}$$

The magnitude of Y is small enough so that Herzberg[3] (p.264) simply refers to the state as case (b), although this is not accurate at small N. The near equality of the upper and lower state B values gives the band no distinct head, and the R and P branches proceed fairly uniformly toward higher and lower wavenumbers (although the slightly larger B_Σ does cause a head in the R branch near N=30). The central piling up of the Q (and associated satellite) branches forms the most marked feature of the spectrum.

Rather than rely on derived constants to provide energy differences, we shall directly use the term values resulting from the measurements of Dixon[116]. The first several of these have been listed in Table XVII. Fig. 39 shows

TABLE XVII

Some Term Values of NH, from Dixon[117]

State	Multiplet	Ω	N	J	Parity	Term (cm^{-1})
$^3\Sigma^-$	1		0	1	-	-0.68
	3		1	0	-	30.88
	1		1	2	-	31.83
	2		1	1	-	32.68
	3		2	1	-	96.89
	1		2	3	-	97.05
	2		2	2	-	98.01
	1		3	4	-	194.86
	3		3	2	-	194.95
	2		3	3	-	195.90
	1		4	5	-	325.12
	3		4	3	-	325.39
	2		4	4	-	326.23
$^3\Pi_0$	3	0	1	0	-	29826.26
	3	0	1	0	-	29828.86
	3	0	2	1	-	29878.91
	3	0	2	1	-	29880.82
	3	0	3	2	-	29970.91
	3	0	3	2	-	29972.31
	3	0	4	3	-	30097.79
	3	0	4	3	-	30098.79
$^3\Pi_1$	2	1	1	1	-	29805.90
	2	1	1	1	-	29806.58
	2	1	2	2	-	29865.40
	2	1	2	2	-	29866.45
	2	1	3	3	-	29959.99
	2	1	3	3	-	29961.35
$^3\Pi_2$	1	2	1	2	-	29769.90
	1	2	1	2	-	29769.90
	1	2	2	3	-	29841.52
	1	2	2	3	-	29841.62
	1	2	3	4	-	29943.05
	1	2	3	4	-	29943.28

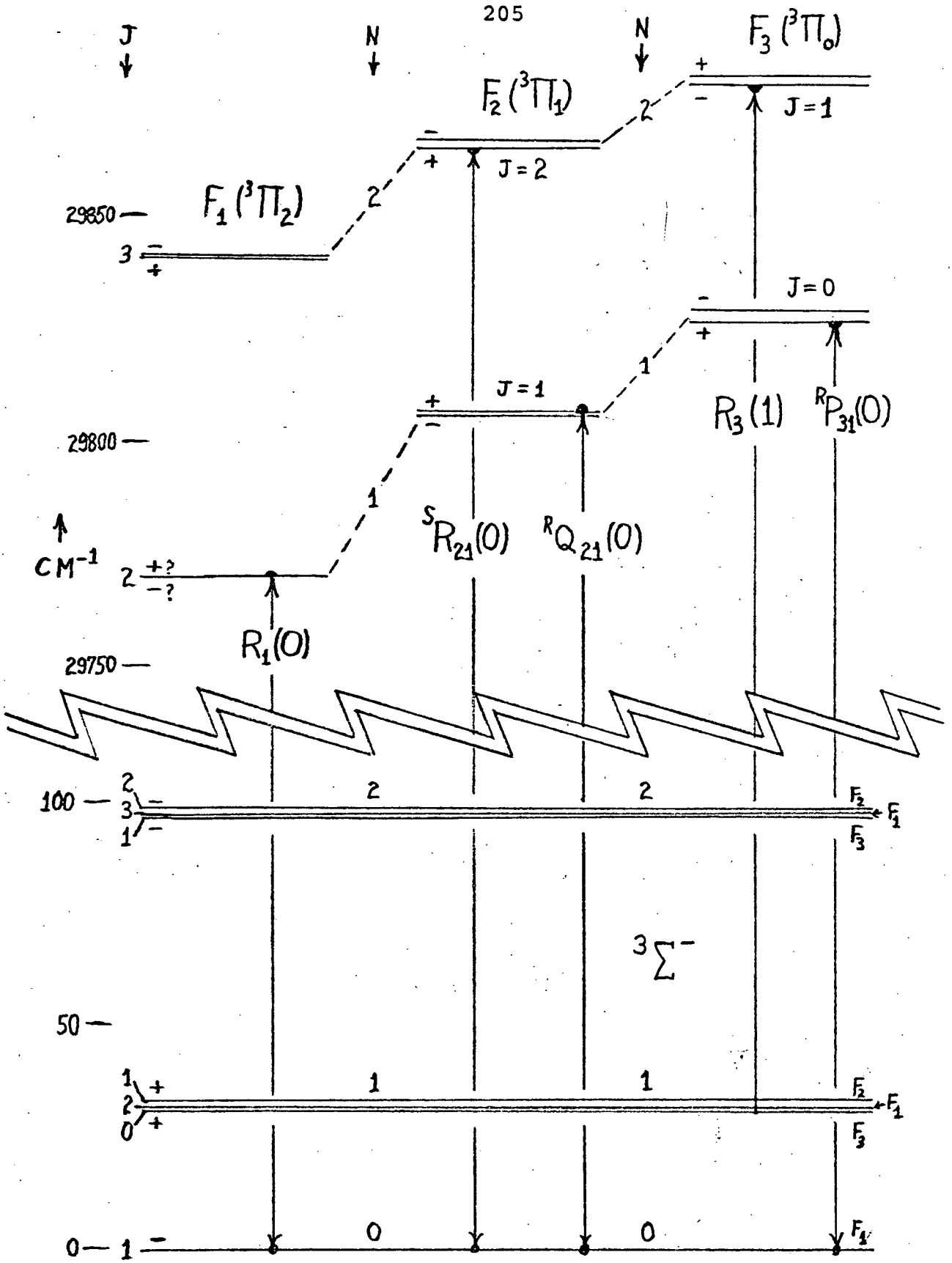

Fig. 39. Energy Levels of the A $^3\Pi_i$ → X $^3\Sigma^-$ Band of NH.

these levels, drawn to scale excepting the gap between electronic states. Note the differences in the ordering of the Λ-doublets and spin-splittings, as compared to Dixon (Fig. 1, p. 1173).

3. Choice of Spectral Line

There are a number of considerations in deciding which energy levels in the $^3\Sigma^+$ state at which to look for second order effects: Apart from problems of intensity and overlapping, we must consider the magnitude of the Stark effect and complications due to the presence of more than one value of M_Σ.

An ideal $^3\Sigma$ level for study may seem to be the f_3 level with $J=0$, which is solely comprised of $M=0$. However, an examination of the matrix of n_z for $^3\Sigma$ (column 3 of Eq. 21) shows that, if energies are given by $BN(N+1)$, second order effects exactly cancel to zero, independent of B or μ! Some Stark effect is re-introduced through interactions with spin-splitting (see Fig.39 and the first line of Eq. 77), but this effect is quite small in NH at fields available (due to the large magnitude of the spin-splitting).

Thus we must use a level with $J_\Sigma=1$ or more, so that polaroid may be needed to separate components of

differing M_Σ (note that components of different M_Π are separated by first order effects).

The second order Stark effects in the level N=1, J=1 are given by the second and third lines (F_4 and F_5, corresponding to M_Σ=0 and 1, respectively) of Eq. (77). The N=2, J=1 (F_3) level has Stark effects markedly smaller than the N=1 level (roughly $\varepsilon^2/70B$ and $-\varepsilon^2/120B$, neglecting interaction with spin splitting, for the M=0 and 1 components of N=2, J=1). Lastly, looking at the level with N=0, J=1 (molecular ground state), there is no spin splitting to consider, so that a straightforward application of the second order energy formula gives:

$$\begin{aligned} M=0: \quad F_\Sigma^{(2)} &= -\varepsilon^2(\tfrac{1}{9} + \tfrac{2}{9})/2B = -\varepsilon^2/6B \\ M=1: \quad F_\Sigma^{(2)} &= -\varepsilon^2(\tfrac{1}{6} + \tfrac{1}{6})/2B = -\varepsilon^2/6B \end{aligned} \qquad (147)$$

We find that the Stark effect is the same for both values of M, rendering separation by polaroid unnecessary! This Stark effect is considerably larger than for the other levels, furthermore, so this level is the logical choice for study. The Stark effect in this level will be examined more closely in section 5, below.

There are several possible lines which involve a transition to the N=0 level, namely the ${}^{T}R_{31}(0)$, ${}^{S}Q_{31}(0)$, ${}^{R}P_{31}(0)$, ${}^{S}R_{21}(0)$, ${}^{R}Q_{21}(0)$, and $R_1(0)$. (The left superscript refers in the standard way to the change in N associated with the transition, and is omitted when the same

as the main letter which describes the change in J. The numeric subscripts refer to multiplet cases, as per Fig.39, and the parentheses enclose the value of N in the lower state.)

Among these, the $^{T}R_{31}(0)$ has not been observed in this work or by Dixon, the $^{S}Q_{31}(0)$ is overlapped by the $R_1(3)$, and the $R_1(0)$ is overlapped by the $Q_3(5)$ and a number of other lines (including N_2) in a dense part of the spectrum. The $^{S}R_{21}(0)$ seems to appear very faintly in some of our plates but shows no Stark effects as expected and might instead be some impurity line.

This leaves the $^{R}P_{31}(0)$ and $^{R}Q_{21}(0)$ lines. The $^{R}P_{31}(0)$ is the brightest (even though its intensity should be zero according to the formulae of Budó[117]). Unfortunately, it has a highly skewed profile in most of our plates, trailing off vaguely on the low frequency side. This is probably due to overlapping by Stark components from the $^{R}Q_{21}(4)$ and $R_2(4)$ lines in the (1,1) band (Murai and Shimauchi[109], pp. 56 and 58).

Our principal results have therefore come from the $^{R}Q_{21}(0)$, which is the same line used by Irwin[71,72] in his study of the $^{3}\Pi$ state. We have principally used the center component (M_Π=0) which exhibits no first order effect, and it has been measured with good accuracy. The $^{R}P_{31}(0)$ line was also measured, but these results were poor and could only confirm results obtained from the $^{R}Q_{21}(0)$ line.

4. Stark Effects in the $^3\Pi$ State

Due to the effects of strong spin-uncoupling, the matrix elements of the Stark effect (n_z) are not given by the case (a) matrix elements of Eqs. (22) - (24), but rather by linear combinations of them. The groundwork for this procedure has been laid in Chap. V, where the correctly coupled wavefunctions for J=0, 1, 2, 3 were given by Eqs. (94), (99), (105), and (110) respectively. The correctly coupled matrix elements are immediately obtained from the above-mentioned resources. For example, the matrix element of n_z between the $^3\Pi_1$, J=1, M=0 (Ψ_{110}) and the $^3\Pi_0$, J=2, M=0 (Ψ_{020}) states is found to be

$$\begin{aligned} \langle\Psi_{110}|n_z|\Psi_{020}\rangle &= c_2 f_1 \langle 010|n_z|020\rangle + c_1 f_2 \langle 110|n_z|120\rangle \\ &= (0.5144)(0.7647)\sqrt{4/15} + (0.8575)(-.6244)\sqrt{1/5} \\ &= -0.03634 , \end{aligned} \tag{148}$$

where the c's are from Eq. (102), the f's are from Eq. (105), and the case (a) matrix elements are from Eqs. (22) and (23). (We retain the previous notation in which $|\Psi_{\Omega JM}\rangle$ are the correctly coupled wavefunctions, and $|\Omega JM\rangle$ are the pure case (a) wavefunctions.) We have, of course, also used the fact that n_z is diagonal with respect to Ω in a pure case (a) representation (changes in the quantum number Σ are not allowed for dipole transi-

tions). Collecting such matrix elements up to J=3, we have the correctly coupled matrix elements of n_z shown in Eq. (149), wherein the columns (and, implicitly, the rows) are labeled by Ω,J pairs.

$$
\begin{array}{cccccccccc}
 & & & & \Omega,J & & & & & \\
0,0 & 0,1 & 1,1 & 0,2 & 1,2 & 2,2 & 0,3 & 1,3 & 2,3 & \\
\hline
0 & 0.49510 & .29699 & 0 & 0 & 0 & 0 & 0 & 0 & \\
.49510 & 0 & 0 & 0.23260 & .12492 & -.03504 & 0 & 0 & 0 & \\
0.29699 & 0 & 0 & -0.03634 & .42107 & .19753 & 0 & 0 & 0 & \\
0 & 0.23260 & -.03634 & 0 & 0 & 0 & 0.48764 & .07036 & -.01898 & (149) \\
0 & 0.12492 & .42107 & 0 & 0 & 0 & -.02235 & .45996 & .11607 & \\
0 & -0.03504 & .19753 & 0 & 0 & 0 & 0.00088 & -.02649 & .39904 & \\
0 & 0 & 0 & 0.48764 & -.02235 & .00088 & 0 & 0 & 0 & \\
0 & 0 & 0 & 0.07036 & .45996 & -.02649 & 0 & 0 & 0 & \\
0 & 0 & 0 & -0.01898 & .11607 & .39904 & 0 & 0 & 0 &
\end{array}
$$

The Stark effect perturbations may now be calculated in a straightforward manner from the usual formulae Eqs.(29) - (35). We may note that the arithmetic of this calculation has been simplified by the fact that we are limiting ourselves to the case of $M_\Pi=0$. This means that first order Stark effects are all zero, and the Λ-doublets

have no interaction with each other. This permits us to use directly the matrix elements of n_z with respect to the wavefunctions $\psi_{\Omega JM}$, without combining these into the linear combinations described by Eqs. (48) and (49). Parity is conserved to first order, and we may treat the rotational levels as being nondegenerate. Thus in considering the $^{R}Q_{21}(0)$ line, we consider only the higher Λ-doublet of $^{3}\Pi_{1}$, J=1 (with positive parity, see Fig. 39) which is the upper state of the allowed transition. For those levels which interact with this one through the matrix of n_z (Eq. 149), we consider only the sublevels of negative parity, and similarly for the $^{R}P_{31}(0)$ line.

The actual Stark effect calculations have been accomplished by feeding the matrix of Eq. (149) (and the energies of the appropriate Λ-doublet sublevels from Table XVII) into a small computer program called PIFIELD, written in the language ALGOL W. Denoting the resulting n^{th} order term values by $F^{(n)}_{\Omega JM}$, we find

$$F^{(2)}_{110} = -0.005865\ \epsilon_{\Pi}^{2} = -2.838\ E^{2} \qquad (150)$$

$$F^{(2)}_{000} = -0.0003235\ \epsilon_{\Pi}^{2} = -0.1566\ E^{2}\ , \qquad (151)$$

where E is in MV/cm, and we have used the result of Irwin

and Dalby[72] for the dipole moment (1.31 D).

Higher order perturbations were also calculated. Third order corrections are necessarily zero, since $M_{\Pi}=0$. Fourth order energies are found to be

$$\begin{aligned} F^{(4)}_{110} &= 5.763 \times 10^{-7}\ \varepsilon^4 \\ &= 0.134\ E^4 \\ &\leq 0.0005\ (cm^{-1}) \end{aligned} \qquad (152)$$

$$\begin{aligned} F^{(4)}_{000} &= -3.842 \times 10^{-7}\ \varepsilon^4 \\ &= -.0.08998\ E^4 \\ &\leq -0.0003\ (cm^{-1})\ . \end{aligned}$$

The last line is valid for $E = 0.288$ MV/cm, the highest usable field obtained in this work. We may thus judge that higher order effects in the $^3\Pi$ state are safely neglected.

5. Stark Effects in the $^3\Sigma^-$ State (N=0)

Examining the second order Stark effect in the J=1, N=0 level of the (v=0) X $^3\Sigma^-$ state, we note that Eq. (147) neglected the effects of spin splitting in the N=1 levels.* These may be partially included by substituting the appropriate term differences from Table XVII for the energy denominator 2B. Denoting term values by F_{NJM}, the second order corrections become

*See also the end of Sec. 7, below.

$$M=0: \qquad F^{(2)}_{010} = -\varepsilon^2\left(\frac{1/9}{31.56} + \frac{2/9}{32.51}\right)$$
$$= -0.01036\ \varepsilon^2 \qquad (154)$$
$$= -2.9206\ \mu_\Sigma^2 E^2$$

$$M=1: \qquad F^{(2)}_{011} = -\varepsilon^2\left(\frac{1/6}{33.36} + \frac{1/6}{32.51}\right)$$
$$= -0.01012\ \varepsilon^2 \qquad (155)$$
$$= -2.8547\ \mu_\Sigma^2 E^2 \quad ,$$

where the $^3\Sigma^-$ state dipole moment μ is in debye and the electric field E is in units of 10^6 V/cm. Thus a difference of some 2% appears between the components of different M. There is no hope of resolving components so close, but we should resist the temptation to average the two, and enquire as to their relative intensity. In an $^RQ_{21}$ transition, we have $J_\Pi = J_\Sigma$ so that (Landau and Lifshitz[1], p. 93) the intensity of light polarized parallel to the electric field ($M_\Pi = M_\Sigma$) is proportional to M^2. Since we are dealing with the center component (M_Π=0), we see that the intensity arising from transitions to the M_Σ=0 sublevel must be zero.

This "selection rule" against the M_Σ=0 component is somewhat relaxed by the presence of the electric field. This has been investigated in the standard manner, assuming that the intensity of the center component of the $^RQ_{21}$ (0) line is proportional to $<\psi^\Pi_{110}|\hat{n}|\psi^\Sigma_{01M_\Sigma}>^2$. From n_z we have a non-zero intensity for M_Σ=0 (parallel component),

while n_x and n_y yield the intensity (perpendicular component) when $M_\Sigma=1$. These two wavefunctions are expanded to first order, by Eq. (30), and terms in the intensity of higher than second order in ε are dropped. The resulting expression for $< \psi^\Pi | \hat{n} | \psi^\Sigma >$ contains similar matrix elements, related to the (square roots of) unperturbed intensities of the corresponding components (same M_Π and M_Σ) of other lines. These intensities were calculated from the formulae of Budo[117], and multiplied by the ratio of the intensity of the component in question ($M=0 \rightarrow M=M_\Sigma$, bearing in mind that if $M_\Sigma>0$ it labels two degenerate sublevels) to the total for the line (Condon and Shortley[64], p.63). Assuming that $\mu_\Pi = 1.3$ and $\mu_\Sigma = 1.5$, this procedure gives

$$I \text{ (parallel)} = 0.22\ E^2 \tag{156}$$

$$I \text{ (perpendicular)} = (0.94 - 0.04\ E)^2 \tag{157}$$

with E in MV/cm. Thus, even at the highest fields used in our experiments (0.3 MV/cm), the ratio I(parallel/ I(perpendicular) is little more than two per cent. We shall consider that this result justifies treating the center component of the $^RQ_{21}(0)$ line as being solely the perpendicular component ($M_\Pi=0 \rightarrow M_\Sigma=1$).

Stark effects have been investigated in third and fourth order, using Eqs. (33) and (35), matrix elements from Eq. (21), and energy levels given by $B_\Sigma N(N+1)$. Third

order effects are zero as expected. With $B_\Sigma = 16.375$ (Veseth[19]), the fourth order effect in the ground state is found to be

$$M=0: \qquad F^{(4)}_{010} = -0.285\ \mu_\Sigma^4 E^4 \tag{158}$$

$$M=1: \qquad F^{(4)}_{011} = -0.327\ \mu_\Sigma^4 E^4\ , \tag{159}$$

where μ_Σ is in debye and E is in MV/cm. These formulae will be further evaluated at the end of Sec. 7 below.

6. Experimental Results

The five photographs used in deriving the dipole moment of the $X\ ^3\Sigma^-$ state are shown in Fig. 40. These were calibrated as discussed in Sec. 1, originally with separate calibrations for the line tops (zero field) and bottoms (maximum field). Although these calibrations were used for the relatively inaccurate $^RP_{31}(0)$ line, it was felt that improved results could be obtained for the $^RQ_{21}(0)$ line by measuring the Stark shifts "directly" by a cyclic process of checking the line top, the line bottom, and the vertical alignment (this last using nearby N_2 lines). The resulting measurements are shown in Table XVIII, together with the electric fields obtained as described in Chap. VII, Sec. 2. In plate 275γ, the top of the $^RP_{31}(0)$ line is not visible, so in this case we have used the average position of the line top (29826.822 cm^{-1}) from

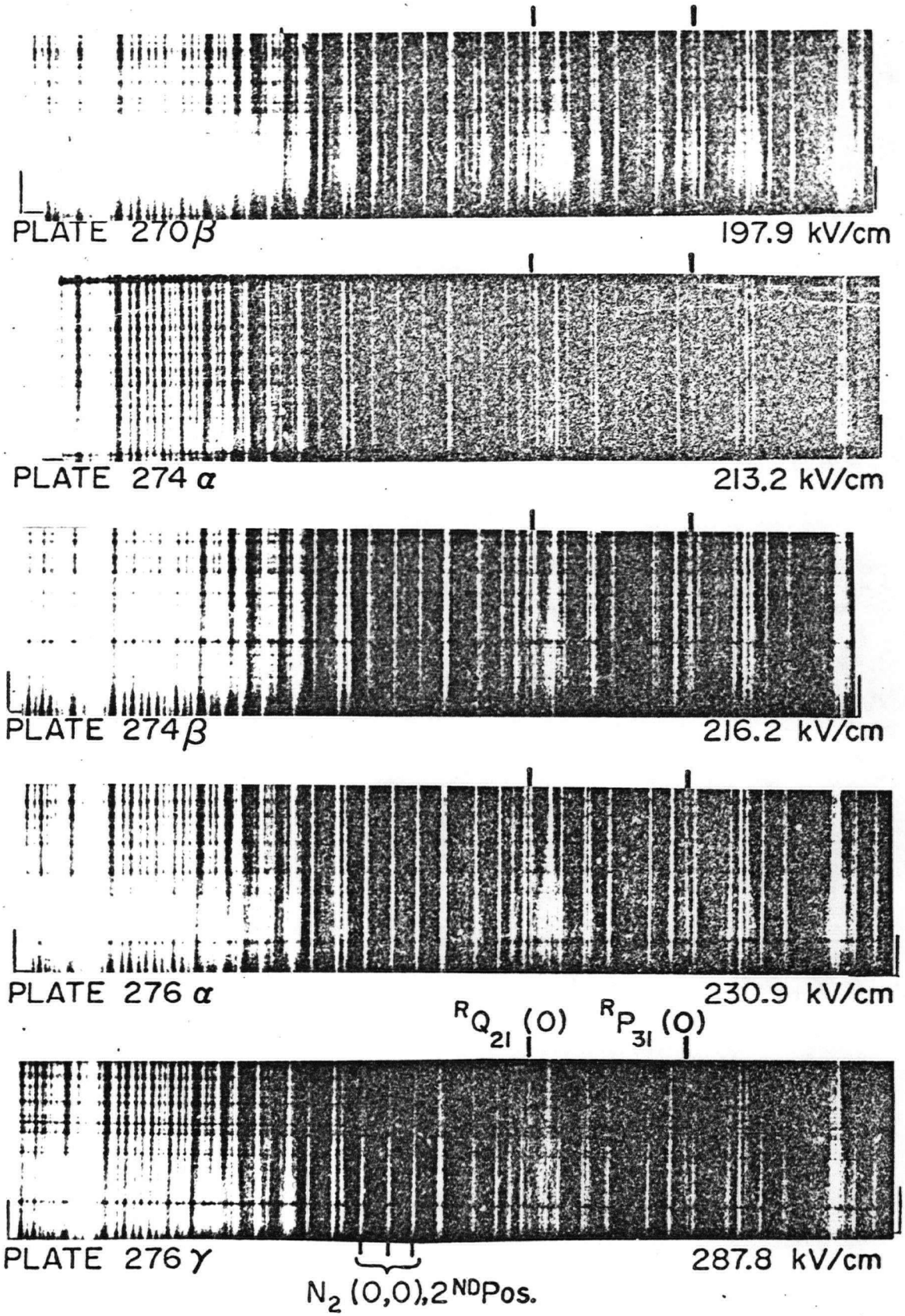

Fig. 40

The (0,0) $A^3\Pi \rightarrow X$ band of NH.

TABLE XVIII

Measured Stark Shifts in the $R_{Q_{21}}(0)$ and $R_{P_{31}}(0)$ Lines in NH $A \longrightarrow X$ (0,0)

Plate	$R_{Q_{21}}(0)$ (microns)	$R_{Q_{21}}(0)$ (cm^{-1})	$R_{P_{31}}(0)$ (cm^{-1})	E (kV/cm) (10^{-3}X(kV/cm)^2)
269β	17.0 ± 1.0	0.100 ± .006	0.27 ± .01	197.9 ± 1.0 (39.16 ± .40)
273α	22.0 ± 5.0	0.120 ± .020	0.21 ± .06	213.2 ± 3.4 (45.45 ± 1.4)
273β	20.3 ± 4.0	0.119 ± .024	0.16 ± .03	216.7 ± 0.8 (46.96 ± .34)
275α	25.6 ± 2.8	0.150 ± .016	0.26 ± .03	230.9 ± 1.2 (53.31 ± .55)
275β	39.9 ± 3.1	0.235 ± .018	0.53(?)	287.8 ± 2.3 (82.83 ± 1.3)

Note: the numbers in parentheses under each value of E represent E^2 after multiplication by 10^{-3}.

the other four exposures. The data for the $^{R}Q_{21}(0)$ line from Table XVIII are graphed in Fig. 41 against the square of the electric field. A best fit straight line was fitted to this data by means of an IBM library least squares fit program called DPLQF (Double Precision Least Squares Fit). The resulting slope, which we call R, is

$$R \equiv \frac{\Delta F^{(2)}}{E^2} = 2.74 \pm 0.30 \ (cm^{-1}/MV^2/cm^2) \tag{160}$$

This line is shown in Fig. 41, as are the error limits of Eq. (160). This tolerance is a cautious estimate based on inspection of Fig. 41. (The DPLQF program gave an error of only ± 0.06.)

Now the net Stark shift is just the difference between that in the $^3\Pi$ state and that in the ground state (counting shifts to higher frequency as positive):

$$\begin{aligned} \Delta F^{(2)} &= \Delta F_{\Pi}^{(2)} - \Delta F_{\Sigma}^{(2)} \\ &= 2.8547 \ \mu_{\Sigma}^2 E^2 - 2.8382 \ E^2 \ , \end{aligned} \tag{161}$$

substituting from Eqs. (150) and (155). Solving for μ_{Σ} gives

$$\mu_{\Sigma} = \sqrt{(R+2.84 \pm 0.13)/2.855} \tag{162}$$

where the error shown on the term from the $^3\Pi$ state is from Irwin and Dalby's error in μ_{Π} (= 1.31 ± 0.03). Using the

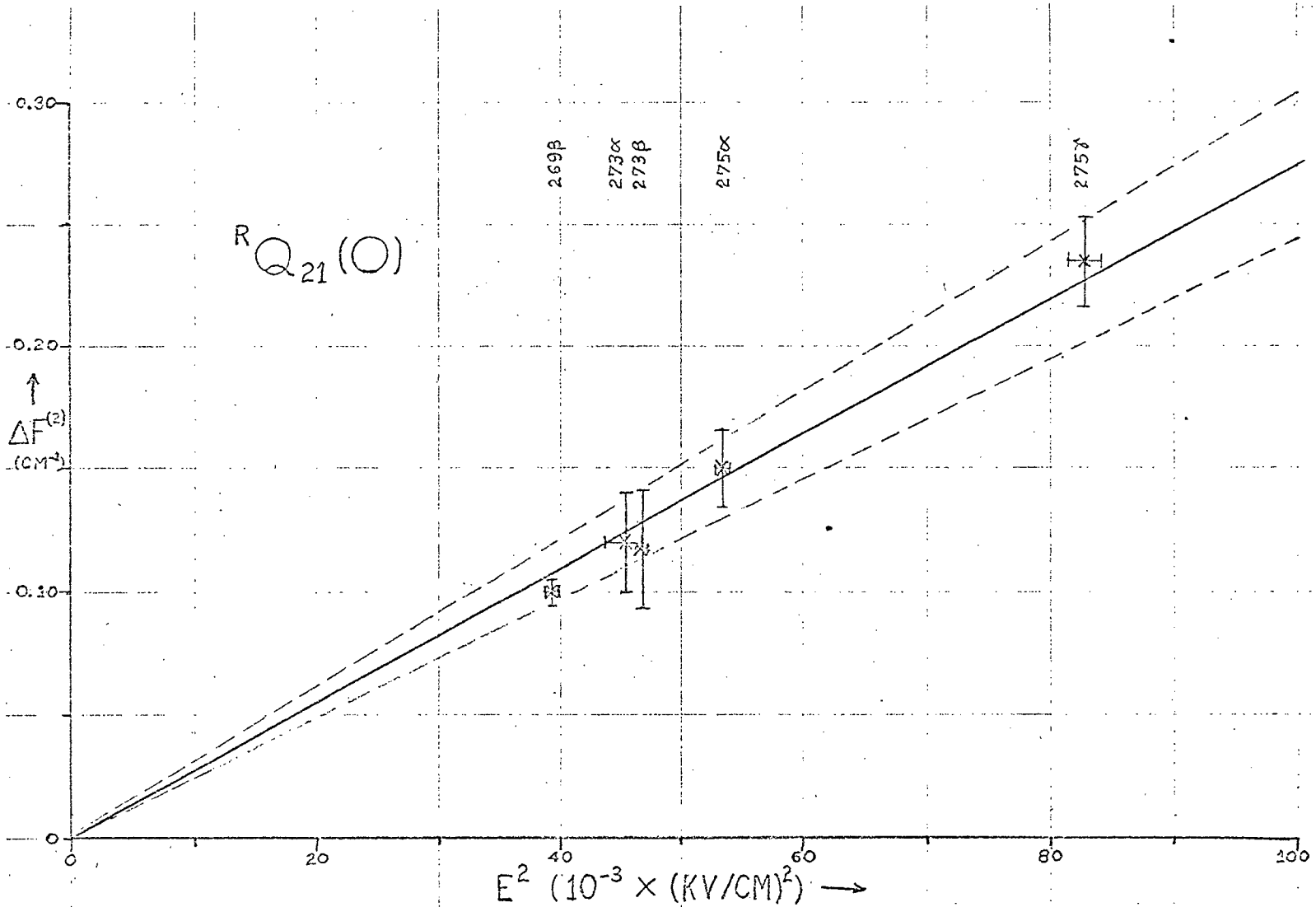

Fig. 41

Determination of μ_Σ from the $^{R}Q_{21}(0)$ Line.

value of R given by Eq. (160), we have

$$\mu_\Sigma = 1.39_8 \pm 0.04_3 \quad \text{(uncorrected)} , \tag{163}$$

and, after reducing this figure by 0.67% in accordance with Chap. VII, Sec. 2, we arrive at

$$\mu_\Sigma = 1.38_9 \pm 0.04_3 \tag{164}$$

for the dipole moment of the $X\ ^3\Sigma^-$ state of NH.

A wide variety of ab initio calculations is available for comparison, and have been brought together in Table XIX. Although no expectations could be derived from such a range of results, the most recent and sophisticated of these tend toward values higher than our own. The suggestion by Weinstock and Zare[102] that "the optical method of Dalby and coworkers may yield systematically high dipole moment values" does not seem to apply in this case unless these recent calculations are still quite inaccurate.

7. Other Considerations

In view of the corrections to the zero-field position found applicable in the case of the Σ state in OH (see Chap. IX, Sec. 3), the question might be raised as to whether some similar correction should be applied to NH. Since first order effects are not simultaneously observable in most cases (see Sec. 8), the same method

TABLE XIX

Comparison with Published Calculations of the Dipole Moment of NH ($X\ ^3\Sigma^-$)

Source	Dipole Moment (debye)
This work	$1.38_9 \pm 0.043$
Bender and Davidson[85]	1.587
Cade and Huo[84]	1.627
Harrison[118]	1.016
Kouba and Öhrn[119]	0.36
Joshi[120]	1.91
Grün[121] (various basis sets)	1.44-2.17
Boyd[122]	0.908
Krauss and Wehner[123]	0.85
Krauss[124]	0.90
Higuchi[125]	1.24
Hurley[126] (various methods)	0.83-1.94

cannot be used here. One can look at the five data points in Fig. 41 collectively, however. A small tendency may be noted wherein the points at higher field lie above the best fit line, while points at lower fields lie below it. Thus, if the best fit line were not constrained to go through the origin, we should obtain a higher slope. A reasonable fit to the five points alone will give $R = 3.025$ ($cm^{-1}/MV^2/cm^2$), and a dipole moment of 1.431 D from Eq. (162). Making the 0.67% reduction, would give $\mu_\Sigma = 1.421$ D, which is still well within tolerance of Eq. (164). Accepting this note of caution that the true value may lie to the high side, we shall continue to hold the result of Eq. (164) as our best value.

While measurements of the $^RP_{31}(0)$ line are too inaccurate to be used in evaluating μ_Σ, they may be checked for consistency with the above reult. The data for this line in Table XVIII is graphed in Fig. 42. Solving Eq. (162) for R, substituting Eq. (163) for μ_Σ, and substituting 0.157 for the 2.838 (Eq. 151), we derive a slope $R = 5.42$. This slope is represented by the straight line in Fig. 43, which is as good a fit as one could expect for such data (particularly recalling the fact that the line could not be measured at zero field in plate 275Y). We can see, however, that the larger deviations of the $^RP_{31}(0)$ line (as compared to the $^RQ_{21}(0)$) visible in Fig. 40, is in accordance with theoretical expectations.

When we use our dipole moment (Eq. 163) together with our highest field (o.2878 MV/cm) in the previous

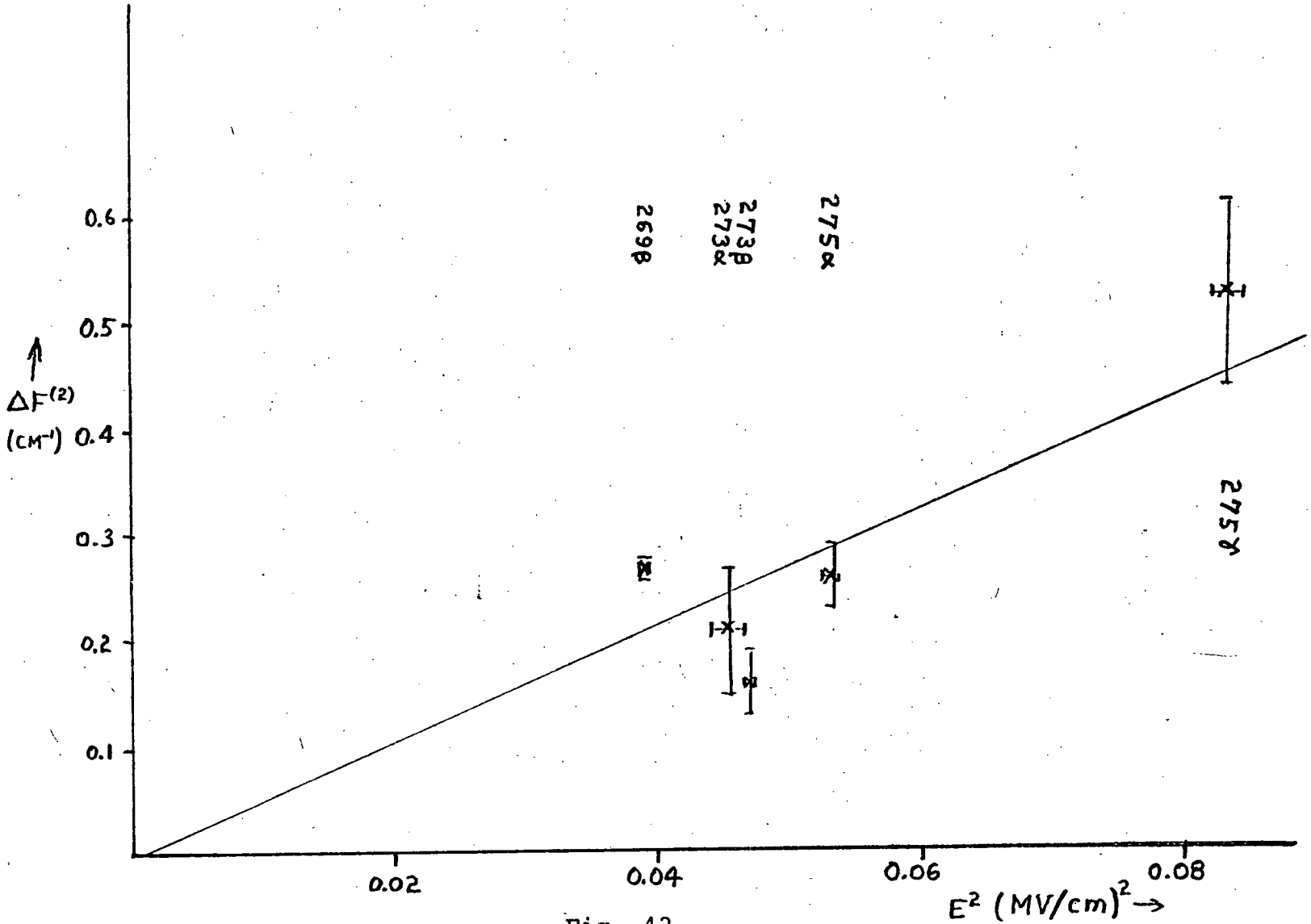

Fig. 42
Determination of the $^{R}P_{31}(0)$ Line from μ_{Σ}.

expressions for fourth order effect (Eqs. 158 and 159), we find that these corrections are less than 0.01 cm^{-1} in the energy levels under consideration. Fourth order effects will therefore be neglected.

The effects of the Stark interaction with the spin splitting can be neglected in the $N_\Sigma=0$ level, as long as the spin splitting in the $N_\Sigma=1$ levels is small compared to the energy denominators ($2B_\Sigma$) of the Stark perturbation. For $M_\Sigma=1$ the matrix elements in Eq. (155) are corrected by finding the eigenvectors of the $M_\Sigma=1$ submatrix (rows and columns labeled 5 and 7) of Eq. (176). The eigenvectors come from Eq. (48), after putting the submatrix into the form of Eq. (43) by subtracting half its trace (see App. D, Eq. D.18). At the highest field used (288 kV/cm), the matrix elements of Eq.(21a) are modified by over 25%, but the sum in Eq.(155) is lowered by less than 0.56%, which raises the dipole moment by less than 0.3%. Effects at lower fields are much smaller, and we shall feel justified in neglecting this interaction.

8. The $^3\Pi$ State

Our plates were examined to see whether the higher fields available would allow us to improve upon the dipole moment derived by Irwin and Dalby[72] for the $^3\Pi$ state. Components with $M_\Pi=1$ were usable in only two plates (269β and 275α), and then only the lower cm^{-1} side since the other was generally obscured by Stark components from the

$R_1(1)$ line. The observed displacements from the center component were 1.88 ± 0.04 cm^{-1} (269β) and 2.10 ± 0.04 cm^{-1} (275α). We take the second order shift of the $M_\Pi=0$ component to be as measured in Table XVIII, and the second order shift in the $^3\Sigma^-$ state to be given by Eq. (155) with the dipole moment of Eq.(163). We note that the second order effect in the $^3\Pi$ state for $M_\Pi=1$ is just $\frac{3}{4}$ of that for $M_\Pi=0$ (given by Eq. 150). After subtracting second order effects and the Λ-doubling (0.68 cm^{-1}, from Dixon[116]) appropriately, the dipole moment is obtained from an equation similar to Eq.(120). The resulting dipole moments (0.967 ± 0.023 D for 269β, and 0.938 ± 0.023 D for 275α) must be corrected for intermediate coupling (Irwin[71], p. 23f.) through division by $c_1^2 = 0.7354$ (Eq. 148).

We obtain

$$\begin{aligned} \mu_\Pi &= 1.31_4 \pm 0.03_1 \text{ D} \quad (269\beta) \\ \mu_\Pi &= 1.27_5 \pm 0.03_1 \text{ D} \quad (275\alpha) \ . \end{aligned} \tag{165}$$

We therefore have no cause to modify the conclusions of Irwin and Dalby that the dipole moment of the A $^3\Pi$ state of NH is 1.31 ± 0.03 D, since our values (no doubt based upon inferior data) are entirely consistent with theirs.

CHAPTER XII

SUMMARY OF RESULTS

We summarize the results of this work in Table XX, along with certain other calculated and experimental results relating to the dipole moment of first-row diatomic hydride molecules. It should be pointed out that the total body of literature,in the field of calculating wavefunctions and dipole moments, is quite large. We have chosen to compare experimental values principally with the work of Bender and Davidson[85] and of Cade and Huo[84], since these represent good examples of configuration interaction (CI) and self-consistent field (SCF) calculations, respectively. The richness of the literature can be surmised from a look at Table XIX dealing with NH; a study of LiH would produce a table many times that size.

All values refer to the ground vibrational states unless otherwise noted, and experimental (X) values are distinguished from calculated (C) by the letter in the third column.

TABLE XX

Dipole Moments of First-Row Diatomic Hydrides

Molecule	Dipole Moment (D)		Source and Comments
LiH ($X^1\Sigma^+$)	5.882	X	Wharton, et.al.[12.7]
	5.85	C	Bender and Davidson[85]
	6.002	C	Cade and Huo[84]

TABLE XX (Cont'd)

Molecule	Dipole Moment (D)		Source and Comments
BeH ($X\ ^2\Sigma^+$)	0.248	C	Bender and Davidson[85]
	0.282	C	Cade and Huo[84]
BH ($X\ ^1\Sigma^+$)	1.260 ± 0.21	X	Thomson and Dalby[75]
	1.470	C	Bender and Davidson[85]
	1.733	C	Cade and Huo[84]
($A\ ^1\Pi$)	0.58 ± 0.04	X	Thomson and Dalby[75]
CH ($X\ ^2\Pi_r$)	1.45 ± 0.06	X	Phelps and Dalby[70]
	1.427	C	Bender and Davidson[85]
	1.570	C	Cade and Huo[84]
($A\ ^2\Delta$)	1.12 ± 0.17	X	Phelps[14]
	0.887 ± 0.045	X	This Work
NH ($X\ ^3\Sigma^-$)	1.389 ± 0.043	X	This Work
	1.587	C	Bender and Davidson[85]
	1.627	C	Cade and Huo[84]
($A\ ^3\Pi_i$)	1.30 ± 0.03	X	Irwin and Dalby[72]
	1.34	C	Huo[128]
($a\ ^1\Delta$)	1.48 ± 0.06	X	Irwin and Dalby[72]
	1.64	C	Huo[128]
($c\ ^1\Pi$)	1.69 ± 0.07	X	Irwin and Dalby[72]
	1.85	C	Huo[128]
OH ($X\ ^2\Pi_i$)	1.720 ± 0.02	X	Phelps and Dalby[8]
	1.709 ± 0.029	X	This Work
	1.633	C	Bender and Davidson[85]
	1.780	C	Cade and Huo[84]
	1.66 ± 0.01	X	Powell and Lide[98]
	1.656 ± 0.04	X	Phelps and Dalby (v=1)[8]
	1.646 ± 0.051	X	This Work (v=1)
	1.626 ± 0.045	X	This Work (v=2)
	1.684 ± 0.032	X	This Work (OD,v=0)
	1.635 ± 0.023	X	This Work (OD,v=1)
	1.557 ± 0.061	X	This Work (od,v=2)
($A\ ^2\Sigma^+$)	1.946 ± 0.085	X	This Work
	2.142 ± 0.080	X	This Work (OD)
	1.72 ± 0.10	X	Weinstock and Zare[102]
HF ($X\ ^1\Sigma^+$)	1.820 ± 0.003	X	Weiss[129]
	1.816	C	Bender and Davidson[85]
	1.942	C	Cade and Huo[84]

For a more detailed survey of the literature involving ab initio calculations of the dipole moment, see the compendia of Krauss[130] and Richards, Walker, and Hinkley[131].

APPENDIX A

UNITS

The units employed in this work are derived from electrostatic cgs units. Energies symbolized by V or H (Hamiltonians) are in ergs, but the end result of all energy calculations will be expressed in the spectroscopic unit cm^{-1} (wavelengths/cm, symbolized by F or σ), the conversion factor being hc (erg-cm). The symbols W and δ (half the Λ-doubling) are in ergs in Chapter VI, but are in cm^{-1} in later chapters. Other symbols have units defined in the text. In Chapter VI, a superscript "σ" is used to indicate cm^{-1} units in some cases.

Thus the equations which introduce the molecular dipole moment (Chapter IV) contain the electronic charge e_i in statcoulombs, the electric field $\vec{E}$ in statcoulombs/cm^2 (commonly called esu), and all coordinates in cm^{-1}. Dipole or transition moments (μ and R, respectively) are then in statcoulomb-cm. $\vec{E}$ is usually converted to volts/cm as an aid to visualization, and dipole moments converted to Debye as a numerical convenience. Esu are multiplied by $10^{11}/c$ to give kilovolts/cm, and statcoulomb-cm are multiplied by 10^{18} to give Debye. Putting all this together, a term in the pertubation expansion usually contains some power of μE ergs, which becomes $\mu E/hc$ cm^{-1}, which is usually denoted by ε. Using $c = 2.99792 \times 10^{10}$ cm/sec, and $h = 6.6262 \times 10^{-27}$ erg-sec, μE ergs is expressed conveniently as $\mu E/59.5479$ cm^{-1} where μ is in Debye and E is in kV/cm, or as $E/0.0595479$ where E is in MV/cm.

APPENDIX B

QUANTUM NUMBERS, HUND'S CASES, AND SELECTION RULES

A brief summary of these is presented here for the convenience of the reader, who is referred to Landau and Lifschitz[1] (Secs. 27-31, 80-85), Hougen[2] (pp. 1ff.), and Herzberg[3] (Chap. V), for full discussion. Selection rules considered are only applicable to electric dipole transitions.

Quantum numbers used in this work are as follows:

J is called the total angular momentum of the molecule, excluding only nuclear spin. I.e., this angular momentum is $\sqrt{J(J+1)}\hbar$ erg-sec. J is always defined (by conservation of total angular momentum) in the abscence of electric fields, since coupling with nuclear spin is small, and obeys $\Delta J = 0, \pm 1$ except that $\Delta J=0$ is forbidden if $J=0$ (also if $\Omega=0$ and $\Delta\Omega=0$).

Ω is the component of J along the internuclear axis; i.e., $\Omega = \hat{n}\cdot\vec{J}$ where $\hat{n}$ is defined as for Eq. (4) below. Ω may be defined in all Hund's cases (Hougen[2], p.2) (but is made explicit in the notation for (a) and (c) only), and obeys $\Delta\Omega = 0,\pm 1$. Except in case (c), Ω is equal to $\Lambda+\Sigma$. Many authors define $\Omega = |\Lambda+\Sigma|$, but we will find it convenient to retain the sign.

M is the absolute value of the component of J along a laboratory-fixed axis, usually the z axis as defined by an external electric field. Allowed transitions may have $\Delta M=0,\pm 1$ but Stark interactions can only exist between levels of equal M. I.e., the Stark effect is diagonal in M. M is defined whenever a z axis is defined. Since the Stark effect does not distinguish the sign of M, we shall defy quantum mechanical convention by defining M to be the absolute value of J_z. In intensity calculations, such as the one referred to in Chap. XIV, Sec. 5, it must be remembered that the selection rule on M really includes a sign. E.g., $M=+1$ does not go to $M=-1$.

L is the total angular momentum of the molecular electrons. L is only well defined in Hund's case (d). In the three other cases considered in this work, L loses definition through the coupling of electronic motion with the internuclear axis.

Λ is the component of L along the internuclear axis; $\Lambda=\hat{n}\cdot\vec{L}$, defined except in Hund's case (c). Λ obeys $\Delta\Lambda=0,\pm1$. When defined, Λ is used to name electronic states: States with $\Lambda = 0,1,2,3,\ldots$ are called $\Sigma,\Pi,\Delta,\Phi,\ldots$ states (this "Σ" is a name, not to be confused with the quantum number defined below). Contrary to common usage, we will allow Λ to have negative values; thus a Π state is associated with $\Lambda=\pm1$.

N is the molecular angular momentum, but excluding electronic as well as nuclear spin. Herzberg[3] and most earlier authors use K for this quantity. N is defined in case (b) and (d), although its definition is often extended to levels described by case(a), when there is a gradual transition from case (b) to (a) at low values of J. N is sometimes used in place of J for singlet states, where they are the same. N obeys $\Delta N=0,\pm1$ except that $\Delta N=\pm1$ when $\Lambda=\Delta\Lambda=0$. N is defined formally in Chap. VII.

S is the total electronic spin. S is defined except in case (c). In other cases, S obeys the rule $\Delta S=0$, and is explicitly indicated by a left superscript $2S+1$ called the multiplicity.

Σ is the component of S along the internuclear axis; $\Sigma=\hat{n}\cdot\vec{S}$. Σ is defined except in case(c). In case (a) it obeys $\Delta\Sigma=0$.

R is the angular momentum of nuclear rotation, and is a valid quantum number only in case (d).

v is the quantum number of nuclear vibration along the internuclear axis. Selection rules are implied for v only by the overlap integral $R_{e',e''}\int\psi_{v'}\psi_{v''}dr$ whose square is proportional to the transition probability of the transition from v' to v". Only for infrared bands (e'=e"), and only for a pure harmonic oscillator potential does $\Delta v=0,\pm1$ hold.

p,± are rotational energy level parity indicators. "-" means that the total wavefunction changes sign under inversion at the origin; "+" means that it remains unchanged. Electric dipole transitions may

not occur between levels of the same parity.

± are also symmetry indicators (superscripts) on $\Sigma^{\pm}$ states (or $0^{\pm}$ states, in case (c)). Non-degenerate energy levels in diatomic (linear) molecules can suffer no physical change under a reflection of coordinates in any plane containing the internuclear axis. Therefore the electronic wavefunction remains the same, in a state designated by "-". Only transitions between states of like sign are allowed.

c,d, are rotational sublevel designators, in states with near-degeneracy ($\Lambda>0$). A sublevel of a Λ-doublet is designated "c" if its dependence of parity upon N is the same as a Σ^+ state, and "d" if the same as a Σ^- state.

a,s, are rotational energy level designators in homonuclear molecules. A level is antisymmetric "a" if the total wavefunction changes sign under interchange of nuclei, and symmetric "s" if it remains the same. Only transitions between levels of the same "a,s" symmetry are allowed.

g,u, are electronic state subscripts in homonuclear molecules. This is a symmetry property of the electronic wavefunction ψ_e, and is "g" if ψ_e remains unchanged (is "even") under inversion through the origin of all electron coordinates, and is labeled "u" if ψ_e changes sign (is "odd") under such an inversion. It differs from parity (±, above) only in that it applies to ψ_e instead of the total wavefunction, so that the nuclear coordinates are not involved, and the "g,u" designator applies uniformly to an electronic state (including all multiplet components) since it is independent of the vibrational and rotational wavefunctions (as well as electronic spin). Transitions between electronic states which are alike (in this symmetry type) are forbidden.

'," refer to the upper and lower levels of a transition, except where otherwise defined in Chap. VI.

Hund's cases:

Case (a) The electric fields along the internuclear axis (which can be visualized as resulting from the distortion of the electron clouds of the separated atoms through the process of forming the molecular bond) are strong enough to cause complete uncoupling (Paschen-Back effect) of the electronic orbital and spin angular momenta L and S. Properly

speaking, the field uncouples L from S, and the resulting component of L along the internuclear axis (Λ) produces a strong magnetic field to which S is coupled. The components of L and S along the internuclear axis are good quantum numbers (Λ and Σ, respectively). The angular momentum of nuclear rotation R is added to the algebraic sum of Λ and Σ (this latter sum being denoted by Ω) to form J. This strong coupling of the electron spin gives large multiplet splittings. Since Stark effects can not remove degeneracy with respect to the sign of the azimuthal quantum number (Λ), energy levels of electronic states with $\Lambda>0$ are doubly degenerate to a first approximation (Λ-doubling). States with $\Lambda=0$ cannot belong to case (a), in general, since L produces no net magnetic field and the electron spin itself cannot interact with electric fields. In Chap. VII and later chapters, case (a) wavefunctions are denoted by the ket $|\ \Lambda S\Sigma; \Omega JM\ >$ containing quantum numbers characterizing the state, and is often abbreviated to $|\ \Omega J>$ or even $|\ \Omega\ >$.

Case (b) is similar to case (a) except that the electronic spin is not coupled to L or any magnetic field along the internuclear axis. Nuclear rotation adds to Λ to form N, which then adds weakly with S to form J. $^2\Sigma$ states always belong to case (b), and Σ states of higher multiplicity (2S+1) are usually close to case (b). (When more than one electron contributes to S, some degree of spin-orbit coupling often takes place which makes a tendency toward case (c). Spin-spin interactions can also augment case (b)'s small multiplet separations.)

Case (c) occurs when S has become more strongly coupled to the magnetic field of L than L is coupled to the internuclear axis. Only the vector sum of L and S is coupled to the internuclear axis, leaving a net component Ω along it, and this is the only valid quantum number besides J and M (Hougens , p.2). Case (c) states are always "singlet" states, therefore, but may have a twofold degeneracy analogous to Λ-doubling when Ω is greater than zero. When $\Omega=0$, then 0^+ and 0^- states are defined similarly to the Σ^+ and Σ^- states of cases (a) and (b).

Case (d) occurs when the electronic angular momenta are completely decoupled from the internuclear axis, and interact only through nuclear rotation.

N is then formed as the vector sum of R and L which are coupled weakly enough that L remains a valid quantum number. S then couples very weakly with N to form J, so that spin splitting can be expected to be negligible.

APPENDIX C

GLOW DISCHARGES

1. Introduction

It is proposed that the form of discharge used to produce electric fields in this research is a special case of a glow discharge. Phenomenological and theoretical descriptions of this discharge can be found in a number of references.[21-27] Field and ionization measurements have been published by many authors over the last 70 years (see earlier references in Loeb[23] and Cobine[22]), those by Warren[28] being perhaps the most trustworthy. Numerical solutions for field and space charge conditions have been achieved by Ward[30-32], with some success. This background material will be summarized in the following subsections. The body of literature in this field is quite large, however, and it should be emphasized that a complete survey of recent progress has not been attempted.

2. General Characteristics

If two electrodes of flat surface are opposed to each other at some separation d, enclosed in a tube with moderate gas pressure (10^{-2} to 10^{2} mm of Hg), and connected to a power supply, then a characteristic voltage curve such as is shown schematically in Fig.C1 will be obtained upon

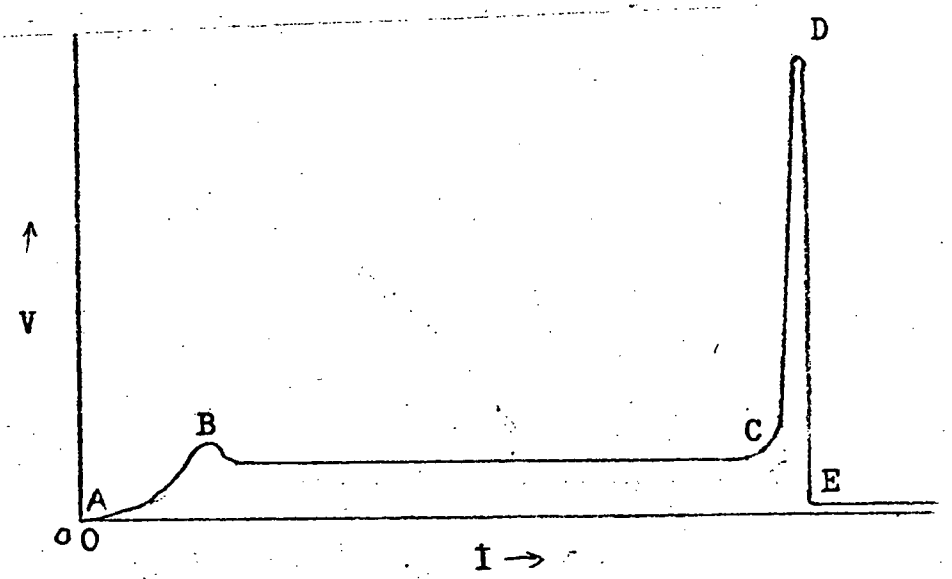

Fig.C1

Current-Voltage Characteristic of a Glow Discharge.

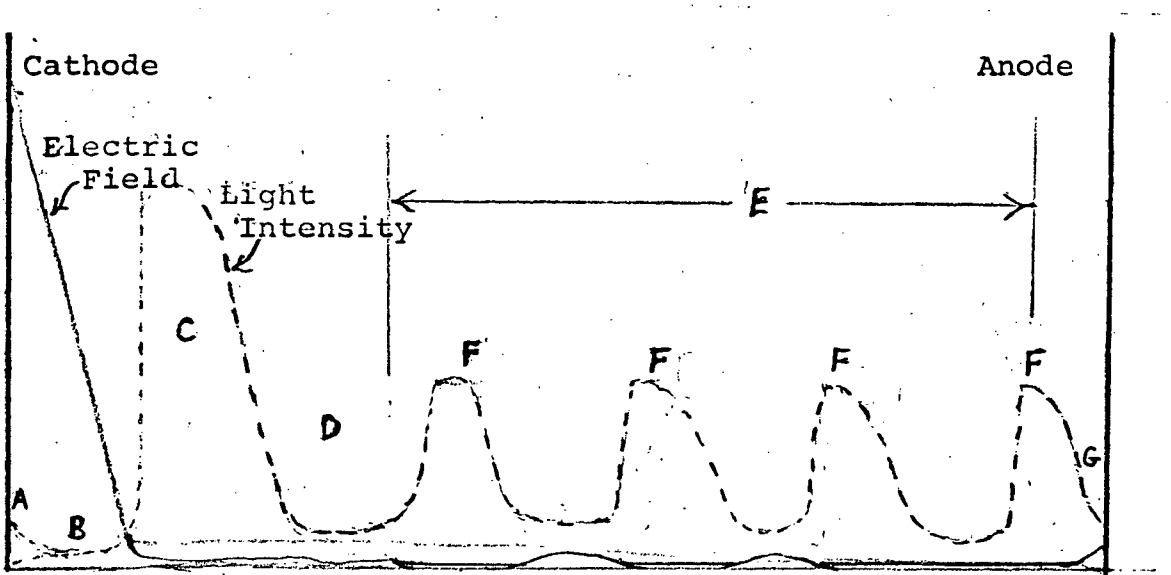

Fig. C2. Field and Intensity vs. position.
A- cathode glow; B- cathode dark space;
C- negative glow; D- Faraday dark space;
E- positive column; F- striations; G- anode glow.

variation of the current. It will be noticed that the portions of the curve to the right of points B and D have negative slope which results in instability and requires good current control properties in the power supply.

The region of Fig.C1 between A and B is a non-self-sustaining discharge, in the sense that it requires some current I_o of external origin (incident photons, may be supplied to the cathode for maintenance. This region is called the "subnormal" or Townsend discharge. If we define α (Townsend's first ionization coefficient) to be the number of ionizing collisions per length of path (along the electric field) per electron, then

$$dI/dx = \alpha(x)I(x) , \qquad (C.1)$$

which can be integrated to give the anode current:

$$I_a = I_o e^{\int_o^d \alpha(x)dx} . \qquad (C.2)$$

α may be more properly understood as a function of the field which, in turn, varies with position. This current will be increased by any mechanism augmenting the regeneration of electrons at the cathode. Now, the ionizations described by α will also create positive ions which will head toward the cathode and may produce electrons when colliding with the cathode material. If each ion hitting the cathode produces γ electrons, then

$$I_c = I_o + \gamma(I_a - I_c) \tag{C.3}$$

where I_c is the total current leaving the cathode. γ is called the second Townsend coefficient. Values of γ for low energy electrons are given in Cobine[22] (p.159). Replacing I_o by I_c in Eq.(C.2) and combining with Eq.(C.3) gives

$$I_a = I_o \frac{\exp(\int \alpha dx)}{1 - \gamma(\exp(\int \alpha dx) - 1)} . \tag{C.4}$$

At point B in Fig. 1, the discharge becomes self-sustaining. I.e., I_a becomes independent of I_o, and limited by other considerations (space charge). This is reflected in Eq.(C.4) by letting I_a be unbounded by the α and γ processes, setting the denominator equal to zero. That is,

$$1 = \gamma(\exp(\int_o^d \alpha dx) - 1) , \tag{C.5}$$

which is often written

$$1 + \frac{1}{\gamma} = e^{\int_o^d \alpha dx} . \tag{C.6}$$

Eq.(C.5) is readily understood: One electron leaving the cathode results in $\exp(\int \alpha dx)$ electrons at the anode through $\exp(\int \alpha dx) - 1$ ionizations along the way. These $\exp(\int \alpha dx) - 1$ ions produce $\gamma(\exp(\int \alpha dx) - 1)$ electrons from the cathode surface which must be exactly one, replacing the original electron. Warren[24] (p. 1658) calls this the "economy

condition", in the right side of which he inserts a multiplier (G) to account for ions losses to the tube walls and recombinations.

Alternative mechanisms to γ, such as photoelectric feedback or ionization of the gas by ions or neutral molecules, are deemed less probable (Loeb[23], pp. 383ff) but lead to indistinguishably similar economy conditions.

Field emission processes should also be considered at the high fields encountered in our experiments, but are not believed by this author to be important except in cathode break-in and in breakdown-to-arc processes (see Sec. 6 below).

Electron emission by impact of fast neutral particles would certainly reduce the ion to electron ratio. However, the economy condition (Eq.C.5,C.6) should be of the same form, since the numbers and energies of fast neutrals should be in proportion to those of ions (see Sec. 7). We need only make γ equal to the number of electrons released upon the impact of one ion plus all the fast neutrals which this ion generated on its way to the cathode.

3. Similarity Relations

It may be shown under reasonably general assumptions that if a discharge tube is altered such that

(1) all dimensions of size including mean free paths are multiplied by a fixed factor,

(2) the gas pressure is divided by this same factor, and

(3) the imposed voltage is unchanged,

then one obtains a scaled version of the original discharge with voltage distribution in exact proportion to the original. The "scaled" discharge will have different values of pressure (p), electric field (E), current density (j), and interelectrode (or other) spacing (d), but the combinations pd, E/p, and j/p^2 can be shown (see, e.g., Cobine[22], pp. 209ff) to be invariant under the change of scale. Thus E, d, and j are often expressed in these combinations for greater generality. In so far as similarity relations are obeyed, then j/p^2 and pd (where d is any characteristic length, such as the cathode dark space or Aston dark space) are each functions of only the cathode fall voltage V_c (Druyvesteyn and Penning[27], p. 131).

4. Normal and Abnormal Glow Discharges

Once the discharge is self-sustaining, current will drop with an increase in voltage (power supply permitting) to the plateau between B and C in Fig. 1, called the "normal" glow. As the current increases toward point C, the glow is observed to spread over the cathode in proportion to the total current, thus maintaining both a constant voltage drop V_n and a constant current density j_n/p^2 which have characteristic values for a given gas and cathode material. For an aluminum cathode under helium these are approximately 140 volts and 20 $\mu A/cm^2\text{-mm Hg}^2$, under hydrogen these are 170 volts and 90 $\mu A/cm^2\text{-mm Hg}^2$. If the current

density j were plotted along the abscissa of Fig.C1 instead of the current I, then between B and C would be a dip, rather than a flat region, with the normal glow at the bottom point.

Ward[32] (p.2791,2794) finds that the characteristics of the Townsend, transitional, and normal glow phenomena (constant V_n and j_n with changing area) may be accounted for by the assumption of a form for the ionization efficiency α/E (often denoted by η) as a function of E/p which achieves a maximum; he assumes that

$$\alpha/E = (p/E)A\exp(-B(p/E)^r) , \qquad (C.7)$$

where A and B are constants and $r=\frac{1}{2}$ for inert gases (He). This has a maximum at $E/p = B^2/4$. Eq. (C.7) with $r=1$ is the theoretical form for α derived by Townsend and other early workers (see Loeb[23], p.358-369 and Sec. 7, below).

In this view, when the cathode area has been covered by the discharge glow, (point C in Fig. 1), the current can only rise by increasing the field and therefore the applied voltage. The ionization efficiency will decrease rapidly with increasing E, according to Eq. (C.7), and even more so for molecular gases like H_2, for which Ward[32] finds that $r=1$ is a better fit to experimental data for α. Thus an increase in voltage is needed to produce any increase in current. This region is called the "abnormal glow" discharge

(principally to distinguish it from the "normal").

At some point (D in Fig.C1 depending on the materials used and the surface condition of the cathode, the abnormal glow will break down into an arc (E in Fig.C1. The mechanism of electron release in the cathode of an arc is quite different from that in the glow (where inelastic collisions between the ions and atoms of cathode metal predominate). In the arc the dominant mechanism is thermionic electron emission by Richardson's equation. Breakdown occurs when the cathode becomes sufficiently hot from the increased power dissipation in the abnormal glow, possibly initiated by field emission processes. This power is mostly dissipated in the cathode, since volt-amp losses are greatest in the cathode fall where ion energies and fast neutral energies are lost to the cathode, while electron and negative ion energies are dissipated in the nearby negative glow (see heat loss measurements quoted in Thomson and Thomson[33], pp. 365ff). At some point thermionic electron emission from the cathode may become comparable to collision processes, with this additional current producing still more heat. The process runs away and results in the sharply negative slope (instability) shown in Fig.C1.

The normal and abnormal glow discharges show a series of well known features, illustrated in Fig.C2 which shows the electric field strength and light intensity as functions of position between anode and cathode.

5. Aston Dark Space and Cathode Glow

The weak light intensity shown right at the cathode, marked A in Fig.C2, is called the cathode glow and is sometimes observed to be separated from the cathode by a narrow dark space (not shown in Fig.C2 nor observed in our apparatus) called the Aston dark space. The cathode glow is in the region of highest field and thus of greatest interest for the purposes of this work (along with the rest of the cathode dark space). A detailed discussion of these features will be deferred until Sec. 8, after the cathode dark space as a whole has been discussed.

6. The Cathode Dark Space

Most of the potential applied between cathode and anode appears across the cathode dark space (also called the cathode fall, or the Crookes or Hittorf dark space) which is labeled B in Fig.C2. The cathode glow is here considered as being a part of the cathode dark space. In the normal glow the cathode dark space has a characteristic length given in centimeters as $0.72/p$ for H_2 and $1.32/p$ for helium with aluminum cathodes (p in mm Hg), and is further characterized by the cathode fall voltages and current densities given in Sec. 4.

Once the cathode has been covered by the glow, and the discharge has entered the abnormal region, then the current density rises with increasing voltage, first very rapidly, then tapering off. For example, multiplying

the normal fall voltage by seven or eight produces a thousandfold increase in current (Cobine[22] p.228; Ward[32] p.2792). Aston[34] gave some empirical relationships among the parameters of the abnormal discharge; for hydrogen and helium over aluminum cathodes they are:

He:
$$j = 10^{-4}(V - 255)^2 p^2 \qquad (C.8)$$
$$d = 0.36/p + 0.0049/j^{\frac{1}{2}} \qquad (C.9)$$

H_2:
$$j = 3 \times 10^{-4}(V - 144)^2 p^2 \qquad (C.10)$$
$$d = 0.265/p + 0.0043/j^{\frac{1}{2}} \qquad (C.11)$$

where d is in cm, j is in mA/cm^2, and p is in mm Hg. These formulae do not describe these parameters in the range of our experiments, however.

The cathode dark space can be considered as the place where most of the action is, with the cathode side of the negative glow serving as a sort of surrogate anode which connects to a conducting (plasma) pathway for the return of current to the positive side of the power supply. The cathode serves as a source of electrons, not by thermionic emission as in an arc, but through the ion-collision or photoelectric processes described in Sec. 2. The "anode" at the edge of the negative glow may be a source of positive ions, unlike the real anode.

Our picture of the cathode dark space, then, consists of a current composed of electrons flowing one way,

and ions flowing the other, with ionizing collisons by electrons throughout the volume which augment both components. The current and space charge in this region are mostly due to the ions, however, since the ion-cathode collisions are of low efficiency (γ of Sec. 2) in producing electrons. Moreover, it is believed that most of the ionizing events within the dark space are caused by electrons rather than the slower-moving ions. A further assymetry is that such ions as enter the cathode fall region do so as a result of diffusion from the low-field negative glow region, and bear no direct relationship to the arrival of electrons at the negative glow "anode".

Loeb[23] (p. 568, 574) believes that the length of the dark space is determined by the requirement that it must encompass a sufficient number of ionizations to provide the electrons needed to carry the current past the dark space through regions where ions (or the fields to move them) are unavailable. He notes that the length of the normal glow dark is a bit more constant (varying by around a factor of two) for different cathode-gas combinations when expressed in terms of molecular free paths than in terms of distance (where differences by a factor of four or five are found): about 100 mean free paths is average. This argument seems a bit unreasonable, however, since the electrons evidently carry enough energy into the negative glow to produce the intense excitation and ionization found there (see Penning[35], for example), and the electric field should distribute itself

appropriately to draw the needed current.

Warren[24] (p. 1658) considers the cathode dark space length rather as that needed for an electron to engage in $1/\gamma$ ionizing collisions, which would ensure the electron's replacement, back at the cathode. He expresses the dark space length as about thirty ionic mean free paths (Warren[24], p. 1663), although Davis and Vanderslice's[36] work gives lower numbers (and often much lower, especially when the ion is not the ionized form of an abundant neutral, see Sec. 7). However, it should be the number of electron mean free paths which matters, since they do the ionizing. Electron free paths are the order of five or six times longer than molecular free paths by ordinary kinetic theory (Millman[21], p. 284) and may be considerably larger for very fast electrons (Cobine[22], P. 30), so reducing Loeb's 100 free paths to less than ten or twenty. Llewellyn-Jones[25] (p.93) says there are five electron free paths in the length of the dark space. Druyvesteyn and Penning[27] (p.135) say four to seven at 200 V drop, and 0.5 at 1000 V. Warren[24](p.1660) concludes from a consideration of available energy that there can be no more than five ionizing events per electron in a normal discharge (at higher potentials the available energy goes up but the collision cross-section and dark space length decrease). He estimates 1 to 10 ionizations per electron at low energies and 0.1 to 1 at higher energies. On the other hand, the required number ($1/\gamma$) is at least fifty.

The conclusion is that all necessary ionization

does not take place in the dark space, and some ions must be formed in the negative glow and fall into the dark space. Volkov[37] calculates that the ion current diffusing down from the negative glow is comparable in magnitude to that produced in the cathode dark space (his Fig. 3 puts the former very nearly equal to the average of the latter, for 1 mm Hg of H_2 over aluminum).

This author has found no mention in the literature of the possibility of field emission operating in conjunction with the γ-process under conditions of large cathode fall; the analysis of such a situation does not appear to be trivial. However, let us first assume that the introduction of a significant field emission electron current at the cathode will have no effect on the γ-process. Then this new current will reduce the net positive space charge in the cathode fall, thereby reducing the field gradient. Thus a negative feedback mechanism is established which should lengthen the dark space, increase the current, and reduce the gain in field strength at the cathode with given voltage increase. If the current is not restricted by the power supply, it would seem that the field induced current would increase the tube current by a substantial amount, in adding to both the α and γ-processes, assuming that ions contributing to these processes are not all coming from the negative glow. Clearly, if more than one ionization per electron is occuring in the dark space, then the field at the cathode may be increased rather than decreased and a runaway field emission process would quickly break down into an arc. Thus we

conclude that at the critical value of cathode field, the current should increase and either the glow should degenerate into an arc or the cathode field should prove difficult to increase. As will be seen below, no such phenomena have been noted for applied voltages far in excess of those reported here.

7. Ionic Collisions and the Shape of the Cathode Fall

The type of collision processes affecting ions in the cathode fall has been rather well established by the experiments of Davis and Vanderslice[36] who measured the energy spectrum by species at the cathode of moderately abnormal glow discharges. They received ions through a central pinhole in the cathode and sent them through energy and mass spectrometers. Their observations are well accounted for by their theory which made the following assumptions: (1) All ions come from the negative glow, or at least several free paths before the cathode. (2) The only effect of a collision is a complete transfer of all kinetic energy. (3) The collision cross section, and thus the mean free path f, do not change appreciably with field or kinetic energy. (4) The field increases linearly from zero at the negative glow ($x=d$, $V=V_c$) to maximum at the cathode ($x = V = 0$). According to assumption (2), the total number of ions N_o is a constant throughout the cathode fall, as is the number $dN_v = N_o\, dx/f$ of ions starting in the region of thickness dx at potential

V (and thus with potential energy eV). The fraction of these dN_V ions which reach the cathode without further collision is a function of the position x (at which the potential is V) and is $e^{-x/f}$. Thus the number dN_{cv} of ions reaching the cathode with kinetic energy eV is

$$dN_{cv} = N_o\, e^{-x/f}\, dx/f \ . \tag{C.12}$$

(Compare the different meaning of this formula in Loeb,[3] p. 647.)

Integrating a linear field dependence

$$-\frac{\partial V}{\partial x} = E = E_m \frac{(d - x)}{d} \tag{C.13}$$

subject to the boundary conditions of assumption (4), and solving for x in terms of V gives

$$x = d(1 - \sqrt{1 - V/V_c}) \ , \tag{C.14}$$

and a maximum field

$$E_m = -2V_c/d \ . \tag{C.15}$$

This immediately gives an energy distribution formula

$$dN_{cv} = \frac{(d/f)\, e^{-d/f} (1 - \sqrt{1 - V/V_c})}{2\sqrt{1 - V/V_c}} dV \ , \tag{C.16}$$

depending on the single parameter d/f. For lower values of d/f a number of ions will reach the cathode with full energy eV_c, having suffered no collisions.

The experimental results strongly suggested that the dominant collision type was symmetrical charge transfer, where an ion encountering its own species of neutral imparts very little energy to the neutral but takes an electron or electrons from it; after such a collision we have a new ion identical to the original but without kinetic energy, and a high energy neutral moving toward the cathode. For H_2^+ in H_2, Ne^+ and Ne^{++} in neon, Ar^+ and Ar^{++} in argon, and (with a large experimental error) He^+ in helium, good fits to theory were achieved yielding sizable cross sections (small values of f). H^+ in H_2 gave a good fit to the theory, with a small cross-section, but with a smaller-than-expected number of ions having full or nearly full energy eV_c. A proton exchange reaction $H^+ + H_2 \rightarrow H_2 + H^+$ combined with an abundance of H near the negative glow may be possible, but Eq.(C.16) could no longer apply exactly since momentum transfer must occur.

H_3^+ in hydrogen seems to fit theory with a moderately small apparent cross section and may be due to a proton exchange mechanism and possibly to formation from "H-pickup" reactions of H_2^+ with H_2. Based on the apparent cross section, some 40 times too many H_3^+ ions reach the cathode

at full energy eV_c, corresponding to the fact that ions originating in the negative glow cannot undergo symmetric charge exchange. He_2^+ in helium, and H^+ and H_2^+ from hydrogen impurities in inert gases, give constant numbers of ions (i.e., independent of V_c and d) with full cathode fall energy. These constitute most of the ionic current for H^+ and H_2^+ impurities, as expected since charge exchanges are ruled out. For He_2^+ there is in addition a low energy constituent which may result from the formation of the ion by the action of low energy electrons near the cathode.

These results do not rule out charge exchange between different species (e.g., $H_2^+ + He \rightarrow H_2 + He^+$ for hydrogen impurity in helium would lose the impurity ion altogether and gain the dominant species ion in accordance with its own distribution). We are left with a clarified picture, however, in which the cathode fall is a region wherein electrons (and perhaps protons) are exchanged rather than momentum. We are also given reason to expect an abundance of fast neutrals reaching the cathode, which clearly accounts for some of the discrepency between $1/\gamma$ and the number of dark space collisions.

The assumption of a linear electric field in the cathode fall (assumption (4) of Davis and Vanderslice, above, and Eqs. (C.13 - C.15) is based on experimental evidence as much as sixty years old (Aston[38]; Loeb[23], p. 578, Fig. 271), and shows the importance of space charge (without which the potential would be linear and the field constant). Warren[28]

has made what may be the best measurements to date using an electron beam as a probe. His curves show a semblance of linearity at higher pressures but with noticeable departures even then.

Warren[24] proceeded to make some calculations based upon simple assumptions: Maxwell's equation for the divergence of the electric field is

$$\frac{dE}{dx} = 4\pi(\rho^+ - \rho^-) = 4\pi\left(\frac{j^+}{v^+} - \frac{j^-}{v^-}\right) \qquad (C.17)$$

where x is distance from the cathode, j is current density, ρ is charge density, v is velocity, and the positive and negative signs make reference to ions and electrons, respectively. Warren[24] neglected the relatively small electron charge density, considered the ionic current density as a constant, and for ionic velocity used

$$v^+ = k(E/p)^{\frac{1}{2}} \qquad (C.18)$$

where k is some constant (mobility). This form was based on the previous work of a number of researchers (see Warren[24], refs. 10 - 13) and is claimed to hold for collision-limited motion at E/p values from 100 to at least 1000 volts/cm-mm Hg. These premises lead to

$$E \propto (Jx)^{\frac{2}{3}} \qquad (C.19)$$

where x is the position in the cathode fall, as measured

from the edge of the negative glow, determined as follows:

To eliminate certain small, peculiar, and sharp drops in the field near the negative glow, Warren extrapolated his field curves to zero (the effective negative glow "anode" location) and replotted them placing this point at a common origin for all curves. He found that plotting $E/J^{\frac{2}{3}}$ against x did indeed remove most of the dependence on J (at constant p) for H_2 and He, and, to a somewhat lesser degree, Ar, N_2, and air. Furthermore, the resultant curves were a close match to the $x^{\frac{2}{3}}$ dependence predicted by Eq.(C.19) at a pressure of 1 mm Hg (and moderately well at 0.3 mm Hg), but with marked deviations at lower pressure. On the whole, the dependence upon $J^{\frac{2}{3}}$ seems applicable over a wider range of pressure than the $x^{\frac{2}{3}}$ dependence.

The systematic inadequacy of Warren's calculated curves is evident at low pressures for all gases treated. This indicates that at lower pressures the net positive space charge is greatest near the cathode rather than near the negative glow (see Eq. (C.17). This is rather reasonable since at high pressures, collisions would keep ion energies too low to cause excitation. The gradual increase in ionic velocity together with the higher space charge from relatively slow electrons, causes the net space charge to fall off near the cathode. At lower pressures, ionization by electron impact becomes rarer since the electron free path becomes longer than the cathode fall, but ionization by ions more

frequent since the ion free path becomes long enough to allow ions to gain the large energies needed to have appreciable ionization cross section. The latter process would happen in the vicinity of the cathode and yield a stronger net positive space charge in the region since the high fields would remove electrons more quickly than ions. One might suppose that the inclusion of ion-impact ionization terms should substantially improve agreement with Warren's data. Examination of that data reveals that where $E/J^{\frac{2}{3}}$ turns out to be a function of J (contrary to Warren's theory) is at higher currents (and thus higher voltages) and lower pressure. Warren's limited publication of light intensity measurements also confirms these ideas, with light from near the cathode rivaling the negative glow itself under conditions of low pressure and high current and voltage in nitrogen (Warren[28], Fig. 17).

The concave field vs. distance curves which Warren found at high currents and low pressures resemble the results of this work, where much higher voltages (and current densities) are present. Ishida and Tamura[29] (p.173) have found that a function of the form

$$E = a_1 e^{-b_1 x} - a_2 e^{-b_2 x} \qquad (C.20)$$

fits their high-voltage observations (a_1, b_1, a_2, b_2 are positive constants for a given discharge condition, with a_2 and b_2 small and x measured from the cathode.

Ward[30-32] used a computer to solve numerically for the parameters of the glow discharge, using Eqs. (C.1) and (C.17) as a pair of coupled differential equations in E and J. Eq. (C.7) was used for $\alpha(E/p)$, with $r=1$ in diatomic and $r=\frac{1}{2}$ in inert gases. This functional form, $\alpha=e^{-1/y^r}$, goes from zero to one as $y \propto E/p$ runs from zero to infinity: It is a monotonically increasing but readily saturated function so that (as mentioned earlier) the ionizing efficiency $\eta \equiv \alpha/E$ passes through a maximum. This was noted by Ward[32] (p.2794) who appears to have been arguing that this can explain the normal discharge condition: Assuming that E is some monotonic function of J at some pressure p, then there is a value of J at which η is a maximum. Deviations from this value of J increase the effective resistivity of the discharge; thus if sufficient cathodic area is available, the area covered will adjust to give this value of J and a path of least resistance.

The electron mobility was found to be not critical and was treated as constant. Ward[30] (p.1857) found, in particular, that the electron mobility affects the Faraday dark space and positive column, while the cathode region is affected by changes in ionic mobility, as one would expect since these are the respectively dominant current carriers.

The primary result of these calculations was the formation of a cathode fall region with linear field connected to the anode by a neutral plasma (Ward[30], p.1856). The dominant current carriers were indeed ions in the cathode

region and electrons in the plasma. Calculated fields were found to obey Warren's $J^{\frac{2}{3}}$ law (Ward[30], p.1855), and rather good agreement was obtained with the bulk of Warren's observations (Ward[32], p.2794) for the inert gases (except at low pressures). Ward's calculations also verified the discharge's independence of the initial value of photoelectric starting current (I_o in Eqs. (C.2)-(C.4) above), once J exceeds the order of 1 mA/cm^2 (current densities encountered in experiments reported here were much higher).

Volkov[37] used a slightly different approach to solving Eq. (C.17) and was able to obtain a closed form solution applicable only in the cathode fall. (He made what appear to be much simpler assumptions about the form of $v^+(E)$, but included ions entering from the negative glow). He obtained close agreement with Warren's data for H_2 at 1 mm Hg, accounting for the small sharp drops in field mentioned earlier.

Another interesting discovery of Warren's, verified by Ward's and Volkov's results, is that replotting the field curves (after normalization by $J^{-\frac{2}{3}}$) with the origin at the edge of the negative glow for fixed pressure but different cathode materials, the curves follow each other quite uniformly from the origin, but extend different distances (corresponding to different cathode dark space lengths), depending upon the material and condition of the cathode.

8. More on the Cathode Glow

Thus it seems that good progress has been made in understanding the processes controlling the cathode regions of glow discharges, with a significant exception in the phenomenon of the cathode glow. No anomalies are found in any of the calculated or observed field curves near the cathode which could differentiate cathode glow from adjoining dark space, although the glow was definitely observed by Warren[28] (p.1656, Fig.17). The calculations by Ward[32] (p.2793f., Fig.9) of light intensity based only on electron current densities and early estimates of excitation efficiencies (Penning[35]) did not produce a cathode glow.

A natural supposition might be that electrons in the Aston dark space have insuffiecient energy to excite the gas and that the cathode glow begins where this energy has been attained. Holst and Oosterhuis[39] first observed under certain low-pressure conditions a whole sequence of glows (striations) extending into the dark space and separated by distance corresponding to the ionization potential of the gas (neon). Ward[32] (p.2790) calculated values for the size of the Aston dark space, defined as "the distance at which an electron can first attain the lowest excitation potential of the gas", and they agree fairly well with the earlier measurements on helium.

In spite of this evidence lending plausibility to an electron excitation process, Loeb[23] (p.570) felt that the electron density would be too low so near the cathode,

considering the low values of γ cited in his book, and that some process involving ions would be more likely. Warren[28] (pp.1655, 1657) agrees , noting that impurities of low excitation potential (nitrogen, for example) are much less dominant in the spectra of cathode glows than in the other bright regions of the discharge which,indicates that high energy particles are responsible. Warren[24] (p.1663) estimates that when E/p is high enough to allow ions to gain over 100 ev per mean free path (roughly 2000 v/cm for H_2^+ according to Davis and Vanderslice[36], p.227), the ionization probability per collision is about one per cent (Varney[40]) so that each ion will make an average of one ionizing collision. Moreover, excitation by energetic neutrals (which should be highly abundant according to Sec. 7) may have even larger cross sections than for ions and may be an even more important cause of gas excitation at the cathode.(See the discussion of Warren's measurements in Sec. 7. The glow has been seen to penetrate through and beyond small holes in the cathode, making electrons seem an unlikely mechanism.

Francis[26] (p.96f) and Druyvesteyn and Penning[27] (p.130) resolve this by suggesting that there are two different kinds of cathode glow. Once would occur at low pressures, exhibit the Aston dark space, and be induced by electrons. The other type is thicker, less sharply defined, often brighter (possibly masking the first type), and caused by ions or fast neutrals. The correlation of light intensity with particle

energies, as a function of position in the cathode fall, would be needed to clearly establish the mechanism of the cathode glow, but this would be a very difficult experiment by the methods of Warren.

9. The Radial Current Distribution

One further matter of importance in the cathode region is the fact that, as the voltage is progressively raised into the abnormal glow region, the current density does not remain uniform over the surface of the cathode. In early work, Chiplonkar[41] measured the current density as a rough function of radius by dividing the cathode into three concentric areas grounded through separate ammeters. Chiplonkar found that for voltages between 1000 and 6000 v the current density could be fitted to a Gaussian distribution e^{-hr^2}, where h is a function of voltage. (He actually decided that h better represented a function of dark space length: a rather questionable conclusion, especially since pressures were not reported.)

In the later work of Chiplonkar and Joshi[43,44], the radial distribution of ionic current density was measured by trapping the "canal" rays coming through a small movable hole in the cathode. Chiplonkar and Joshi[43] found that, in discharges maintained at constant current in hydrogen with an aluminum cathode, low voltages, and moderate pressures (e.g., 236 v at 0.5 mm Hg), the current density was fairly uniform over the cathode, dropping off slightly at the edges.

At higher voltage and lower pressure (e.g., 1800v at 0.033 mm Hg) the current was highly centralized and dropped to very small values well short of the edge. A region of fairly constant (maximum) current was always present in the center, but the curves gave the impression that for higher voltages (lower pressures) they might become truly Gaussian in appearance. A glass tube supported over the center of the discharge would further centralize a discharge, the greater the effect (unsurprisingly) the closer the tube to the cathode. Changing the total current at constant pressure (by moderate changes in voltage) had less effect on the radial current distribution than changing voltage and pressure at constant current. Applying an external positive potential to the outer tube walls had a small centralizing effect on the current. Voltages were applied only up to the supplied discharge potential difference. Kamke[44] used much higher voltages (20,000 - 30,000 volts) and obtained radial distributions which consistently showed a central peak far too sharply pointed to be truly Gaussian. He extended Chiplonkar's[41] measurements to conclude that a centralized discharge with a 4 mm radius (of half intensity) at 1000 volts would drop to around 0.5 mm radius at 20,000 volts. Kamke found that the use of an aluminum cathode caused a noticeably more centralized distribution of current, and reduced by some 25% the pressure needed to draw a given current, as compared to copper, carbon, or steel cathodes.

It appears that the centralization of discharge at

the cathode is nevertheless primarily due to the accumulation of positive charge at the walls. In the cathode fall region there are presumed to be many more ions than electrons carrying the current (see preceding sections), and that diffusion will therefore carry a predominantly positive charge to the walls. If most ionic collisions are purely charge exchange then we can expect a number of ions to be formed with thermal velocities moving toward the walls so that substantial potentials may develop at the walls which will serve to re-focus ions toward the center. It would seem that radial electric fields applied by Chiplonkar and Joshi[44] (p.146ff) must have been far lower than those occuring naturally from diffused wall charge. Only very near the cathode, where the electrons are still of low energy (and thus may contribute substantially to the net space charge), would their higher mobility allow them to reduce the wall potential. Chiplonkar and Joshi[45] (p.148f) added plausibility to radial charge diffusion as a mechanism with their finding that a magnetic field along the tube axis will serve to reduce the centralization of current. It is hard to visualize an alternative mechanism.

Chiplonkar and Joshi[43](p.1753) found that their integrated ionic current density accounted for only 5-10% of the total current, although this did not seem to shake their faith in the predominance of positive current carriers. Although the release of electrons at the cathode by fast neutrals would reduce the number of ions needed to maintain the discharge, it is felt that this result must be in serious

error.

10. The Negative Glow

We shall briefly discuss the remaining portions of the glow discharge, heretofore described as merely a conductor of neutral plasma connecting the "effective anode" at the end of the cathode fall to the real anode; these portions are not essential in the sense that they disappear as the anode is moved closer to the cathode, without affecting the cathode region. Although often larger and more spectacular than the regions already considered, theyhave less interest here.

The negative glow (marked C in Fig.C2)is a region of high luminosity and low electric field, which latter has been measured by Warren[28](p.1657) to be $\frac{1}{4}$ to $\frac{1}{2}$ volt/cm. This can be thought of as the region wherein the excess energy of electrons accelerated by the cathode fall is dissipated through ionizations and excitations. Indeed, the length of the negative glow has been correlated with the range of electrons in the plasma (Cobine[22]p.219, Fig. 8.6). It is clear that some net electric field must be maintained in the negative glow to maintain a neutral plasma; electrons are steadily arriving from the cathode and ions lost when they stumble into the fall.

11. The Faraday Dark Space

By the time they reach the Faraday dark space, labeled D in Fig.C2,few electrons are sufficiently energetic

to cause excitation (let alone ionization) and the density of charged particles declines as our point of observation moves towards the anode.

The principal mechanism is thought to be recombination at the walls. Since electrons have a much longer mean free path than ions, they will reach the wall more rapidly until sufficient negative charge is established on the wall to prevent further buildup. The electric field of this charge enhances the diffusion of ions to the wall, where they are neutralized and re-enter the discharge as gas, but in the steady state, a negative wall charge is maintained. (Warren's[24] (p.1662) statement that positive charges accumulate on the walls must certainly be an unintended error.) This process is likely to be present all along the discharge except in the cathode region (see Sec.10). Warren[28] (p.1654, Fig.16) has measured the wall potential and found it to be some 20% lower than that calculated from the average field across the tube diameter, except near the cathode. With large kinetic energies present in the negative glow, this process of charge depletion is relatively unimportant. In the Faraday dark space, however, it is thought to reduce the available space charge to the point that the tube current causes voltage differences to rise. The resulting field accelerates electrons to the ionization threshold (the start of the positive column) whereby the charge carriers are replenished. Warren's[28] (p.1657) measurements of field strength in the Faraday dark space are as low as, or lower than those in the negative

glow ($\frac{1}{4}$ to $\frac{1}{2}$ volt/cm), so either the mechanism or the measurements must be in doubt. (E.g., the 25 ev ionization potential of helium divided by $\frac{1}{2}$ volt/cm gives 50 cm for the length of the Faraday dark space, while Warren's entire tube was only 40 cm long!) Francis[26](p.179f) notes that in electronegative gases, where negative ions rather than free electrons predominate, most of the potential drop of the Faraday dark space exists across a very narrow layer just preceding the positive column. In H_2 and inert gases, however, the high mobility of free electrons makes such a narrow field region seem improbable as an explanation for Warren's low measurements. In any event it has been observed that the larger the tube (and thus the smaller the wall losses) the longer the Faraday dark space. Furthermore, in spherical discharge tubes, where there are no wall losses, the Faraday dark space reaches the anode. Warren's[24](p.1659) observation that the Faraday dark space is longer for higher currents and voltages (thus causing greater space charge excess) appears to be in contradiction with an earlier argument by Thomson and Thomson[33](p.358ff) (repeated by Cobine[22], p. 232f), that this length should be inversely proportional to the current (or, at low pressures, to the square root of the current).

12. The Positive Column, Plain

When electron energies are sufficiently increased to cause renewed ionization (and excitation) the positive

column begins. Fig.C2 shows the column (marked E) as being striated with peaks of light intensity marked F, although unstriated columns are more common. In the unstriated column, it is imagined that the diffusion losses to recombinations at the walls, discussed in the last section, are continuing and are compensated by particles from new ionizations caused by a field which (through the effective resistivity of the plasma) adjusts itself to this end. Warren's[28](p.1657) field measurements here give one or two volts/cm. Ward's[30](p.1856, Fig.10) calculations show a field of over 5 volts/cm along a positive column with pd = 10 cm-mm Hg (d is the anode-cathode gap), the field being roughly proportional to pressure; this is the field necessary to overcome the intrinsic resistivity due to pressure-decreased mobility, and does not even include wall losses. Thus it appears that Warren's measurements may well be in error in these low-field regions, although they have been described as a classic experiment (Volkov[37]). It is well to point out, however, that there is never any certainty that an apparently uniform column does not contain rapidly moving striations (Francis[26], p.114). We shall ignore this possibility and, in fact, the whole difficult subject of moving striations, since they are usually not visible in our apparatus.

13. The Positive Column, Deluxe

With some gases, under the proper conditions, striations of high contrast appear. It is generally supposed

that the mechanisms underlying striated and unstriated positive columns are the same, but that conditions are more uniformly defined along the discharge axis under some conditions, allowing zones of alternate acceleration and ionization/excitation to become visible. Loeb[23](p.573) summarizes an argument to the effect that striations may be destroyed through the transportation of excitation energy by metastable excited atoms or molecules, which can travel independently of the electric fields. It follows that mixtures or impurities (having a component with ionization potential lower than the metastable excitation energy) can be the vehicles by which metastable excited states may be deactivated ("Penning effect"), destroying said energy transport process and allowing striations to appear.

Warren's[25](p.1657, Fig.18) field measurements upon striated positive columns seem eminently more reasonable than those previously mentioned for the unstriated type. His graph shows fields averaging around 7 volts/cm and varying over the course of each striation by 1 or $1\frac{1}{2}$ volts/cm either way. He obtained potential drops between striations along the axis which correspond to the ionization potential in inert gases and to about double the ionization potential in diatomic gases. These potential drops, moreover, appear to depend only on the gas and not on the pressure or current, lending further plausibility to the proposed mechanism.

14. The Anode

A mechanism is roughly described by Loeb[23](p.596f) and Cobine[22](p.246f) for the generation of a fall of potential at the anode. Basically, it would seem that the repulsion of the ions in the plasma by the anode would keep the region fairly well clear of ions, leaving a net negative space charge, which, by Maxwell's equation (Eq. C.17), creates an electric field of positive slope (increasing toward the anode). Since electrons are far more readily moved by a field than are ions, the net electronic space charge near the anode is far smaller than the ionic space charge in the cathode fall, and the electric fields correspondingly smaller. In other words, where the carriers are electrons (at the anode), much smaller fields are needed to move the discharge current than where the carriers are ions (at the cathode). Loeb also argues for the necessity of accelerating electrons hard enough to create new ions which can replace ion losses to the walls and into the plasma, although there may be some circularity in this. Ward's[28](p.1856) computer-generated potential curves do show a small anode fall, and his rather roughly calculated light output curves (Ward[32], p.2794) seem to exhibit an anode dark space for the highest current density shown.

APPENDIX D

SOME BACKGROUND IN MOLECULAR QUANTUM MECHANICS

To review the principles involved, when the Hamiltonian matrix is diagonal, then all of the wavefunctions ψ_j (with respect to which the matrix elements have been taken: $H_{ij} = \int \psi_i^* H \psi_j \, dq$) are eigenfunctions of H and thus describe actual states of the system. For example, consider state ψ_1: Operating on ψ_1 with the diagonal Hamiltonian in a matrix representation:

$$H\psi_1 = \begin{pmatrix} H_{11} & 0 & \cdots \\ 0 & H_{22} & \cdots \\ \vdots & \vdots & \vdots \end{pmatrix} \begin{pmatrix} 1 \\ 0 \\ \vdots \end{pmatrix} = H_{11} \begin{pmatrix} 1 \\ 0 \\ \vdots \end{pmatrix} = W\psi_1 \quad , \tag{D.1}$$

showing that ψ_1 is a possible state of the system with energy $W = H_{11}$. If the Hamiltonian is not diagonal, then ψ_1 may not be an eigenfunction of H, but in general some combination

$$\phi_i = \sum_j c_{ij} \psi_j \tag{D.2}$$

will be. The coefficients c_{ij} are the elements of a matrix C which transforms each ψ_j (a column vector which is all zeroes except for a 1 in row j) into one of the actual

eigenvectors Φ_i. In matrix notation (C and H are matrices, Ψ and Φ are vectors, and W is a scalar):

$$H\,\Phi_i = W\,\Phi_i \tag{D.3}$$

$$H\,(C\Psi_j) = W(C\Psi_j) = C(W\Psi_j) \quad . \tag{D.4}$$

Now, is is postulated that C is a unitary transformation, (thereby preserving the length: If $\Phi=C\Psi$ then $\Phi^\dagger\Phi=\Psi^\dagger\Psi$ where "†" means the transposed complex conjugate), wherefrom it may be shown that $C^{-1} = C^\dagger$ so that Eq. (D.3) becomes

$$(C^\dagger HC)\Psi = W\Psi \quad . \tag{D.5}$$

Thus the transformation C has two interpretations: From Eq. (D.3) it transforms the vector of the basis set functions Ψ into the eigenvectors of H. Alternatively, by Eq. (D.5) C transforms H into an operator $C^\dagger HC$ which is diagonal with respect to the basis Ψ.

Eq. (D.4) may be written out as

$$\sum_j (H_{ij} - W_n\delta_{jn})c_{jn} = 0 \quad . \tag{D.6}$$

It may be shown that Eq. (D.6) has a solution, in which not all the c_{jn} are zero, only if the determinant of the expression in parentheses vanishes, and from the resulting equation all possible eigenvalues W_n may be found.

Substituting these eigenvalues back into Eq. (D.6) gives a system of simultaneous equations which, in conjunction with the normalization condition

$$\sum_j c_{jn}^2 = 1 \qquad \text{(D.7)}$$

determines the c_{jn} to within a constant phase factor.

In practice, general formulae will be used for the case of 2×2 matrices, while for larger matrices it is convenient to use numerical solutions.

The Molecular Hamiltonian

The first step in following the procedure described in the last section is to set up the appropriate Hamiltonian and to evaluate its matrix elements with respect to some convenient basis set of wavefunctions. We shall not deal with any interactions between electronic states, nor shall we include any of a number of finer interactions such as spin-spin, spin-rotation, or rotational distortion terms (see Merer[16], for example). It will be sufficient for our needs to consider only (1) a pure rotational Hamiltonian H_r along with (2) a spin-orbit term H_{so} and (3) an unspecified term H_{ev} which is assumed constant for the electronic and vibrational state under consideration:

$$H = H_{ev} + H_{so} + H_r \ . \qquad \text{(D.8)}$$

H_{so} and H_r may be readily written as

$$H_{so}/hc = A\,\vec{L}\cdot\vec{S} \tag{D.9}$$

$$H_r/hc = B\,\vec{R}^2 \tag{D.10}$$

where A and B are referred to as the spin coupling and rotational constants, respectively, and have units of cm^{-1}. R (nuclear rotation) is not a good quantum number in Hund's cases (a) and (b), so we will need to express its operator in terms of others which do have valid quantum numbers. In our notation, (ξ,η,ζ) are a set of cartesian coordinates fixed in the molecule with origin at the center of positive charge and both nuclei imbedded in the ζ axis. R_ζ is necessarily zero, since $\vec{R}$ does not include nuclear spin or electronic angular momenta. Now,

$$\vec{J} = \vec{R} + \vec{L} + \vec{S}\ , \tag{D.11}$$

so we may write Eqs. (D.9) and (D.10) in molecule-fixed components as

$$H_{so}/hc = A(L_\xi S_\xi + L_\eta S_\eta + L_\zeta S_\zeta) \tag{D.12}$$

and

$$\begin{aligned} H_r/hc &= B(R_\xi^2 + R_\eta^2) \\ &= B(J_\xi - L_\xi - S_\xi) + B(J_\eta - L_\eta - S_\eta)^2 \\ &= B(J_\xi^2 + J_\eta^2 + L_\xi^2 + L_\eta^2 + S_\xi^2 + S_\eta^2) - 2B(J_\xi S_\xi + J_\eta S_\eta + J_\xi L_\eta + J_\xi L_\eta) \\ &\quad + 2B(L_\xi S_\xi + L_\eta S_\eta) \quad . \end{aligned} \tag{D.13}$$

We define the "raising" and "lowering" operators J_+ and J_- by

$$J_\pm \equiv J_\xi \pm iJ_\eta \ , \tag{D.14}$$

and $L_\pm$ and $S_\pm$ analogously, it easily follows that

$$L_+S_- + L_-S_+ = 2(L_\xi S_\xi + L_\eta S_\eta) \tag{D.15}$$

with similar formulae obtained by substituting J for either L or S. Using these relations, and the fact that $J^2 - J_\zeta^2 = J_\xi^2 + J_\eta^2$ (and similarly for L and S), we have

$$\begin{aligned} H/hc &= H_{ev}/hc + AL_\zeta S_\zeta + B(J^2 - J_\zeta^2) + B(L^2 - L_\zeta^2) + B(S^2 - S_\zeta^2) \\ &\quad - B(J_+S_- + J_-S_+) - B(J_+L_- + J_-L_+) + (B + \tfrac{1}{2}A)(L_+S_- + L_-S_+) . \end{aligned} \tag{D.16}$$

The Diagonal Matrix Elements of the Hamiltonian

Since we are assuming case (a) wavefunctions, in which J, S, Ω, Λ, and Σ are all valid quantum numbers, we may evaluate most of the first line of Eq. (D.16) immediately, replacing

$$J^2 \rightarrow J(J+1)\hbar^2$$

$$S^2 \rightarrow S(S+1)\hbar^2$$

$$J_\zeta \rightarrow \Omega\hbar$$

$$L_\zeta \rightarrow \Lambda\hbar$$

$$S_\zeta \rightarrow \Sigma\hbar \ .$$

It must be remembered that these terms are all zero when evaluated between wavefunction differing in any of the quantum numbers; i.e., they are diagonal with respect to all of them.

The term involving L cannot be evaluated since L is not a good quantum number for case (a). It would seem that Eq. (D.16) has gained nothing over Eq. (D.10); however, L (unlike R) can be taken to be diagonal with respect to Λ, S, Σ, and Ω, and furthermore can be shown to be independent of these quantum numbers. (This result is dependent upon the separability of the spin and orbital wavefunctions and therefore the smallness of spin-orbit coupling energies; see Hougens[2], p.25. Since the magnitude of Λ is fixed for the electronic state, it is actually the sign of Λ of which $< L^2 - L_\zeta^2 >$ is independent.) The term $B(L^2 - L_\zeta^2)$ is therefore a constant within any given electronic

state and will hereafter be assumed to be absorbed within H_{ev}. The matrix elements of the first line of Eq. (D.16) are thus readily evaluated. In summary, they appear only on the diagonal of the full matrix, and they include a constant term $H_{ev} + B(L^2 - L_\zeta^2)$, which will normally be omitted. Omission of the constant terms (i.e., subtracting the identity matrix multiplied by the constant) is justified by considering the diagonalization of H:

$$C^\dagger H\, C = D \tag{D.17}$$

where D is a diagonal matrix containing the eigenvalues of H (multiplication from the right by a vector Ψ makes Eq. (D.17) equivalent to Eq. (D.4)). Then if k represents the constant matrix element of $H_{ev}/hc + B(L^2 - L_\zeta^2)$, and I is the identity matrix,

$$\begin{aligned} C^\dagger(H - kI)C &= (C^\dagger H - C^\dagger kI)C \\ &= C^\dagger H\, C - C^\dagger kI\, C \\ &= D - kC^\dagger C \\ &= D - kI \end{aligned} \tag{D.18}$$

which is also diagonal. Thus the omission of k makes no change in the eigenvectors (C) which diagonalize H, but causes the eigenvalues to each be low, each by an amount k.

The Off-Diagonal Matrix Elements of the Hamiltonian

The second line of Eq. (D.16) contains only the "raising" and "lowering" operators whose matrix elements are well known; their effects on a wavefunction, characterized by Λ, S, Σ, Ω, J, and M and written $|\Lambda S\Sigma; \Omega JM>$, are given by

$$S_{\pm} |\Lambda S\Sigma; \Omega JM> = \hbar\sqrt{S(S+1) - \Sigma(\Sigma\pm1)}\, |\Lambda S\ \Sigma\pm1; \Omega JM> \quad (D.19)$$

$$L_{\pm} |\Lambda S\Sigma; \Omega JM> = \hbar\sqrt{L(L+1) - \Lambda(\Lambda\pm1)}\, |\Lambda\pm1\ S\Sigma; \Omega JM> \quad (D.20)$$

$$J_{\pm} |\Lambda S\Sigma; \Omega JM> = \hbar\sqrt{J(J+1) - \Omega(\Omega\pm1)}\, |\Lambda S\Sigma; \Omega\pm1\ JM> . \quad (D.21)$$

Thus, in a typical calculation, the only non-zero matrix element of L_+S_- may be

$$\begin{aligned} &<\Lambda'S'\Sigma'; \Omega'J'M'|L_+S_-|\Lambda S\Sigma; \Omega JM> \\ &\quad = \hbar^2\sqrt{(S(S+1) - \Sigma(\Sigma-1))(L(L+1) - \Lambda(\Lambda+1)} \\ &\qquad \times \delta_{\Lambda'\Lambda+1}\delta_{S'S}\delta_{\Sigma'\Sigma-1}\delta_{\Omega'\Omega}\delta_{J'J}\delta_{M'M} \end{aligned} \quad (D.22)$$

The reversal of sign in Eq. (D.21), as compared to Eqs. (D.19) and (D.20), requires some explanation. It stems from the fact that we are using molecule-fixed coordinates: L and S may be definable in this system, but J includes the nuclear rotation so that the effect of its components in the rotating frame is not obvious. Van Vleck[17] has shown that the commutator of J (e.g., $J_\xi J_\zeta - J_\xi J_\zeta$) in molecule-

fixed coordinates have signs opposite to those of the normal commutation relations (i.e., of J in the space-fixed system or of L and S in either system.), by taking the (normal) space-fixed relations through the coordinate transformation in a straightforward manner. This in turn produces the sign change in Eq. (D.21). We may notice however, that this peculiar sign is necessary to obtain non-zero matrix elements for the terms, in the second line of Eq. (D.16), which are consistent with the condition $\Omega = \Lambda+\Sigma$. Whenever (for example) Σ increases, Ω must increase and the term J_-S_+ accomplishes just this. This problem stems from the rather peculiar role of the quantum number Ω in the theory of linear molecules: Because R_ζ is always zero, Ω can be considered either as a space-fixed system quantum number J_ζ, or a molecule-fixed parameter $\Lambda+\Sigma$. The requirement that these be equal implies that the raising and lowering operators of L,S, and J may occur in no other combinations (of order less than quartic) than are found in Eq. (D.16).

Finally, we may note that the last two terms of Eq. (D.16) contain L_+ and L_- and thus connect wavefunctions which differ in Λ by one unit. It is these Coriolis terms which are responsible for the interactions of Π states with Σ and Δ states, causing Λ-doubling (when the states are far apart). However, a single case (a) or (b) electronic state consists of wavefunctions with $+\Lambda$ and $-\Lambda$ only; since Λ may not be half integral these

never differ by unity and such terms contribute nothing. The off-diagonal matrix elements are thus due only to the term $-B(J_+S_- + J_-S_+)$.

A note of caution must also be added if the Hamiltonian of Eq. (D.16) is to be applied to interactions between different electronic or vibrational states. The factors A and B are in fact functions of internuclear distance (B is proportional to r^{-2} while A varies as $(dV/dr)r^{-1}$). Unless it can be assumed that the two interacting states have the same values of L and S (the "pure precession" hypothesis), A and B cannot be treated as constants and matrix elements will have to be integrated explicitly over r to include these dependencies. Furthermore, L and S must then be replaced by the sums over individual electrons which they normally symbolize.

APPENDIX E

CALCULATING THE MATRIX ELEMENTS OF n_z

1. Summary of Related Formulae

This appendix will summarize the formulae and methods of computing the matrix elements of n_z:

$$< \psi_m | n_z | \psi_{m'} > = \int \psi_m^* \, n_z \, \psi_m \, dq \qquad (E.1)$$

were m and m' denote the aggregates of all quantum numbers specifying the wavefunctions, and q the aggregate of all coordinates, the latter being integrated over all possible values. These matrix elements will be sufficient to calculate the Stark effect, with the help of the perturbation theory discussed in Chap. IV: the matrix elements of n_x and n_y enter into intensity calculations but not the Stark effect, and will not be discussed here.

We will be able to use the various coupling schemes of the angular momenta (see App. B) to simplify the calculation of Eq.(E.1). That expression can be resolved into a small number of partial factors which are commonly available in standard forms, without ever having to deal with the wavefunctions themselves.

The most complicated general case with which we shall deal is a matrix element of the form

$$< \; N \; J \; M \; |n_z| \; N' \; J' \; M' \; > \qquad \text{(E.2)}$$

which represents a case (b) type of coupling: the diatomic molecule has an angular momentum along $\hat{n}$, which is combined with the end-over-end (nuclear) rotation of the molecule to form the angular momentum $\vec{N}$. Thus, $\vec{N} = \vec{R} + \vec{\Omega}\cdot\hat{n}$, and $\vec{\Omega} = \vec{N}\cdot\hat{n}$. Furthermore, $\vec{N}$ is coupled (weakly) to the spin ($\vec{S}$) to form $\vec{J}$ which can be quantized with component M along the space-fixed z axis. Simplifications are possible when J=N (S=0) or N=R as in Σ states. The full matrix elements of Eq. (E.1) can be factored into

$$n(N) \times P(N,J) \times X(J,M) \quad . \qquad \text{(E.3)}$$

The factor n(N) has three useful forms (Landau and Lifshitz[1], p. 295):

$$n_o(N) = \langle N|\hat{n}|N\rangle = \Omega/N(N+1) \qquad \text{(E.4)}$$

$$\begin{aligned} n_-(N) &= \langle N|\hat{n}|N-1\rangle = \langle N-1|\hat{n}|N\rangle \\ &= \frac{1}{N}\left[\frac{(N-\Omega)(N+\Omega)}{(2N-1)(2N+1)}\right]^{\frac{1}{2}} \end{aligned} \qquad \text{(E.5)}$$

$$\begin{aligned} n_+(N) &= \langle N|\hat{n}|N+1\rangle = \langle N+1|\hat{n}|N\rangle = n_-(N+1) \\ &= \frac{1}{(N+1)}\left[\frac{(N-\Omega+1)(N+\Omega+1)}{(2N+1)(2N+3)}\right]^{\frac{1}{2}} \quad . \end{aligned} \qquad \text{(E.6)}$$

The factor X(J,M) has also three forms (Landau and Lifshitz[1], p.93):

$$X_o(J,M) = \frac{\langle J\ M|\hat{n}|J\ M\rangle}{\langle J|\hat{n}|J\rangle} = M \tag{E.7}$$

$$X_-(J,M) = \frac{\langle J\ M|\hat{n}|J-1\ M\rangle}{\langle J|n|J-1\rangle} = \frac{\langle J-1\ M|\hat{n}|J\ M\rangle}{\langle J-1|n|J\rangle} = \sqrt{J^2 - M^2} \tag{E.8}$$

$$X_+(J,M) = \frac{\langle J\ M|\hat{n}|J+1\ M\rangle}{\langle J|n|J+1\rangle} = \frac{\langle J+1\ M|\hat{n}|J\ M\rangle}{\langle J+1|n|J\rangle} = X_-(J+1)$$

$$= \sqrt{(J+1)^2 - M^2} \tag{E.9}$$

We will not define the quantities in the above ratios rigorously (the denominators are simply $n(J)$, of course), but they help to give a feeling for the kind of factorization that Eq.(E.3) involves.

The factor $P(N,J)$ we shall write in seven forms (Landau and Lifshitz[1], p.104f):

$$P_=(N,J) = \frac{\langle N\ J|\hat{n}|N-1\ J-1\rangle}{\langle N|\hat{n}|N-1\rangle} = \frac{\langle N-1\ J-1|\hat{n}|N\ J\rangle}{\langle N-1|\hat{n}|N\rangle}$$

$$= \sqrt{\frac{(J-S+N)(J+S+N+1)(J+N-S-1)(J+S+N)}{4J^2(2J-1)(2J+1)}} \tag{E.10}$$

$$P_-(N,J) = \frac{\langle N\ J|\hat{n}|N-1\ J\rangle}{\langle N|\hat{n}|N-1\rangle} = \frac{\langle N-1\ J|\hat{n}|N\ J\rangle}{\langle N-1|\hat{n}|N\rangle}$$

$$= \frac{\sqrt{(J-S+N)(J+S+N+1)(S+N-J)(J+S-N+1)}}{2J(J+1)} \tag{E.11}$$

$$P_o(N,J) = \frac{\langle N\ J-1|\hat{n}|N-1\ J\rangle}{\langle N|\hat{n}|N-1\rangle} = \frac{\langle N-1\ J|\hat{n}|N\ J-1\rangle}{\langle N-1|\hat{n}|N\rangle}$$

$$= \sqrt{\frac{(S+N-J)(J+S-N+1)(S+N-J+1)(J+S-N)}{4J^2(2J-1)(2J+1)}} \tag{E.12}$$

$$P_{\overline{o}} = \frac{\langle N\ J|\hat{n}|N-1\ J+1\rangle}{\langle N|\hat{n}|N-1\rangle} = P_{\overline{o}}(N,J) = P_o(N,J+1)$$

$$= \sqrt{\frac{(S+N-J-1)(J+S-N+2)(S+N-J)(J+S-N+1)}{4(J+1)^2(2J+1)(2J+3)}} \qquad (E.13)$$

$$P_{\underline{+}}_{o} = \frac{\langle N\ J|\hat{n}|N+1\ J-1\rangle}{\langle N|\hat{n}|N+1\rangle} = P_o(N+1,J) = P_{\underline{+}}_{o}(N,J)$$

$$= \sqrt{\frac{(S+N-J+1)(J+S-N)(S+N-J+2)(J+S-N-1)}{4J^2(2J-1)(2J+1)}} \qquad (E.14)$$

$$P_+(N,J) = \frac{\langle N\ J|\hat{n}|N+1\ J\rangle}{\langle N|\hat{n}|N+1\rangle} = P_-(N+1,J)$$

$$= \frac{\sqrt{(J-S+N+1)(J+S+N+2)(S+N-J+1)(J+S-N)}}{2J(J+1)} \qquad (E.15)$$

$$P_{\underline{+}}(N,J) = \frac{\langle N\ J|\hat{n}|N+1\ J+1\rangle}{\langle N|\hat{n}|N+1\rangle} = P_{\underline{=}}(N+1,J+1)$$

$$= \sqrt{\frac{(J-S+N+2)(J+S+N+3)(J+N-S+1)(J+S+N+2)}{4(J+1)^2(2J+1)(2J+3)}} \qquad (E.16)$$

It may be noted that all these expressions are real and therefore are elements of symmetric matrices, although this is explicitly indicated only for the first few. Only two each of the formulae for $n(N)$ and $X(J,M)$ are distinct, as indicated. Similarly only three of the $P(N,J)$ formulae are independent, but it is convenient to list all variations explicitly. There also exist forms of $P(N,J)$ which are diagonal in N, but we need not consider them here, since we will only use $P(N,J)$ in dealing with Σ states (in which Ω is effectively zero so that matrix elements diagonal in N are

already multiplied by zero (Eq. E.4). Moreover, for $N(N)$ we give only those matrix elements which are diagonal in Ω. Otherwise the formulae given are complete in accordance with the selection rules $\Delta N = 0, \pm 1$, $\Delta J = 0, \pm 1$, and (for n_z) $\Delta M = 0$.

In the sections that follow, the vibration of the nuclei was not considered explicitly. All results are diagonal in v and apply equally well for all values of v.

2. $^1\Sigma$ States

Setting $N=J$ and $S=0$ in Eqs. (E.10) - (E.16), we find that all $P(N,J)$ are zero except for $P_{\neq}$ and $P_{=}$ which are unity, corresponding respectively to the D and B interactions of Fig. 1 in Chap. III. The matrix element for interaction B is seen to be

$$n_-(J) \cdot X_-(J,M) = \sqrt{\frac{J^2-M^2}{4J^2-1}} \tag{E.17}$$

while that for D is

$$n_+(J) \cdot X_+(J,M) = \sqrt{\frac{(J+1)^2-M^2}{(2J+1)(2J+3)}} = \sqrt{\frac{(J+1)^2-M^2}{4(J+1)^2-1}} \tag{E.18}$$

It is to be expected that the interaction D should have the same matrix elements as interaction B but evaluated at one level higher J; this stems from the symmetric nature of all matrices considered: It is clear that the "D" interactions

for one level are just the "B" interactions for the one just above it.

3. $^1\Pi$ States

The rotational energy levels of $^1\Pi$ states are very similar to those of $^1\Sigma$ states shown in Fig.1, Chap. III. The only differences are that the $J=0$ level does not exist ($J \geq J_\zeta = \Lambda = 1$) and all levels are doubly degenerate (Λ-doubling) with the two sublevels having opposite parity signs. The interactions indicated by B and D in Fig. 1 for $J=2$ must be taken between those sublevels with opposite parity. Differences in the Stark effect matrix elements come from the fact that $\Omega=\Lambda=1$. We must multiply $n_-(J)$ in Eq. (E.17) by $\sqrt{(J-1)(J+1)}/J$ according to Eq. (E.5), and $n_+(J)$ by $\sqrt{J(J+2)/(J+1)}$ by Eq. (E.6). Moreover, there now exist matrix elements diagonal in J. From Eqs. (E.4) and (E.7) these elements, (which are diagonal in all quantum numbers except parity) are given by

$$M_o(J) \cdot X_o(J) = \frac{M\Omega}{J(J+1)} \quad , \tag{E.19}$$

which in this case is just $M/J(J+1)$. Eq. (E.19) is the general form for the rotational matrix elements of the first order Stark effect in Hund's case (a). Eq. (E.19) can be interpreted as the fraction of the dipole moment projected onto the space-fixed z axis, via intermediate projection along the direction of $\vec{J}$ (this assumes that $\vec{\mu}$ precesses

very fast about $\vec{J}$, which in turn precesses much more slowly about $\vec{E}$). Eq. (E.19) is then the product of $\cos(\vec{\mu},\vec{J})$ $= \Omega/\sqrt{J(J+1)}$ and $\cos(\vec{J},\vec{E}) = M/\sqrt{J(J+1)}$ (see Phelps[14], p.10ff). The results are shown in the matrices of Eqs. (16) and (17), Chap. III.

4. $^2\Sigma$ States

The energy levels of a $^2\Sigma^+$ state are shown to scale in Fig. 2, Chap. III for a very large spin-splitting constant γ (see Chap. IV, Sec. 6). Comparison with the $^1\Sigma^+$ state shows that the principal difference is that the electronic spin ($S=\frac{1}{2}$) splits all levels with $N>0$ into two components. According to the rules of vector addition (Landau and Lifshitz[1], p.100) $\vec{J} = \vec{N} + \vec{S}$ means that $J = N - \frac{1}{2}$ or $N + \frac{1}{2}$ as long as $N>0$. When $N = 0$, the only possibility is $J = S = \frac{1}{2}$. It is convenient to categorize the rotational levels according to the direction of S, or more properly, by its component Σ along the internuclear axis. Since we are assuming negligible interaction between $\vec{N}$ and $\vec{S}$, we can quantize J, N, and S and $\vec{J}_\zeta = \vec{N}_\zeta \pm \vec{S}_\zeta$, or $\Omega = \Lambda \pm \Sigma = \Sigma = \pm\frac{1}{2}$. We denote levels with $\Omega=+\frac{1}{2}$ as f_1 levels, in which $J=N+\frac{1}{2}$. The levels with $\Omega=-\frac{1}{2}$ and $J=N-\frac{1}{2}$ are called f_2 levels. The case of $N=0$ we call on f_1 level since formally $J=N+\frac{1}{2}$, even though this level contains both signs of Σ, with respect to which it is degenerate.

Interactions (labeled A) which are diagonal in N have zero matrix elements by Eq. (E.4). The others are given in the following table, wherein the order of the factors $n(N) \cdot P(N,J) \cdot S(J,M)$ has been preserved:

Table E.I

The Squares of the Matrix Elements of a $^2\Sigma$ State. The row and column designators are defined by the interaction labels in Fig. 2, Chap. III.

	1	2
B	$\frac{1}{(4N^2-1)} \cdot \frac{2N-1}{2N+1}((N+\frac{1}{2})^2 - M^2)$	$\frac{1}{(4N^2-1)} \cdot \frac{4}{(4N^2-1)} \cdot M^2$
C	$\frac{1}{(2N+1)(2N+3)} \cdot \frac{4}{(2N+1)(2N+3)} \cdot M^2$	$\frac{1}{(4N^2-1)} \cdot \frac{2N+1}{2N-1} \cdot ((N-\frac{1}{2})^2 - M^2)$
D	$\frac{1}{(2N+1)(2N+3)} \cdot \frac{2N+1}{2N+3} \cdot ((N+\frac{3}{2})^2 - M^2)$	$\frac{1}{(2N+1)(2N+3)} \cdot \frac{2N+3}{2N+1} \cdot ((N+\frac{1}{2})^2 - M^2)$

Since we have included electronic spin through the factor $P(N,J)$, we omit it in evaluating $n(N)$ by setting $\Omega=\Lambda=0$.

As noted for $^1\Sigma$ states, these matrix elements are not all independent; half of them are the same as some other element with N increased by one. This is illustrated in the following diagram which shows how the position of a matrix element is shifted in Table E.I if N is replaced by N+1:

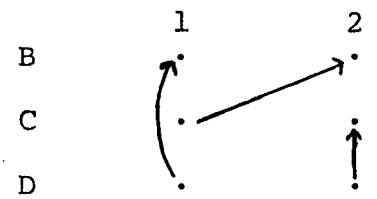

(E.20)

The formulae of Table E.I may be written more concisely in terms of J as follows:

Table E.II

Formulae of Table E.I written in terms of J.

	1	2
B	$\frac{J^2-M^2}{4J^2}$	$\left(\frac{M}{2J(J+1)}\right)^2$
C	$\left(\frac{M}{2J(J+1)}\right)^2$	$\frac{J^2-M^2}{4J^2}$
D	$\frac{(J+1)^2-M^2}{4(J+1)^2}$	$\frac{(J+1)^2-M^2}{4(J+1)^2}$

To interpret the equalities visible in Table E.II, it must be remembered that grouping by equal J causes different interactions to be compared than grouping by equal N: specifically, B2, C2, and D2 must be interpreted as applying to the next higher value of N than that for which they are illustrated in Fig. 2. This makes it obvious that the entries for C1 and B2 should be equal, since they are the same interaction. The relations implied by the vertical arrows in Eq. (E.20) are still valid, replacing J by $J+1$. More interesting, however, are the equalities $B1 = C2$ and $D1 = D2$ in Table E.II. These imply that interactions which are diagonal in Σ (but not in J) are independent of Σ. Such considerations reveal that there are really only two distinct matrix elements: those which are diagonal in Σ but not J (B1, D1, C2, D2), and those which are diagonal in J but not Σ. (B2, C1).

5. $^2\Pi$ States

We shall assume Hund's case (a) coupling. The electronic spin is entirely contained within Ω, so that the factor $P(N,J)$ may be dropped, as for singlet states. The factors $X(J,M)$ are the same as in $^2\Sigma$ states. $n(N)$ becomes $n(J)$, since J is now the resultant of axial and rotational angular momentum. Due to the electric dipole selection rule on Σ ($\Delta\Sigma=0$), different values of Σ (and therefore of Ω) can not interact in pure case (a). This is quite convenient, because it means that each multiplet

sequence ($^2\Pi_{\frac{1}{2}}$ or $^2\Pi_{\frac{1}{2}}$) may be treated as a separate $^1\Pi$ state with half-integral values of J and Ω. The levels of a $^2\Pi$ state are illustrated in Fig. 3, Chap. III, qualitatively as they are found in the ground electronic and vibrational state of the OH molecule (after Moore and Richards[15]). The subscript i indicates an inverted state, meaning that the $\Pi_{\frac{3}{2}}$ multiplet lies energetically lower than the $\Pi_{\frac{1}{2}}$. The rotational levels may be categorized as f_1 and f_2, and values of N assigned according to $N \equiv J-\frac{1}{2}$ for f_1 and $N \equiv J+\frac{1}{2}$ for f_2 levels.

The interactions shown in Fig. 3, Chap. III are for one sublevel of a Λ-doublet only; the other sublevel enjoys entirely equivalent interactions with neighbouring levels of opposite parity. The same formulae for the squares of n_z are applicable to both f_1 and f_2 levels:

$$B \qquad \frac{(J^2-\Omega^2)(J^2-M^2)}{J^2(4J^2-1)} \qquad (E.21)$$

$$D \qquad \frac{((J+1)^2-\Omega^2)((J+1)^2-M^2)}{(J+1)^2(4(J+1)^2-1)} \quad .$$

Since all non-zero matrix elements are diagonal in Σ (i.e., there are none between f_1 and f_2 levels), there are only two distinct types of terms: those diagonal (A) and those off-diagonal (B,D) in J. It should be

remembered that we are evaluating these for pure case (a), which (unlike the structure shown in Fig. 3, Chap. III) must be such that the distance between the f_1 and f_2 levels of same J is much larger than the differences between adjoining rotational levels.

6. $^3\Sigma$ States

Rotational energy levels with parities appropriate for a $^3\Sigma^-$ state are shown schematically in Fig. 4, Chap. III. It should be noted that the order and spacing of levels within each triplet is shown for convenience in labeling; in a more typical case (NH, see Fig. 39, Chap. XI) the f_2 level is highest, and f_3 lowest. These level categories are defined in Chap. V. In the ground state, J equals S, and the degeneracy of levels of different (and thus different M) is not removed. The matrix elements of n_z are calculated in the same way as for the doublet case, setting $\Omega=\Lambda=0$ in Eqs. (E.4) to (E.6). Fig. 4, Chap. III, shows that the factors P_o^+ and P_o^- appear in the interactions labeled B1 and C3, respectively. The results are summarized in Table E.III.

Table E.III

The squares of the matrix elements of n_z in a $^3\Sigma$ state. The row and column designators are defined by Fig. 4, Chap. III.

	1	2	3
B	$\frac{(N+1)^2 - M^2}{(N+1)^2(2N+1)^2(2N+3)^2}$	$\frac{M^2}{N^2(N+1)(2N+1)}$	$\frac{M^2}{N^2(N-1)(2N-1)}$
C	$\frac{M^2}{(N+1)^2(N+2)(2N+3)}$	$\frac{M^2}{N(2N+1)(N+1)^2}$	$\frac{N^2-M^2}{N^2(2N-1)^2(2N+1)^2}$
D	$\frac{((N+2)^2 - M^2)(N+1)}{(2N+3)^2(N+2)}$	$\frac{((N+1)^2-M^2)N(N+2)}{(N+1)^2(2N+1)(2N+3)}$	$\frac{(N^2-M^2)(N+1)}{N(2N+1)^2}$
E	$\frac{((N+1)^2-M^2)N}{(N+1)(2N+1)^2}$	$\frac{(N^2-M^2)(N-1)(N+1)}{N^2(2N-1)(2N+1)}$	$\frac{((N-1)^2-M^2)N}{(N-1)(2N-1)^2}$

As before, half of the formulae in Table E.III can be obtained from the remainder by replacing N with N+1. These relationships are summarized in the diagram of Eq.(E.22), which illustrates where matrix elements reappear when the next higher value of N is used:

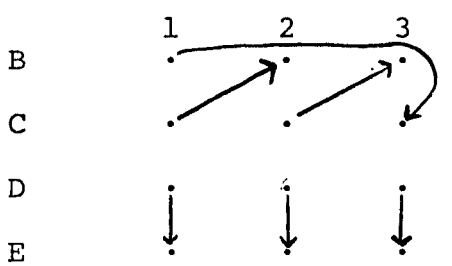

(E.22)

The equivalent of Table E.III expressed in terms of J may be written out in a straightforward manner; no marked simplification results in the case, however.

7. $^3\Pi$ States

The upper half of Fig. 39, Chap. XI, depicts the energy levels of a $^3\Pi_i$ state as they lie in the excited NH molecule. This state is treated exactly the same as the $^2\Pi$ state, and Eqs. (E.19) and (E.21) are still valid.

REFERENCES

1. L.D. Landau and E.M. Lifshitz, "Quantum Mechanics", (Addison-Wesley Publishing Co.,Inc., Reading, Mass., 1958, 1st edit.).

2. J.T. Hougen, "The Calculation of Rotational Energy Levels andRotational Line Intensities in Diatomic Molecules" (Nat. Bur. Std.(U.S.), Monogr. 115, 1970).

3. G.Herzberg, "The Spectra of Diatomic Molecules" (D. Van Nostrand Reinhold Co.,New York, 1950).

4. W.S. Benedict and E.K. Plyler, U.S. Nat. Bur. Stds. Circ. 523, "Energy Transfer in Hot Gases", p.57 (U.S. Govt. Printing Office, Washington, D.C., 1954).

4a. J.M. Brown, A.R.H. Cole, and F.P. Honey, Mol.Phys.,23, 287 (1972).

4b. F.A. Blum, K.W. Nill, and A.J. Strauss, J. Chem. Phys., 58, 4968 (1973).

5. M.F. Crawford, and I.R. Dagg, Phys. Rev., 91, 1569 (1953).

6. M.F. Crawford, H.L. Welsh, and J.L. Locke, Phys. Rev., 75, 1607, (1949).

7. J.K.L. McDonald, Proc. Roy. Soc.(London), 123, 103 (1929).

8. D.H. Phelps and F.W. Dalby, Can. J. Phys., 43, 144 (1965).

9. P.M. Morse and H. Feshbach, "Methods of Theoretical Physics" (McGraw-Hill, New York, 1953).

10. P. Kusch and H.K. Hughes, Handbuch der Physik, 37, p.139, (Springer-Verlag, Berlin, 1956).

11. R.K. Hinkley, J.A. Hall, T.E.H. Walker, and W.G. Richards, J. Phys. B, 5, 204 (1972).

12. L. Veseth, Mol. Phys., 21, 287 (1971).

13. J.C. Swartz and J.W. Trischka, Phys. Rev.,88, 1085 (1952).

14. D.H. Phelps, Ph.D. thesis (Univ. of British Columbia, 1966).

15. E.A. Moore and W.G. Richards, Physica Scripta, 3, 223 (1971).

16. A.J. Merer, Mol. Phys., 23, 309 (1972).

17. J.H. Van Vleck, Rev. Mod. Phys., 23, 213 (1951).

18. E. Hill and J.H. Van Vleck, Phys. Rev., 32, 250 (1928).

19. L. Veseth, J. Phys. B, 5, 229 (1972).

20. J.T. Hougen, J. Chem. Phys., 37, 1433 (1962).

21. J. Millman, "Vacuum Tube and Semiconductor Electronics" (McGraw-Hill, New York, 1958), pp.295-304.

22. J.D. Cobine,"Gaseous Conductors" (McGraw-Hill, New York, 1941) Chap. VIII.

23. L.B. Loeb, "Fundamental Processes of Electrical Discharges in Gases" (John Wiley, New York, 1939)

24. R. Warren, Phys. Rev., 98, 1658 (1955).

25. F. Llewellyn-Jones, "The Glow Discharge" (Methuen and Co., Ltd. of Spottiswoode, Ballantyne and Co., Ltd., London, 1966).

26. G. Francis, Handbuch der Physik, 22, 53 (Springer-Verlag, Berlin, 1956), S. Flügge, ed.

27. M.J. Druyvesteyn and F.M. Penning, Rev. Mod. Phys., 12, 87 (1940), pp.128-140 in particular.

28. R. Warren, Phys. Rev., 98, 1650 (1955).

29. Y. Ishida and T. Tamura, Sci. Pap. Inst. Phys. Chem. Res. (Japan), 21, 158 (1933).

30. A.L. Ward, Phys. Rev., 112, 1852 (1958).

31. A.L. Ward and E. Jones, Phys. Rev., 122, 376 (1961).

32. A.L. Ward, J. Appl. Phys., 33, 2789 (1962).

33. J.J. Thomson and G.P. Thomson, "Conduction of Electricity through Gases", Vol. 2 (Cambridge Press, Cambridge, 3rd edit., 1933).

34. F.W. Aston, Proc. Roy. Soc.(London) A, 79, 80 (1907).

35. F.M. Penning, Physica, 5, 286 (1938).

36. W.D. Davis and T.A. Vanderslice, Phys. Rev., 131, 219 (1963).

37. N.V. Volkov, Sov. Phys.—Tech. Phys. (U.S.A.), 13 765 (1968).

38. F.W. Aston, Proc. Roy. Soc. (London), 84, 526 (1911).

39. G. Holst and E. Oosterhuis, Phil. Mag., 46, Ser. 6, 1117 (1923). Also R.G.Fowler, Handbuch der Physik,22,209.

40. R.N. Varney, Phys. Rev., 93, 1156 (1954).

41. V.T. Chiplonkar, Proc. Indian Acad. Sci. A, 12, 440 (1940).

42. D. Kamke, Z. Physik, 128, 212 (1950).

43. V.T. Chiplonkar and S.N. Toshi, Physica, 30, 1746, (1964).

44. V.T. Chiplonkar and S.N. Toshi, Physica, 32, 145, (1965).

45. A. LoSurdo, Rend. Accad. Lincei, 22, 665 (1913).

46. J. Stark, Ann. Physik, 43, 965 (1914).

47. Y. Ishida, Nature, 122, 277 (1928).

48. Y. Ishida, Nature, 124, 129 (1929).

49. Y. Ishida and G. Kamijima, Sci. Pap. Inst. Phys. Chem. Res. (Japan), 9, 117 (1928/29).

50. Y. Ishida and S. Hiyama, Sci. Pap. Inst. Phys. Chem. Res. (Japan), 9, 1 (1928).

51. Y. Ishida, Sci. Pap. Inst. Phys. Chem. Res. (Japan), 13, 115 (1930).

52. Y. Ishida, Sci. Pap. Inst. Phys. Chem. Res. (Japan), 14, 49 (1930).

53. Y. Ishida, S. Hiyama, and H. Kubata, Sci. Pap. Inst. Phys. Chem. Res.(Japan), 31, 265 (1937).

54. M. Kiuti, Z. Physik, 57, 658 (1929).

55. M. Kiuti, K. Ochiai, and Y. Nishimura, Japan J. Phys., 5, 139 (1929).

56. M. Kiuti, Japan J. Phys., 1, 29 (1922); 4, 13 (1924).

57. Y. Ishida, Sci. Pap. Inst. Phys. Chem. Res. (Japan), 9, Supp. no. 6, 1 (1928); 29, 9 (1936).

58. Y. Ishida and M. Fukishima, Sci. Pap. Inst. Phys. Chem. Res. (Japan), 14, 123 (1930).

59. Y. Ishida, T. Tamura, and G. Kamijima, Sci. Pap. Inst. Phys. Chem. Res. (Japan), 36, 12 (1939).

60. Y. Ishida and S. Hiyama, Sci. Pap. Inst. Phys. Chem. Res. (Japan), 36, 390 (1939); 37, 227 (1940).

61. H. Kubota, Sci. Pap. Inst. Phys. Chem. Res. (Japan), 36, 7 (1939).

62. Y. Ishida and M. Fukishima, Sci. Pap. Inst. Phys. Chem. Res. (Japan), 9, 141 (1928).

63. K. Liden, Ark. Mat. Astr. Och. Fys., 35, no. 23 (1948).

64. E.U. Condon and G.H. Shortley, "The Theory of Atomic Spectra" (Cambridge Press, Cambridge, England, 1964).

65. J.S. Foster, Proc. Roy. Soc. (London), 117, 137 (1927).

66. H. Snell, Phil. Trans. Roy. Soc. (London), 234A, 115 (1935).

67. G. Hayakawa, Proc. Phys. Math. Soc. Japan (Nippon Suugaku-Buturigakkwai Kizi), Series 3, 23, 318 (1941).

68. J.K.L. MacDonald, Proc. Roy. Soc. (London), A, 138, 183 (1932).

69. H.A. Bethe and E.E. Salpeter, "The Quantum Mechanics of One and Two Electron Atoms" (Springer-Verlag, Berlin, 1957).

70. D.H. Phelps and F.W. Dalby, Phys. Rev. Letters, 16, 3 (1966).

71. T.A.B. Irwin, Master's Thesis, U.B.C., (April, 1965).

72. T.A.B. Irwin and F.W. Dalby, Can. J. Phys., 43, 144 (1965).

73. S.Y. Wong, Master's Thesis, U.B.C., (Sept., 1966).

74. R. Thomson and F.W. Dalby, Can J. Phys., 46, 2815 (1968).

75. R. Thomson and F.W. Dalby, Can. J. Phys., 47, 1155 (1969).

76. N.J. Fisher, Master's Thesis, U.B.C., (Sept., 1972).

77. E.A. Scarl and F.W. Dalby, Can. J. Phys., 49, 2825 (1971).

78. K. Takatsu and T. Toda, Electrical Engineering in Japan, 86, 29 (1966).

79. H. Plesse, Ann. Physik, 22, 473 (1935).

80. P.D. Kueck and A.K. Brewer, Rev. Sci. Instr., 3, 427 (1932).

81. W.H. McCurdy, Phil. Mag., 48, 898 (1924).

82. K.T. Compton, L.A. Turner, and W.H. McCurdy, Phys. Rev., 24, 597 (1924).

83. M. Yoshimini, Phys. Soc. Jap., 25, 1103 (1968).

84. P.E. Cade and W.M. Huo, J. Chem. Phys., 45, 1063 (1966).

85. C.F. Bender and E.R. Davidson, Phys Rev., 183, 23 (1969).

86. R.N. Taylor, W.H. Parker, and D.N. Langenberg, Rev. Mod. Phys., 41, 477 (1969).

87. L.T. Earls, Phys. Rev., 48, 423 (1935).

88. G.H. Dieke and H.M. Crosswhite, "The Ultraviolet Bands of the OH Molecule" (Bumblebee Report No. 87, Johns Hopkins University, 1948), also reprinted in J. Quant. Spectrosc. Radiat. Transfer, 2, 97 (1962).

89. H. Oura and M. Ninomiya, Proc. Phys. Math. Soc. Japan (Nippon Suugaku-Buturigakkwai Kizi), 25, 335 (1943).

90. M. Ishaq, Proc. Nat. Inst. Sci. India, 3, 389 (1937), supplemented by Proc. Nat. Inst. Sci. India, 5, 309 (1939).

91. M. Ishaq, Proc. Phys. Soc., 53, 355 (1941).

92. M.G. Sastry, Indian J. Phys., 15, 455 (1941).

93. G.C. Dousmanis, T.M. Sanders, Jr., and C.H. Townes, Phys. Rev., 100, 1735 (1955).

94. P.N. Clough, A.H. Curran, and B.A. Thrush, Proc. Roy. Soc. (London) A, 323, 541 (1971).

95. K.P. Lee, W.G. Tam, R. Larouche, and G.A. Woonton, Can. J. Phys., 49, 2207 (1971).

96. E. Radford, Phys. Rev.,126, 1035 (1962).

97. R.L. Poynter and R.A. Beaudet, Phys. Rev. Lett., 21, 305 (1968).

98. F.X. Powell and D.R. Lide, J. Chem. Phys., 42, 4201 (1965).

99. P.E. Cade, J. Chem. Phys.,47, 2390 (1967).

100. P.E. Cade, private communication (1971).

101. C. Carlone and F.W. Dalby, Can. J. Phys., 47, 1945, (1969).

102. E.M. Weinstock and R.N. Zare, to be published.

103. A.E. Douglas and P.M. Routly, Astrophys. J. Suppl., 1, 295 (1955).

104. I. Gerö, Z. Physik, 118, 27 (1941).

105. N.H. Keiss and H.P. Broida, Astrophys. J., 123, 166 (1956).

106. A.E. Douglas and G.A. Elliott, Can. J. Phys., 43, 496 (1965).

107. G. Funke, Z. Physik, 96, 787 (1935), also Z. Physik, 101, 104 (1936).

108. R.N. Dixon, Can. J. Phys., 37, 1171 (1959).

109. T. Murai and M. Shimauchi, Science of Light (Japan), 15, 48 (1966).

110. R.W.B. Pearse, Proc. Roy. Soc. (London) A, 143, 112 (1934).

111. G.H. Dieke and R.W. Blue, Phys. Rev., 45, 395 (1934).

112. G. Nakamura and T. Shidei, Jap. J. Phys., 10, 5 (1934).

113. M. Shimauchi, Science of Light, 13, 53 (1964).

114. D. Coster, F. Brons, and A. van der Ziel, Z. Physik, 84, 304 (1933).

115. M. Horani, J. Rostas, and H. Lefebvre-Brion, Can. J. Phys., 45, 3319 (1967).

116. R.N. Dixon, private communication (1972).

117. A. Budó, Z. Physik, 105, 579 (1937).

118. J.F. Harrison, Ph. D. Thesis, Princeton University (1967). The dipole moment given in Table XIX was quoted by Krauss[130]

119. J. Kouba and Y. Öhrn, J. Chem. Phys., 52, 5387 (1970).

120. B.D. Joshi, J. Chem. Phys., 43, No. 10, S40 (1965).

121. N. Grün, Z. Naturforsch., 21A, 1869 (1966).

122. M.E. Boyd, J. Chem. Phys., 29, 108 (1958).

123. M. Krauss and J.F. Wehner, J. Chem. Phys., 29, 1287 (1958).

124. M. Krauss, J. Chem. Phys., 28, 1021 (1958).

125. J. Higuchi, J. Chem. Phys., 24, 535 (1956).

126. A.C. Hurley, Proc. Roy. Soc. (London) A, 248, 131 (1958).

127. L. Wharton, L. Gold, and W. Klemperer, J. Chem. Phys., 37, 2149 (1962).

128. W. Huo, J. Chem. Phys., 49, 1482 (1968).

129. R. Weiss, Phys. Rev., 131, 659 (1963).

130. M. Krauss, "Compendium of ab initio Calculations of Molecular Energies and Properties" (Nat. Bur. Std. (U.S.), Technical Not 438, 1967).

131. W.G. Richards, T.E.H. Walker, and R.K. Hinkley, "A Bibliography of ab initio Molecular Wave Functions" (Oxford University Press, London, 1971).